GLOBAL POLARIZATION OF THE $\Lambda/\overline{\Lambda}$ SYSTEM IN THE STAR BES

DISSERTATION

Presented in Partial Fulfillment of the Requirements for the Degree Doctor of Philosophy in the Graduate School of The Ohio State University

By

Isaac Upsal, B.S. & M.S.

Graduate Program in Physics

The Ohio State University

2018

Dissertation Committee:

Dr. Michael Lisa, Advisor

Dr. Andrew Heckler

Dr. Ulrich Heinz

Dr. Thomas Humanic

ABSTRACT

We present the global polarization of Λ and $\overline{\Lambda}$ hyperons in Au+Au collisions at $\sqrt{s_{\rm NN}}$ = 7.682, 11.454, 14.546, 19.564, 26.994, and 38.996GeV [1]. The global polarization is a measure of the alignment of final state particle spin with total collision system angular momentum, and is given as a percentage. Averaging over $\sqrt{s_{\rm NN}}$ the values of the polarization for these particles is $\overline{P}_{\Lambda} = 1.08 \pm 0.15(\text{stat}) \pm 0.11(\text{sys})\%$ and $\overline{P}_{\overline{\Lambda}} = 1.38 \pm 0.30(\text{stat}) \pm 0.13(\text{sys})\%$. This represents the first non-trivial measurement of this type. The data was recorded by the STAR collaboration. Positive polarization represents positive vorticity in the fireball. We also present a method for extracting this vorticity from the data while accounting for polarized particle feed down [2]. The extracted vorticity is $\omega = (9 \pm 1) \times 10^{21} \text{s}^{-1}$ with a systematic scaling uncertainty of 2, primarily due to uncertainty in the temperature. Such a vorticity far exceeds any other known vorticity lending a new superlative to the QGP: "the most vortical fluid".

I dedicate this thesis to THOR computing

VITA

December, 1988	Born—Tucson, Arizona
May, 2011	B.S. in Physics, University of Arizona, Tucson, Arizona
September, 2013	M.S. in Physics, The Ohio State University, Columbus, Ohio

Publications

Primary author on research papers #13 and #18 as well as conference proceedings #4 and #20.

1. **"Correlation Measurements Between Flow Harmonics in Au+Au Collisions at RHIC"**
   J. Adam *et al.* [STAR Collaboration].
   arXiv:1803.03876 [nucl-ex]
   INSPIRE-HEP entry

2. **"Azimuthal anisotropy in Cu+Au collisions at $\sqrt{s_{NN}}$ = 200 GeV"**
   L. Adamczyk *et al.* [STAR Collaboration].
   arXiv:1712.01332 [nucl-ex]
   INSPIRE-HEP entry

3. **"Transverse spin-dependent azimuthal correlations of charged pion pairs measured in $p^{\uparrow}$+p collisions at $\sqrt{s}$ = 500 GeV"**
   J. Adams *et al.* [STAR Collaboration].
   arXiv:1710.10215 [hep-ex]
   INSPIRE-HEP entry

4. **"Observation of Global Hyperon Polarization in Ultrarelativistic Heavy-Ion Collisions"**
   I. Upsal [STAR Collaboration].
   DOI:10.1016/j.nuclphysa.2017.05.118
   Nucl. Phys. A **967**, 760 (2017).
   INSPIRE-HEP entry

5. **"Measurement of ${}^{3}_{\Lambda}$H lifetime in Au + Au collisions at the Relativistic Heavy-Ion Collider"**
L. Adamczyk *et al.* [STAR Collaboration].
arXiv:1710.00436 [nucl-ex]
INSPIRE-HEP entry

6. **"Collision Energy Dependence of Moments of Net-Kaon Multiplicity Distributions at RHIC"**
L. Adamczyk *et al.* [STAR Collaboration].
arXiv:1709.00773 [nucl-ex]
INSPIRE-HEP entry

7. **"Beam-Energy Dependence of Directed Flow of Λ, $\bar{\Lambda}$, $K^{\pm}$, K^{0}_{s} and ϕ in Au+Au Collisions"**
L. Adamczyk *et al.* [STAR Collaboration].
arXiv:1708.07132 [hep-ex]
DOI:10.1103/PhysRevLett.120.062301
Phys. Rev. Lett. **120**, no. 6, 062301 (2018)
INSPIRE-HEP entry

8. **"Azimuthal transverse single-spin asymmetries of inclusive jets and charged pions within jets from polarized-proton collisions at $\sqrt{s} = 500$ GeV"**
L. Adamczyk *et al.* [STAR Collaboration].
arXiv:1708.07080 [hep-ex]
DOI:10.1103/PhysRevD.97.032004
Phys. Rev. D **97**, no. 3, 032004 (2018)
INSPIRE-HEP entry

9. **"Beam Energy Dependence of Jet-Quenching Effects in Au+Au Collisions at $\sqrt{s_{\rm NN}}$ = 7.7, 11.5, 14.5, 19.6, 27, 39, and 62.4 GeV"**
L. Adamczyk *et al.* [STAR Collaboration].
arXiv:1707.01988 [nucl-ex]
INSPIRE-HEP entry

10. **"Coherent diffractive photoproduction of 0 mesons on gold nuclei at 200 GeV/nucleon-pair at the Relativistic Heavy Ion Collider"**
L. Adamczyk *et al.* [STAR Collaboration].
arXiv:1702.07705 [nucl-ex]
DOI:10.1103/PhysRevC.96.054904
Phys. Rev. C **96**, no. 5, 054904 (2017)
INSPIRE-HEP entry

11. **"Measurements of jet quenching with semi-inclusive hadron+jet distributions in Au+Au collisions at $\sqrt{s_{NN}}$ = 200 GeV"**
L. Adamczyk *et al.* [STAR Collaboration].
arXiv:1702.01108 [nucl-ex]
DOI:10.1103/PhysRevC.96.024905
Phys. Rev. C **96**, no. 2, 024905 (2017)
INSPIRE-HEP entry

12. **"Bulk Properties of the Medium Produced in Relativistic Heavy-Ion Collisions from the Beam Energy Scan Program"**

L. Adamczyk *et al.* [STAR Collaboration].
arXiv:1701.07065 [nucl-ex]
DOI:10.1103/PhysRevC.96.044904
Phys. Rev. C **96**, no. 4, 044904 (2017)
INSPIRE-HEP entry

13. **"Global Λ hyperon polarization in nuclear collisions: evidence for the most vortical fluid"**
L. Adamczyk *et al.* [STAR Collaboration].
arXiv:1701.06657 [nucl-ex]
DOI:10.1038/nature23004
Nature **548**, 62 (2017)
INSPIRE-HEP entry

14. **"Constraining the initial conditions and temperature dependent transport with three-particle correlations in Au+Au collisions"**
L. Adamczyk *et al.* [STAR Collaboration].
arXiv:1701.06497 [nucl-ex]
INSPIRE-HEP entry

15. **"Harmonic decomposition of three-particle azimuthal correlations at RHIC"**
L. Adamczyk *et al.* [STAR Collaboration].
arXiv:1701.06496 [nucl-ex]
INSPIRE-HEP entry

16. **"Measurement of D^0 Azimuthal Anisotropy at Midrapidity in Au+Au Collisions at $\sqrt{s_{NN}}$=200GeV"**
L. Adamczyk *et al.* [STAR Collaboration].
arXiv:1701.06060 [nucl-ex]
DOI:10.1103/PhysRevLett.118.212301
Phys. Rev. Lett. **118**, no. 21, 212301 (2017)
INSPIRE-HEP entry

17. **"Measurement of the cross section and longitudinal double-spin asymmetry for di-jet production in polarized pp collisions at $\sqrt{s}$ = 200 GeV"**
L. Adamczyk *et al.* [STAR Collaboration].
arXiv:1610.06616 [hep-ex]
DOI:10.1103/PhysRevD.95.071103
Phys. Rev. D **95**, no. 7, 071103 (2017)
INSPIRE-HEP entry

18. **"Global hyperon polarization at local thermodynamic equilibrium with vorticity, magnetic field and feed-down"**
F. Becattini, I. Karpenko, M. Lisa, I. Upsal and S. Voloshin.
arXiv:1610.02506 [nucl-th]
DOI:10.1103/PhysRevC.95.054902
Phys. Rev. C **95**, no. 5, 054902 (2017)
INSPIRE-HEP entry

19. **"Dijet imbalance measurements in $Au+Au$ and pp collisions at $\sqrt{s_{NN}} = 200$GeV at STAR"**
L. Adamczyk *et al.* [STAR Collaboration].

arXiv:1609.03878 [nucl-ex]
DOI:10.1103/PhysRevLett.119.062301
Phys. Rev. Lett. **119**, no. 6, 062301 (2017)
INSPIRE-HEP entry

20. **"Observation of Global Hyperon Polarization in Ultrarelativistic Heavy Ion Collisions"**
I. Upsal [STAR Collaboration].
DOI:10.1088/1742-6596/736/1/012016
J. Phys. Conf. Ser. **736**, no. 1, 012016 (2016).
INSPIRE-HEP entry

21. **"Υ production in U + U collisions at $\sqrt{s_{NN}} = 193$ GeV measured with the STAR experiment"**
L. Adamczyk *et al.* [STAR Collaboration].
arXiv:1608.06487 [nucl-ex]
DOI:10.1103/PhysRevC.94.064904
Phys. Rev. C **94**, no. 6, 064904 (2016)
INSPIRE-HEP entry

22. **"Charge-dependent directed flow in Cu+Au collisions at $\sqrt{s_{NN}}$ = 200 GeV"**
L. Adamczyk *et al.* [STAR Collaboration].
arXiv:1608.04100 [nucl-ex]
DOI:10.1103/PhysRevLett.118.012301
Phys. Rev. Lett. **118**, no. 1, 012301 (2017)
INSPIRE-HEP entry

23. **"Energy dependence of J/ψ production in Au+Au collisions at $\sqrt{s_{NN}} = 39$, 62.4 and 200 GeV"**
L. Adamczyk *et al.* [STAR Collaboration].
arXiv:1607.07517 [hep-ex]
DOI:10.1016/j.physletb.2017.04.078
Phys. Lett. B **771**, 13 (2017)
INSPIRE-HEP entry

24. **"Direct virtual photon production in Au+Au collisions at $\sqrt{s_{NN}}$ = 200 GeV"**
L. Adamczyk *et al.* [STAR Collaboration].
arXiv:1607.01447 [nucl-ex]
DOI:10.1016/j.physletb.2017.04.050
Phys. Lett. B **770**, 451 (2017)
INSPIRE-HEP entry

25. **"Jet-like Correlations with Direct-Photon and Neutral-Pion Triggers at $\sqrt{s_{NN}} = 200$ GeV"**
L. Adamczyk *et al.* [STAR Collaboration].
arXiv:1604.01117 [nucl-ex]
DOI:10.1016/j.physletb.2016.07.046
Phys. Lett. B **760**, 689 (2016)
INSPIRE-HEP entry

26. **"Near-side azimuthal and pseudorapidity correlations using neutral strange baryons and mesons in d+Au, Cu+Cu and Au+Au collisions at $\sqrt{s_{NN}}$ = 200 GeV"**
B. Abelev *et al.* [STAR Collaboration].

arXiv:1603.05477 [nucl-ex]
DOI:10.1103/PhysRevC.94.014910
Phys. Rev. C **94**, no. 1, 014910 (2016)
INSPIRE-HEP entry

27. **"J/ψ production at low transverse momentum in p+p and d+Au collisions at $\sqrt{s_{NN}}$ = 200 GeV"**
L. Adamczyk *et al.* [STAR Collaboration].
arXiv:1602.02212 [nucl-ex]
DOI:10.1103/PhysRevC.93.064904
Phys. Rev. C **93**, no. 6, 064904 (2016)
INSPIRE-HEP entry

28. **"Measurement of elliptic flow of light nuclei at $\sqrt{s_{NN}} = 200$, 62.4, 39, 27, 19.6, 11.5, and 7.7 GeV at the BNL Relativistic Heavy Ion Collider"**
L. Adamczyk *et al.* [STAR Collaboration].
arXiv:1601.07052 [nucl-ex]
DOI:10.1103/PhysRevC.94.034908
Phys. Rev. C **94**, no. 3, 034908 (2016)
INSPIRE-HEP entry

29. **"Beam Energy Dependence of the Third Harmonic of Azimuthal Correlations in Au+Au Collisions at RHIC"**
L. Adamczyk *et al.* [STAR Collaboration].
arXiv:1601.01999 [nucl-ex]
DOI:10.1103/PhysRevLett.116.112302
Phys. Rev. Lett. **116**, no. 11, 112302 (2016)
INSPIRE-HEP entry

30. **"Measurement of the transverse single-spin asymmetry in $p^{\uparrow} + p \to W^{\pm}/Z^0$ at RHIC"**
L. Adamczyk *et al.* [STAR Collaboration].
arXiv:1511.06003 [nucl-ex]
DOI:10.1103/PhysRevLett.116.132301
Phys. Rev. Lett. **116**, no. 13, 132301 (2016)
INSPIRE-HEP entry

31. **"Centrality dependence of identified particle elliptic flow in relativistic heavy ion collisions at $\sqrt{s_{NN}}$=7.762.4 GeV"**
L. Adamczyk *et al.* [STAR Collaboration].
arXiv:1509.08397 [nucl-ex]
DOI:10.1103/PhysRevC.93.014907
Phys. Rev. C **93**, no. 1, 014907 (2016)
INSPIRE-HEP entry

32. **"Measurement of Interaction between Antiprotons"**
L. Adamczyk *et al.* [STAR Collaboration].
arXiv:1507.07158 [nucl-ex]
DOI:10.1038/nature15724
Nature **527**, 345 (2015)
INSPIRE-HEP entry

33. **"Centrality and transverse momentum dependence of elliptic flow of multistrange hadrons and ϕ meson in Au+Au collisions at $\sqrt{s_{NN}}$ = 200 GeV"**
L. Adamczyk *et al.* [STAR Collaboration].
arXiv:1507.05247 [nucl-ex]
DOI:10.1103/PhysRevLett.116.062301
Phys. Rev. Lett. **116**, no. 6, 062301 (2016)
INSPIRE-HEP entry

34. **"Beam-energy dependence of charge balance functions from Au + Au collisions at energies available at the BNL Relativistic Heavy Ion Collider"**
L. Adamczyk *et al.* [STAR Collaboration].
arXiv:1507.03539 [nucl-ex]
DOI:10.1103/PhysRevC.94.024909
Phys. Rev. C **94**, no. 2, 024909 (2016)
INSPIRE-HEP entry

35. **"Probing parton dynamics of QCD matter with Ω and ϕ production"**
L. Adamczyk *et al.* [STAR Collaboration].
arXiv:1506.07605 [nucl-ex]
DOI:10.1103/PhysRevC.93.021903
Phys. Rev. C **93**, no. 2, 021903 (2016)
INSPIRE-HEP entry

36. **"Azimuthal anisotropy in U+U and Au+Au collisions at RHIC"**
L. Adamczyk *et al.* [STAR Collaboration].
arXiv:1505.07812 [nucl-ex]
DOI:10.1103/PhysRevLett.115.222301
Phys. Rev. Lett. **115**, no. 22, 222301 (2015)
INSPIRE-HEP entry

37. **"Observation of charge asymmetry dependence of pion elliptic flow and the possible chiral magnetic wave in heavy-ion collisions"**
L. Adamczyk *et al.* [STAR Collaboration].
arXiv:1504.02175 [nucl-ex]
DOI:10.1103/PhysRevLett.114.252302
Phys. Rev. Lett. **114**, no. 25, 252302 (2015)
INSPIRE-HEP entry

38. **"Measurements of Dielectron Production in Au+Au Collisions at $\sqrt{s_{\rm NN}}$ = 200 GeV from the STAR Experiment"**
L. Adamczyk *et al.* [STAR Collaboration].
arXiv:1504.01317 [hep-ex]
DOI:10.1103/PhysRevC.92.024912
Phys. Rev. C **92**, no. 2, 024912 (2015)
INSPIRE-HEP entry

39. **"Observation of Transverse Spin-Dependent Azimuthal Correlations of Charged Pion Pairs in $p^{\uparrow}+p$ at $\sqrt{s} = 200$ GeV"**

L. Adamczyk *et al.* [STAR Collaboration].
arXiv:1504.00415 [hep-ex]
DOI:10.1103/PhysRevLett.115.242501
Phys. Rev. Lett. **115**, 242501 (2015)
INSPIRE-HEP entry

40. **"The $\phi(1020) \to e^+e^-$ meson decay measured with the STAR experiment in Au+Au collisions at $\sqrt{s_{NN}}$ = 200 GeV"**
L. Adamczyk *et al.* [STAR Collaboration].
arXiv:1503.04217 [hep-ex]
INSPIRE-HEP entry

41. **"Long-range pseudorapidity dihadron correlations in d+Au collisions at $\sqrt{s_{\rm NN}} = 200$ GeV"**
L. Adamczyk *et al.* [STAR Collaboration].
arXiv:1502.07652 [nucl-ex]
DOI:10.1016/j.physletb.2015.05.075
Phys. Lett. B **747**, 265 (2015)
INSPIRE-HEP entry

42. **"Energy dependence of acceptance-corrected dielectron excess mass spectrum at mid-rapidity in Au+Au collisions at $\sqrt{s_{NN}} = 19.6$ and 200 GeV"**
L. Adamczyk *et al.* [STAR Collaboration].
arXiv:1501.05341 [hep-ex]
DOI:10.1016/j.physletb.2015.08.044
Phys. Lett. B **750**, 64 (2015)
INSPIRE-HEP entry

43. **"Effect of event selection on jetlike correlation measurement in d+Au collisions at $\sqrt{s_{\rm NN}} = 200$ GeV"**
L. Adamczyk *et al.* [STAR Collaboration].
arXiv:1412.8437 [nucl-ex]
DOI:10.1016/j.physletb.2015.02.068
Phys. Lett. B **743**, 333 (2015)
INSPIRE-HEP entry

Fields of Study

Major Field: Physics

Table of Contents

List of Figures

Figure **Page**

List of Tables

Table **Page**

Chapter 1

INTRODUCTION TO HEAVY-ION PHYSICS

Heavy-ion collision physics is the study of the strong nuclear force, described by quantum chromodynamics (QCD), through the collisions of heavy atomic nuclei (typically systems of Gold-on-Gold or Lead-on-Lead). The unique feature of quantum chromodynamics (QCD) is that the force carrier, the gluon (a massless boson), carries color charge and thus has a self interaction. At high-energy transfer QCD calculations are perturbative (a property known as asymptotic freedom), however at low-energy transfer QCD is non-perturbative, making traditional calculation techniques impossible. Low-energy QCD calculations are performed on finite computer lattices, a technique known as lattice QCD.

At finite baryon/anti-baryon asymmetry (net baryon density) lattice QCD calculations encounter the "numerical sign problem" and break down. It is typical to represent this baryon asymmetry by a chemical potential, the baryon chemical potential (or baryochemical potential) μ_B, which has the units of energy. At zero asymmetry (e.g. early universe) is $\mu_B = 0$, while for normal baryonic matter (e.g. nuclear matter) $\mu_B \sim 1\text{GeV}$ (the scale of nucleon mass). It is possible to extrapolate lattice QCD calculations made at zero baryochemical potential to finite, but low, chemical potential. Such extrapolations quickly become extremely computationally expensive and, thus, untenable. These lattice limitations fall below the densities of normal nuclear matter, and far below that of more exotic systems (e.g. neutron stars, which are more baryon dense due to intense gravity). The baryochemical potential of heavy-ion collisions can be tuned, by adjusting the collision energy, to fall inside or outside of this range.

Unless otherwise stated quantities are quoted in so called "natural units" where the fundamental constants $\hbar = k_B = c = 1$ (that is, in order, the Reduced Planck's constant, the Boltzmann constant and the speed of light).

1.1 Historical overview

The origins of heavy-ion physics predate QCD. In the early days on particle physics there was a veritable gold rush in the identification of new hadronic states. In the mid-1960s Rolf Hagedorn noted that the number of hadronic states of a given mass range increased exponentially with mass. Additionally it was noted at the time that the average transverse momentum of the great majority of the produced particles in a collision did not seem to scale with the energy of the collision (very high-energy collisions were reachable with high-energy cosmic rays). This low momentum spectrum led Hagedorn to suspect that the emission was from a common thermal source and, by fitting this mass spectrum by an exponential function of particle mass over temperature, this temperature was extractable. The extracted temperature, called the "Hagedorn Temperature", was measured to be $\sim$160MeV). Thermal studies struggled at describing the spectrum of the lightest hadron, the pion (m_π $\sim$140MeV). Hagedorn solved this problem with the Statistical Bootstrap Model (SBM), which imagined heavier hadronic states as composites of lighter ones (at this point the lighter particles are understood to be point like), explaining the yields [3, 4, 5].

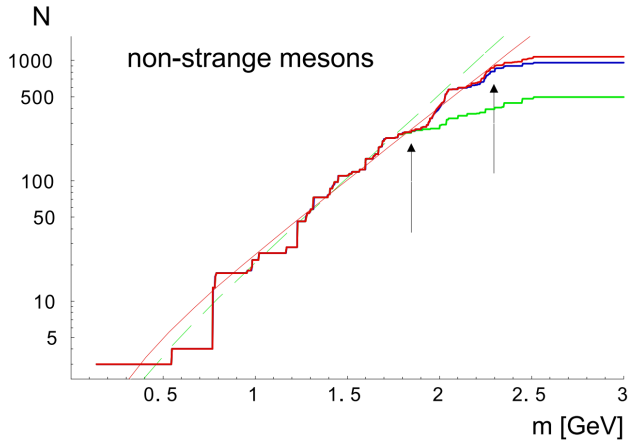

Figure 1.1: Non-strange meson mass spectrum [6]. The lowest red stepped curve is an older collection of mesons, which the higher curves include some newer mesons and mesons expected from theory. Straight lines represent exponential fits of the functional form $\frac{dN}{dM} \sim M^{\alpha}\exp\left(\frac{M}{T_H}\right)$, clearly demonstrating the observations which motivated Hagedorn's suppositions.

Hagedorn imagined that energy added to the system went into making an ever more compressed gas

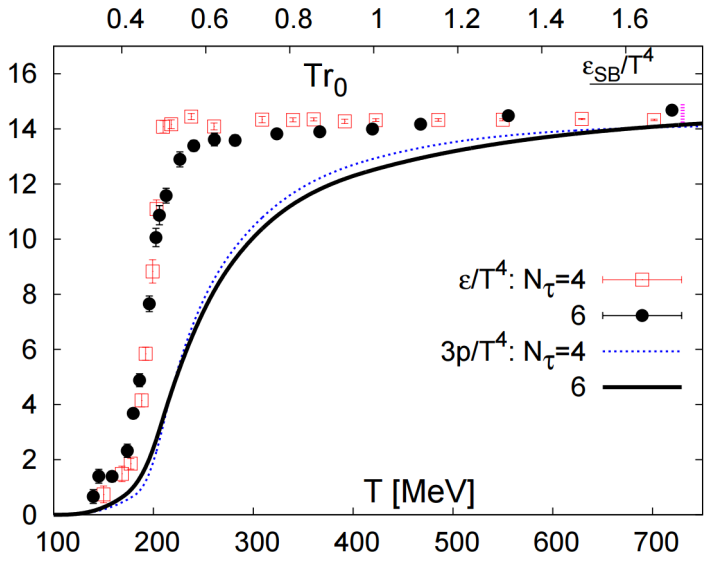

Figure 1.2: Lattice calculations of energy density divided by T^4 [7] which scales as the number of degrees of freedom. The red squares with a 4 temporal bins seem to indicate a flat (and thus no) dependence of ε/T^4 as a function of temperature. The black filled circles show a later calculation with 6 temporal bins. This demonstrates a clear rising of ε/T^4 with temperature.

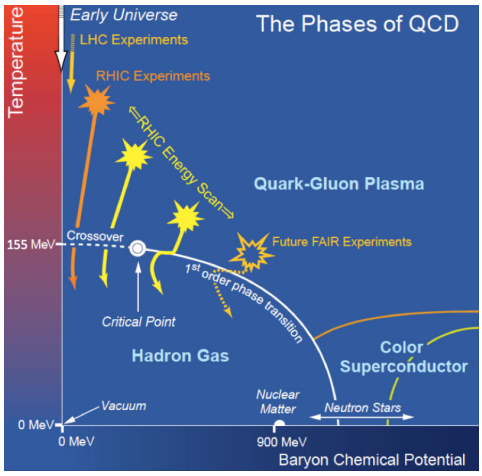

Figure 1.3:

QCD phase diagram [8]. The locations of the great majority of the features of this figure in the T-μ_B space are largely speculative.

of heavier and heavier hadronic states which radiated particles as a 'fireball'. Today we understand these hadronic states in terms of their quark component, but the implication of a maximum temperature for a hadronic gas remains an important and compelling point (in fact the SBM was later modified to consider quarks, but I will not go into this model). From QCD we know that at very high energies quarks are asymptotically free so at some sufficiently high temperature (e.g. in the early universe) the constituent partons should escape their hadronic bounds. This new phase of deconfined and color-charged quarks and gluons is known as the Quark Gluon Plasma (QGP) – the phase of matter the universe was in for the first few microseconds after the Big Bang. The Hagedorn temperature can then be understood as the constant temperature over which energy is transferred into the medium as a latent heat, or, from the other direction, as freezeout temperature of the fluid when the QGP evaporates into hadronic matter. To learn something more exact we can look at lattice QCD data. Fig. 1.2 depicts the energy density divided by the temperature to the fourth power as a function of temperature from lattice calculations, which is proportional to the number of degrees of freedom in the system.

As described by the SBM as the temperature increases the number of degrees of freedom rapidly grows near the freezeout temperature as more and more hadronic states are created. Suddenly the number of degrees of freedom starts to level off as the system becomes a deconfined state of quarks and gluons. Earlier data (red) with larger lattice spacing seemed to suggest a flattening of the curve at the onset of deconfinement which would suggest a saturation in the number of degrees of freedom. As seen in photon ideal gas used to describe black body radiation ε/T^4 being constant is a tell-tale signal of a non-interacting gas. Consequently at the turn on of RHIC in 2000 it was expected that this deconfined state would be best described as a weakly interacting gas. Instead what was found was a strongly coupled plasma of color charges. Retrospectively the non-flatness at high temperature of the lattice data can be seen clearly in the more precise black points with the smaller lattice spacing.

If there is a phase transition it is important to try to characterize the baryonic phase diagram as best we can. Lattice calculations conclude that the transition from baryonic to partonic matter at low baryochemical potential is a smooth crossover [7]. At large baryochemical potential and low temperature several model calculations have led to a (less robust) consensus that there is a first order phase transition [9, 10]. By Gibbs' phase rule these two conditions imply that there must be a critical point. Lattice calculations extrapolated to finite baryochemical potential have been unable to find any signatures of criticality (e.g. divergence of correlation lengths within the medium). The accepted understanding is that the critical point lies in a region of baryochemical potential beyond the acceptable range of extrapolation for lattice calculations. Thus the existence and location of the first-order phase transition as well as the critical point are almost completely unknown. With the information at hand we can sketch any number of qualitatively similar phase diagrams pictures. One such picture is fig. 1.3. Points of orientation are the limits of baryochemical potential and the measured freezeout temperature.

1.2 Modern heavy-ion collision physics

After the millennium the thrust of the field, experimentally, has largely been in the large accelerator projects the Relativistic Heavy-Ion Collider (RHIC) and the Large Hadron Collider (LHC) (though older-style fixed target experiments NA61/SHINE at the SPS and HADES at SIS-18 are still in operation). RHIC is a purpose-built heavy-ion collider which had it's first physics collisions in 2000. At the start of it's operation RHIC

had four separate experiments, all of which were dedicated to heavy-ion measurements (though RHIC has an additional ability to provide polarization proton beams for spin physics). Of the four initial detectors only STAR (to be described in detail later) remains in operation, though data analysis is still underway on others. The LHC is a machine built primarily with high-energy physics in mind, though it is capable of providing heavy-ion beams. The LHC turned on in 2009 with four detectors, one of which (ALICE - A Large Ion Collider Experiment) was built for heavy-ion physics and shares very similar basic design and detection goals with STAR. Two detectors designed for high-energy physics, ATLAS and CMS, have additionally contributed significantly to heavy-ion physics.

In the parlance of heavy-ion collider physics collision energies are quoted in $\sqrt{s_{\mathrm{NN}}}$ which is the center of mass energy of a nucleon-nucleon pair system. Additionally the collision system is abbreviated by the atomic abbreviation for an element (generically an element is abbreviated with an 'A'), p is for proton, d for deuteron, and t for tritium. Discounting datasets not interesting to heavy-ion physics the LHC has provided collisions of pp, pPb, and PbPb at 2.76 and 5.02TeV. RHIC has provided collision systems of pp, pAu, dAu, AuAu, AlAl, CuCu, CuAu, and UU. Most of these systems are collided at or near top RHIC energy (200GeV), though CuCu and dAu collisions were also provided at 62.4 and 19.6GeV. In order to scan the temperature-baryochemical phase space RHIC has provided a suite of AuAu data at 200, 62.4, 39, 27, 19.6, 14.5, 11.5, and 7.7 GeV. AuAu collision data below 62.4GeV is typically branded as the Beam Energy Scan (BES) (though it would be reasonable to include any higher energy in this definition). The goal of the BES program is to explore the QCD phase diagram. As $\sqrt{s_{\mathrm{NN}}}$ is decreased the initial temperature is decreased, but also, due to complicated collision dynamics, the baryochemical increases at the same time. STAR has installed a Au fixed target to increase the $\sqrt{s_{\mathrm{NN}}}$ coverage of the second BES, set to start taking data in 2018.

The relevant scales of a heavy-ion collision are the spatial size ($O(\mathrm{fm})$) and the temporal extent of the fireball ($O\left(\mathrm{fm}/c = 10^{-23}\mathrm{s}\right)$ – the scale of the strong interaction). In most cases the speed of the particles we talk about is so great that it is reasonable to take the approximation that they're going at the speed of light. The nuclei themselves are significantly Lorentz contracted (at top RHIC energy the gamma factor is approximately 100) in the lab frame so nuclei look more like pancakes than spheres. At infinitely high $\sqrt{s_{\mathrm{NN}}}$ the nuclei pass through each other, leaving a energy behind with zero net baryon density. At lower $\sqrt{s_{\mathrm{NN}}}$ original participant nucleons don't totally escape the fireball and deposit non-zero baryochemical potential into it. These violent collisions break the nuclei apart and send the remnants far forward.

Collisions themselves are messy due to the inherent lumpiness of a nucleus (as well as the nucleons themselves) which, subsequently, make a lumpy material of non-homogeneous energy scales and thermalization. The first $\sim$ fm$/c$ of a collision, before any kind of equilibrium is possible, is difficult to describe and is generically called the "pre-equilibrium stage". Afterwards the collision rapidly thermalizes and becomes a QGP (depending on initial energy of the collision). The QGP then freezes out into a gas of hadrons. As this hadron gas becomes sufficiently diffuse the inelastic particles collisions cease and chemical potential ratios are locked in, this is called chemical freezeout. Afterwards all elastic particle interactions cease and the particle momenta are locked in, this is called kinetic freezeout. Realistically the freezeout surfaces for each particle species is different. Of course particles without strong interactions immediately escape the QGP, but the hadrons themselves have different temperature freezeout surfaces generically depending on their mass.

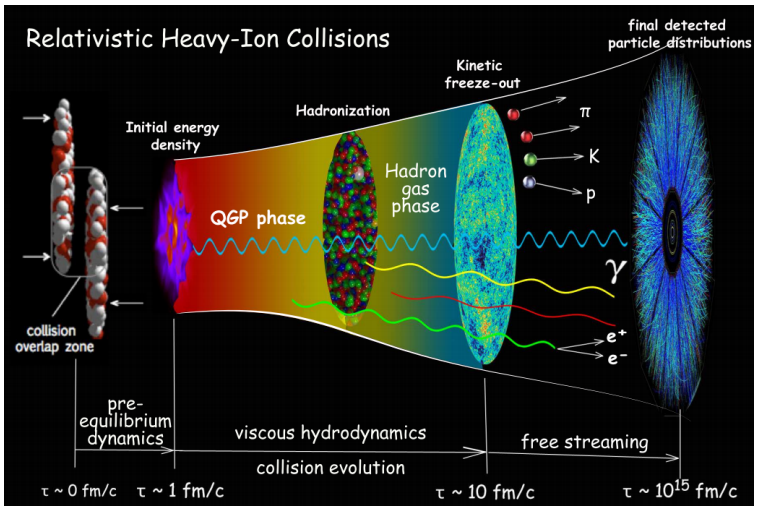

Figure 1.4: Cartoon of freezout for a heavy-ion collision [11].

Due to density fluctuations a real collision carves out a non-zero-width area of the phase diagram as it makes it's way from QGP to non-interacting hadrons. Though the average temperature of the QGP itself is above the perturbative natural scale of QCD, the lumpiness of the collisions is such that the collision dynamics cannot be well described perturbatively. Descriptions of the data are thus phenomenological and are often hybrid models cobbled together to best describe the different stages of the collision. Broadly models may

contain any number of theoretical descriptions or parameterizations of the initial stage, string fragmentation and transport models (UrQMD and AMPT), and hydrodynamic calculations. Initial densities generally start from nucleon densities given by the Woods-Saxon distribution, which is determined experimentally. A nucleon distribution found by sampling a Woods-Saxon is called a Glauber distribution.

1.3 Variables of general interest in heavy-ion collisions physics

There are a number of variables of interest to heavy-ion physics which require some explanation. The first thing to note is that in a collider experiment particle production is greatest along the direction transverse to beam axis ($\hat{z}$). The sign of the z coordinate as well as the choice of the traverse coordinates ($\hat{x}$ and $\hat{y}$) are, in a detector at least, chosen arbitrarily. There is some convention that, in the collision coordinate system, the impact parameter ($\vec{b}$) points in $\hat{x}$ direction. It is thus the case that the transverse momentum, $p_T = \sqrt{p_x^2 + p_y^2}$ is a very common variable in the field. The azimuthal angle is always given in this convention.

Another common variable is the rapidity:

$$y = \frac{1}{2}\log\left(\frac{E + p_z c}{E - p_z c}\right) \tag{1.1}$$

The rapidity is a measure of how far away from the plane of the collision the momentum of the particle points. $y = 0$ at $p_z = 0$ (called midrapidity) and $y = \pm\infty$ for $p_T = 0$ and $p_z > 0$ or $p_z < 0$ (called forward or backward rapidity). The primary advantage of y is that a boost of velocity β along the $\hat{z}$ direction is simply additive in $\tanh^{-1}\beta$. Thus the difference in rapidities between two different particles is a Lorentz invariant. The trouble with rapidity is that it requires knowledge of the energy of the particle (typically the sticking point is the particle's identity). Pseudorapidity is a purely geometric approximation of the rapidity and a perfect match if $\gamma = \infty$. It is defined as $\eta = -\log(\theta/2)$. Aside from describing unidentified particles η is useful for characterizing the coverage of detectors (assuming zero mass particles created in the center of the detector).

Since the nuclei themselves aren't point particles a collision can exhibit a large range of impact parameters. Knowing the degree of overlap is tremendously important for the understanding of many observables. The variable defined for this task is the centrality. Details on the definition of centrality depend on the data under consideration, but the common element is that it is characterized in terms of a percentage of

events with 0% being "very central" and 100% being "very peripheral". Ultimately, of course, this should be chosen to correspond best to impact parameter.

1.4 Overview of heavy-ion physics theory and event generators

The most basic event generators used in some data comparisons are mostly parameterizations of the data. Such generators are not typically used to reconstruct data, but, knowing what goes into the generator allows them to be used as a null hypothesis when compared to data. Another usage is the calculation of detector efficiencies. One such example of an event generator is HIJING. PYTHIA is a parameterization of well understood pp data. HIJING simply constructs AuAu data by sampling nucleon distributions and judiciously placing PYTHIA events at the points of nucleon-nucleon interactions.

Ultra-relativistic Quantum Molecular Dynamics (UrQMD) and A Multi-Phase Transport model AMPT are both models which seek to describe heavy-ion data by calculating all of the dynamics of each particle interaction. Typically both hadronic and partonic transport are components of a calculation. AMPT assumes a change of phase from partonic to hadronic physics. The dynamics of string-based transport calculations is complicated and beyond the scope of this thesis.

Since the system is a thermalized (or mostly thermalized) plasma it can be described by relativistic hydrodynamics for some period of it's evolution. Instead of calculating single particle transport, the interactions are essentially averaged and described with fluid dynamics. Typically full hydrodynamic models are quite complicated sets of different conditions. The first thing one needs are initial conditions for the pre-equilibrium stage. Afterwards the hydrodynamic code is run. Depending on the model in question it may be 2+1 or 3+1 dimensional (that last dimension is time) and may or may not include bulk and shear viscosity. Finally the hydrodynamic simulation reaches some critical temperature where particles are frozen out. At this point it is typical to use an "afterburner" to describe the hadronic interactions until kinetic freezeout occurs. The equation of state from a lattice calculation is an input during the hydrodynamic phase and the shear viscosity is typically found by comparing to flow measurements (more on this later). The initial conditions are still quite poorly understood and different initial conditions will give different values of the viscosity, giving a sense of the theoretical error. In principal if one has every stage of the model under control it would be possible to back-calculate the equation of state (EOS) and compare it to the lattice

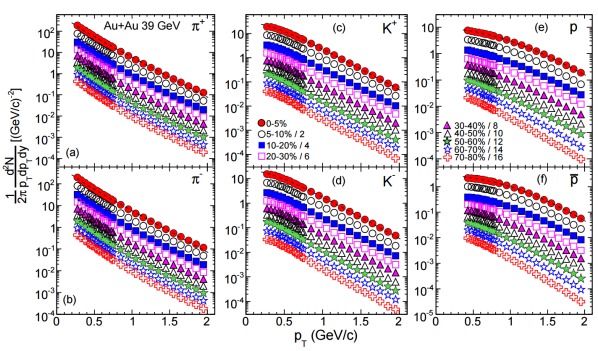

Figure 1.5: STAR particle spectra at $\sqrt{s_{NN}}$ = 39GeV [12]. These figures all depict particle multiplicity as a function of transverse momentum. Different cells are for different identified particles and the different trends are for different event centralities.

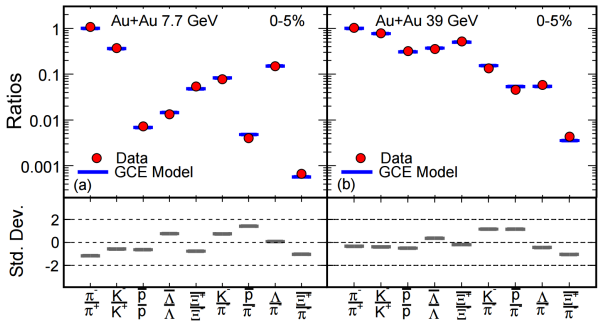

Figure 1.6:
STAR particle spectra fits for 7.7 and 39GeV collisions [12]. The fit function used is a Grand Canonical Ensemble (abbreviated GCE). As can be seen the fit works quite well on the data.

calculations. This is not simply circular as the lattice can only be trusted to small baryochemical potential. The success of hydrodynamic lends considerably confidence to the thermalization hypothesis of heavy-ion collisions.

More simplistic thermal fits of the momentum spectra for hadrons (which, as it happens, is the same exponential slope as found by Hagedorn) fit the data quite nicely once one takes into account the boost the spectrum gets as particles are emitted from an expanding source. The model typically used to correct for this boost (radial flow) is called Blast-Wave. Thermal fits of STAR data are shown in figure 1.6. As one can see the fits describe the data remarkably well. Since this is a measurement of the freezeout surface temperature one will measure the same temperature regardless of how much the maximum temperature of the fireball exceeded the freezeout temperature. In this way the measurement is totally analogous to the temperature measured from the CMB (once it is corrected for red-shift) which is the temperature of the electromagnetic freezeout of the universe.

Perhaps the most basic correlation measurement which is used to test models is flow. Initial position space anisotropies in energy density exist due to basic collision geometry (the nuclei used are typically spheres contracted into disks so the overlap of two nuclei is more typically almond shaped than circular) and fluctuations (nucleon density follows random sampling of a the nuclear density distribution). These position space anisotropies are transferred to momentum space anisotropies via pressure gradients in hydrodynamic

evolution/transport interactions. The momentum space anisotropies can be decomposed into harmonics representing shapes and measured experimentally.

$$E\frac{d^3N}{d^3p} = \frac{1}{2\pi}\frac{d^2N}{p_T dp_T dy}\left(1+\sum_{n=1}^{\infty} 2v_n \cos\left(n\left(\phi-\Psi_n\right)\right)\right) \tag{1.2}$$

The cumulants of this distribution v_n are the flow coefficients and can be found by averaging over particles of interest. They're expressed in terms of their event planes Ψ_n which describe the orientation of the momentum anisotropy. The event planes are found from the "Q-vector"s for particles i and some weight w_i (the weight can be chosen arbitrarily)

$$\vec{Q}_n = \left(\sum_i \cos(n\phi_i), \sum_i \sin(n\phi_i)\right) \tag{1.3}$$

From the Q-vector using the C++ function atan2:

$$\Psi_n = \text{atan2}\left(Q_{n,x}, Q_{n,y}\right)/n. \tag{1.4}$$

Knowing Ψ_n one can get a flow coefficient by averaging over all particles of interest in all collisions

$$v_n = \langle \cos\left(n\left(\phi_i - \Psi_n\right)\right)\rangle \tag{1.5}$$

The second order harmonic decomposition, v_2, represents an elliptic deformation, the third, v_3, represents a triangular deformation, etc. Even orders (especially v_2) are expected from the rough geometry of the overlap region, while odd orders can only come from density fluctuations (which is not to say that such fluctuations are less relevant for the even harmonics). Flow data is fit quite well by hydrodynamic models. The viscosity in the model is chosen by the value which best fits the data. This may seem to diminish the quality of the model as a describer of flow, but it must be remembered that the same fluid gives rise to all orders of flow and that different viscosities could not guarantee the shape of the flow.

It would be difficult to overstate the progress in modeling over the last decade or so. Not long ago calculations in heavy-ion physics were able to match data qualitatively at best. Calculations now take care to include fluctuations, which was ignored for a long time, and are really reaching quantitative descriptions of the data. The popular view of heavy-ion collision physics modeling has reached a sort of consensus under

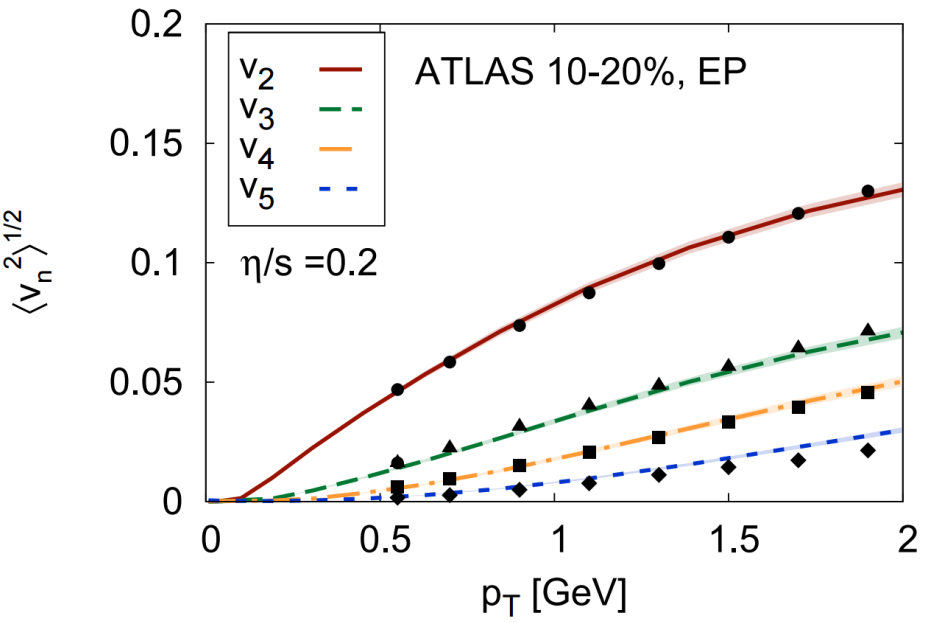

Figure 1.7: Several order of the flow parameter as calculated by the MUSIC hydrodynamic model [13]. The shear viscosity is tuned so that the model can match the v_2, but it is important to note that the code reproduces the higher order flow very well and that the shape of the flow is not so easily matched by varying one parameter.

the banner of viscous hydrodynamics (for $T \gtrsim 165$MeV). This is commonly referred to as the "standard model of heavy-ion physics" [14]. With this model convergence it is becoming possible to rely on well understood features of the models (e.g. afterburners by way of transport in the hadronic stage) to quantitatively understand fairly robust parameters (e.g. shear viscosity) and qualitatively compare difficult-to-understand parameters (e.g. initial conditions from the pre-equilibrium stage of the collision).

To this end Markov chain Monte Carlo (MCMC) calculations have been performed to work backwards from parametrically driven descriptions of the data to the EOS. The input data for the MCMC calculation I'll describe are from the LHC at $\sqrt{s_{\rm NN}} = 2.76$TeV and top RHIC energy of $\sqrt{s_{\rm NN}} = 200$GeV. 30 input parameters where chosen (15 for each beam energy) from particle spectra (yields and average particle p_T), femtoscopic radii (a sort of quantum statistical interference measurement which will not be described in this thesis), and flow. The parameters where taken from very central (0-5% centrality) and mid-central (20-30%) collisions. The model used to describe the data was the MUSIC hydrodynamic code with 14 parameters. The initial conditions for the calculation are a parameterization of saturation model assumptions. The MCMC

calculation requires many iterative runs over the data and the hydrodynamic code is very computationally expensive. To save time the this is not full event-by-event hydrodynamics, but rather involves averaged initial conditions. Since much of the flow is driven by the "lumpy" initial state, which is partially washed out in the averaging process, the calculation included a 10% fudge-factor increase of the flow values. The 14 model parameters are event split between the two $\sqrt{s_{\mathrm{NN}}}$. Of them 10 are for describing the initial stages of the collision (pre-equilibrium flow and energy density) before the hydrodynamic stage, two are for describing the shear viscosity and its energy dependence, and two are for the EOS. After a principal component analysis was performed on the 30 input parameters they were reduced to 14 principal components. After this the MCMC process was run over 1000 events. It is plain to see that the randomly sampled model predictions prior to the MCMC fit the data quite poorly while the posterior data fits quit well. In the interest of brevity I'll just show the results of the EOS in fig. 1.8.

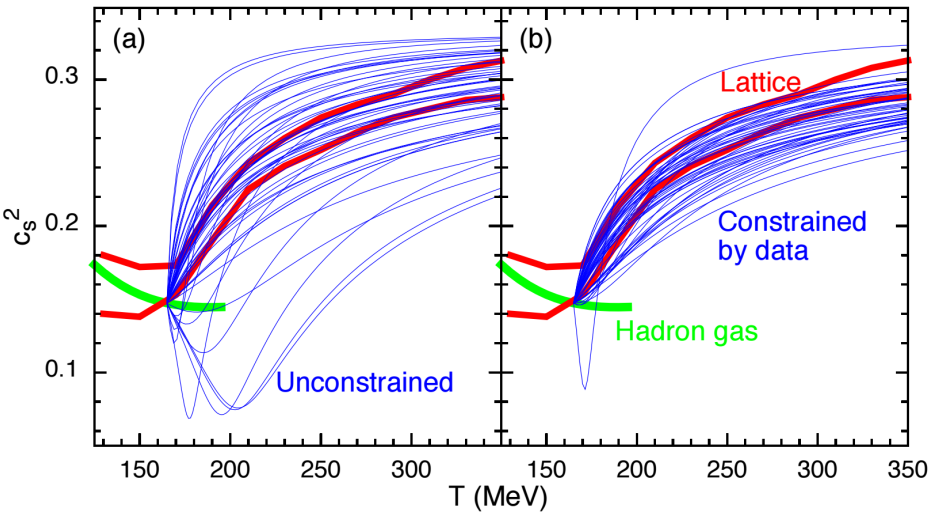

Figure 1.8: EOS constrained by MCMC calculation [15]. The EOS is constrained by lattice calculations (red) and the EOS for an ideal non-interacting gas (green). Panel (a) depicts 50 randomly sampled EOS from the prior while panel (b) depicts the same sampling of the distribution except weighted by the posterior likelihood to find such an EOS.

1.5 Description of apparatus

RHIC is a 3.8km circumference ring in which clockwise circulating ions (called the "blue beam") can be collided with counterclockwise circulating ions ("yellow beam") at 6 fixed interaction regions. RHIC was built on top of existing BNL high-energy and heavy-ion experiments which act as injectors for the accelerator. Ions are injected into RHIC by the Alternating Gradient Synchrotron (AGS) at 19.6 GeV. They're injected in bunches (at $\sim 10^9$ ions per bunch) in resonant cavities of radio-frequency electromagnetic fields. The bunches are accelerated by electric fields and guided around the ring by a large array of powerful dipolar magnets.

At the turn-on of RHIC (2000) there were four detectors at various interaction points, but today STAR is the only operating detector. RHIC has demonstrated the rare ability to provide a very diverse set of collision systems in a very wide range of $\sqrt{s_{\mathrm{NN}}}$. In collider mode this range for heavy-ion physics is 7.7-200GeV, while the upper limit on pp collisions is 500GeV. There is a fixed-target program at STAR to reach lower energies, but I will not go into detail about that here. Uniquely RHIC is capable polarizing proton beams to study polarized pp collisions, which has allowed a RHIC spin program to flourish at a facility purpose-built for heavy-ion physics.

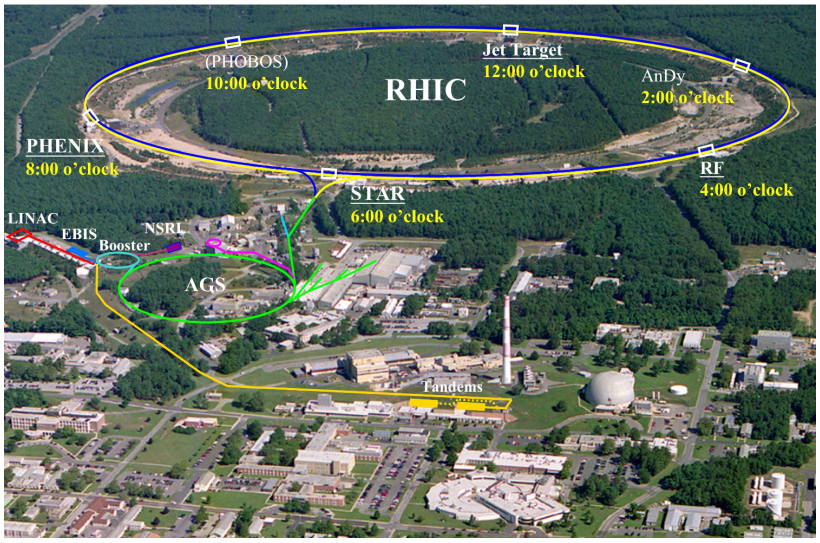

Figure 1.9: Aerial view of RHIC with important components labeled. For reasons unknown to me PHOBOS is in parentheses. AnDy was a proposed spin detector. That interaction point was actually occupied by BRAHMS. Also not pictured are the Roman Pot detectors which were moved to STAR a few years ago.

The work reported in this thesis was done with the STAR detector at the 6 O'clock position on RHIC. There are approximately 600 physicists in the STAR collaboration working to record data, analyze data, and maintaining the complicated detector system. Generically STAR is a cylindrically symmetric "barrel" detector. Most of the instrumentation is at mid-rapidity. A three-dimensional model of the detector, a schematic drawing, and an event display can all be seen below. All such drawings neglect the Zero Degree Calorimeter (ZDC), which lies 18m from the interaction point and is, thus, too far to draw on a reasonable scale. Naturally, as a living detector, STAR has changed considerably over it's relatively long lifetime. Upgrades for the detector are currently underway.

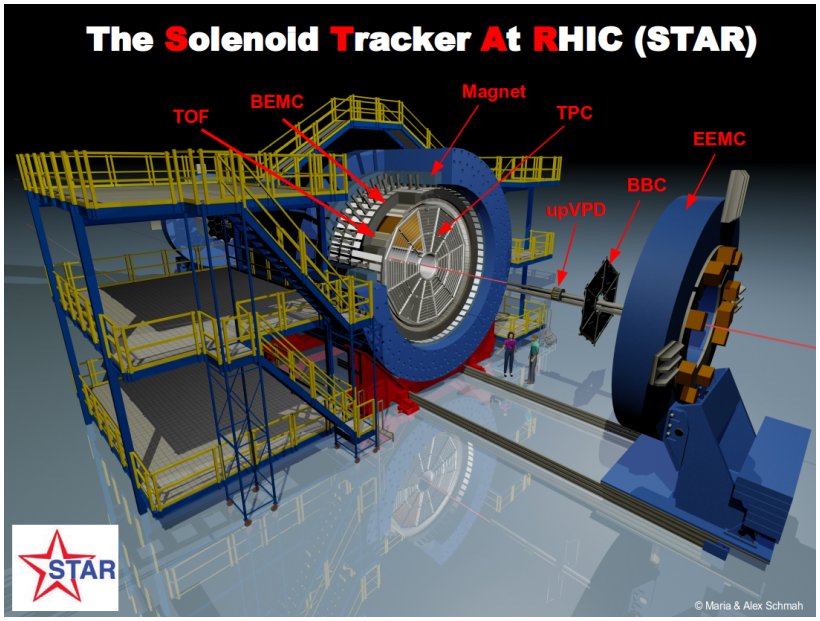

Figure 1.10: 3D picture of STAR showing all major subsystems aside from the ZDC. The VPD and the BBC are symmetric in rapidity, so the other half of these subsystems is not clearly visible at this angle.

Due to the size and complexity of the STAR detector it would not make sense to describe the detector in it's entirety. As quite detailed descriptions of the subsystems are available on the STAR webpage, I'll only provide schematic descriptions of detectors subsystems which I have made explicit use of in this analysis. STAR is limited to recording events (that is, collisions) at a 1kHz rate by the data acquisition (DAQ), which is often below the event rate of the collider. As the recording of events is thus at a premium STAR

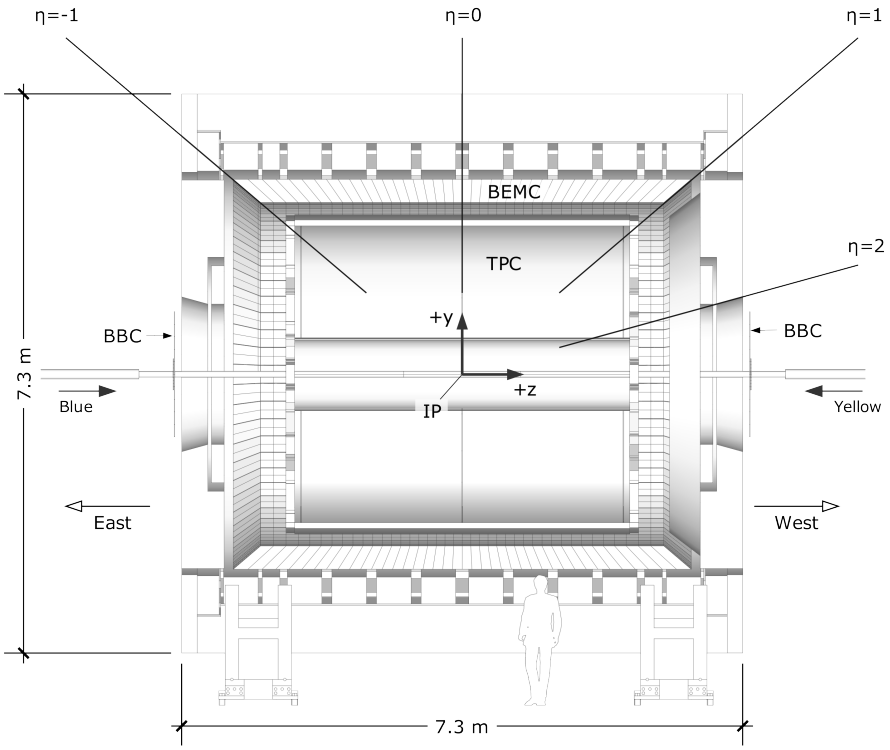

Figure 1.11: Schematic of the STAR coordinate system.

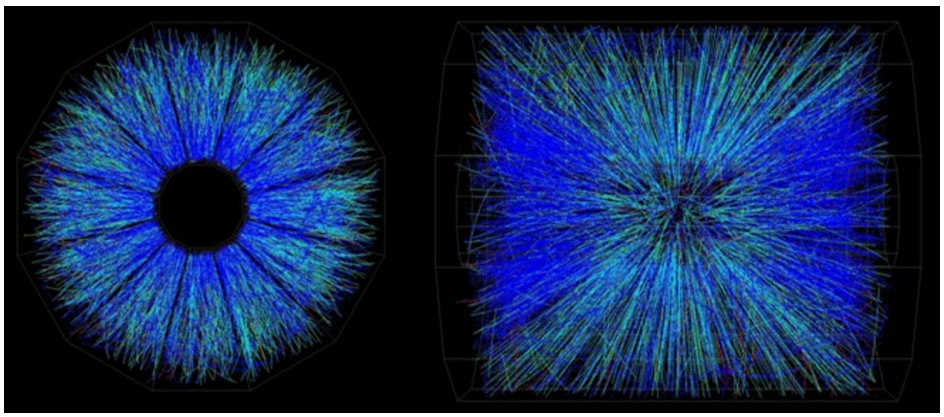

Figure 1.12: Event display of STAR demonstrating the tracking capabilities of the detector. Blue and green tracks are oppositely charged. Gaps are TPC sector boundaries.

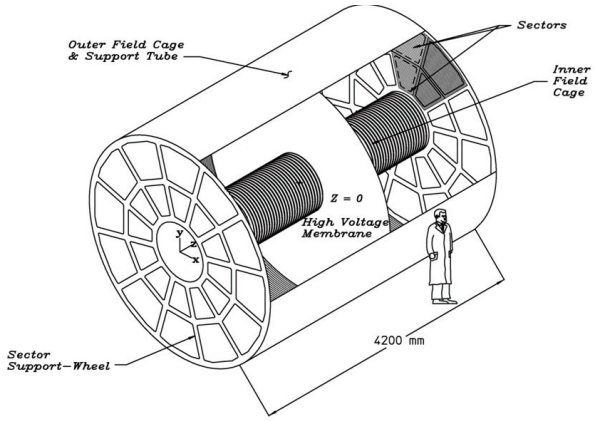

Figure 1.13: Schematic of the TPC.

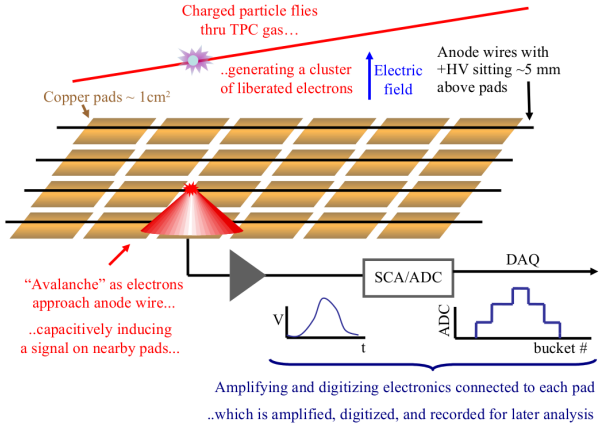

Figure 1.14: Full walkthrough of how the TPC pad planes are used to detect, and thus track, charged particles passing through the gas volume. Figure courtesy of Mike Lisa.

must make very quick decisions about which events are likely to be worth recording and which are not (e.g. collisions of the beam onto the beampipe, rather than the oppositely circulating bunch). Making such decisions in real time is called "triggering". Triggering is quite complicated and requires the use of many of the STAR subsystems. It is, in principal, possible to set up triggers which look for very rare events (e.g. events containing rare particles), or some type of event (e.g. events with 0-10% centrality). The majority of the data recorded by STAR is "minimum bias", which is to say that an event is recorded as long as it is deemed to be good. Since very peripheral heavy-ion collisions are, due to low particle statistics, difficult to distinguish from beam-pipe events or remnants from an older collision, STAR traditionally only uses 0-80% centrality collisions for physics analysis. The subsystems used in this analysis are the Time Projection Chamber (TPC), the Time Of Flight (TOF), and the Beam Beam Counter (BBC).

1.5.1 Subsystem: STAR TPC

The TPC is a mid-rapidity cylindrically-symmetric detector which is responsible for charged-particle tracking and particle identification (PID). Inside the TPC there is a uniform electric field of 135V/cm pointing away from the endcaps, a central membrane separating the east and west sides of the detector, and a uniform 0.5T magnetic field pointing in the beam direction (the polarity can be reversed and the strength can be changed). The TPC is filled with P10 gas (90% Ar and 10% CH_4).

Charged particles passing through the TPC ionize the gas. Ionized electrons drift to the endcaps due to the electric field. As the electrons approach the TPC anode wires (which carry high voltages) the electrons create showers of charged particles. These showers make image charges on the other side of the TPC pad row (pads are small squares of copper). The signal from the pads is then carried off to be amplified and digitized by Analog to Digital Converters (ADCs) which is fed into the DAQ.

The path of the charged particles is bent into the shape of a helix by the magnetic field. The collection of pad hits are fit to a helix to find the trajectory of the particle. At typical position space resolution of this trajectory is $\sim 500\mu$m. Momentum longitudinal to the magnetic field is simply found from the declination of the helix while the transverse momentum is found by the curvature. Typical momentum resolution is $\sim 2\%$. The collection of tracks from an event are fit back to a single origin, which is where we get the location (or primary vertex) of the collision.

The TPC also provides PID through energy loss in the gas. The Bethe-Bloch formula relates energy loss of a particle per unit distance traveled in a medium to (among other things) particle velocity. At low momentum there is a significant difference between the characteristic energy loss for different species of particles. This method is useful for particle momentum up to about 0.8GeV. The STAR TPC provides a resolution of $\sim 7.5\%$ on the energy loss as a function of distance.

1.5.2 Subsystem: STAR TOF

The TOF is a barrel shaped detector with basically the same coverage as the TPC ($|\eta| < 0.9$). The TOF measures the speed of a particle by first measuring the difference between the start time given by the Vertex Position Detector (VPD) and the end time outside of the TPC. One must match the TOF hit with a track in the TPC and know the momentum of the particle that passed through the detector. The TOF must be very fast, which makes it an integral part of the trigger. The time resolution for the speed measurement is on the order of 100ns. Once the particle speed and momentum is known one can trivially calculate the mass, which provides additional PID for this measurement.

The barrel TOF uses an array of Multi-gap Resistive Plate Chambers (MRPCs), each of which is essentially a collection of many thin (0.54mm) layers of resistive glass (resistivity on the order of $10^{13}\Omega/\text{cm}$) with very small separations (0.22mm). On the outside of these the STAR TOF has electrodes with high voltage (order of kV) making a uniform electric field. Outside of the electrodes are copper pads which gather

the signal. The goal here is to make many showers in the small gaps between the glass plates whenever a charged particle passes through. In effect the voltages for each plate are added up to make the signal.

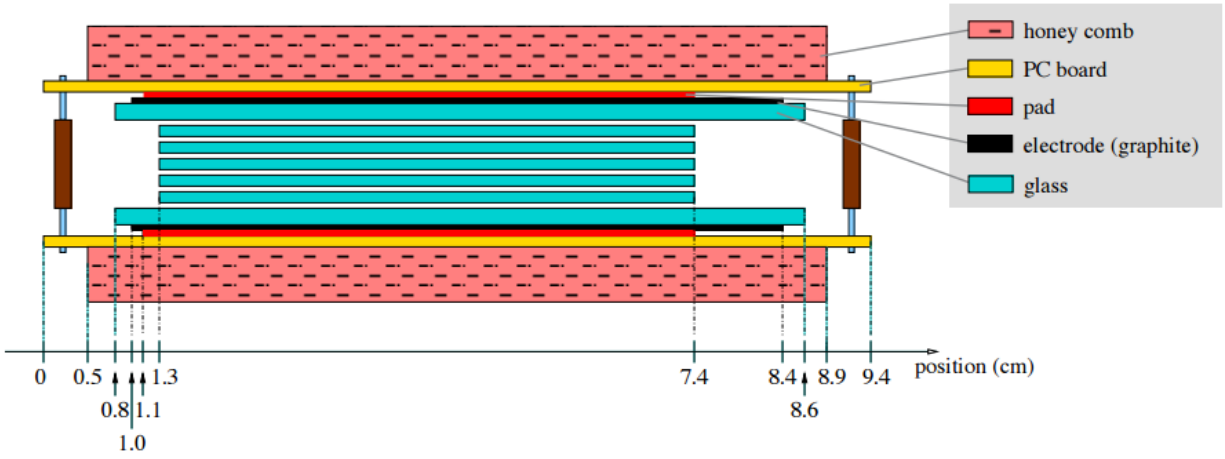

Figure 1.15: In the TOF MRPC mini-showers are generated in the spaces between the glass plates due to the electric field from the electrodes. Signal is carried off by the pads (in red).

The MRPC has a few advantages over a traditional RPC. With a larger gap there is more uncertainty on where the initial ionization occurs. This can be further complicated by shower electrons being recaptured and photons in primary ionization making more avalanches. Smaller gaps are built with larger relative uncertainties, but, as it happens, the size uncertainties are counterbalanced. If a gap is unusually small it will have a larger electric field gradient. So, even though the avalanche is given less space to develop, it will develop faster. The primary disadvantage is that close plates are prone to make a noisy detector due to thermionic emission from very small "mountains" of non-uniformity in the glass. In the electric field these electrons can create avalanches which look just like the signal induced by a real particle.

The actual mechanics of signals in the many chambers "adding" as previously described is quite complicated and not well understood, but has been copiously tested. The charge induced on the copper pads from the showers is compared to the signal induced by the slower "holes" of ions traveling the opposite direction.

1.5.3 Subsystem: STAR BBC

The BBC is a pair of two scintillator disks 3.75m from the interaction point. Each are made up of hexagonal lattices. There is a small lattice made up of 18 tiles. On could inscribe a circle of radius 9.64cm in each hexagon. The outer tiles are 4x this size, but, owing to some calibration issues, they've never been used for physics analysis. Considering just the small tiles this makes the coverage of the detector $3.4 < |\eta| < 5.0$. Over the beam energy scan this pseudorapidity coverage includes both produced and transported particles. The tiles are 1cm thick and are coupled to photomultiplier tubes (PMT) via wavelength shifting fiber. The fiber is air coupled to the scintillator via grooves in the front and back of the scintillator. The embedded end of the fibers are aluminized to reflect light. Each groove holds two fibers, so there are typically four fibers per PMT. Each side has 16 channels so there are two PMTs on each side with eight fibers, as those tiles are read out together.

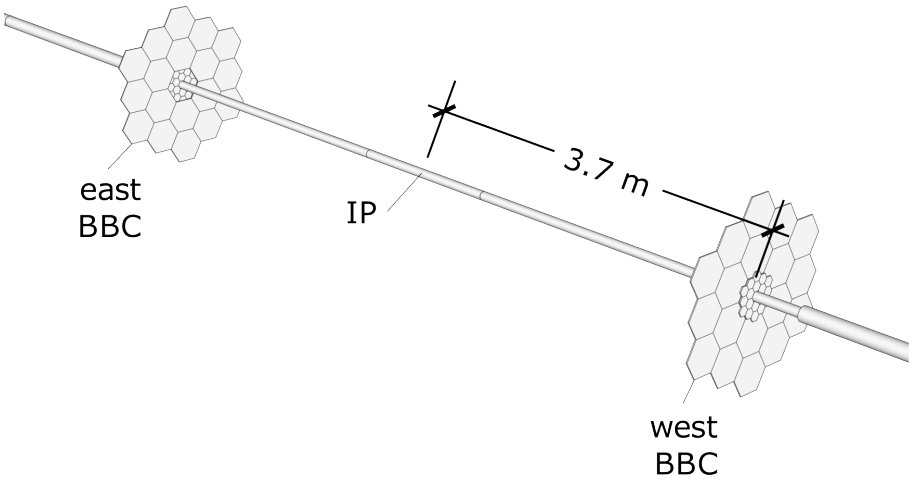

Figure 1.16: To-scale diagram of the BBC. Only the smaller honeycomb is actually used.

The first order particle flow (v_1) has a very distinctive shape at forward rapidities. Since it is explicitly odd with rapidity $v_1 = 0$ at $y = 0$. The maximum of the flow is beam-energy dependent, but the location of the maximum is always forward. Since the signal is so small in the TPC finite statistics limits the resolution of the orientation of the collision. The coverage of the BBC was quite good at these beam energies for

measuring the orientation of this collision.

Chapter 2

THEORY OVERVIEW OF GLOBAL POLARIZATION

The basic underpinning of global polarization in heavy-ion collisions is quite simple. As previously mentioned the nuclei themselves are roughly spherical. Off-center collisions (as must generally happen) have an angular momentum $O\left(10^3\hbar\right)$ (this is a $\sqrt{s_{\mathrm{NN}}}$ dependent statement, the radius of a gold nucleus is about 5fm). Most of the angular momentum will be carried down the beam pipe and large rapidities by the spectators of the collision, but it is likely that some fraction of that angular momentum sticks with the fireball at midrapidity. It is important to point out that this is due to the non-trivial nuclear thickness function. If the "pancake" was uniformly dense no such angular momentum would be left at midrapidity, but even a hard sphere will be more dense at the center, leading to non-zero average angular momentum in the overlap region.

As $\sqrt{s_{\mathrm{NN}}}$ is increased the total angular momentum would also increase, however the fraction of that angular momentum transferred to the fireball would decrease. This is do to a complicated and generally poorly understood phenomenon called stopping. At arbitrarily high $\sqrt{s_{\mathrm{NN}}}$ nuclei pass through each other leaving energy density at the collision point. The fireball from such a collision would have zero net baryon number and zero electric charge. The energy from the collision would still break apart the nucleus. In theory parlance such a collision is boost invariant, and is the justification behind 2+1 dimensional hydrodynamics. At lower collision energies some amount of the charge and baryon number from the original nuclei doesn't quite pass through the fireball and becomes part of it. Additionally collisions at higher $\sqrt{s_{\mathrm{NN}}}$ have higher temperatures and are longer lived. As the system expands the angular momentum is constant, but the vorticity (which gives rise to polarization and is *not* conserved) decreases. Thus the scaling of fireball

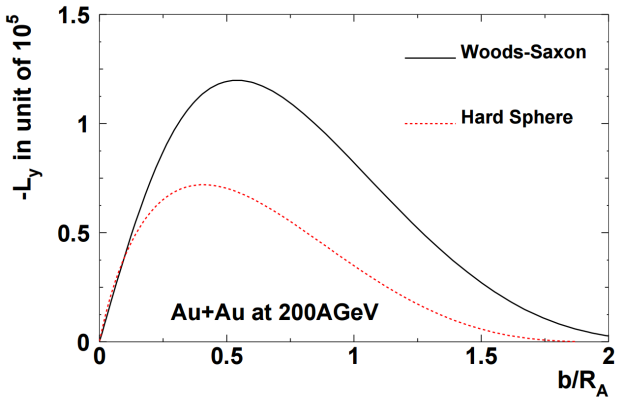

Figure 2.1: Angular momentum in the overlap region of a Au+Au collision [16]. Angular momentum is given in units of $\hbar$ and the x axis is the impact parameter scaled by the "nuclear radius" ($R_A \equiv 1.2\text{fm} \times A^{1/3}$). Note that this is the sum of the angular momentum in the overlap region, but not *necessarily* the total angular momentum transferred to the fireball, which can only be some fraction of this.

angular momentum is nontrivial and requires a quantitative, rather than a qualitative, description of collision dynamics to predict $\sqrt{s_{\text{NN}}}$ dependence.

The net angular momentum of the fireball can be transferred to the particles which make it up via spin-orbit coupling. Such an interaction qualitatively has no requirement on the phase of the matter and can be expected regardless of whether hadronic or partonic degrees of freedom dominate. Naturally if one starts from a situation of nonzero net partonic spin, by angular momentum conservation, one expects at least some nonzero spin to end up in the final hadronic states. Measuring particle spin is difficult, generally, but some particles decay via a weak decay which violates parity conservation. In such interactions it is possible to determine the spin, statistically, from the decay topology. (Anti)Lambda baryons have such a decay and are relatively abundant, as can be seen in fig. 1.6. This idea first came about in 2004 [17, 18]. Shortly afterwards it was noted that the same effect could be measurable with vector mesons (e.g. the ϕ meson) [19].

There is an interesting non-relativistic parallel in the Barnett Effect [20, 21]. In the Barnett Effect an uncharged object rotate with angular velocity ω will be measured to have spontaneous magnetization $M = \chi\omega/\gamma$ (where χ is the magnetic susceptibility and γ is the gyromagnetic ratio of the electron). The experimental observation that the magnetization is proportional to the angular velocity predates a modern understanding of intrinsic particle spin. The Barnett Effect is an example of spin alignment due to bulk rotation.

The analysis presented in this thesis is a measurement of the alignment of Λ ($\overline{\Lambda}$) spin with system angular momentum. Such a quantity is called the "Global Polarization", or $\overline{P}_{\mathrm{H}}$. More detail about the measurement will be provided in sec. 3, but, since several theory calculations compare to this data, it makes sense to show the data independent of the theory here in fig. 2.2.

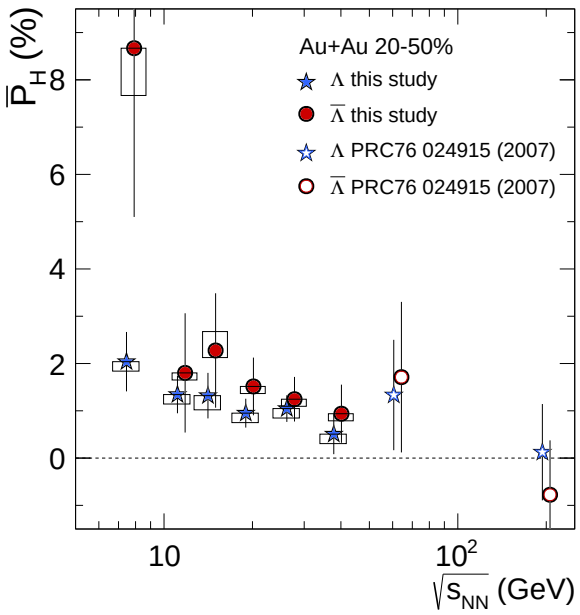

Figure 2.2: $\left\langle \frac{8}{\pi\alpha} \sin\left(\Psi_1 - \phi^*_{\Lambda,\bar{\Lambda}}\right) \right\rangle$ vs. $\sqrt{s_{NN}}$ for 20-50% centrality [1]. P_H characterizes the global correlation between Λ ($\overline{\Lambda}$) net spin and system angular momentum.

There was a significant effort, especially early on, to calculate the polarization of the quarks which make up a QGP due to an off-center collision [17, 22, 16]. These calculations are quite difficult so a number of simplifications needed to be employed. The first paper [17] limits the calculation to perturbative regimes where the transverse kinetic energy of the quark-quark interaction being considered is small. It is estimated in this case that the quark polarization would be on the order of a few tens of percentage points. It is not trivial to estimate hadron polarization given the quark polarization in all possible hadronization schemes, so we're really only afforded qualitative statements, which are nonetheless informative. If hadronization is primarily achieved via quark recombination one can expect the hadron polarization to be similar to the quark polarization. It is also expected that the polarization would increase approximately linearly with

impact parameter and be the same for particles as for their anti-particles. Hadrons of very high transverse momentum are not expected to be polarized as they come from hard collisions.

This calculation was expanded upon in a later publication [16] and generalized to not only consider small-angle quark-quark scattering. Implicit in the small-angle approximation is the assumption that the initial longitudinal shear of the QGP is large or that qq interactions occur only at high center of mass energies. This approximation is relaxed via finite temperature QCD. It is assumed that the medium thermalizes instantly and that the onset of the QGP is immediate. The flow profiles of the pre-equilibrium stage of the collision are important and far from trivial. This calculation method is limited to perturbative QCD. In fact, despite the high temperatures achieved in a heavy-ion collision, many QCD interactions are still non-perturbative. This calculation is valid only in the weak coupling limit, and it is acknowledged in the paper that significant contributions may come from strong coupling. This is hinted at in the calculation itself as the quark polarization is not vanishing as the coupling increases (though, of course, in this limit the calculation is less reliable). At top RHIC energy the average quark polarization of semi-peripheral collisions is calculated to be $< 4\%$.

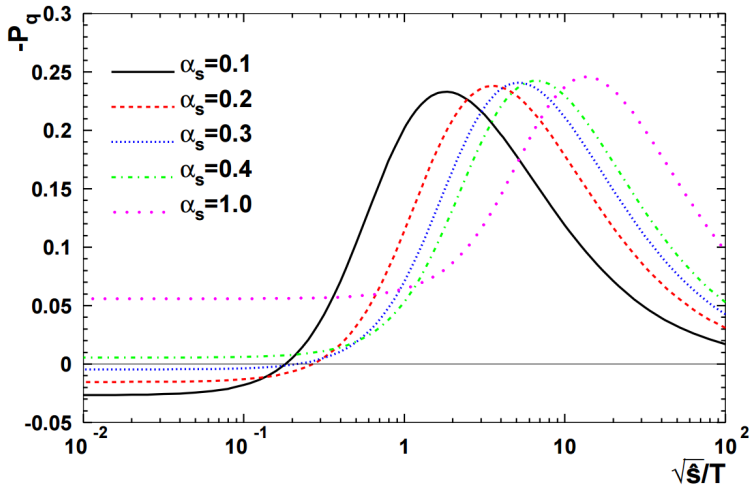

Figure 2.3: Quark Polarization as a function of qq collision center-of-mass energy scaled by medium temperature in mid-central collisions [16]. The average center-of-mass energy depends on the model one uses to describe the early longitudinal shear flow.

The quark polarization calculations give us a very interesting view into the microscopic interactions

of the quarks, but it isn't easy to translate the results into the average polarization of final state hadrons. Another way of looking at these collisions is to treat the interactions statistically by considering the quarks as constituents of a fluid, which is to say describe the collision hydrodynamically, as was done in [23, 24, 25, 26, 27, 28, 29, 30, 31, 32, 33, 32, 34, 35]. Classically vorticity is $\vec{\omega} \equiv \frac{1}{2}\vec{\nabla} \times \vec{v}$, for some fluid-cell velocity $\vec{v}$, which simplifies to angular velocity in the rigid-body rotational limit. This was first touched on in [36]. The equations governing polarization in a hydrodynamic thermal framework where worked out in [23, 37]. Much of the discussion at this point is focused on the modification of v_2 due to a rotating equilibrated fireball to counterbalance viscous effects. If the spin degrees of freedom are in local thermal equilibrium at hadronization then hadron polarization can be determined statistically at the freezeout hypersurface. This is in exact analogy to how hadron momenta are determined in hydrodynamic models and simply represents and extension to the (standard) Cooper-Frye formula (the extension to spin 1/2 particles can be seen in Ref. [38]). The hadron polarization determined in this way is proportional to the spin of the particle and the vorticity of the system. This is discussed in much greater detail in sec. 7. There are several possible relativistic extensions of the classical vorticity. The thermal vorticity, ϖ, is

$$\varpi_{\mu\nu} = -\frac{1}{2T}\left(\partial_\mu u_\nu - \partial_\nu u_\mu\right) \tag{2.1}$$

In eq. 2.1 T is the temperature and u is the velocity of the fluid cell. The thermal vorticity is a unitless quantity which clearly is just a factor of T off from reducing to classical vorticity. It's a variable of interest here because the polarization of hadrons is proportional to it. For spin 1/2 hadrons this proportionality is

$$\Pi_\mu(x,p) = -\frac{1}{8}\varepsilon_{\mu\rho\sigma\tau}\left(1-n_F\right)\varpi^{\rho\sigma}\frac{p^\tau}{m} \tag{2.2}$$

where Π_μ is the 4-vector polarization, m is the mass, p^τ is the 4-momentum, and n_F is the Fermi-Dirac-Jüttner distribution for baryons of baryochemical potential μ_B

$$n_F = \frac{1}{e^{u(x)\cdot p/T - \mu_B/T}}. \tag{2.3}$$

A global polarization signal aligned with system angular momentum clearly requires a three dimensional description of the collision, which is generally computationally expensive. Especially early on an inviscid relativistic Particle In a Cell (PICR) model was used [24, 25, 26, 29]. As can be seen from that

list of citations the PICR model is still used, even at very low (NICA/FAIR) energies where the viscosity is very large. Other calculations have used ECHO-QGP (a hydro solution from astrophysics) with dissipative hydrodynamics and isochronous freezeout surfaces [27]. Finally calculations have more recently been made using the vHLLE hydrodynamic solution with 3+1D viscous hydrodynamics and UrQMD-based initial conditions [30, 33]. Probably what is most comparable to this is CLVisc, a GPU based 3+1D hydro code which uses AMPT initial conditions [28, 34]. The initial conditions, namely the flow and energy density distribution one feeds into the hydrodynamics, is very important. Typically this is a large source of uncertainty in hydrodynamic models.

Naturally not all Λs are primary (in fact most are not). Λs coming from decays of heavier resonances modify the measured polarization, which should be considered for quantitative comparisons. Correcting for such parent contributions is typically called a "feed-down" correction. Some such comparisons correct for this.

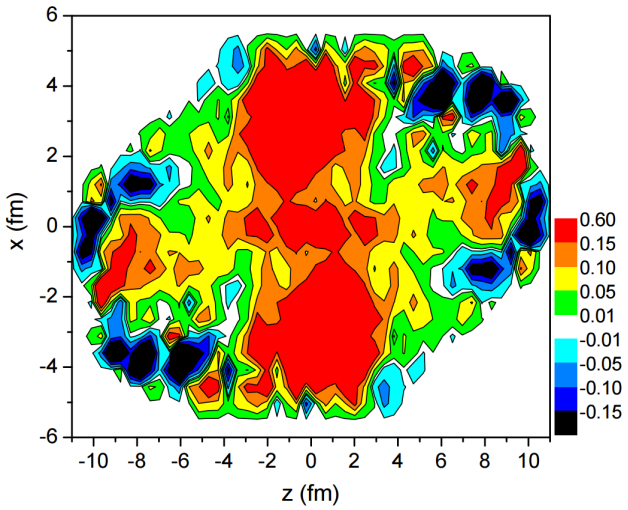

Figure 2.4: The thermal vorticity scaled by hydro cell energy density for a mid-central 200GeV collision at time $t = 4.75\text{fm}/c$ [24].

The other model under consideration is the AMPT model, as used in [39, 40, 41, 42]. Since it it a microscopic model one can track individual particle interactions and their momentum/spin exchanges. Ref. [39] provided reasonable expectations of vorticity. In order to describe vorticity in AMPT it is necessary

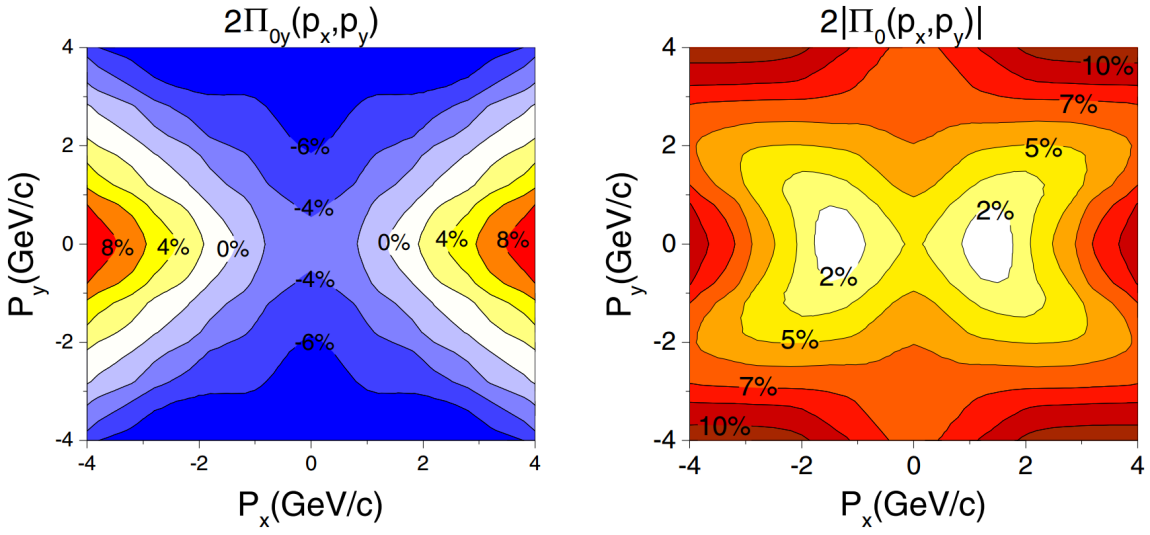

Figure 2.5: Λ polarization as a function of azimuthal momentum [24]. The angular momentum points in the $-\hat{y}$ direction, so negative polarization projected on the $\hat{y}$ axis means that the spin aligns with the system angular momentum.

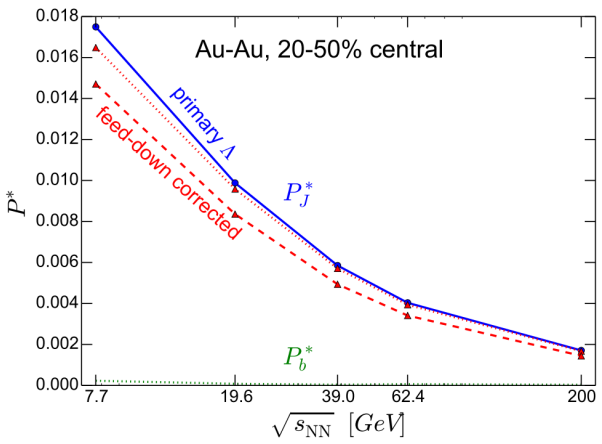

Figure 2.6: Λ polarization as a function of $\sqrt{s_{\rm NN}}$ [30]. The dotted red line corrects for Λ feed down from Σ^0 and Σ^0 (1385) and the dashed line corrects for feed down up to Σ^0 (1670). In this calculation the primary Λ polarization is identical to the $\overline{\Lambda}$ polarization.

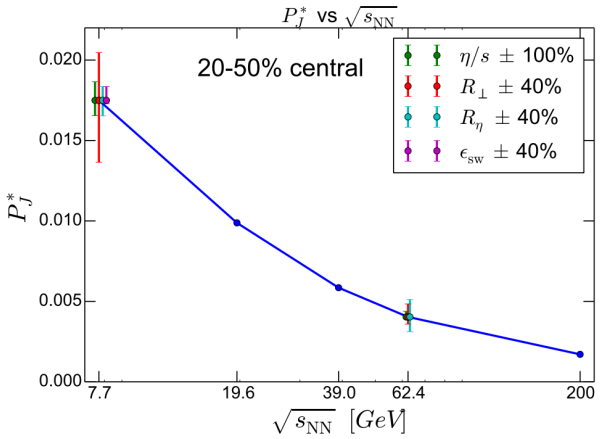

Figure 2.7: Λ polarization as a function of $\sqrt{s_{\rm NN}}$ [30] showing how much the polarization varies from the nominal value due to set variations of the model parameters. η/s is the shear viscosity scaled by the entropy density for the fluid. $R_\perp$ and R_η are initial-state parameters which control the course-graining of the model. $\varepsilon_{\rm SW}$ is the particlization energy density. Clearly errors are dominated by initial-state parameters at both $\sqrt{s_{\rm NN}}$ values.

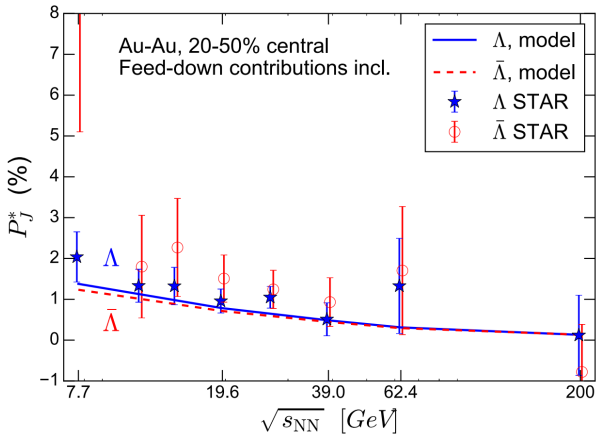

Figure 2.8: Λ polarization as a function of $\sqrt{s_{NN}}$ as compared to the data [33] in a vHLLE hydrodynamic model.

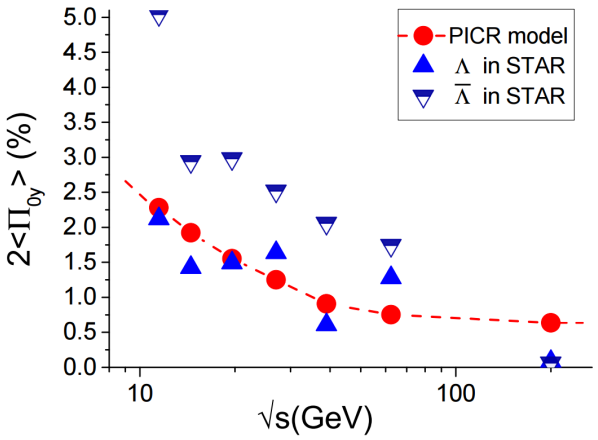

Figure 2.9: Λ polarization as a function of $\sqrt{s_{NN}}$ as compared to the data [31] in a PICR model. Errors for the data have been removed.

to calculate it microscopically within some cell. In ref. [41] AMPT is used primarily for initial conditions. The motivation for that study is the idea that hydrodynamic initial conditions may well describe equilibrium mechanics, but a significant amount of initial quark polarization comes from non-equilibrium sources. That calculation thus somewhat belongs to the quark polarization studies mentioned earlier. After the AMPT initial conditions the model proceeds to find Λ polarization with a coalescence description by way of a chiral kinetic calculation.

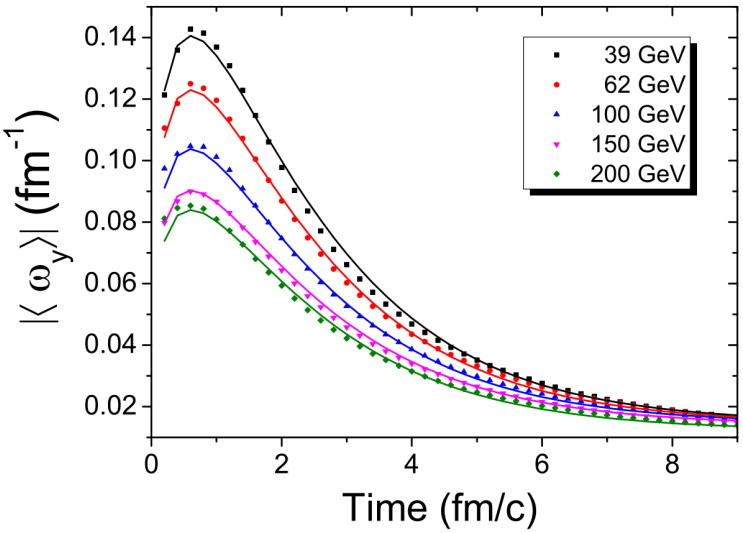

Figure 2.10: Vorticity as a function of time from AMPT [39]. One can clearly see a decrease of the maximum with an increase of $\sqrt{s_{\rm NN}}$. Since the higher $\sqrt{s_{\rm NN}}$ collisions live longer one would even expect this difference to be more stark at freezeout.

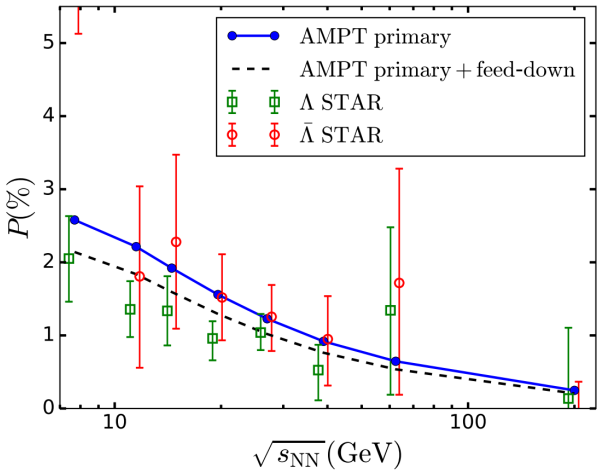

Figure 2.11: Λ polarization as a function of $\sqrt{s_{\rm NN}}$ from AMPT [40].

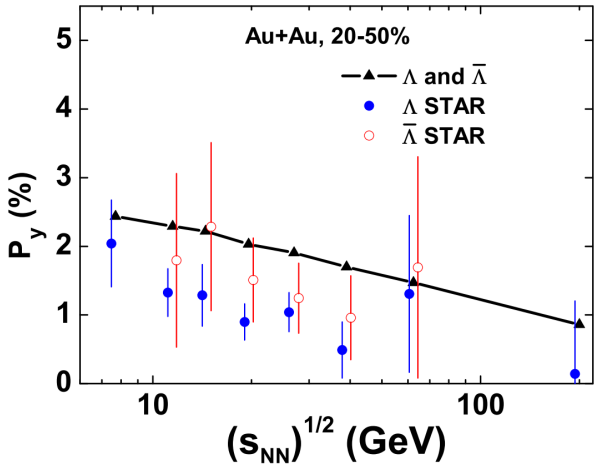

Figure 2.12: Λ polarization as a function of $\sqrt{s_{\rm NN}}$ from a quark coalescence model [41]. No feed-down correction is made. This is expected to decrease calculated polarization by 15-20%.

Chapter 3
DATA ANALYSIS

For some heavy-ion collision with orbital angular momentum direction $\hat{L}$ the Λ hyperon polarization relative to that angular momentum can be determined by the distribution of the Λs decay products. For the decay $\Lambda \to p + \pi^-$ the angular distribution of protons in the parent Λ rest frame is given by

$$\frac{dN}{d\cos\theta^*} = \frac{1}{2}\left(1 + \alpha_H |P_H| \cos\theta^*\right) \tag{3.1}$$

Where P_H is the average polarization of the Λs, α_{H} is the decay parameter of the Λ, and θ^* is the angle between the proton momentum in the mother Λ rest frame and $\hat{L}$. The 'H' in the subscripts denotes hyperon. For an anti-hyperon, e.g. the $\overline{\Lambda}$, the script is delineated by an overline. From the particle data group α_Λ = -$\alpha_{\overline{\Lambda}}$ = 0.642$\pm$0.013 [43], which is discussed in more detail in sec. A.3. Statistically the daughter proton is emitted in the parent Λ ($\overline{\Lambda}$) frame in (opposite) the direction of the Λ ($\overline{\Lambda}$) spin. The polarization may depend on Λ emission angle and pseudorapidity. What is reported here is an acceptance integrated measurement. There are a few simplifications that can be made to the description due to the STAR acceptance, which is even in rapidity and azimuthal angle. the coordinate system is shown in fig. 3.2.

By integrating over solid angle it is possible to express the global polarization in terms of the variables available to the experiment

$$P_H = \frac{3}{\alpha_H}\langle \cos\theta^* \rangle \tag{3.2}$$

Where angled brackets denote an the average over events and Λs for all events. $\cos\theta^* = \sin\theta^* \sin\left(\Psi_{\mathrm{RP}} - \phi^*\right)$.

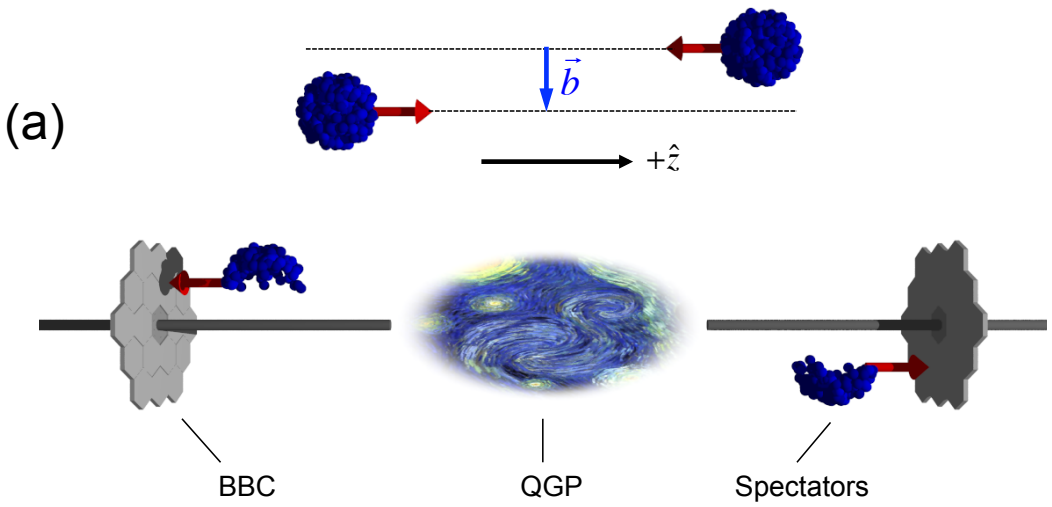

Figure 3.1: The impact parameter $\vec{b}$ of the collision as well as the longitudinal $\hat{z}$ coordinate.

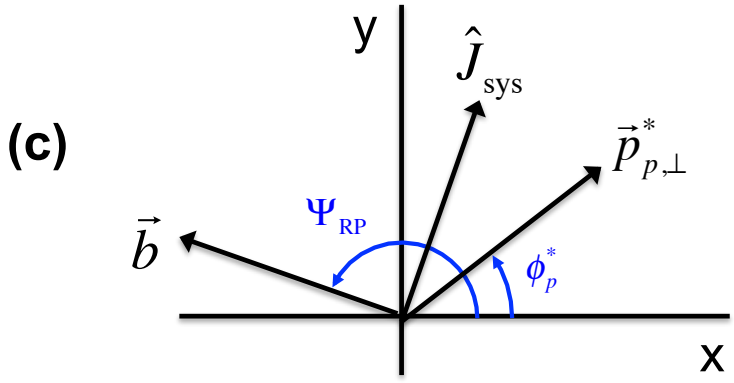

Figure 3.2: Azimuthal coordinates of a collision. The total system angular momentum $\hat{J}_{\text{tot}}$ is perpendicular to the impact parameter, $\vec{b}$. In azimuthal coordinates the angle between the impact parameter and the detector coordinate x axis is the reaction plane, Ψ_{RP}. The azimuthal projection of the proton's momentum in its parent Λ rest frame is $\vec{p}^{\,*}_{p,\perp}$. The angle that this momentum makes relative to detector coordinates is ϕ^*_p.

By integrating over θ^* we get

$$P_H = \frac{8}{\pi\alpha_H} \langle \sin(\Psi_{\mathrm{RP}} - \phi^*) \rangle \tag{3.3}$$

The reaction plane is estimated by the first-order event plane, Ψ_1. This is determined via the BBCs. The formula also assumes perfect detector acceptance, this will be discussed, along with a number of other experimentally necessary corrections, later in this section. Finite statistics and particle position resolution limit how well we can measure the first-order event plane. In terms of measured quantities the polarization is

$$P_H = \frac{8}{\pi\alpha_H} \frac{\langle \sin(\Psi_1 - \phi^*) \rangle}{R_1} \tag{3.4}$$

where R_1 is the first-order event plane resolution.

In this section I'll include some final and corrected results, explain what corrections are made, and talk about some efficiency and reconstruction issues that occur in the measurement. Aside from the final result, and unless otherwise mentioned, most plots depict $\langle \sin(\Psi_1 - \phi^*_\Lambda) \rangle$ with a resolution correction, which neglects the constant factor $\frac{8}{\pi\alpha}$. The general idea of this section is to provide both the steps for doing this analysis and to explain issues that are deemed fundamentally important to the QA of the analysis. In order to do this measurement the following must be done

- Determine the event plane (sec. 3.1)
- Identify Λ ($\overline{\Lambda}$) candidates (sec. 4.4.2)
- Apply resolution correction (sec. 3.2)
- Apply acceptance correction (sec. 3.3)
- Apply mass purity correction (sec. 3.4)
- Apply helicity efficiency correction (sec. 3.5.2)

See sec. 3.6 for a brief discussion of the statistical errors and sec. 5 for a discussion of the systematic errors. Note that the decay parameter α_H is taken to be 0.647 ± 0.013 for both the Λ and $\overline{\Lambda}$ results. This is

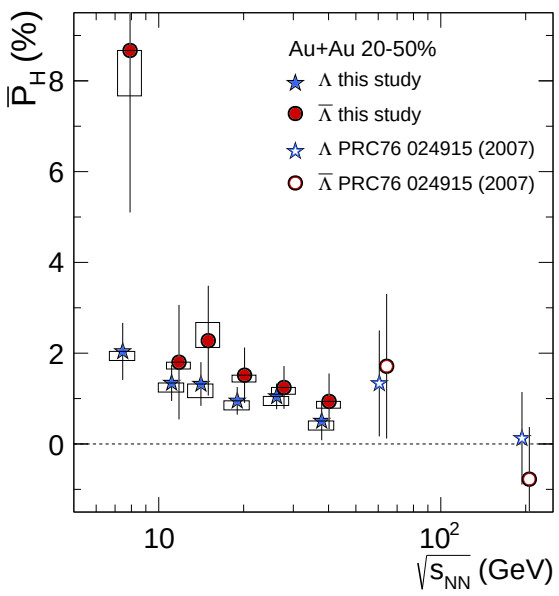

Figure 3.3: $\left\langle \frac{8}{\pi\alpha} \sin\left(\Psi_1 - \phi^*_{\Lambda,\bar{\Lambda}}\right)\right\rangle$ vs. $\sqrt{s_{NN}}$ for 20-50% centrality [1]. P_H characterizes the global correlation between Λ ($\overline{\Lambda}$) net spin and system angular momentum. Also seen in fig. 2.2.

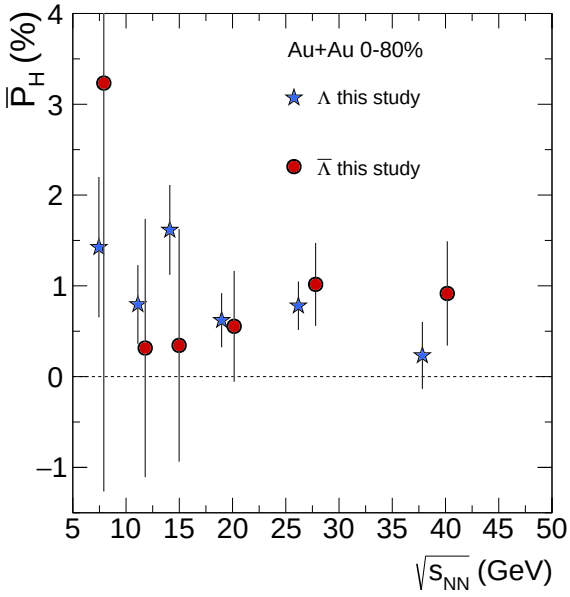

Figure 3.4: $\left\langle \frac{8}{\pi\alpha} \sin\left(\Psi_1 - \phi^*_{\Lambda,\bar{\Lambda}}\right)\right\rangle$ vs. $\sqrt{s_{NN}}$ for 0-80% centrality. Sytematic error bars are not shown because the bulk of the systematics come from the off-mass signal at 20-50% collisions. Further studies are required for 0-80%. Comparable results for [44] have not been calculated.

the decay parameter of the Λ. This may seem an odd choice as $\alpha_{\overline{\Lambda}}$ has been measured independently. It is of fundamental interest whether these values differ but measured values have consistently found to be the same within statistical errors and it is largely assumed that they are, in fact, identical. Using different values would be confusing in as far as we are looking for differences in the data between Λ and $\overline{\Lambda}$ polarization. It might seem to be endorsing the more unlikely scenario that they are different. At any rate it is evident that the difference is small and the errors in the α_H are nearly negligible compared to the relatively large statistical uncertainty in the measure.

The final extracted polarization is in fig. 3.3. Averaging over $\sqrt{s_{\rm NN}}$ the values of the polarization for these particles is $\overline{P}_\Lambda = 1.08 \pm 0.15(\text{stat}) \pm 0.11(\text{sys})\%$ and $\overline{P}_{\overline{\Lambda}} = 1.38 \pm 0.30(\text{stat}) \pm 0.13(\text{sys})\%$.

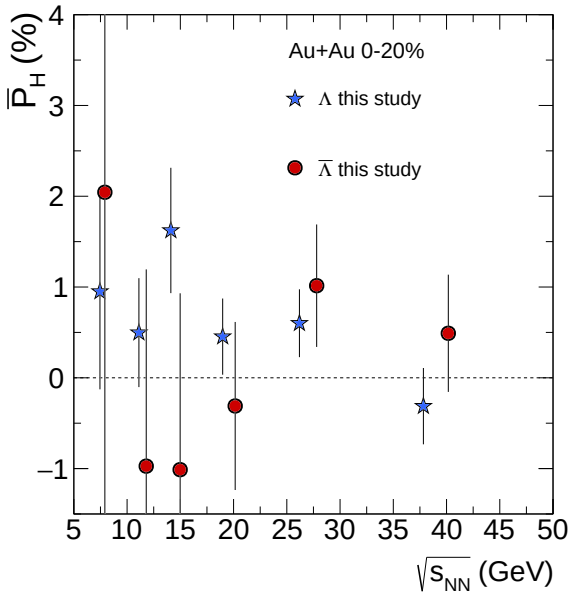

Figure 3.5: $\left\langle \frac{8}{\pi\alpha} \sin\left(\Psi_1 - \phi^*_{\Lambda,\bar{\Lambda}}\right)\right\rangle$ vs. $\sqrt{s_{NN}}$ for 0-20% centrality. Sytematic error bars are not shown because the bulk of the systematics come from the off-mass signal at 20-50% collisions. Further studies are required for 0-20%. Comparable results for [44] have not been calculated.

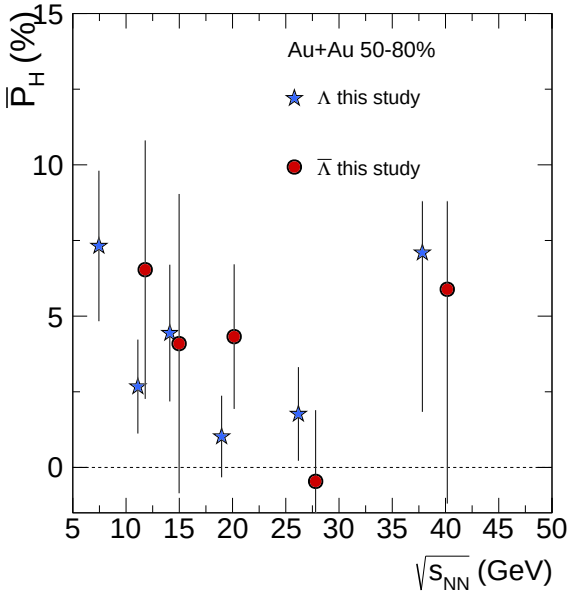

Figure 3.6: $\left\langle \frac{8}{\pi\alpha} \sin\left(\Psi_1 - \phi^*_{\Lambda,\bar{\Lambda}}\right)\right\rangle$ vs. $\sqrt{s_{NN}}$ for 50-80% centrality. Sytematic error bars are not shown because the bulk of the systematics come from the off-mass signal at 20-50% collisions. Further studies are required for 50-80%. Comparable results for [44] have not been calculated. The 7GeV $\overline{\Lambda}$ point is not shown as it is $-19 \pm 12\%$. Statistical errors are symmetric, though 39GeV error bars are cut off by the legend.

3.1 Event plane determination

The analysis uses the first-order event plane, Ψ_1, determined by the east and west BBCs. In fact three separate planes are used in the analysis: one determined only in the east BBC, one in the west BBC, and a third "full" event plane which is an ADC weighted average of the other two. The first two event planes are calculated solely for the estimation of the resolution while the full event plane is used in the analysis to estimate the impact parameter direction. All corrections for each of the three event planes are done totally separately. Generally an event plane is found by weighting the tile geometry by the ADC (analog to digital conversion) value for that given tile. The ADC is roughly proportional to the number of charged particles passing through the tile. The numbering scheme for the inner tiles of the detector (only the inner tiles are used) is shown in fig. 3.7 from the perspective of one looking at the detector from a very large $|z|$ vantage point.

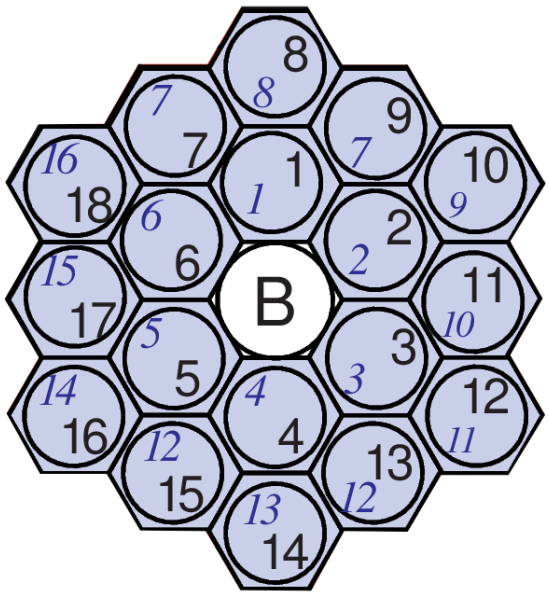

Figure 3.7: BBC numbering scheme looking from very large $|z|$. Black numbers represent tile number while blue numbers represent PMT number.

Tiles 7 and 9 (13 and 15) share PMTs which means it is impossible to tell whether one was hit or the

other. Many analyses deal with this ambiguity by randomly assigning the ADC value in its entirety to tile 7 (13) XOR tile 9 (15). I prefer to count the tile pair's contribution as being between them so $\pi/2$ ($3\pi/2$). I think that this scheme makes more sense and certainly makes comparisons with ones own code or the code of others much easier. In practice I have not seen a noticeable difference between the two methods. Note that either way the tiles are mirrored about the x axis but not the y axis so that a line parallel to the z axis might go through tile 11 on the West BBC and tile 17 on the East BBC while such a line could go through both tile 8s.

$v_1 * y > 0$ by conventions most reasonable to the STAR event plane. Therefore the west BBC reconstructs the "correct" event plane. Spectators on the east side BBC hit a position which is 180°s in $x - y$ from those that hit the west. This means that there is a negative sign for the east BBC event plane. More simply $\Psi_E = 0 \implies Q_{x,West} = x_{STAR}$ which would mean $\Psi_E = \pi \implies Q_{x,East} = -x_{STAR}$.

The "raw" (uncorrected) event plane is found by by weighting tile geometry by the ADC for the relevant tile. This sum over the ADC channels creates a standard flow Q vector, $Q_1 = (\sum_{i=1}^{16} ADC_i * \cos(\phi_i), \sum_{i=1}^{16} ADC_i * \sin(\phi_i))$. We make (and correct) Q vectors for east and west separately which allows us to get a resolution correction later. The Q vector for the full event plane is basically made by taking $Q_{1,W} - Q_{1,E}$. After this raw event plane is found we do a series of corrections to the event plane The corrections are done in the following order:

- Gain correction: The idea of the gain correction is that not all BBC tiles may output the same ADC value for the same hit, some can be hot/cold. To correct for this we normalize the number of hits in each tile by the amount that tile fired relative to the other tiles making sure that the bank of "other tiles" is equally likely to be hit. So, innermost tiles 1-6 are normalized together while, separately tiles 7-18 are normalized together. This normalization should be done over enough time to get reasonable statistics and a small enough time that the normalization is relevant. I do this normalization for each new run number. This is made somewhat more complicated by the shared tiles, see sec. A.2 for details.

- Recentering correction: The Q vector averaged over all events has to be zero since, of course, there is no preferred impact parameter. Even with the gain correction it is possible that the Q vector doesn't average to zero since ADCs can saturate and it is possible that a particular ADC is more likely to saturate than the others. In principal the recentering correction is well motivated, in practice this

correction tends to be minimally impactful

- Ψ shift correction: This is the least well motivated of the corrections. In principal the event plane distributions should all be flat since there is no preferred event plane, this correction takes each Ψ distribution (full/east/west) and applies a flattening method which flattens in harmonics of the distribution (decomposed into sines and cosines). The harmonics of the distribution are then subtracted off. Typically only the first few harmonics are non-zero. This is a steamroller that runs over the distribution. The best justification for why the shift correction is okay is the Ψ_E vs Ψ_W plot where the Ψ_E vs Ψ_W are separately corrected. In such a plot the correlation is seen to be better after the shifting. We have done nothing, in such a case, to require that to happen. The correction is done to 20th order, this is overkill but it isn't expensive to do.

For plots illustrating the different event planes at various degrees of correction see sec. 4.2.

3.2 Resolution correction

Due to finite particle statistics any event plane has some limitation on how well it can be measured. The resolution is given by the deviation of the measured plane (see eq. 1.4) from the true reaction plane (averaging over all events)

$$R_n = \langle \cos\left(n\left(\Psi_n - \Psi_{\mathrm{RP}}\right)\right)\rangle \tag{3.5}$$

This resolution is driven by the resolution parameter, χ,

$$\chi = v_n\sqrt{M} \tag{3.6}$$

where M is the particle multiplicity and v_n is the flow coefficient from eq. 1.5. The greater the flow the tighter the momentum correlation and the higher the multiplicity the more fully the width of the distribution is determined. The resolution can be written in terms of the resolution parameter and modified bessel functions I_α

$$R_n(\chi) = \frac{\sqrt{\pi}}{2}\chi e^{-\chi^2/2}\left[I_{\frac{(n-1)}{2}}\left(\chi^2/2\right) + I_{\frac{(n+1)}{2}}\left(\chi^2/2\right)\right] \tag{3.7}$$

Thus we can find the resolution if we know the true reaction plane. Of course in any experimental context this is impossible. To get at this we will consider two subevents (fractions of the total coverage used to find Ψ_n) A and B chosen such that they are equal haves of the coverage and thus have equal multiplicity. The resolution of these subevents must be equal and thus the sub-event plane resolution is given by

$$R_{n,\text{sub}} = \sqrt{\langle \cos\left(n\left(\Psi_n^A - \Psi_n^B\right)\right)\rangle} \tag{3.8}$$

The full event plane resolution can be solved using the sub-event plane resolution by using eq. 3.7 iteratively using

$$R_{n,\text{full}} = R_n\left(\sqrt{2}\chi_{\text{sub}}\right) \tag{3.9}$$

It is important to note that this formulation of the resolution only takes into account the size of the flow and the finite statistical effect. Other effects may alter the calculation of the resolution. If the subevents come very close in phase space they may share particle correlations from resonance decays. The subevents for this analysis are the east and west BBC event planes. These are well separated in rapidity, so resonance decays are not a concern. Event planes get decorrelated with increased rapidity. This is a physics effect which is not taken into account in the calculation of the resolution. One would have to perform a study on decorrelation to know the size of this effect, which is especially difficult for a first-order analysis since the v_1 is identically zero at midrapidity. Another physics correlation not taken into account is momentum conservation which could affect the forward-backward asymmetry of measured particles.

The resolution is calculated in discrete centrality bins. On a bin-by-bin basis it represents a scaling of the data as seen in eq. 3.4, which has no affect on the relative uncertainty of the datapoint. However, adding several such scaled bins together increases the relative error of the datapoints. The resolution can be seen in fig. 3.8.

Since the v_1 is maximum in mid-central collisions the resolution peaks there. One might expect that the resolution would increase with $\sqrt{s_{\text{NN}}}$, however the opposite effect is seen. This is because the flow in the BBC coverage increases with decreasing $\sqrt{s_{\text{NN}}}$. The uncorrected polarization can be seen in fig. 3.9.

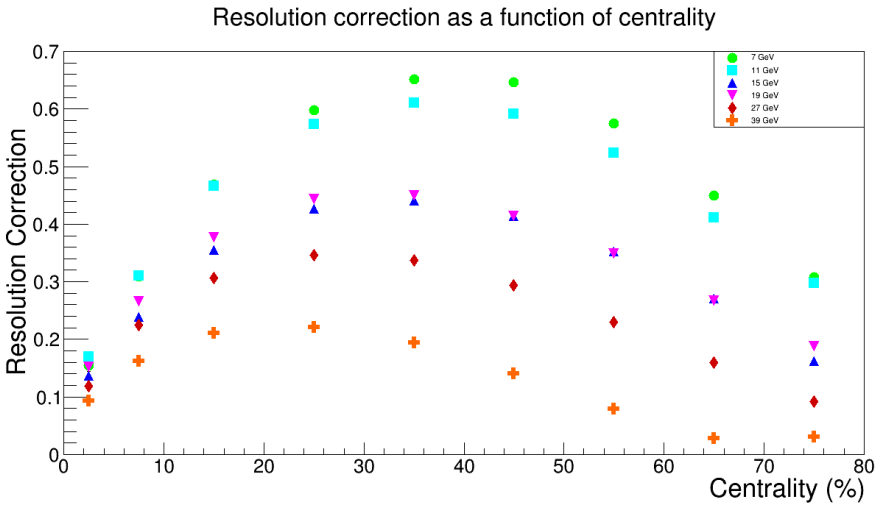

Figure 3.8: Resolution correction as a function of centrality

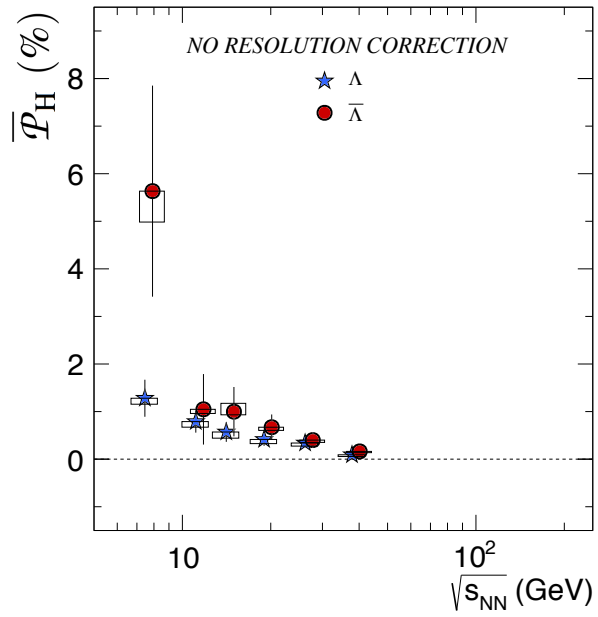

Figure 3.9: Polarization measure without applying resolution correction.

3.3 Detector acceptance correction

The polarization as described in eq. 3.4 assumes a perfect 4π detector. When we performed the integral over the solid angle in eq. 3.2 the metric used should be $d\Omega_p^* = d\phi_p^* \sin(\theta_p^* d\theta_p^*)$. What we actually get when we consider limited detector acceptance is

$$\langle \sin\left(\Psi_{RP} - \phi_p^*\right)\rangle = \int \frac{d\Omega_p^*}{4\pi}\frac{d\phi_H^*}{2\pi} A(\mathbf{p}_H, \mathbf{p}_p^*) \int_0^{2\pi} \frac{d\Psi_{RP}}{2\pi} \sin\left(\Psi_{RP} - \phi_p^*\right)\left[1 + \alpha_H P_H\left(\mathbf{p}_H, \Psi_{RP}\right)\sin\theta_p^* \cdot \sin\left(\Psi_{RP} - \phi_p^*\right)\right] \tag{3.10}$$

where $\mathbf{p}_H$ is the hyperon 3-momentum and $A(\mathbf{p}_H, \mathbf{p}_p^*)$ is a function to account for the acceptance; the integral of which is unity. Since the polarization can, in principle, depend on the Lambda's azimuthal angle and the detector is even with respect to ϕ we can expand the polarization into a sum over even harmonics:

$$P_H\left(\Psi_{RP} - \phi_p^*, p_T^H, \eta^H\right) = \sum_{n=0}^{\infty} P_H^{(2n)}\left(p_T^H, \eta^H\right)\cos\left\{2n\left[\Psi_{RP} - \phi_p^*\right]\right\}. \tag{3.11}$$

In this polarization analysis we are not quoting any such azimuthal dependence of the signal so we quote the polarization averaged over all possible values of $\phi_H - \Psi_{RP}$:

$$P_H\left(p_T^H, \eta^H\right) \equiv \overline{P_H\left(\Psi_{RP} - \phi_p^*, p_T^H, \eta^H\right)} = P_H^{(0)}\left(p_T^H, \eta^H\right) \tag{3.12}$$

By substituting eq. 3.11 into eq. 3.10 and integrating over the reaction plane we get

$$\langle \sin\left(\Psi_{RP} - \phi_p^*\right)\rangle = \frac{\alpha_H}{2}\int \frac{d\Omega_p^*}{4\pi}\frac{d\phi_H^*}{2\pi} A(\mathbf{p}_H, \mathbf{p}_p^*)\sin\theta_p^*\left[P_H\left(p_T^H, \eta^H\right) - \frac{1}{2}\cos\left[2\left(\phi_H - \phi_p^*\right)\right]P_H^{(2)}\left(p_T^H, \eta^H\right)\right]. \tag{3.13}$$

From here the observable $P_H = \frac{8}{\pi\alpha_H}\langle \sin\left(\Psi_{RP} - \phi_p^*\right)\rangle$ can be written

$$\begin{aligned}\frac{8}{\pi\alpha_H}\langle \sin\left(\Psi_{RP} - \phi_p^*\right)\rangle &= \frac{4}{\pi}\overline{\sin\theta_p^*} P_H\left(p_T^H, \eta^H\right) - \frac{2}{\pi}\overline{\sin\theta_p^* \cos\left[2\left(\phi_H - \phi_p^*\right)\right]} P_H^{(2)}\left(p_T^H, \eta^H\right) \\ &= A_0\left(p_T^H, \eta^H\right) P_H\left(p_T^H, \eta^H\right) - A_2\left(p_T^H, \eta^H\right) P_H^{(2)}\left(p_T^H, \eta^H\right),\end{aligned} \tag{3.14}$$

where the functions $A_0\left(p_T^H, \eta^H\right)$ and $A_2\left(p_T^H, \eta^H\right)$ are defined by the average of $\sin\theta_p^*$ and

$\sin\theta_p^* \cos\left[2\left(\phi_H - \phi_p^*\right)\right]$ over the detector acceptance according to

$$A_0\left(p_T^H, \eta^H\right) = \frac{4}{\pi}\overline{\sin\theta_p^*} \equiv \frac{4}{\pi}\int \frac{d\Omega_p^*}{4\pi}\frac{d\phi_H^*}{2\pi} A(\mathbf{p}_H, \mathbf{p}_p^*)\sin\theta_p^* \tag{3.15}$$

$$A_2\left(p_T^H, \eta^H\right) = \frac{2}{\pi}\overline{\sin\theta_p^* \cos\left[2\left(\phi_H - \phi_p^*\right)\right]} \equiv \frac{2}{\pi}\int \frac{d\Omega_p^*}{4\pi}\frac{d\phi_H^*}{2\pi} A(\mathbf{p}_H, \mathbf{p}_p^*)\sin\theta_p^* \cos\left[2\left(\phi_H - \phi_p^*\right)\right]. \tag{3.16}$$

$\sqrt{s_{NN}}$	A_0	A_0 error
7.7GeV	1.034	2.56e-4
11.5GeV	1.032	1.59e-4
14.5GeV	1.026	1.23e-4
19.6GeV	1.027	9.26e-5
27GeV	1.026	6.45e-5
39GeV	1.022	5.75e-5

Table 3.1: A_0 averaged over p_T^H and η^H

3.3.1 Detector acceptance correction results

Tab. 3.1 shows the numerical results for A_0 averaged over p_T^H and η^H. We do not look at the dependencies for this measurement since the quoted values for the measurement itself already are integrated over p_T^H and η^H. The polarization is divided by these numbers to arrive at the acceptance corrected values.

3.4 Mass background

When we try to find Λs and $\overline{\Lambda}$s it is done statistically by cutting on the spatial properties of the final state daughters as can be seen in sec. 4.4.2. Thus a significant number of the "Λs" we measure are, in fact, statistical combinations of otherwise unrelated protons and pions. These particles make up the mass background of the measurement. The Λs are taken from the proton-pion invariant mass range $1.108\text{GeV} < m_{\text{inv}} < 1.125\text{GeV}$ which is illustrated in fig. 3.10.

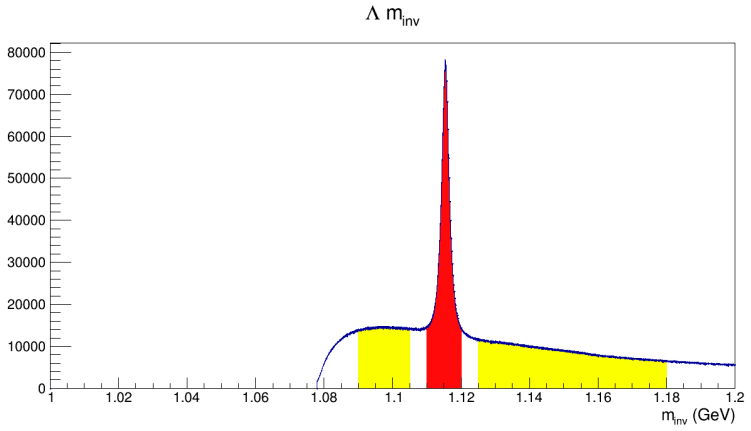

Figure 3.10: Λ counts as a function of invariant mass. The signal region ($1.108\text{GeV} < m_{\text{inv}} < 1.125\text{GeV}$) is highlighted in red.

We need to scale the data appropriately by the purity of this signal. The size of the background contribution is estimated by a linear extrapolation from between the two limits. The counts under that line is the "background" (denoted B) and the total counts in the signal region minus the background is the "signal" (denoted S). The purity is shown in tab 3.2.

The signal for the Lambda polarization could leak into the mass wings via protons which are real Lambda daughters being paired with pions which are not their siblings. This effect is difficult to quantify but it isn't as incredible as it might sound. Proton DCA cuts are designed to pick only non-primary protons, the majority of which should come from Lambdas. The off mass signals we see may turn out not to be anomalies, as they persist through systematic checks of signal dependencies (as in different regions of E_Λ, y_Λ, centrality, ϕ_Λ, and the suite of topology cuts). If the the signal in the on-peak portion of the mass distribution is S

$\sqrt{s_{NN}}$	Λ: $(S+B)/S$	$\overline{\Lambda}$: $(S+B)/S$
7.7GeV	1.57137	1.21407
11.5GeV	1.53215	1.2381
14.5GeV	1.77936	1.40786
19.6GeV	1.52895	1.29553
27GeV	1.54274	1.34728
39GeV	1.5029	1.36051

Table 3.2: Purities for Λ and $\overline{\Lambda}$. The 14.5GeV values are noticeable worse. It is likely that this is due to a detector (the HFT) which was only in during that data collecting period. This deviation can be seen in fig. 4.55.

and the height of the background is B we can do a similar subtraction of the off mass component as a flow measurement would do. In the final analysis we to not take this scaling into account (we assume zero background) but this calculation is important for the systematic errors. The off mass component is averaged from the $m_{\text{inv}} > m_{\Lambda}$ and the $m_{\text{inv}} > m_{\Lambda}$ component. Looking at the on mass peak Lambdas we measure

$$\langle \sin(\Psi_1 - \phi^*_{\Lambda}) \rangle_{\text{On Peak}} = \frac{S\langle \sin(\Psi_1 - \phi^*_{\Lambda}) \rangle_{\Lambda} + B\langle \sin(\Psi_1 - \phi^*_{\Lambda}) \rangle_{\text{Off Peak}}}{S+B} \tag{3.17}$$

Of course we want to know the Λ portion of the above equation so the mass corrected value takes the form

$$\langle \sin(\Psi_1 - \phi^*_{\Lambda}) \rangle_{\Lambda} = \frac{S+B}{S}\langle \sin(\Psi_1 - \phi^*_{\Lambda}) \rangle_{\text{On Peak}} - \frac{B}{S}\langle \sin(\Psi_1 - \phi^*_{\Lambda}) \rangle_{\text{Off Peak}} \tag{3.18}$$

Since we relegate the consideration of a signal in the off mass term to the systematic errors only the first term in eq. 3.18 is relevant here. Thus the purity correction is multiplicative and does not affect the significance of the data.

3.5 Helicity efficiency

An efficiency issue which is important for this analysis has to do with the direction the Lambda daughters are emitted in the rest frame of the Lambda with respect to the momentum of the Lambda in the lab frame. The root of this issue is that very low momentum protons are much more likely to be measured than very low momentum pions. As can be seen in sec. 4.3 the analysis is performed with minimum requirements on the p_T and the number of TPC pad rows the track to ensure track quality. The radius of curvature is proportional to the mass, thus the radius of curvature for the helix of a proton in a magnetic field is approximately 7 times larger than for the pion. A low momentum pion may simply circulate inside the TPC or hit very few pad planes.

Since the emission direction of a proton in the Λ's rest frame is, statistically, determined by the Λ's spin a positive helicity Λ will emit a pion opposite it's direction of motion. In such a case the pion has a very small momentum in the detector frame due to the direction of the boost. In the opposite scenario of a negative helicity Λ the resulting proton will have low momentum, but a considerably higher reconstruction efficiency than the low momentum pion for a the positive helicity Λ. This is, of course, the opposite scenario for the $\overline{\Lambda}$ due to the tendency for the anti-proton to be emitted *opposite* the direction of the $\overline{\Lambda}$ spin (thus the negative value of $\alpha_{\overline{\Lambda}}$). To summarize **STAR has a higher efficiency to measure positive helicity Λs** and **STAR has a higher efficiency to measure negative helicity $\overline{\Lambda}$s**. An example for Λs is shown in fig. 3.11.

It's plain to see that in the absence of a global polarization signal this cannot *create* a polarization signal. The affect on the signal from an overabundance of Lambdas emitted in some direction relative to the coordinates of the fireball (e.g. due to v_2) is explicitly canceled by the same abundance with opposite average helicity emitted 180° in ϕ. In sec. 3.5.1 I'll show this effect in data and simulation. In sec. 3.5.2 I'll describe how this efficiency modifies the measured (ϕ averaged) polarization signal given a nonzero measure of P_H. It is roughly estimated that this efficiency increases the measured polarization by 7%. This could also have some relevance to Chiral Vortical Effect (CVE) measurements. Appropriate systematic error bars are considered in sec. 5.3. In these sections I'll use a "*" to denote the rest frame of a Lambda.

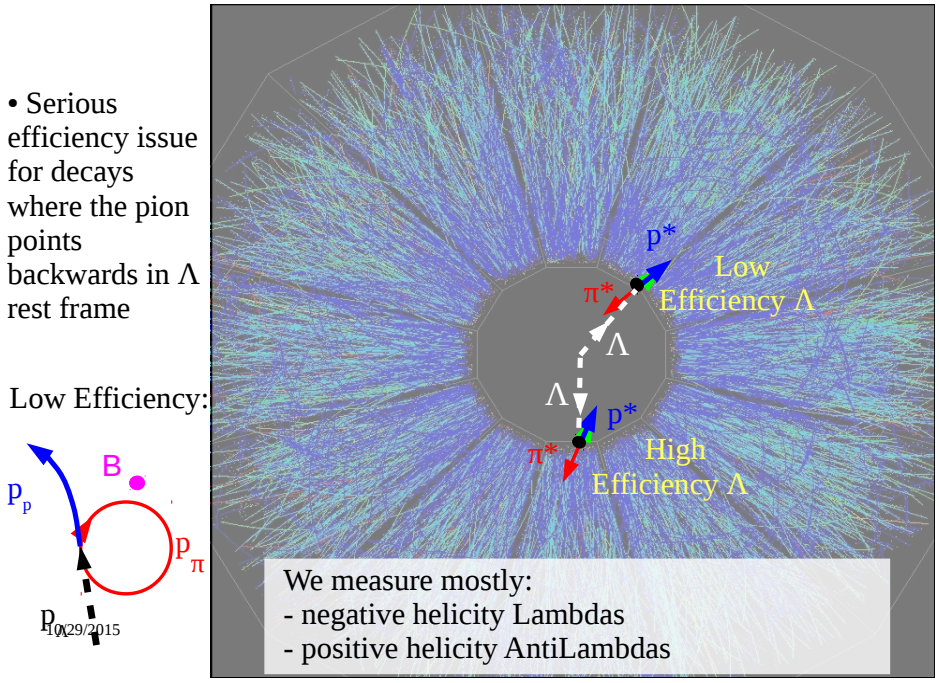

Figure 3.11: Diagram to show the poor efficiency of Lambdas with low momentum pion daughters as compared to Lambdas with low momentum proton daughters. Dashed white lines are Λs' momenta in the lab frame (the two examples are chosen to have the same finite decay length), blue arrows show proton momentum direction the the mother Λ frame, and red arrows depict the pion momentum direction the the mother Λ frame. The "*" denotes the rest frame of the Λ.

3.5.1 Description of helicity efficiency

One of the ways to see this helicity efficiency is to look at the dot product between a Lambda's momentum direction in the lab frame and the proton's momentum direction in the rest frame of the Lambda ($\hat{p}^*_p \cdot \hat{p}_\Lambda$). The polarization itself is small enough that it is appropriate to take $P_H = 0$ when interpreting the figures in this section. Even with polarization if we don't input anything about the collision orientation in the detector coordinate system one would expect the emission direction of the proton to be totally independent of the Λ momentum. For collected data shown in fig. 3.12 there is a clear bias for $\hat{p}^*_p$ to point in the opposite direction as $\hat{p}_\Lambda$. The simulation data in fig. 3.13 is the same cut, but from HIJING simulation data. In the simulation data we can take the pure Λs with no cuts applied and compare the distribution when we require a minimum p_T (as in done in the data). Clearly the driver of this effect is the pion p_T.

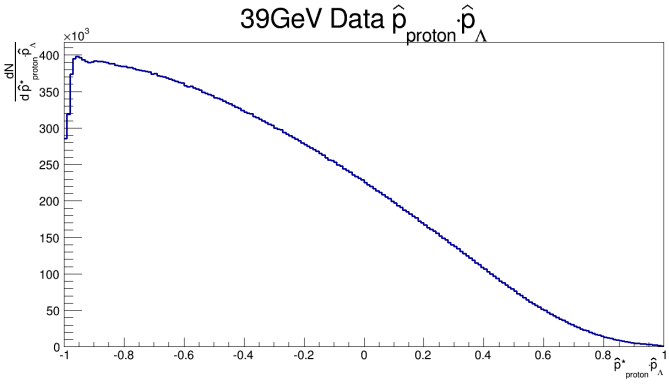

Figure 3.12: $\hat{p}^*_{\text{proton}} \cdot \hat{p_\Lambda}$ for 39GeV. Despite the axis label this is not normalized. This quantity essentially the same for all $\sqrt{s_{\text{NN}}}$. Naturally, physically, this plot should be totally flat since there should be no preferred direction for proton momentum (ignoring some sort of coupling of polarization with emission angle and Lambda yields - which we can basically ignore).

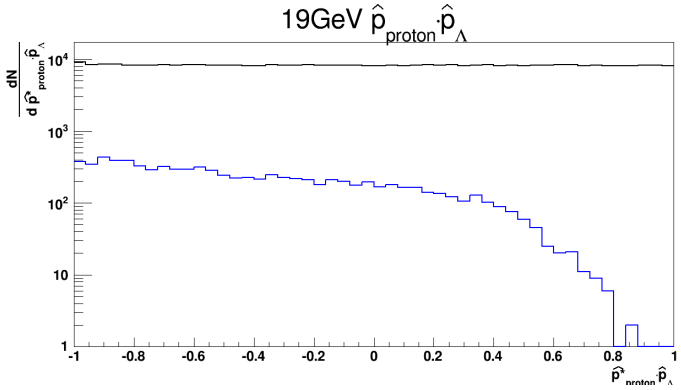

Figure 3.13: This is the same as fig. 3.12, but made using HIJING data. The black curve is from pure simulation Λs. The blue curve is made from requiring a minimum track $p_T = 0.15$GeV.

To see how this affects the data one can look at $\left\langle \sin\left(\Psi_1 - \phi^*_{\Lambda,\bar{\Lambda}}\right)\right\rangle$ vs. $\Psi_1 - \phi_{\Lambda,\bar{\Lambda}}$. There is a sign error In the following plots the quantity $-\left\langle \sin\left(\Psi_1 - \phi^*_{\Lambda,\bar{\Lambda}}\right)\right\rangle$ (that is, without all possible scalings) is plotted. One might readily notice that there is a sign error in this expression as compared to eq. 3.13. This is due to a sign error in the original STAR paper [44], for which there is now a published erratum.

I've elected to show two energies to make a particular point here. The Λ results for 39GeV are shown in fig. 3.14 and the results for 27GeV are shown in fig. 3.16. Similarly The $\overline{\Lambda}$ results for 39GeV are shown in fig. 3.15 and the results for 27GeV are shown in fig. 3.17. The most striking feature of these figures, the sinusoidal behavior, is quite readily understood. As one rotates around the fireball starting from $p_{\Lambda,\overline{\Lambda}}$ pointing in 0° (relative to the fireball coordinates) one expects there to be no effect from the helicity dependence, because, regardless of value of the inefficiency the distribution of $\hat{p}^*_{p,\overline{p}}$ is still centered around 180°. When $p_{\Lambda,\overline{\Lambda}}$ points at 90° then, on average, $\hat{p}^*_{p,\overline{p}}$ points down towards 270°, which, as we know from fig. 3.2 is the direction of the angular momentum of the system. For all of these figures I made the rather large minimum p_T cut of 1GeV. This is done merely to accentuate these effects. It can change the size, but not the sign.

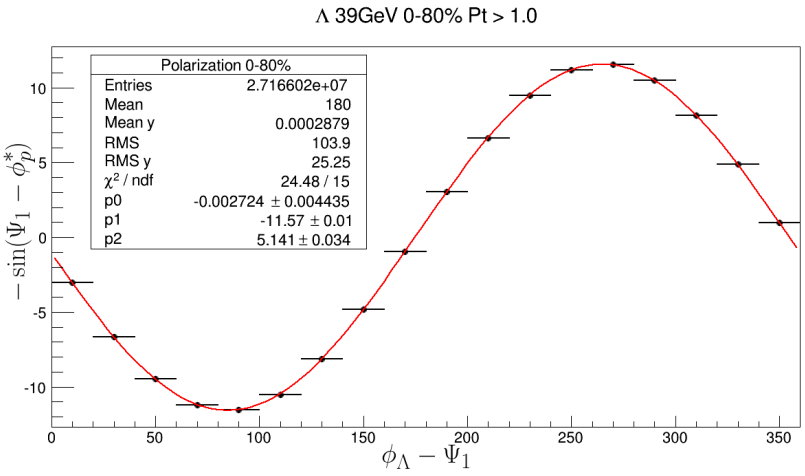

Figure 3.14: $-\langle \sin(\Psi_1 - \phi^*_\Lambda)\rangle$ vs. $\Psi_1 - \phi_\Lambda$ for 39GeV Λs with $p_T > 1$GeV. The data have been fit by the function p0 + p1*sin(x+p2). The overall sinusoidal shape comes from the effect mentioned above and seen in fig. 3.12. The specific phase shift comes from the STAR magnetic field which increases with p_T. 39GeV data has a RFF field alignment. The minus sign on the y axis corrects a sign mistake made early in the analysis.

There is a more subtle effect going on in the phases, which is why 27GeV and 39GeV data is shown

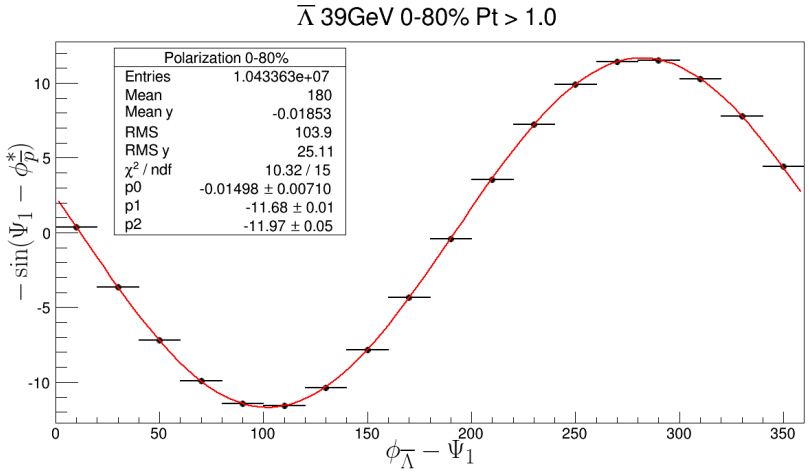

Figure 3.15: $-\langle \sin\left(\Psi_1 - \phi^*_{\bar{\Lambda}}\right)\rangle$ vs. $\Psi_1 - \phi_{\bar{\Lambda}}$ for 39GeV Λs with $p_T > 1$GeV. The data have been fit by the function p0 + p1*sin(x+p2). The overall sinusoidal shape comes from the effect mentioned above and seen in fig. 3.12. The specific phase shift comes from the STAR magnetic field which increases with p_T. 39GeV data has a RFF field alignment. Note that the phase is opposite in sign to what is seen in fig. 3.14. The minus sign on the y axis corrects a sign mistake made early in the analysis. For $\overline{\Lambda}$s, since the decay parameter is negative, this axis is true to the sign of the polarization.

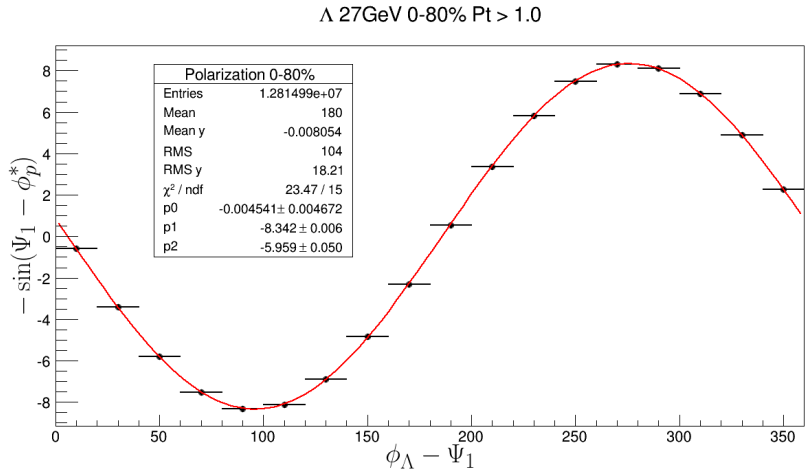

Figure 3.16: $-\langle \sin\left(\Psi_1 - \phi^*_{\Lambda}\right)\rangle$ vs. $\Psi_1 - \phi_{\Lambda}$ for 27GeV Λs with $p_T > 1$GeV. The data have been fit by the function p0 + p1*sin(x+p2). The overall sinusoidal shape comes from the effect mentioned above and seen in fig. 3.12. The specific phase shift comes from the STAR magnetic field which increases with p_T. 27GeV data has a FF field alignment. Note that the phase is opposite in sign to what is seen in fig. 3.14. The minus sign on the y axis corrects a sign mistake made early in the analysis.

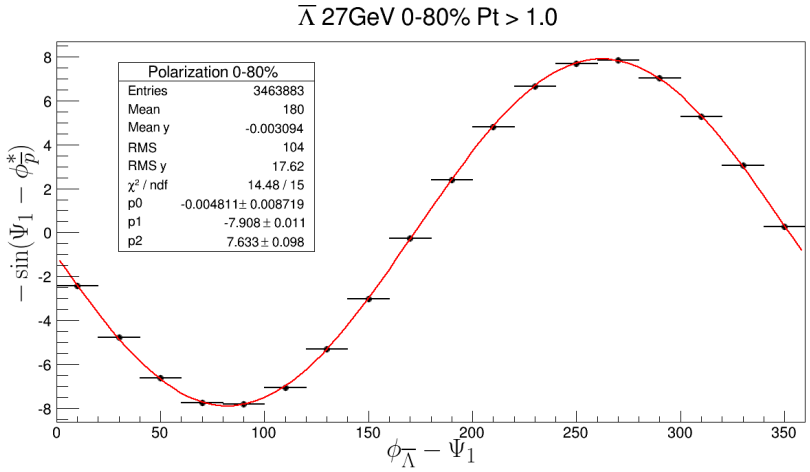

Figure 3.17: $-\left\langle \sin\left(\Psi_1 - \phi^*_{\overline{\Lambda}}\right)\right\rangle$ vs. $\Psi_1 - \phi_{\overline{\Lambda}}$ for 27GeV Λs with $p_T > 1$GeV. The data have been fit by the function p0 + p1*sin(x+p2). The overall sinusoidal shape comes from the effect mentioned above and seen in fig. 3.12. The specific phase shift comes from the STAR magnetic field which increases with p_T. 27GeV data has a RFF field alignment. Note that the phase is opposite in sign to what is seen in fig. 3.16. The minus sign on the y axis corrects a sign mistake made early in the analysis. For $\overline{\Lambda}$s, since the decay parameter is negative, this axis is true to the sign of the polarization.

here. One might see that the phase for Λs (which can be seen from the fit values) has an opposite sign between fig. 3.14 and fig. 3.16. The same is true for fig. 3.15 and fig. 3.17. Furthermore the sign of the phase for Λs is opposite that for $\overline{\Lambda}$s for plots of the same $\sqrt{s_{\mathrm{NN}}}$. The STAR magnet can be operated at 0.5T, which is called Full Field (FF), and -0.5T, which is called Full Field (RFF). The 27GeV was recorded in the FF configuration, while the rest of the BES (including 39GeV) was recorded using the RFF alignment. The phase thus must have some dependence on the charge of the daughter particles under consideration. Our conclusion is that this phase is a result of finite resolution in the creation vertex of the daughters. For $p_{\Lambda,\overline{\Lambda}}$ pointing in 0° in the FF configuration the magnetic field points in $+\hat{z}$ so the proton will appear to be bent slightly towards positive $\hat{y}$ which means negative $\hat{L}$. This imperfection leads to a negative value of $\sin\left(\Psi_1 - \phi^*_{\Lambda}\right)$ for such Λs. This effect is opposite for $\bar{\Lambda}$s. For the RFF this effect acquires yet another negative sign to keep track of and, thus, the observed phase qualitatively matches the prediction of finite vertexing.

Finally I want to compare these results to HIJING data as seen in fig. 3.18. In the HIJING data we are unable to reconstruct and angular momentum, so it is taken to be in the $+y$ direction (owing to the previously mentioned sign error from older published STAR data). In fact the HIJING data depicts a variant of the

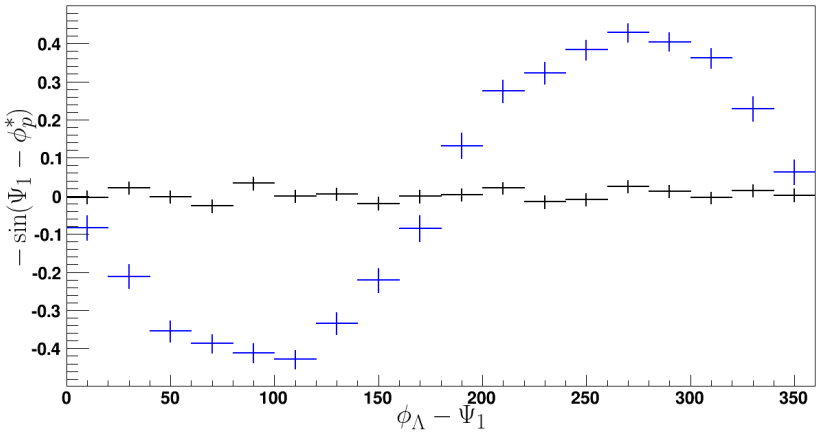

Figure 3.18: As in fig. 3.13 with HIJING data. The black curve is from pure simulation Λs. The blue curve is made from requiring basic reconstruction cuts. This has the assumption that the $\Psi_1 = 0$.

polarization measure where the spin of the Lambda is first determined via the direction of the (anti)proton. This spin 4-vector is given the magnitude of 1/2 and it is then boosted into the detector frame. Fig. 3.18 depicts the cosine of the angle of this boosted spin vector. Figs. 3.19, 3.20, and 3.21 use a related measure, which has since been abandoned, $S_y \equiv \vec{\text{spin}} \cdot \hat{L}$. One thing to note is that S_y is not technically constrained because a boost factor can be arbitrarily large. However, as can be seen from fig. 4.56, the Lambdas are fairly classical so the boost typically does very little. The magnitude of S_y/S is (mostly) constrained to be less than 1. We have found that this value is quantitatively *very* comparable to P_H, and no variations are known to exist qualitatively. I think taking these values to be qualitative markers of P_H is totally acceptable.

At any rate there is no particularly strong conclusion we can reach from HIJING given the relatively poor statistics, but it is of some value to see that we can turn the effect off by removing the minimum p_T requirement of the track, as seen in fig. 3.18. HIJING also allows us to at the effects of detector acceptance, which is of some archival value. Fig. 3.19 shows the effect that the $|\eta| < 1$ cut has on the data, fig. 3.20 shows what the minimum p_T cut does to limited acceptance window, and fig. 3.21 shows what this value looks like in very extreme η windows.

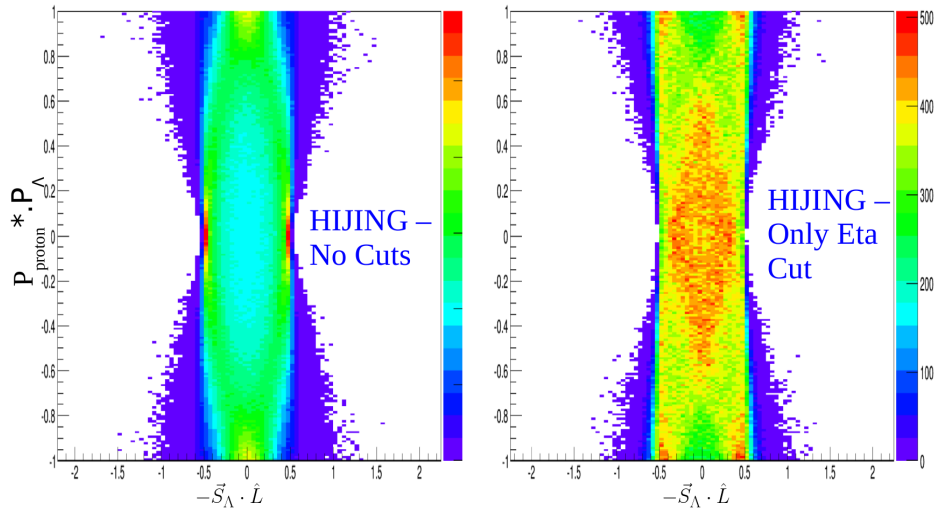

Figure 3.19: As in fig. 3.13 fig. 3.21 tells us how looking at S_y within the STAR η range changes the underlying distribution.

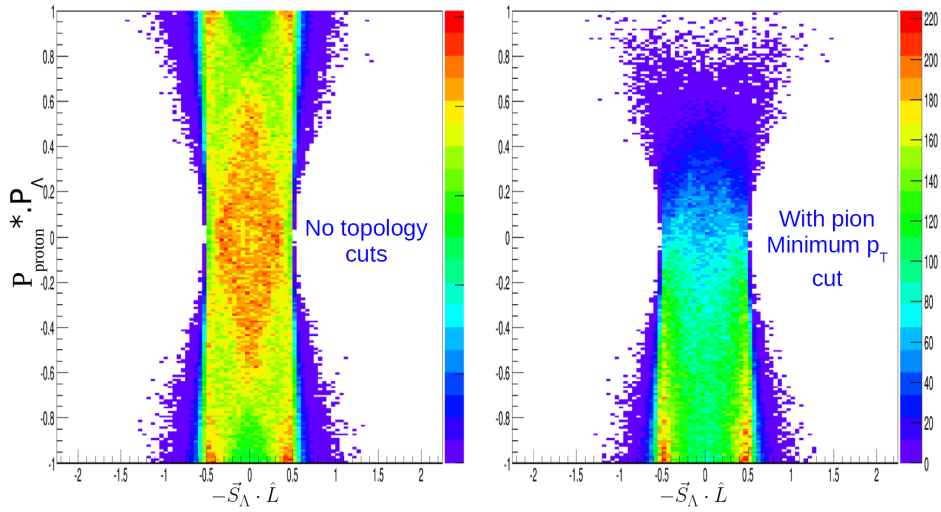

Figure 3.20: Finally we see what the effect the helicity efficiency (Fig 3.12) has on the underlying distribution (fig. 3.19). Now we see an asymmetry in the S_y distribution from the efficiency.

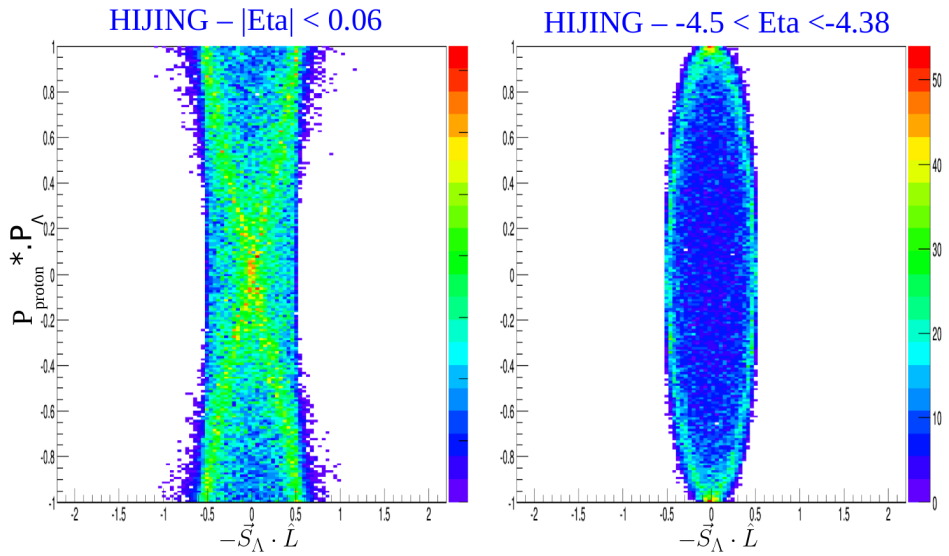

Figure 3.21: As in fig. 3.13 The figure on the left is a S_y for a narrow slice η_Λ at mid-rapidity while the figure on the right is a narrow slice very backward in η. For the first case the Λ in emitted in the same $x-y$ plane as $\hat{L}$ in the second figure it is almost perpendicular to $\hat{L}$. Since the proton tends to be emitted with basically the same momentum as the Lambda these tendencies make sense. The left figure is for collisions in the center of the detector and the right figure is for very forward collisions.

3.5.2 Consequence of helicity efficiency

For the figures in sec. 3.5.1 if we assume that there is no net-polarization signal all of those plots of polarization as a function of ϕ_Λ will average to zero, as any sine or cosine will over that range. If there actually is a polarization signal then there are some modifications which must be made to that conclusion. The first exception I'll point out is that the polarization could have a dependence on ϕ_Λ. As long as that dependence is second order it will still cancel. We haven't seen any evidence of any second order signal, which likely means the signal itself is just very small. Higher order ϕ_Λ could potentially exist, but we will assume that no such signal exists. This section will investigate a different affect assuming some nonzero polarization.

First I'll have to point out that the y axis of fig. 3.14 actually depicts the projection of the proton's momentum in the Λ mother's frame onto the direction *opposite* the angular momentum, thus it is requiring an overall sign flip in y. For a polarized Λ emitted in the $\phi_\Lambda = \pi/2$ direction the polarization measure will be some combination of the real tendency for Λs to be polarized and the tendency to not reconstruct Λs which would be called "negatively polarized". The real polarization of the Λs is going to modify the underlying distribution seen in the black line of fig. 3.13 into a line which is higher on the left-hand side of the figure and

lower on the right-hand side. The finite polarization will decrease the pion momentum distribution further leading to a sort of feed-back effect where the number of reconstructed Λs at $\phi_\Lambda = \pi/2$ is *larger* given a finite global polarization signal. Similarly the number of reconstructed Λs at $\phi_\Lambda = 3\pi/2$ is *smaller* given a finite global polarization signal. The overall effect is that given a finite global polarization signal one cannot rely on periodicity seen fig. 3.14 to cancel. This argument is shown pictorially below. Fig. 3.22 is a cartoon of a medium which is polarization while fig. 3.23 is a cartoon of the inverse scenario. Fig. 3.5.2 is a cartoon of adding these two effects together and fig. 3.25 shows the addition and depletion of Λs as a function of ϕ_Λ.

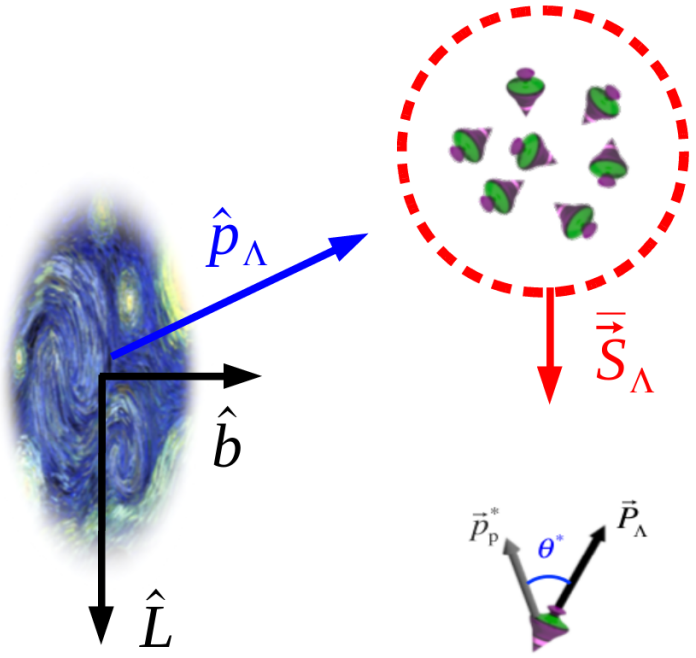

Figure 3.22: A polarized medium with no efficiency effect. An ensemble of spinning Λs (represented as tops) is emitted with momentum p_Λ which has net spin $\vec{S}_\Lambda$ pointing in the direction of angular momentum.

We can learn something from a relatively simple simulation. In the simulation the azimuthal distribution of the Lambda daughters are chosen by sampling the polarization distribution with a given input polarization. Then a minimum daughter p_T cut is applied to the decayed Lambdas. After the cuts is applied we "measure" the polarization of the Lambdas and check how much it differs from the input. Naturally this could depend on other cuts. Not topology cuts (listed in sec. 4.4.2) are possible in a simple simulation and the p_T cut

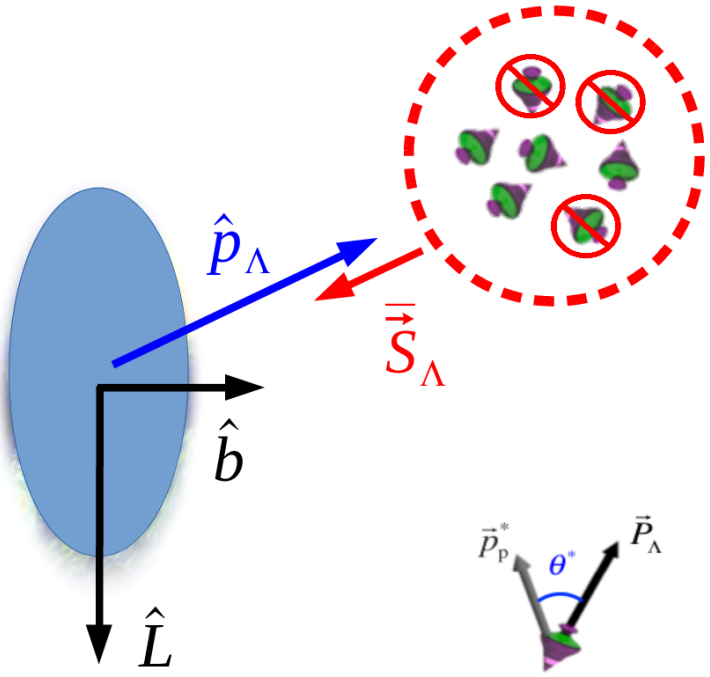

Figure 3.23: An unpolarized medium with the efficiency effect. An ensemble of spinning Λs (represented as tops) is emitted with momentum p_Λ which has no net spin, but ends up with net spin $\vec{S}_\Lambda$ due entirely to the efficiency effect.

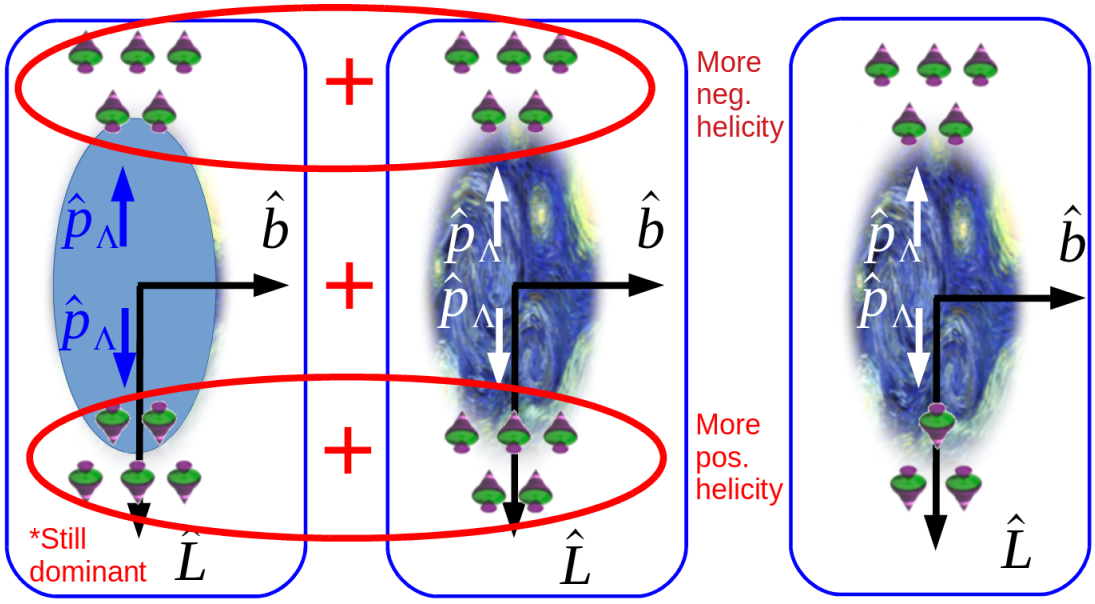

Figure 3.24: A polarized medium with the efficiency effect. When you add the effects together you get an apparent polarization which is larger than the real polarization.

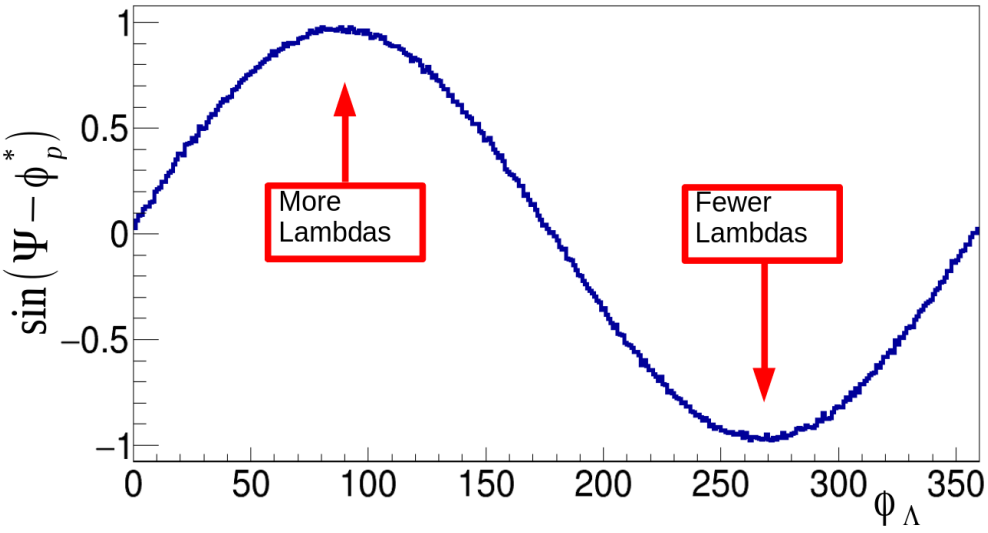

Figure 3.25: Efficiency addition/depletion effect on polarization as a function of ϕ_Λ. The natural variance of the spin is not properly demonstrated due to the complexity of that charge and limited space.

is *by far* the most important cut. The Lambda momentum for the simulation is chosen by sampling a real Lambda momentum distribution. Fig. 3.26 shows the ratio of the output to the input polarization as a function of the p_T cut. The simulation data is quite well behaved. The ratio looks fairly linear as a function of p_T cut and dramatically changing the polarization doesn't seem to have a large affect on the position of the points. Our nominal cut of $p_T > 0.15$GeV seems to make the apparent polarization about 7%. As discussed in sec. 5.3 there is a 3.5% systematic error associated with this scaling. This is a little overkill, but we're being especially careful. A complimentary study is shown with $\overline{\Lambda}$s in fig. 3.27. Since this effects the abundances of Λ and $\overline{\Lambda}$ as a function of emission angle it could have some effect on Chiral Vortical Effect (CVE) measurements, which seek to measure baryon number separation along the direction of vorticity (as mentions in sec. 7.6). To avoid charged particles, the $\Lambda/\overline{\Lambda}$ system is a common tool for measuring the CVE.

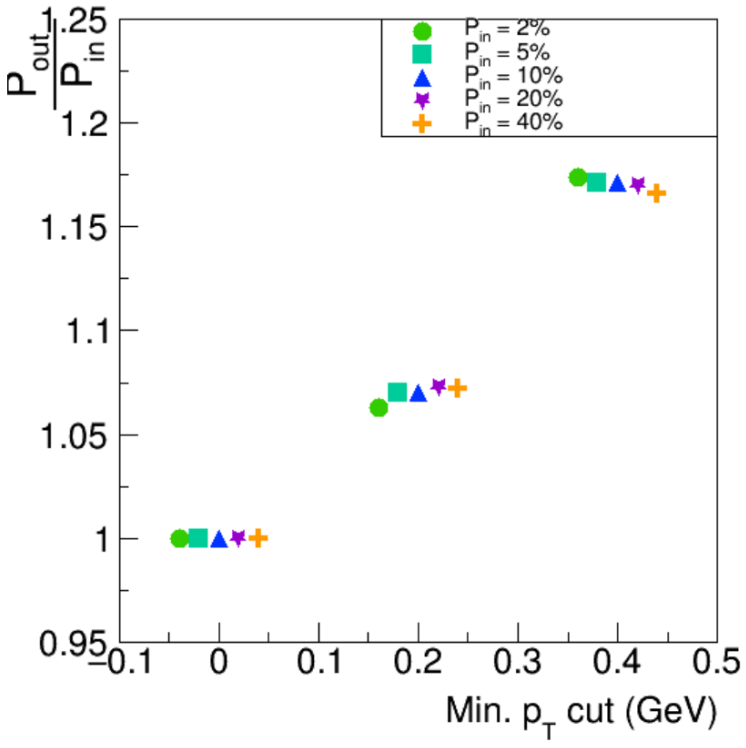

Figure 3.26: Ratio of apparent polarization (P_{out}) as a function of input polarization (P_{in}) as a function of the minimum p_T cut applied to the Λ daughters. Several different input polarizations are sampled, these datapoints were spread out for clarity.

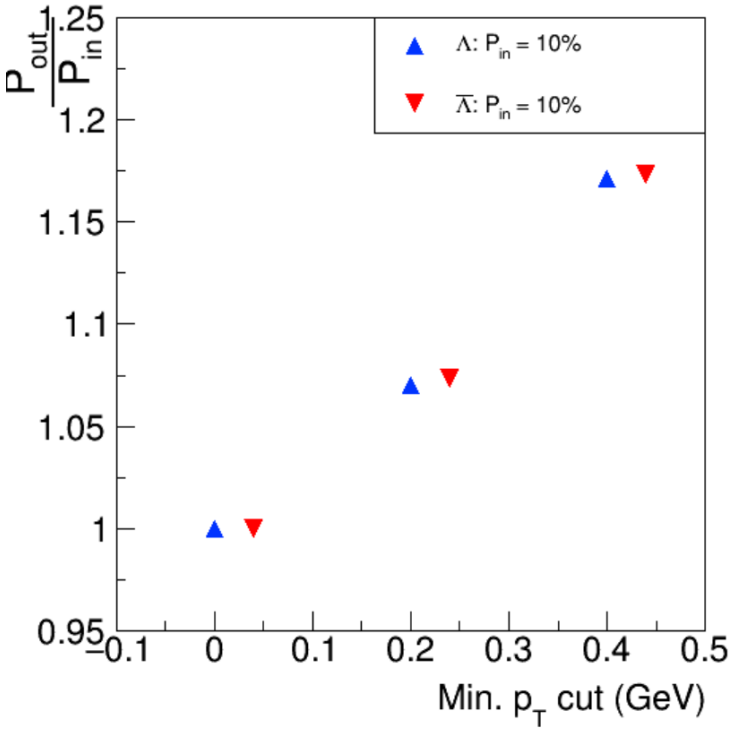

Figure 3.27: Ratio of apparent polarization (P_{out}) as a function of input polarization (P_{in}) as a function of the minimum p_T cut applied to the $\Lambda/\overline{\Lambda}$ daughters.

3.6 Discussion of statistical error

There is not much to discuss in this section but I want to clearly enumerate the sources of statistical error. Systematic errors are discussed in sec. 5. Of course the first thing is the statistical error itself coming from the variance of the polarization measure. The error bars are appropriately scaled with the various scalings and corrections we do to the data. The errors on these scalings make up the systematic error of the measurement. A detailed discussion on the error for the mass purity correction can be found in sec. 5.1.2. The other scalings (α_H the decay parameter, the event plane resolution correction, and the acceptance correction) all have associated errors which fall under systematics, and are discussed in sec. 5.3.

Chapter 4
QUALITY ASSURANCE

When working with real data there are a number of cross-checks we must perform in order to be sure the data is of high quality. In fact, the data we work with has already gone through a rigorous calibration effort by members of the collaboration. These checks and cuts are separated into different sections according to what sort of cuts they are. This section is primarily of archival importance.

4.1 Event QA

The events used in the analysis have the following cuts

- The magnitude of the z component of the primary vertex is $\leq$ 70cm. At 39GeV this is a 40cm cut and at 11GeV this is 50cm cut.
- TOF multiplicity ≥ 1
- the R vertex component is required to be less than 2cm except in the case of 15GeV where it is less than 1cm and centered at (0, -0.89) cm.
- The ADC sum for the East and West BBC are separately required to be ≥ 75
- Additionally there is an η symmetry cut so that $\left|\left(N_{\eta>0} - N_{\eta>0}\right)/N_{\text{total}}\right| \leq 5$
- The centrality ID that we get from StRefMultCorr (the STAR centrality definition algorithm) must be ≥ 0

The trigger list for each energy is

- 7.7GeV: 290001, 290004
- 11.5GeV: 310004, 310014
- 14.5GeV: 440005, 440015
- 19.6GeV: 340001, 340011, 340021
- 27GeV: 360001, 360002
- 39GeV: 280001, 280002

Additionally there is a list of rejected runs which is

- 7.7GeV: 11199124, 11100002, 11100045, 11101046, 11102012, 11102051, 11102052, 11102053, 11102054, 11102055, 11102058, 11103035, 11103056, 11103058, 11103092, 11103093, 11105052, 11105053, 11105054, 11105055, 11107007, 11107042, 11107057, 11107061, 11107065, 11107074, 11108101, 11109013, 11109077, 11109088, 11109090, 11109127, 11110013, 11110034, 11110073, 11110076, 11111084, 11111085
- 11.5GeV: 11148039, 11148045, 11149001, 11149008, 11149010, 11149011, 11149015, 11149047, 11150016, 11150025, 11150028, 11151036, 11151040, 11151050, 11152016, 11152036, 11152078, 11153032, 11153042, 11155001, 11155009, 11156003, 11156009, 11157012, 11158006, 11158022, 11158024
- 14.5GeV: 15046073, 15046089, 15046094, 15046096, 15046102, 15046103, 15046104, 15046105, 15046106, 15046107, 15046108, 15046109, 15046110, 15046111, 15047004, 15047015, 15047016, 15047019, 15047021, 15047023, 15047024, 15047026, 15047027, 15047028, 15047029, 15047030, 15047039, 15047040, 15047041, 15047044, 15047047, 15047050, 15047052, 15047053, 15047056, 15047057, 15047061, 15047062, 15047063, 15047064, 15047065, 15047068, 15047069, 15047070, 15047071, 15047072, 15047074, 15047075, 15047082, 15047085, 15047086, 15047087, 15047093, 15047096, 15047097, 15047098, 15047100, 15047102, 15047104, 15047106, 15048003, 15048004, 15048012, 15048013, 15048014, 15048016, 15048017, 15048018, 15048019, 15048020, 15048021, 15048023, 15048024, 15048025, 15048026, 15048028, 15048029, 15048030, 15048031, 15048033,

15048034, 15048074, 15048075, 15048076, 15048077, 15048078, 15048079, 15048080, 15048081, 15048082, 15048083, 15048084, 15048085, 15048086, 15048087, 15048088, 15048089, 15048091, 15048092, 15048093, 15048094, 15048095, 15048096, 15048097, 15048098, 15049002, 15049003, 15049009, 15049013, 15049014, 15049015, 15049016, 15049017, 15049018, 15049019, 15049020, 15049021, 15049022, 15049023, 15049025, 15049026, 15049027, 15049028, 15049030, 15049031, 15049032, 15049033, 15049037, 15049038, 15049039, 15049040, 15049041, 15049074, 15049077, 15049083, 15049084, 15049085, 15049086, 15049087, 15049088, 15049089, 15049090, 15049091, 15049092, 15049093, 15049094, 15049096, 15049097, 15049098, 15049099, 15050001, 15050002, 15050003, 15050004, 15050005, 15050006, 15050010, 15050011, 15050012, 15050013, 15050014, 15050015, 15050016, 15051131, 15051132, 15051133, 15051134, 15051137, 15051141, 15051144, 15051146, 15051147, 15051148, 15051149, 15051156, 15051157, 15051159, 15051160, 15052001, 15052004, 15052005, 15052006, 15052007, 15052008, 15052009, 15052010, 15052011, 15052014, 15052015, 15052016, 15052017, 15052018, 15052019, 15052020, 15052021, 15052022, 15052023, 15052024, 15052025, 15052026, 15052040, 15052041, 15052042, 15052043, 15052060, 15052061, 15052062, 15052063, 15052064, 15052065, 15052066, 15052067, 15052068, 15052069, 15052070, 15052073, 15052074, 15052075, 15053027, 15053028, 15053029, 15053034, 15053035, 15053052, 15053054, 15053055, 15054053, 15054054, 15055018, 15055137, 15056117, 15057055, 15057059, 15058006, 15058011, 15058021, 15059057, 15059058, 15061001, 15061009, 15062006, 15062069, 15065012, 15065014, 15066070, 15068013, 15068014, 15068016, 15068018, 15069036, 15070008, 15070009, 15070010

- 19.6GeV: 12113091, 12114007, 12114035, 12114078, 12114092, 12114116, 12115009, 12115014, 12115015, 12115016, 12115018, 12115019, 12115020, 12115022, 12115023, 12115062, 12115073, 12115093, 12115094, 12116012, 12116054, 12117010, 12117016, 12117020, 12117065, 12119040, 12119042, 12120017, 12120026, 12121017, 12121022, 12121034, 12121050, 12121067, 12122019

- 27GeV: 12172050, 12172051, 12172055, 12173030, 12173031, 12173032, 12173033, 12173034, 12174067, 12174085, 12175062, 12175087, 12175113, 12175114, 12175115, 12176001, 12176044, 12176054, 12176071, 12177015, 12177061, 12177092, 12177099, 12177101, 12177106, 12177107, 12177108, 12178003, 12178004, 12178005, 12178006, 12178013, 12178099, 12178120

- 39GeV: 11199124, 11100002, 11100045, 11101046, 11102012, 11102051, 11102052, 11102053, 11102054, 11102055, 11102058, 11103035, 11103056, 11103058, 11103092, 11103093, 11105052, 11105053, 11105054, 11105055, 11107007, 11107042, 11107057, 11107061, 11107065, 11107074, 11108101, 11109013, 11109077, 11109088, 11109090, 11109127, 11110013, 11110034, 11110073, 11110076, 11111084, 11111085

In addition to the bad runs list 15GeV events are taken only from running days 53-70.

The multiplicity of charged particles tracked by the TPC at midrapidity ($|\eta| < 1$) is shown in fig. 4.1. This quantity, called the reference multiplicity (or RefMult) is the basis for the STAR centrality determination and is thus central to our understanding of the collision. Very low multiplicity events may, in fact, not be collider events. To avoid contamination from incorrectly associated tracks STAR analyses generally do not use the most peripheral 20% of recorded events. Since the detector is cylindrically symmetric it performs best when the collisions occur at the center of the detector $(0,0,0)$. It is typical to split consideration between the the z component of the vertex position (so called Z Vertex) as seen in fig. 4.2 and the distance from the center in the $x-y$ plane (the R vertex) seen in fig. 4.6-4.11.

The Time Of Flight system also has a separate multiplicity. Often this is checked against the TPC multiplicity to make sure the detectors are working. The TOF is a fast detector which is an important part of the trigger. The TOF multiplicity can be seen in fig. 4.3. Since we also use the Beam Beam Counters in this analysis it's good to check the sum of the ADC (analog to digital conversion) for the west and the east BBC separately. This measure is just the sum over the 16 relevant ADCs and can be seen for all relevant $\sqrt{s_{\mathrm{NN}}}$ in fig. 4.4 and fig. 4.5. The BBCs are also part of the STAR trigger.

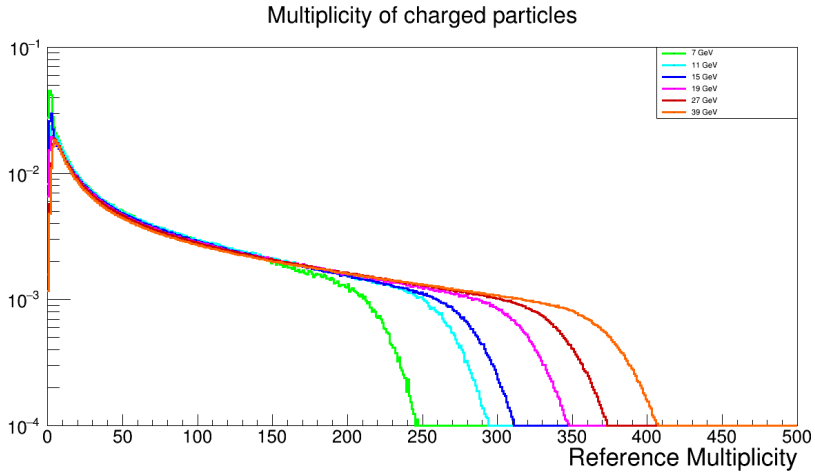

Figure 4.1: Multiplicity of charged tracks (normalized by number for easy comparison) for each $\sqrt{s_{\mathrm{NN}}}$ used in this analysis.

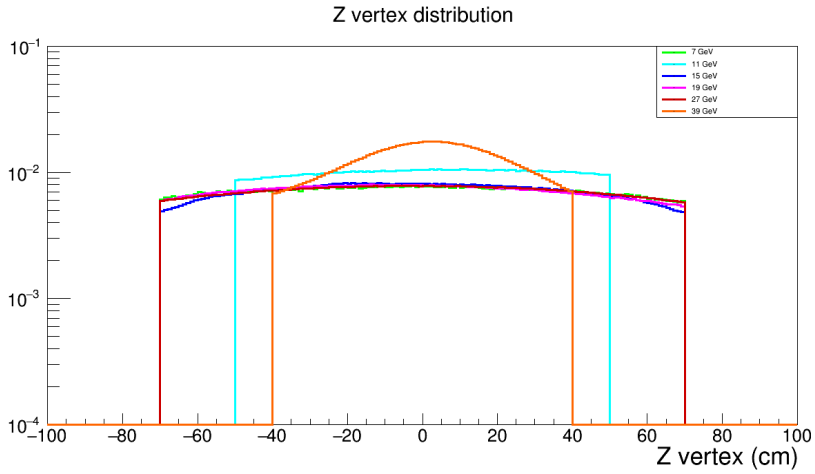

Figure 4.2: Z component of event vertex (normalized by number for easy comparison) in cm for each $\sqrt{s_{\mathrm{NN}}}$ used in this analysis.

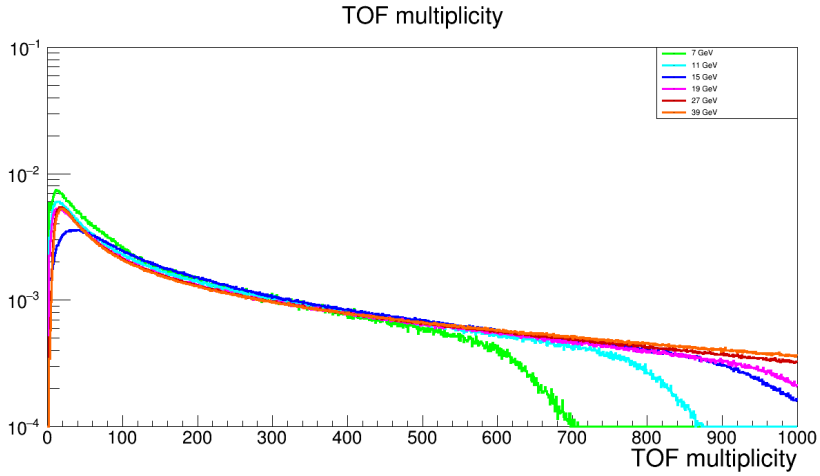

Figure 4.3: Multiplicity of charged particles as measured by the TOF (normalized by number for easy comparison) for each $\sqrt{s_{\mathrm{NN}}}$ used in this analysis.

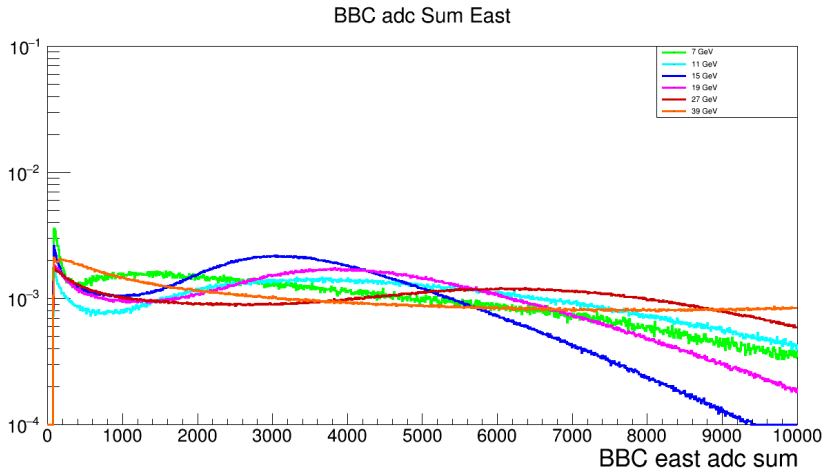

Figure 4.4: BBC East ADC sum (normalized by number for easy comparison) for each $\sqrt{s_{\mathrm{NN}}}$ used in this analysis. ADC is analog to digital conversion. It is unitless and is roughly proportional to the number of charged particles that hit the detector.

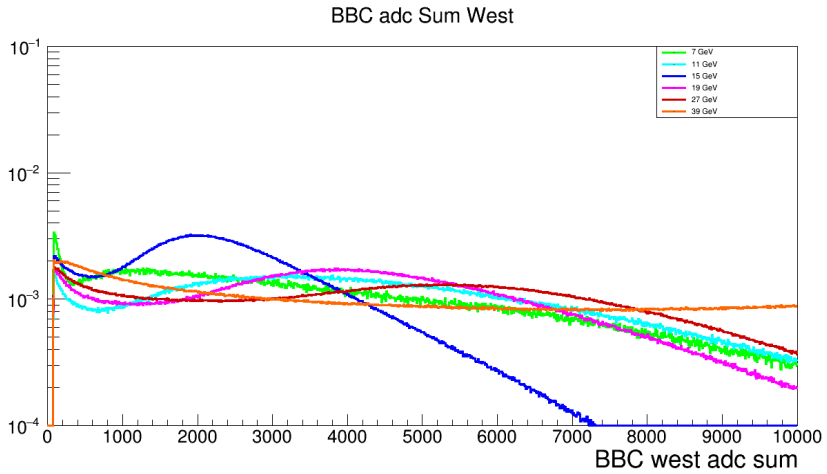

Figure 4.5: BBC West ADC sum (normalized by number for easy comparison) for each $\sqrt{s_{\mathrm{NN}}}$ used in this analysis. ADC is analog to digital conversion. It is unitless and is roughly proportional to the number of charged particles that hit the detector.

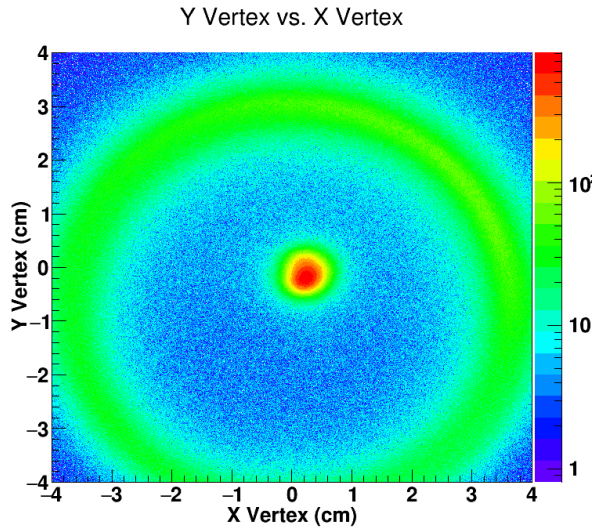

Figure 4.6: y component of primary vertex vs. x component of primary vertex (in cm) for 7GeV

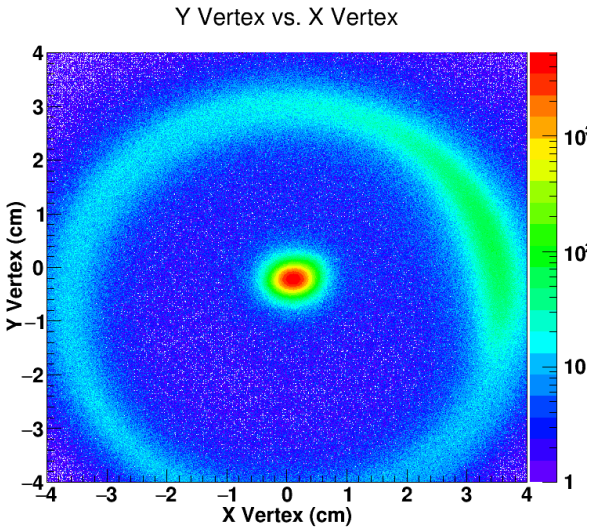

Figure 4.7: y component of primary vertex vs. x component of primary vertex (in cm) for 11GeV

4.2 Event plane determination

For discussion on how the event planes are found see sec. 3.1.

The following plots show the event plane distributions as they are corrected for all relevant energies. Various corrections are made to three planes. The east event plane is found only via the east BBC, the west plane is found by the west BBC, and the full event plane is found by combining the Q-vectors of the subevents. The "recentering correction" and the "shift correction" for the three planes are made totally independent of each other. The effect of the corrections on the average distribution can be seen in fig. 4.12-4.17. It is important to note that the distributions become flatter as the corrections are made. The distribution of event planes themselves must, physically, be flat. The corrections take into account the imperfections of the detectors.

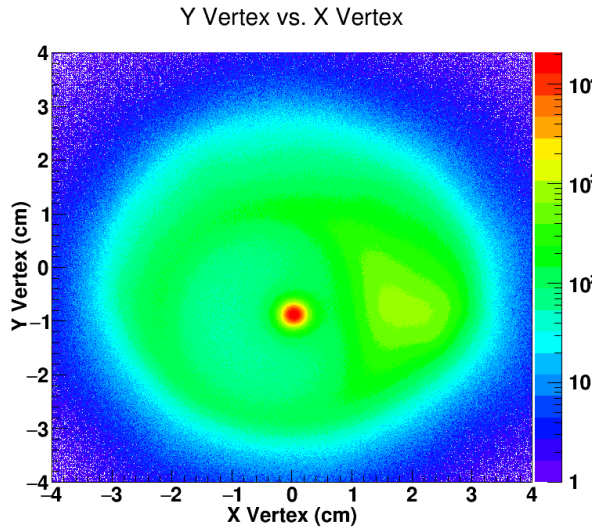

Figure 4.8: y component of primary vertex vs. x component of primary vertex (in cm) for 15GeV

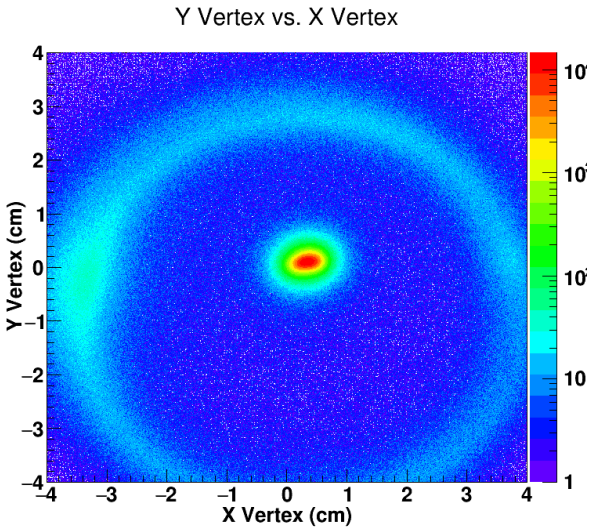

Figure 4.9: y component of primary vertex vs. x component of primary vertex (in cm) for 19GeV

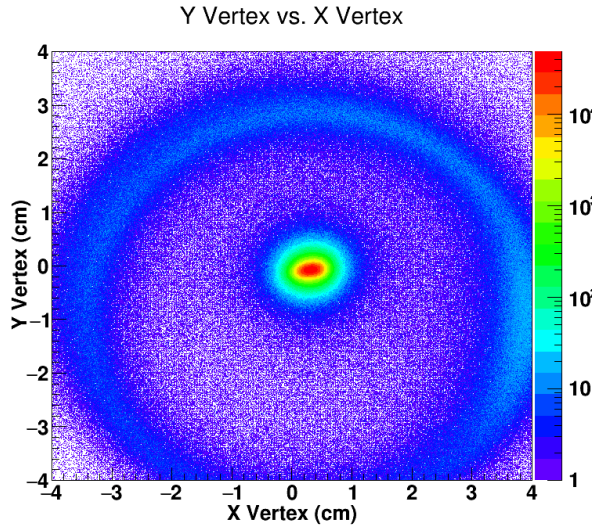

Figure 4.10: y component of primary vertex vs. x component of primary vertex (in cm) for 27GeV

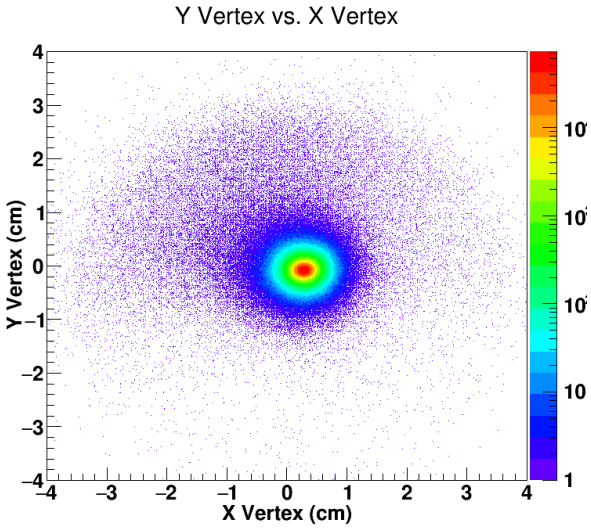

Figure 4.11: y component of primary vertex vs. x component of primary vertex (in cm) for 39GeV

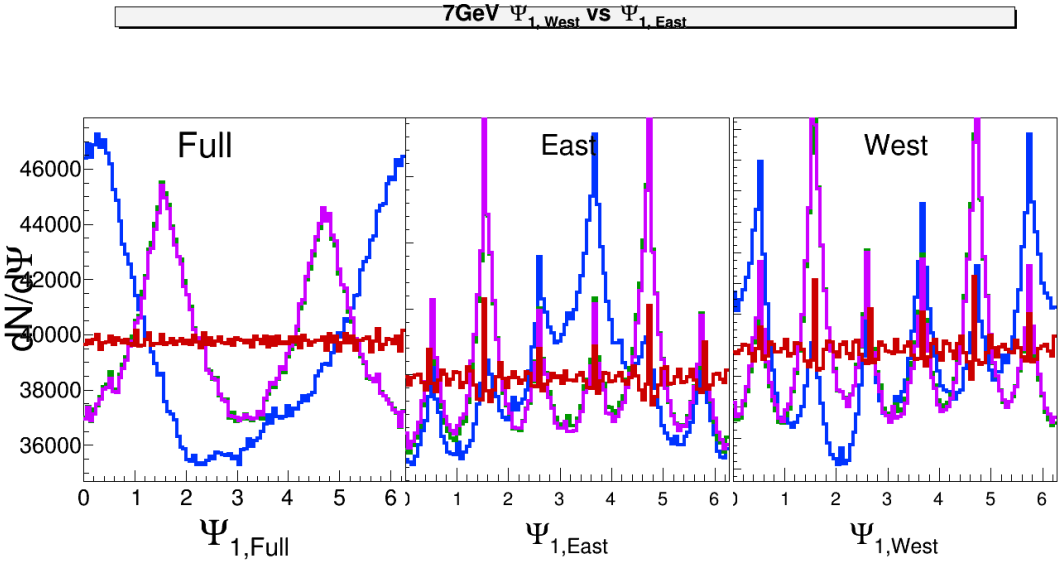

Figure 4.12: 7GeV Ψ_1 distribution as corrections are applied. Blue - Raw, Green - Gain corrected, Magenta - Recentered, Red - Shifted.

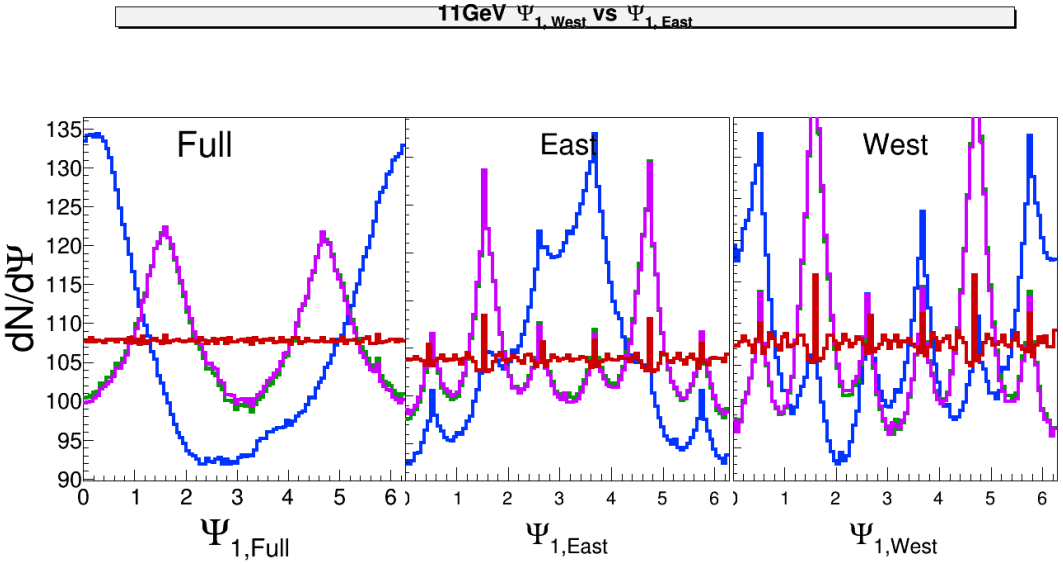

Figure 4.13: 11GeV Ψ_1 distribution as corrections are applied. Blue - Raw, Green - Gain corrected, Magenta - Recentered, Red - Shifted.

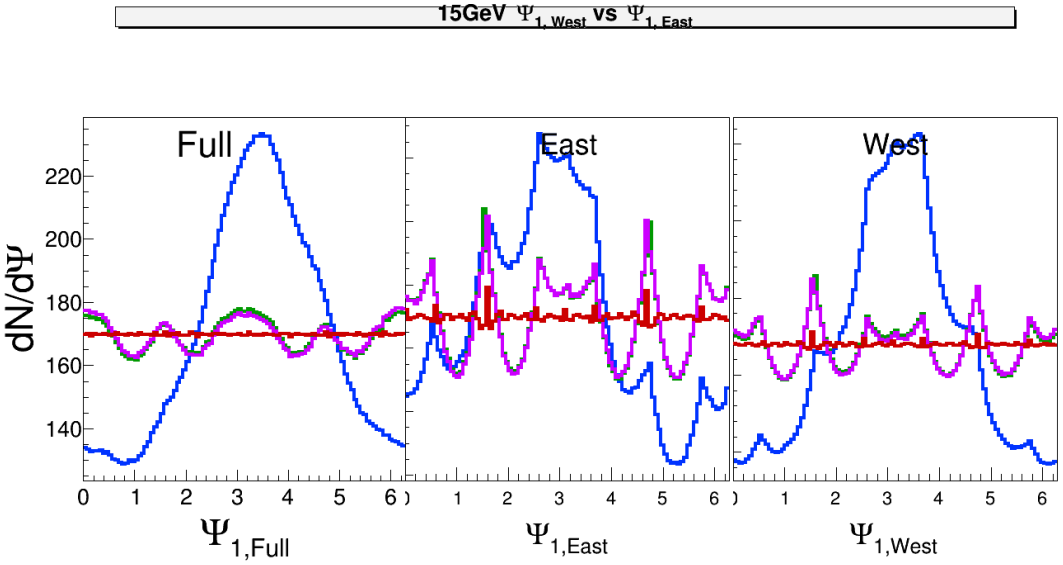

Figure 4.14: 15GeV Ψ_1 distribution as corrections are applied. Blue - Raw, Green - Gain corrected, Magenta - Recentered, Red - Shifted.

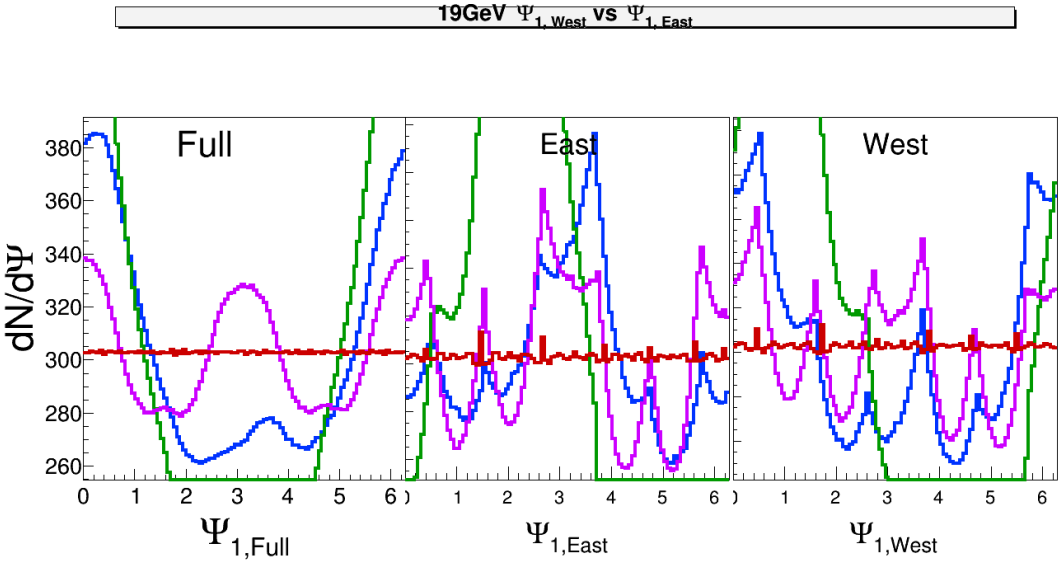

Figure 4.15: 19GeV Ψ_1 distribution as corrections are applied. Blue - Raw, Green - Gain corrected, Magenta - Recentered, Red - Shifted.

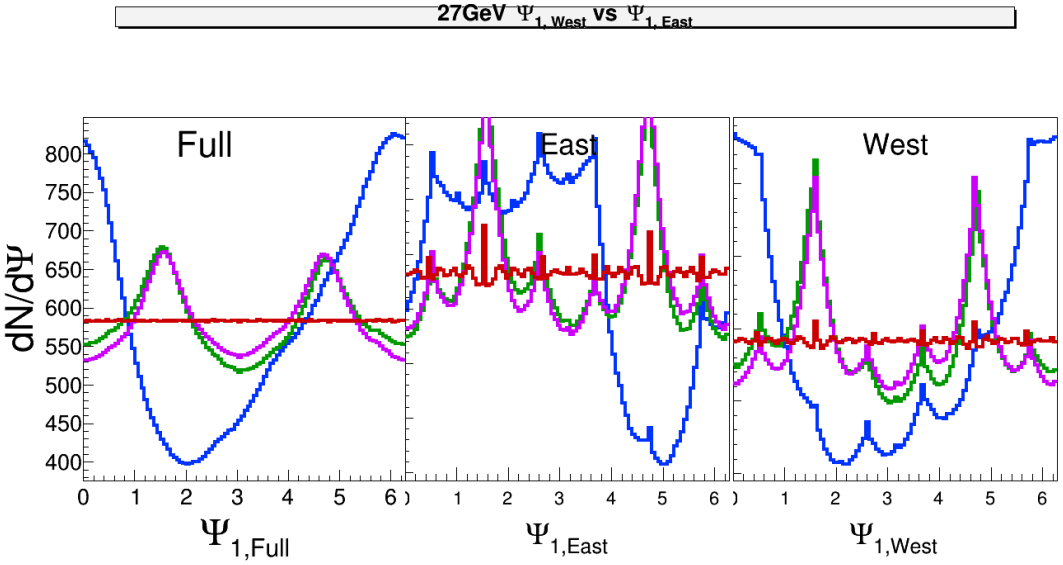

Figure 4.16: 27GeV Ψ_1 distribution as corrections are applied. Blue - Raw, Green - Gain corrected, Magenta - Recentered, Red - Shifted.

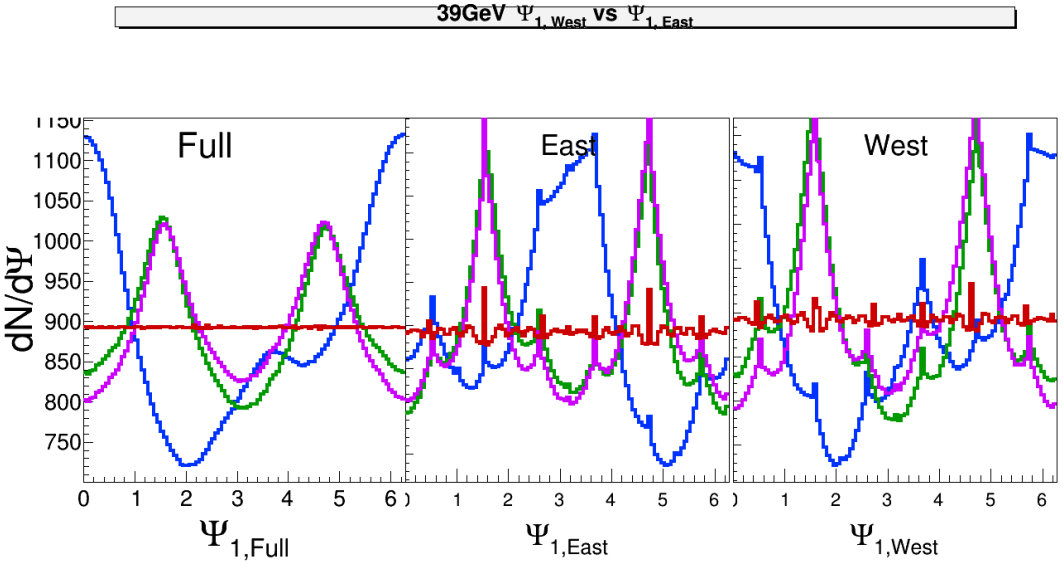

Figure 4.17: 39GeV Ψ_1 distribution as corrections are applied. Blue - Raw, Green - Gain corrected, Magenta - Recentered, Red - Shifted.

The one-dimenstional histograms of event plane distributions give some sense of the effect of the corrections, but they tell you nothing about how well the planes are correlated. The resolution of the full event plane (that is, how well it is determined) is found via the correlation between the east and west planes. Since the first-order plane is explicitly anti-symmetric in η and ϕ we expect the west plane to be anti-correlated to the east plane. If this anti-correlation is exact the resolution is 1 (see sec. 3.2). It is one thing to take the correlation as just a number (as in sec. 4.2.1), but it is also useful to look at this correlation by eye. The correlation can be seen as a two dimensional histogram in fig. 4.18-4.23 for each relevant $\sqrt{s_{NN}}$.

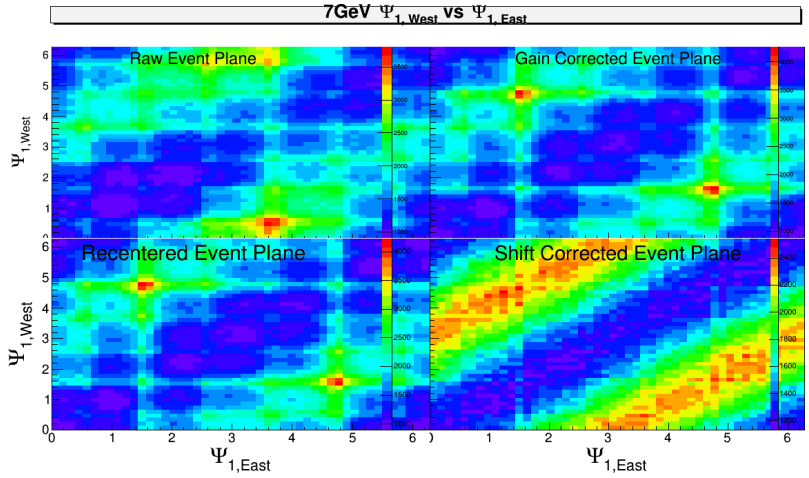

Figure 4.18: BBC West Ψ_1 vs. BBC East Ψ_1 for 7GeV collisions as corrections are applied. Since the first-order plane is explicitly anti-symmetric in η and ϕ we expect the west plane to be anti-correlated to the east plane.

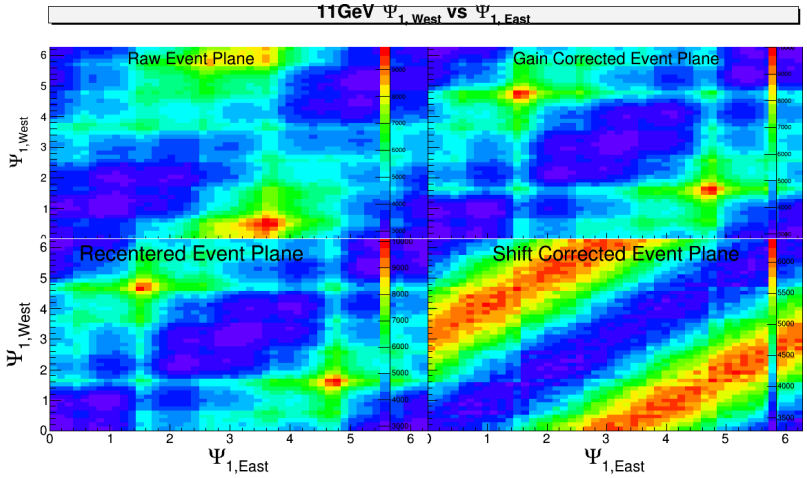

Figure 4.19: BBC West Ψ_1 vs. BBC East Ψ_1 for 11GeV collisions as corrections are applied. Since the first-order plane is explicitly anti-symmetric in η and ϕ we expect the west plane to be anti-correlated to the east plane.

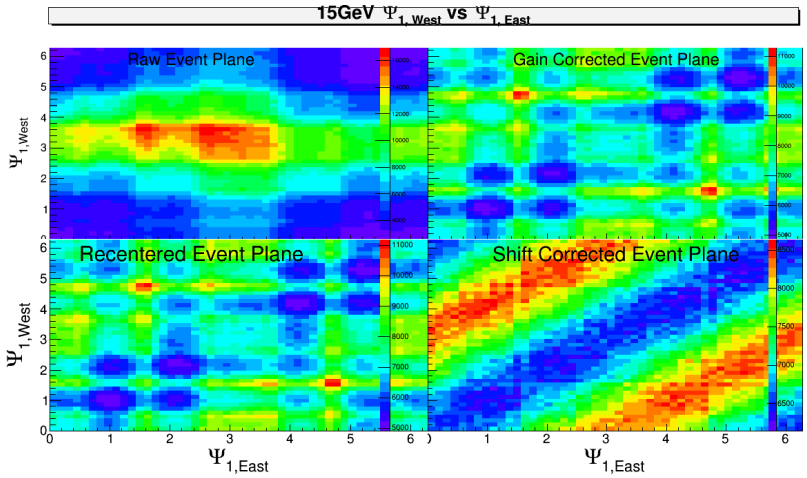

Figure 4.20: BBC West Ψ_1 vs. BBC East Ψ_1 for 15GeV collisions as corrections are applied. Since the first-order plane is explicitly anti-symmetric in η and ϕ we expect the west plane to be anti-correlated to the east plane.

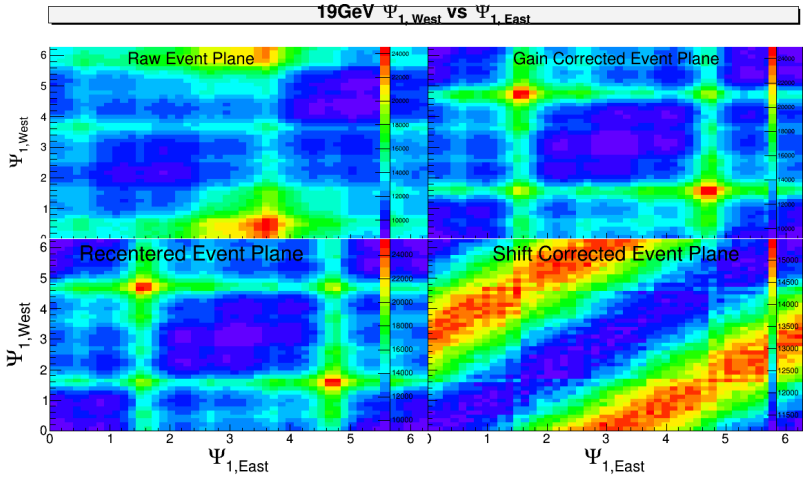

Figure 4.21: BBC West Ψ_1 vs. BBC East Ψ_1 for 19GeV collisions as corrections are applied. Since the first-order plane is explicitly anti-symmetric in η and ϕ we expect the west plane to be anti-correlated to the east plane.

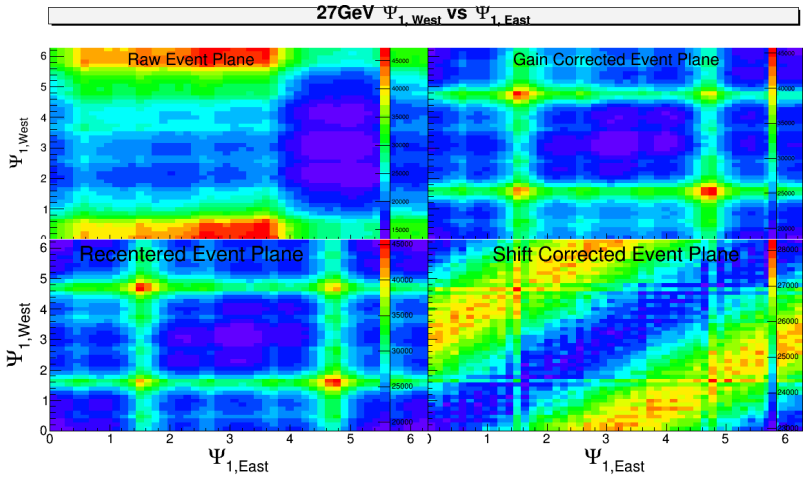

Figure 4.22: BBC West Ψ_1 vs. BBC East Ψ_1 for 27GeV collisions as corrections are applied. Since the first-order plane is explicitly anti-symmetric in η and ϕ we expect the west plane to be anti-correlated to the east plane.

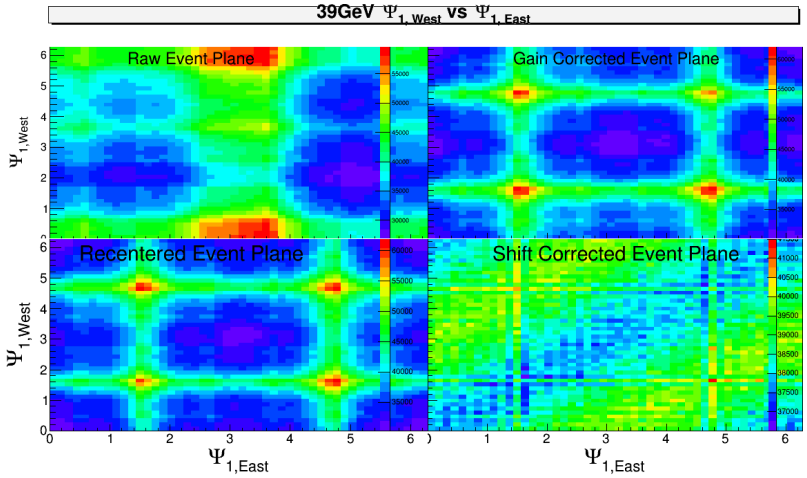

Figure 4.23: BBC West Ψ_1 vs. BBC East Ψ_1 for 39GeV collisions as corrections are applied. Since the first-order plane is explicitly anti-symmetric in η and ϕ we expect the west plane to be anti-correlated to the east plane.

4.2.1 Event plane resolution

Finally we have a resolution correction factor which is found as described in sec. 3.2. The relative magnitude of the corrections is the correlator of the east and west planes: $\cos(\Psi_{1,W} - \Psi_{1,E})$, the actual values are found by inverting Bessel equations (eq. 3.7) using the sub event plane resolution. This resolution is solved for each central value of the sub-event plane resolution as well as the statistical error bars. Of course the statistical error bars of the sub-event plane resolution are symmetric, but this is not guaranteed when they are put through the root finding algorithm. If the sizes of the up and down error bars differed by less than a percent I just defined the error bar to be the average of them. In fact the difference was less than 1% every time so I never had to consider what to do in case of asymmetry. The values are

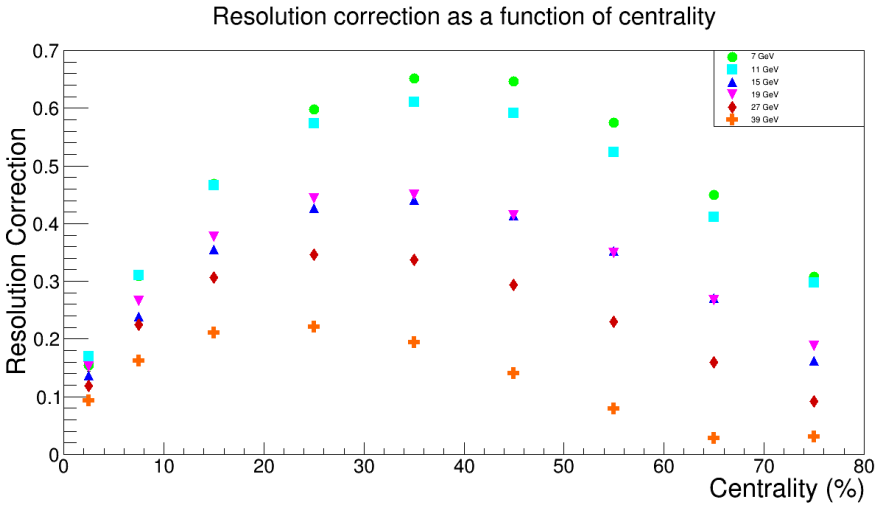

Figure 4.24: Resolution correction as a function of centrality

4.3 Track QA

An analysis starts with a collection of tracks. In this analysis I do not wish to select tracks which come directly from the primary vertex. The protons and pions I'm interested in are secondary. Thus the "global" track list is used. Such tracks do not use the primary vertex as a fit point. It is necessary to apply some selection criteria to the tracks to ensure their quality. The cuts I use to select tracks are

- Track flag ≥ 0
- $0.15\text{GeV} < p_T < 10\text{GeV}$
- $|\eta| < 1$
- NHitsPossible ≥ 5
- $15 <$ Number of hits < 100
- NHitsFit/NHitsPossible ≥ 0.52.

The track flag is a STAR specific thing which is not worth going into detail about here. Tracks of very low transverse momentum will circulate in the transverse plane of the detector. If the track doesn't reach sufficiently far into the TPC it will have fewer fit points and, thus, be of very low quality. To mitigate this problem we have a minimum p_T cut. Very high transverse momentum tracks do not bend much in the magnetic field. The momentum of the particle is measured by the radius of curvature. If the radius is too big the momentum resolution suffers. Furthermore we're interested in "low momentum" physics (that is particles not produced in hard nucleon-nucleon collisions). For these reasons we have a maximum p_t cut and fig. 4.25 is referenced for comparison.

Technically the TPC can measure tracks beyond $|\eta| = 1$, but the efficiency decreases as fewer TPC sectors are hit for very forward tracks. The η cut is chosen so that the track detection efficiency is roughly uniform over the coverage. The η distribution can be seen in fig. 4.26. In addition to the spatial and resolution considerations of the η and p_T cuts we have corresponding cuts directly on the possible number of TPC hits, the number of hits recorded, and the ratio of these quantities. These cuts are somewhat more esoteric and sometimes redundant. In such cases the specific value of the cut is motivated by code considerations

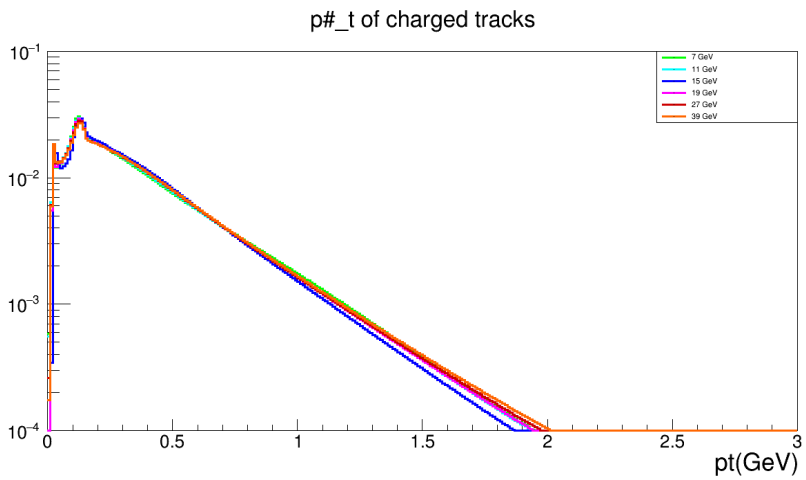

Figure 4.25: $\frac{\mathrm{dN}}{\mathrm{d}(p_T)}$ vs p_T for charged tracks in the TPC.

(for example to make sure that no division by 0 occurs) rather than physical consideration, though, qualitatively, the cuts are physically motivated. The NHitsPossible (as seen in fig. 4.27) cut makes sure that the reconstructed cut would have passed by a minimum number of TPC rows. This is redundant given the η and p_T. Furthermore there is a cut on the number of hits recorded in the TPC (as seen in fig. 4.28). More hits means a more well constrained track. In reality there is no chance to get "too many hits", that is merely put in the code to be careful. Finally there is a cut on the ratio of these quantities (as seen in fig. 4.29). If the track passed through the whole TPC but only a few hits were recorded this may be a bug in the track finding algorithm. Such a track should be thrown away.

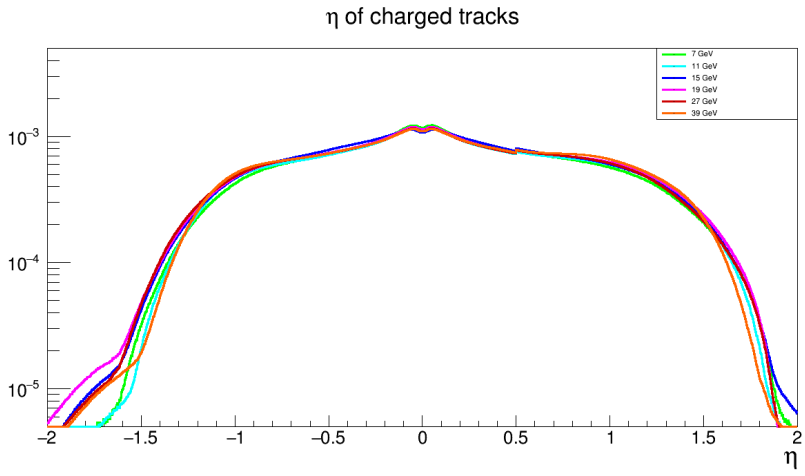

Figure 4.26: $\frac{dN}{d\eta}$ vs η for charged tracks in the TPC.

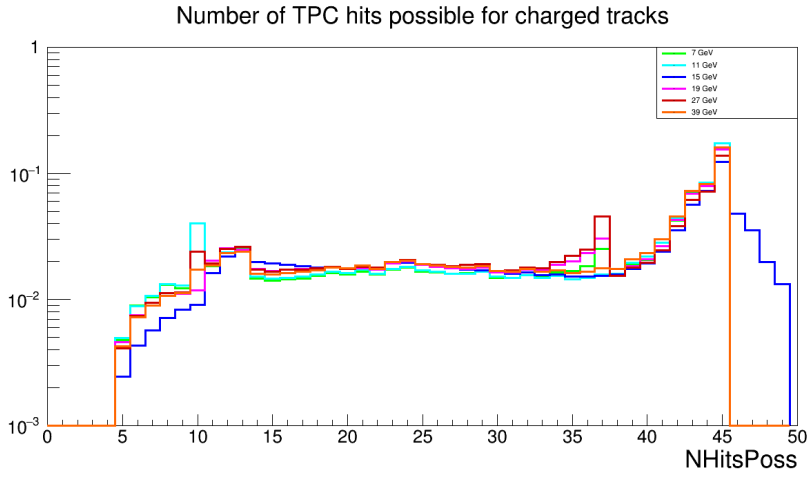

Figure 4.27: $\frac{dN}{dN_{\text{Hits Possible}}}$ vs $N_{\text{Hits Possible}}$ for charged tracks in the TPC.

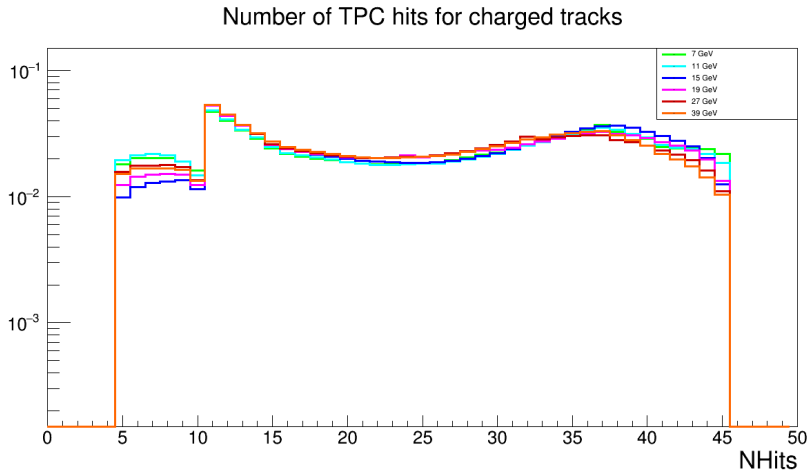

Figure 4.28: $\frac{dN}{dN_{Hits}}$ vs N_{Hits} for charged tracks in the TPC.

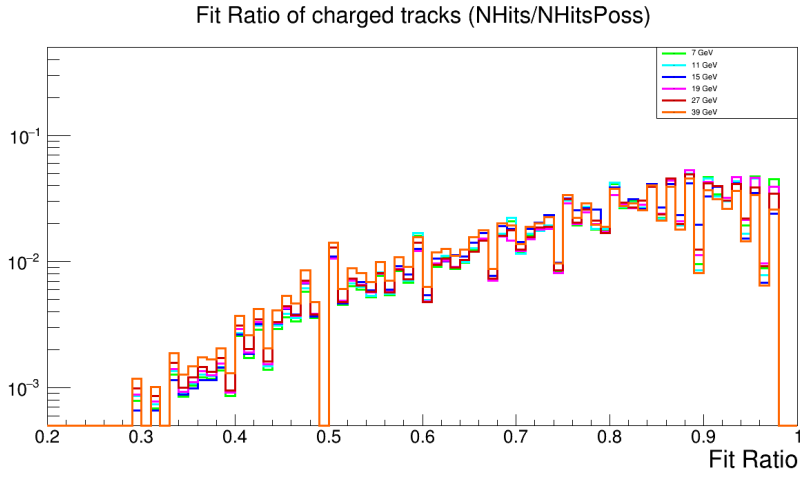

Figure 4.29: $\frac{dN}{d(\text{Fit Ratio})}$ vs Fit Ratio for charged tracks in the TPC.

4.4 Lambda reconstruction

Now that we have selected "good" events and a have a collection of only the "good" tracks we can start finding Λs. (Anti)Lambdas are reconstructed from (anti)proton and (anti)pi-minus tracks, so the first step in the reconstruction is the proton and pion track particle identification. This is discussed in sec. 4.4.1. Once we have identified the daughters we make a number of cuts based on the topology, or the shape of the reconstruction. This is discussed in sec. 4.4.2. Reconstruction methodology in no sense differs for Λs as compared for $\overline{\Lambda}$s (except in the particles of interest). The final subsection (sec 4.4.2) shows some distributions of quantities intrinsic to Λs and $\overline{\Lambda}$s.

4.4.1 Daughter PID

This analysis uses TPC dE/dx and the TOF 1/β for PID. TOF information is not required so the TOF mass cuts are only used if the information exists. The cuts are as follows

- Proton: $\left|\mathrm{N}_{\sigma,\,\mathrm{proton}}\right| < 3$
- Proton: $0.5\mathrm{GeV}^2 < m^2_{\mathrm{TOF}} < 1.5\mathrm{GeV}^2$
- Pion: $\left|\mathrm{N}_{\sigma,\,\mathrm{pion}}\right| < 3$
- Pion: $0.017\mathrm{GeV}^2 - 0.013\mathrm{GeV}^2 * p < m^2_{\mathrm{TOF}} < 0.04\mathrm{GeV}$

The dE/dx, as mentioned in sec. 1.5.1, is the characteristic energy loss of a charged particle per unit distance as it moves through some medium. This energy loss depends on the charge of the particle, the details of the medium, and the speed of the particle. The first quantity is found from the curvature of the track. Almost all measured particles have unit charge. The TPC is filled with so called P10 gas. It is the mass of the particles that differentiates them by the relation between measured momentum and characteristic speed. The bands of identification can be seen quite clearly in fig. 4.30-4.35. In such figures the energy loss is often multiplied by the charge of the particle to separate the particles from the anti-particles. The lines are fit by the Bethe-Bloch formula in momentum slices and tracks are described by their distance from these fit lines in units of standard deviations (σs). The cuts of 3σ used in this analysis are quite weak and include a

number of other types of particles. This PID method does not work well for very high momentum particles as the lines run together at momentum around 0.8GeV.

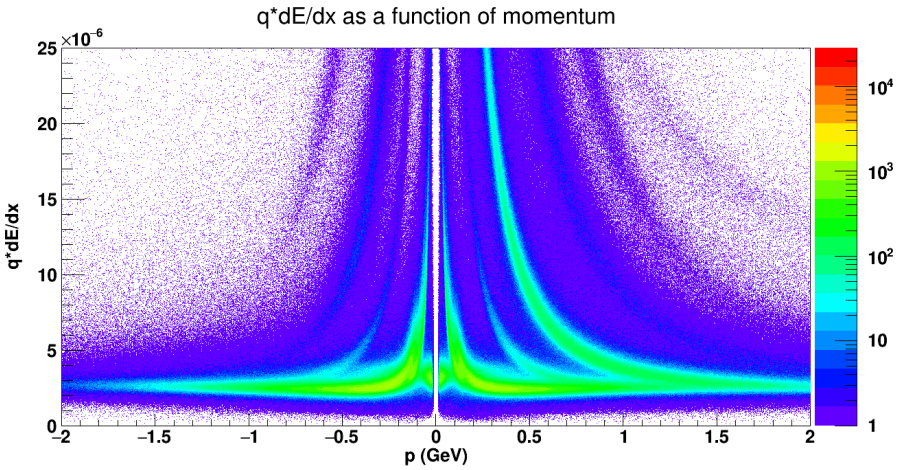

Figure 4.30: 7GeV charged track dE/dx vs. p for charged tracks in the TPC.

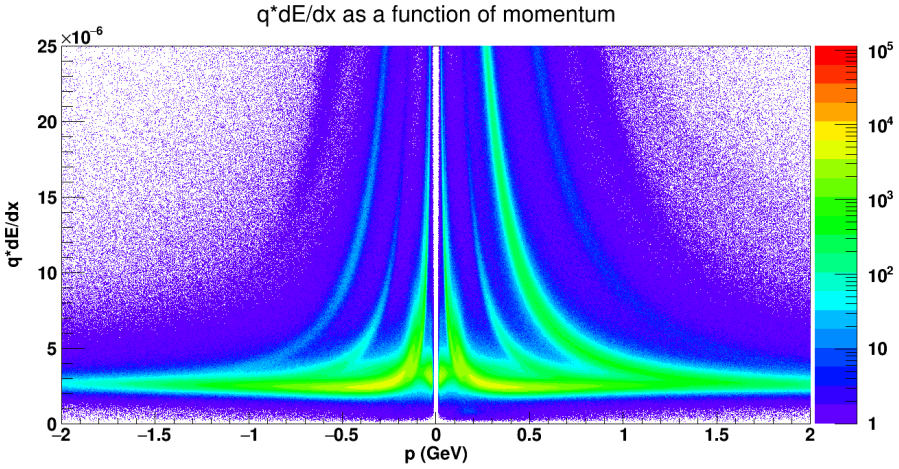

Figure 4.31: 11GeV charged track dE/dx vs. p for charged tracks in the TPC.

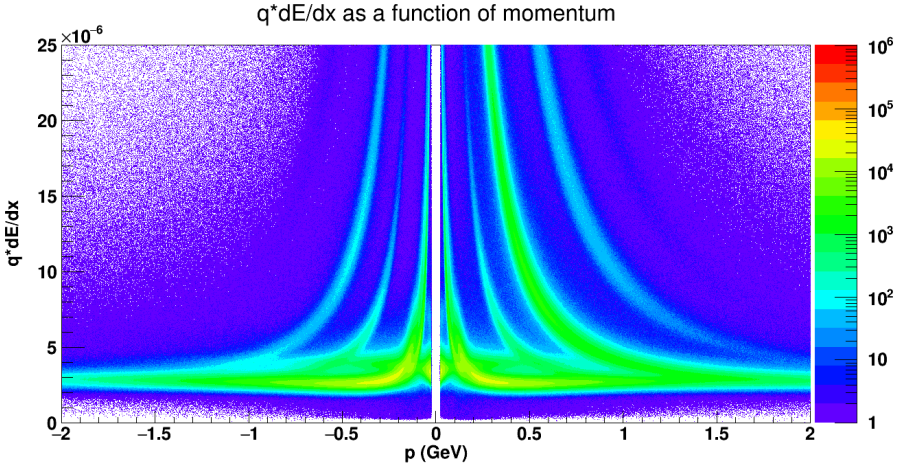

Figure 4.32: 15GeV charged track dE/dx vs. p for charged tracks in the TPC.

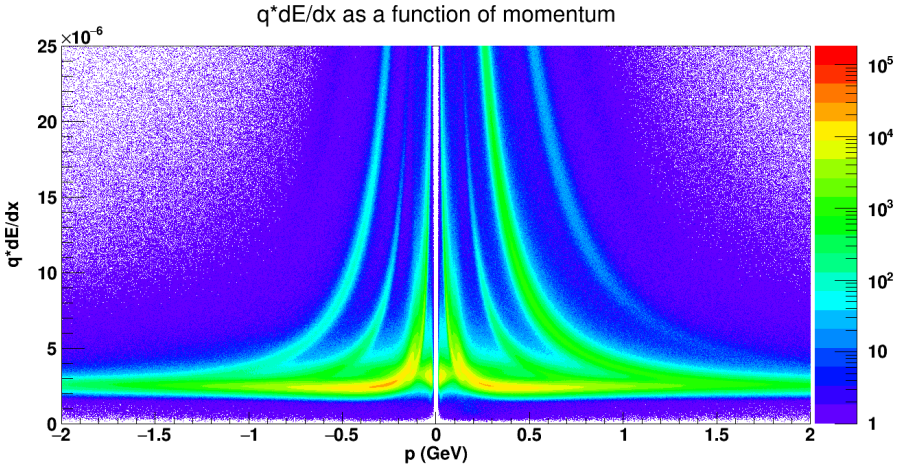

Figure 4.33: 19GeV charged track dE/dx vs. p for charged tracks in the TPC.

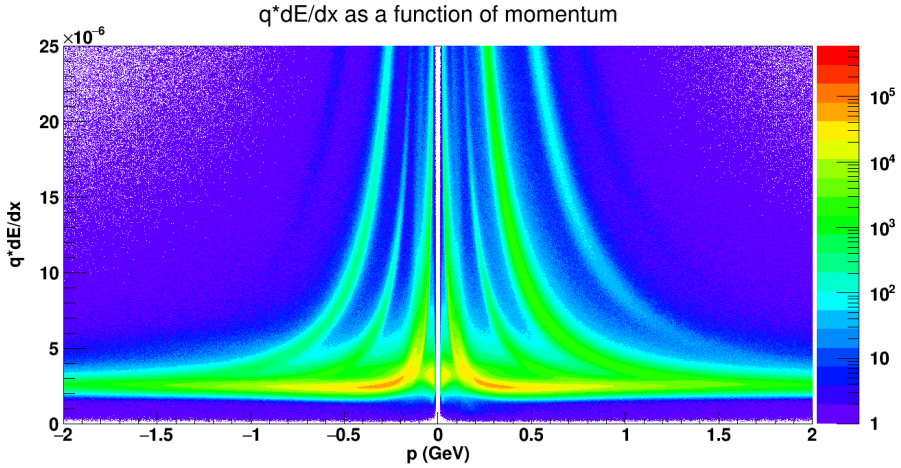

Figure 4.34: 27GeV charged track dE/dx vs. p for charged tracks in the TPC.

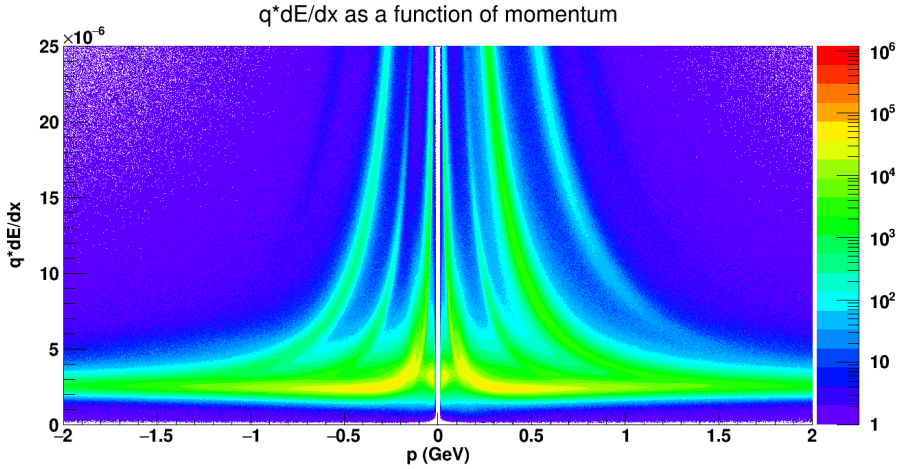

Figure 4.35: 39GeV charged track dE/dx vs. p for charged tracks in the TPC.

The next round of PID comes from the time of flight (see sec. 1.5.2). The TOF measures the total time it takes for a particle to go from the collision point to the TOF, which is just outside of the TPC. The timescale of collision evolution (as seen in fig. 1.4) and the specific freezeout surface of the particle is much too small an effect to be relevant here. The time measured is discusses as a speed, β. What we get from the TOF, knowing the momentum from the TPC, is the mass of the particle. Thus PID plots depict inverse β or m^2 as a function of momentum. Inverse β can be seen in fig. 4.36-4.41 while the mass squared scaling can be seen in fig. 4.42-4.47.

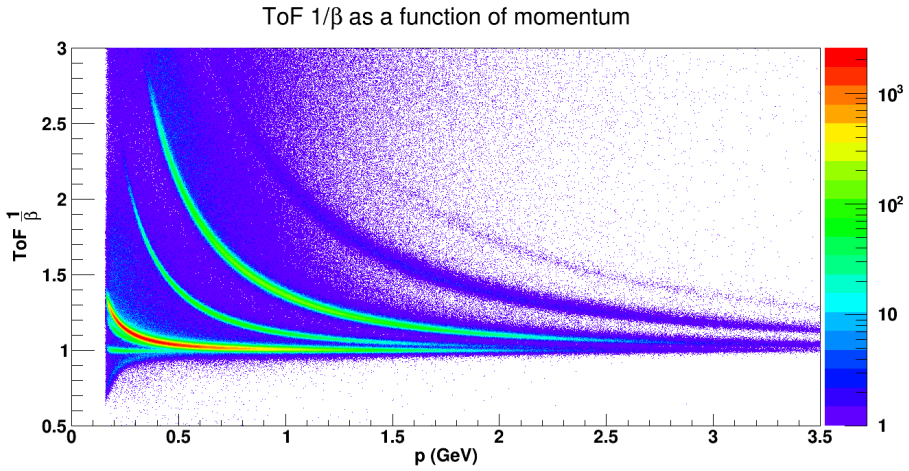

Figure 4.36: 7GeV charged track 1/β vs. p from the TOF with track momentum from the TPC.

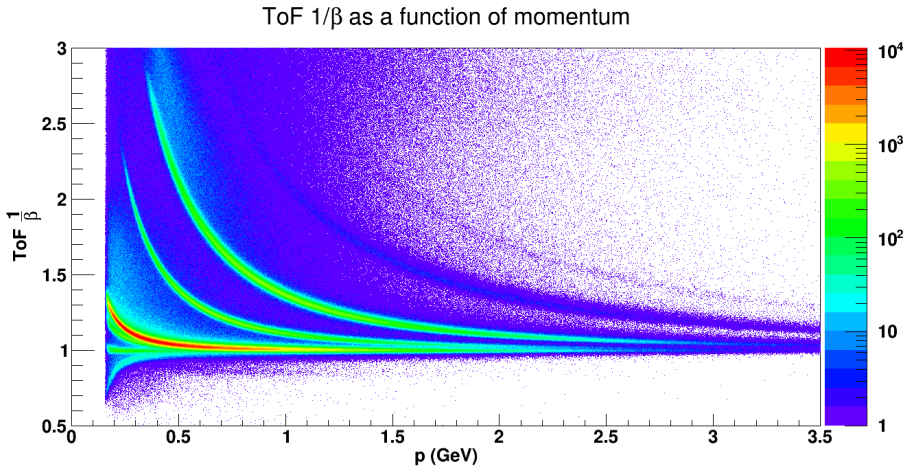

Figure 4.37: 11GeV charged track 1/β vs. p from the TOF with track momentum from the TPC.

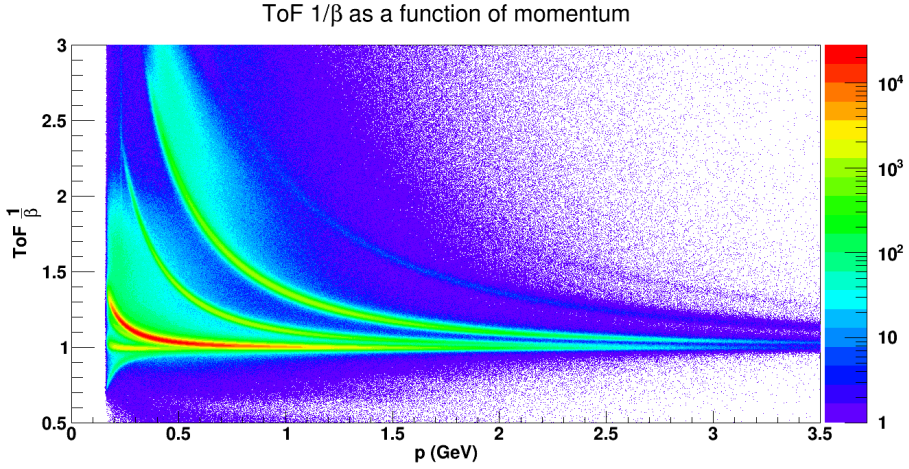

Figure 4.38: 15GeV charged track 1/β vs. p from the TOF with track momentum from the TPC.

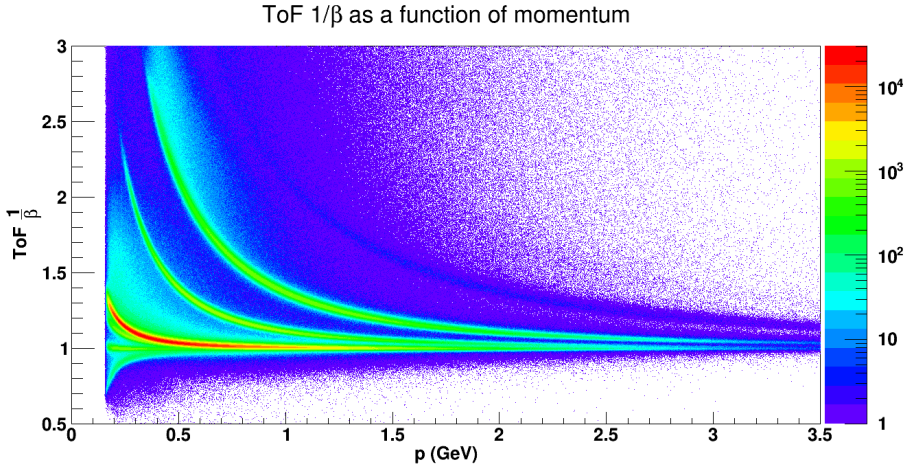

Figure 4.39: 19GeV charged track 1/β vs. p from the TOF with track momentum from the TPC.

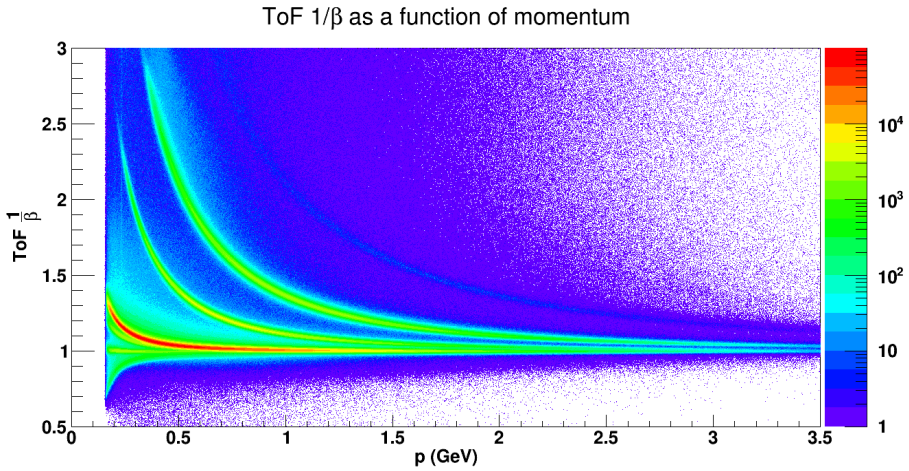

Figure 4.40: 27GeV charged track 1/β vs. p from the TOF with track momentum from the TPC.

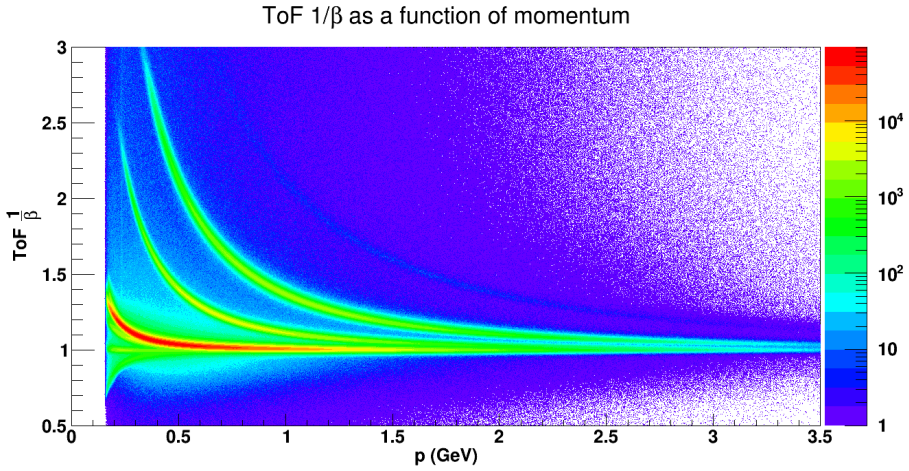

Figure 4.41: 39GeV charged track 1/β vs. p from the TOF with track momentum from the TPC.

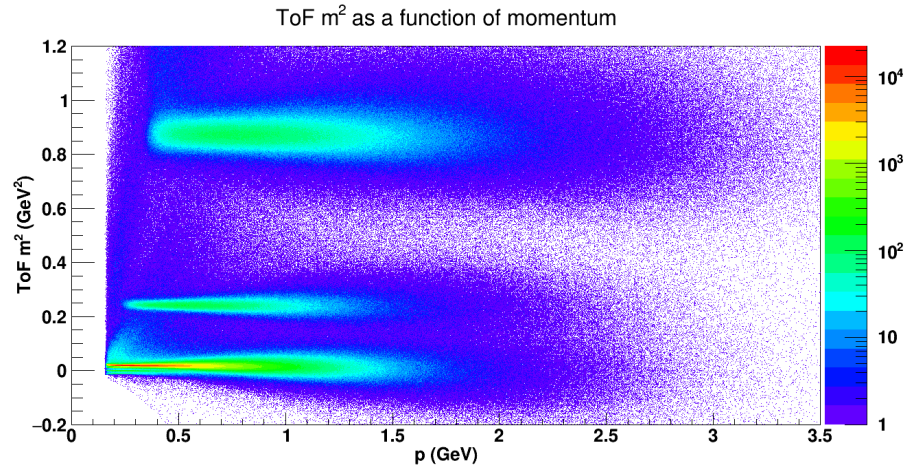

Figure 4.42: 7GeV charged track m^2 vs p from the TOF with track momentum from the TPC.

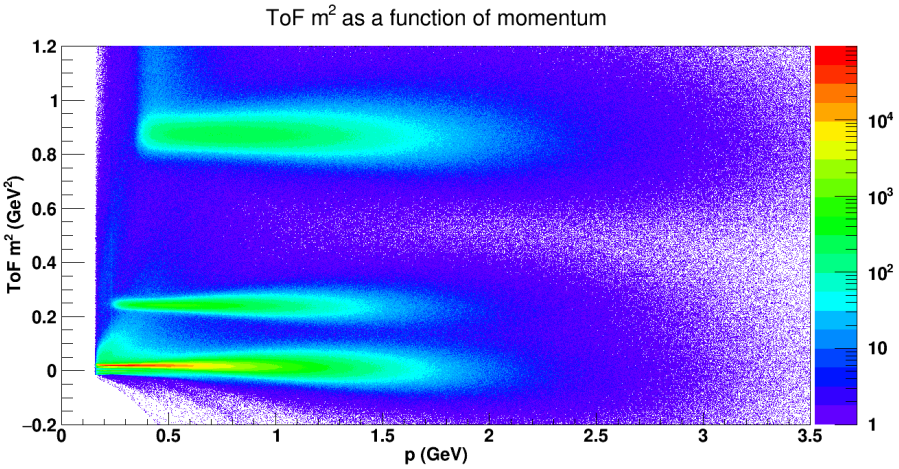

Figure 4.43: 11GeV charged track m^2 vs p from the TOF with track momentum from the TPC.

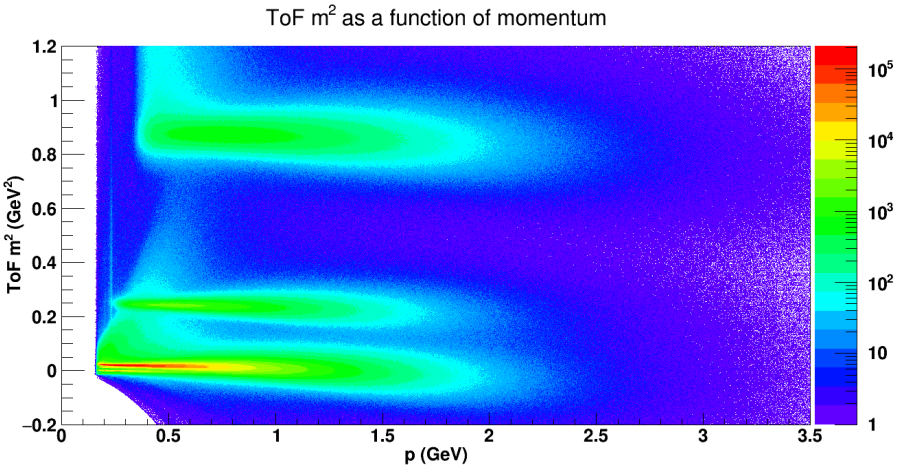

Figure 4.44: 15GeV charged track m^2 vs p from the TOF with track momentum from the TPC.

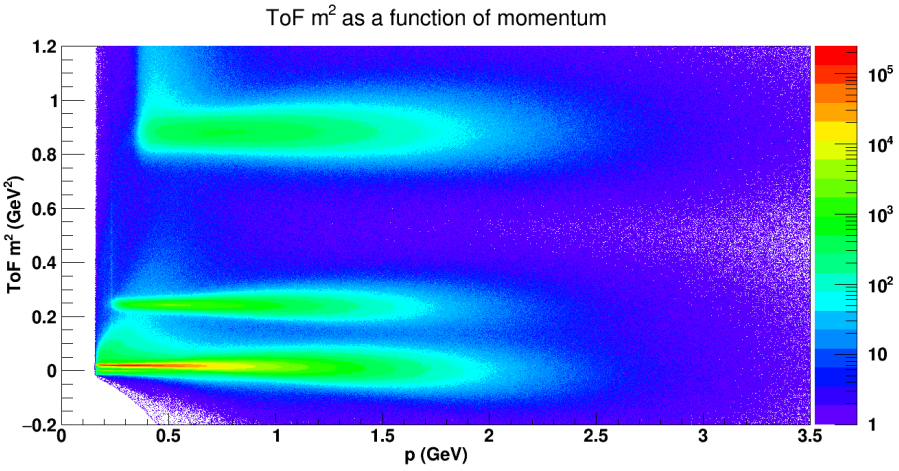

Figure 4.45: 19GeV charged track m^2 vs p from the TOF with track momentum from the TPC.

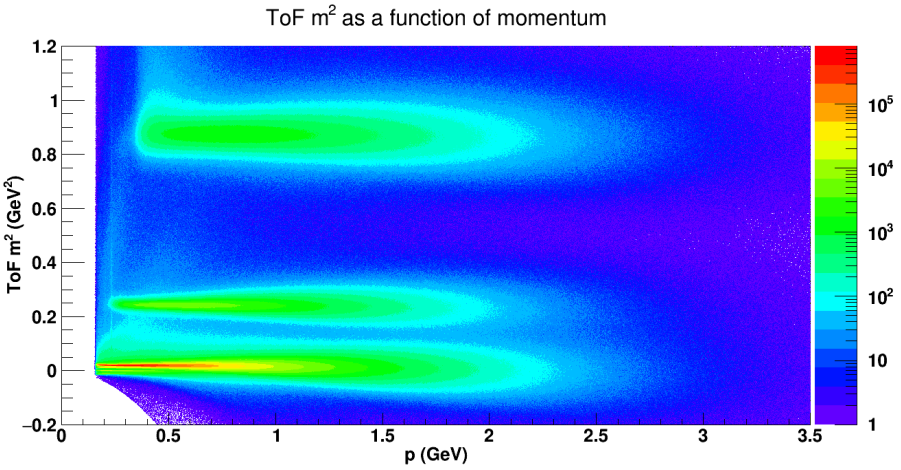

Figure 4.46: 27GeV charged track m^2 vs p from the TOF with track momentum from the TPC.

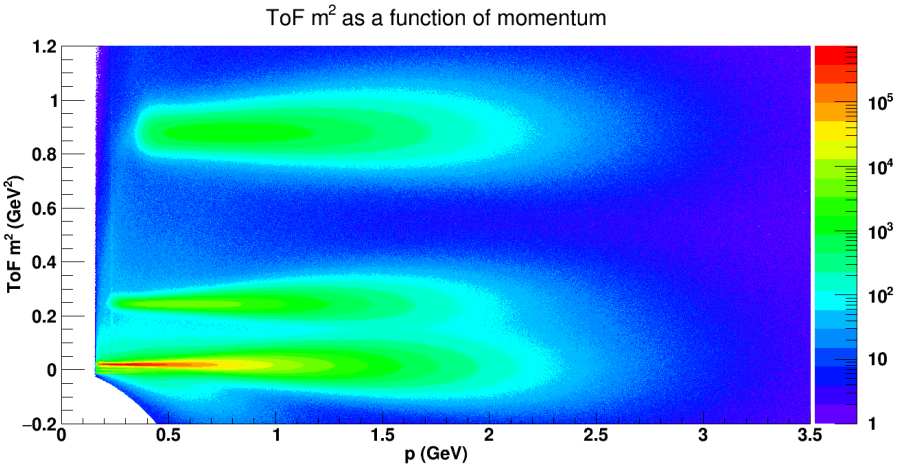

Figure 4.47: 39GeV charged track m^2 vs p from the TOF with track momentum from the TPC.

4.4.2 Lambda topological cuts

Lambdas are found by comparing pairs of proton and pion tracks and then using selection criteria to narrow those pairs down to ones which are most likely daughters of Lambdas. This is because we are only capable of tracking charged tracks and the Lambda decay length is not particularly long. One can see a schematic of such a pairing in fig. 4.48.

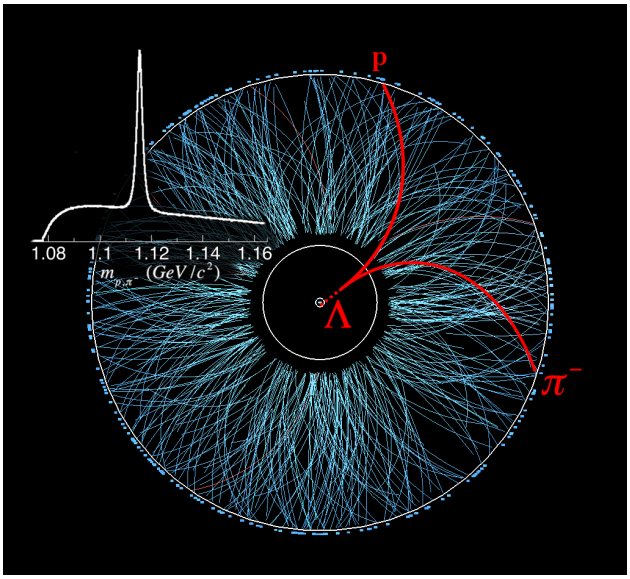

Figure 4.48: Lambda reconstruction schematic displayed on a real STAR event.

The selection criterion on pairs of tracks are called topological cuts. Frequently I refer to the DCA, or distance of closest approach. This can mean the closest approach of two helices extended forward and backward in time. It can also mean the distance of closest approach for a helix to a given point. The scheme for the cuts is rather complicated as the cut values themselves depend on whether or not the candidate proton and pion separately have TOF information.

- (Proton TOF and Pion TOF, Proton TOF and !Pion TOF, !Proton TOF and Pion TOF, !Proton TOF and !Pion TOF)
- Proton DCA to PV $\geq$ (0.1, 0.15, 0.5, 0.6) cm

- Pion DCA to PV $\geq$ (0.7, 0.8, 1.5, 1.7) cm
- Lambda DCA to PV $\leq$ (1.3, 1.2, 0.75, 0.75) cm
- Lambda decay length $\geq$ (2, 2.5, 3.5, 4) cm
- Proton to Pion DCA to each other $\leq$ 1 cm
- $p_\Lambda \cdot \text{EndVertex} > 0$ is a cut ensuring that the Lambda is moving away from the primary vertex. "End-Vertex" is the decay vertex of the Lambda.
- Lambdas are taken in the mass window (1.115683 ± 0.005)GeV
- As described in section 5.1 for systematic error reasons we actually do not include Lambdas for which the pion has TOF data and the proton does not

The meaning of these quantities can be seen in fig. 4.49.

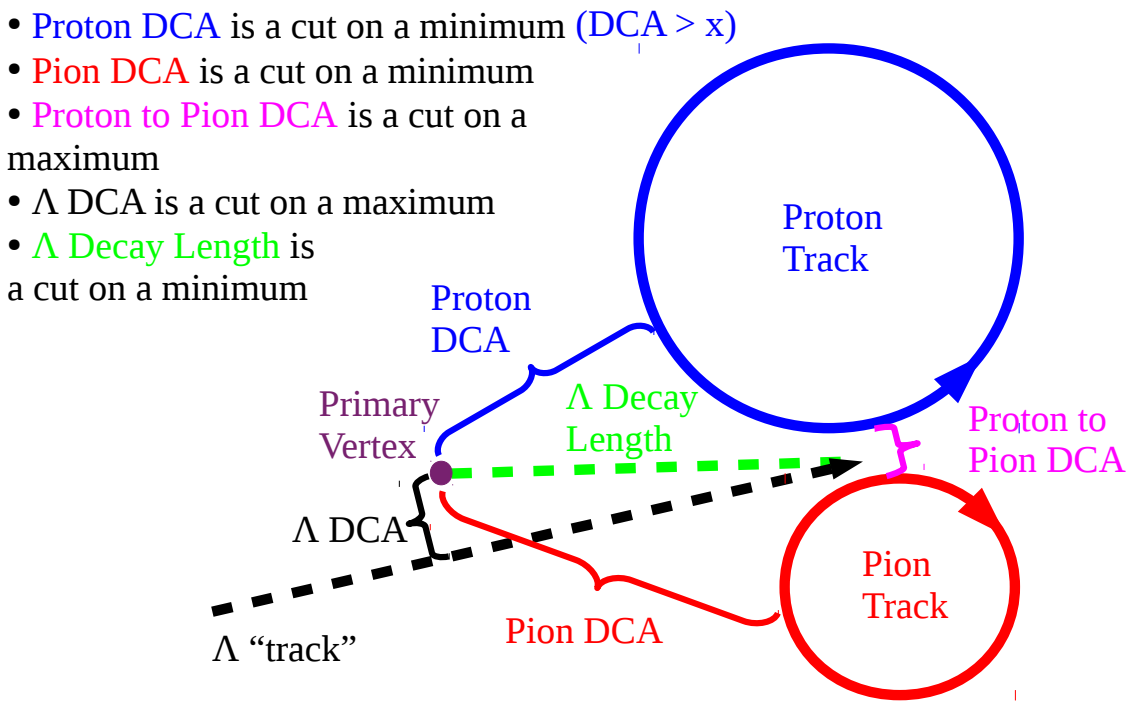

Figure 4.49: Diagram of how cuts are applied to reconstruct Lambdas. The proton and pion are depicted as circles in order to represent that they are, in fact, helices of the given radius. The diagram is thus a depiction in the transverse plane.

It should be mentioned here that the quantities I am plotting below are made by greatly loosening, though not eradicating, the cuts. Therefore all such plots display quantities after all of the cuts, in some form, have been applied to them. This means that there will be some non-trivial structure. The DCA distribution of the protons can be seen in fig. 4.50, while that for the pions can be seen in fig. 4.51. We want the protons and the pions to be coming from a Lambda, and thus be not primary. One expects daughters of Lambdas (since the Lambda has some finite decay length) to have helices which miss the primary vertex of the collision. This means we have a minimum cut on the daughter DCA to primary vertex.

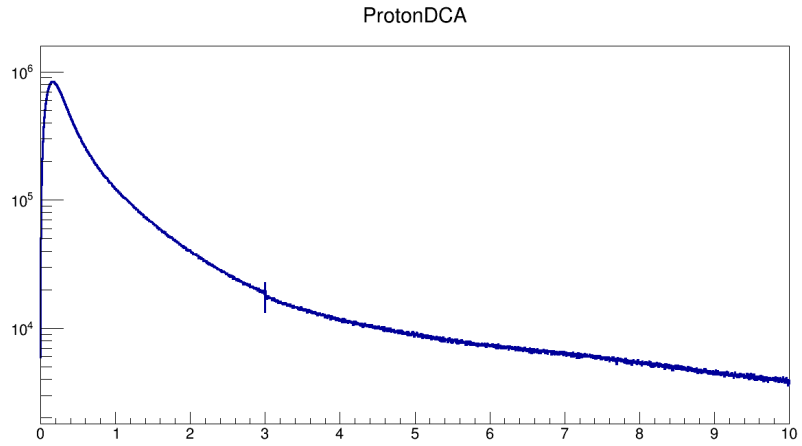

Figure 4.50: Counts vs. proton DCA to the primary vertex (cm) for 19GeV collisions.

In order for the two daughters to be at all related by a Lambda mother vertex the proton and pion must have been born very close to each other. To ensure this we have a maximum on the DCA from the proton helix to the pion helix. This quantity, here denoted as the "daughter DCA", is shown in fig. 4.52. Unlike the daughters, we want the reconstructed Lambdas to be primary. Thus we have a maximum on the DCA of the Lambda to the primary vertex. This quantity is shown in fig. 4.53. Finally we have a minimum reconstructed decay length for the Lambda. Combinatoric Lambdas with very low decay lengths are likely to be random combinations of protons and pions. Thus we have a minimum cut on the decay length. This quantity is shown in fig. 4.54.

Finally to evaluate the efficacy of our collection of cuts we must look at the invariant mass distribution

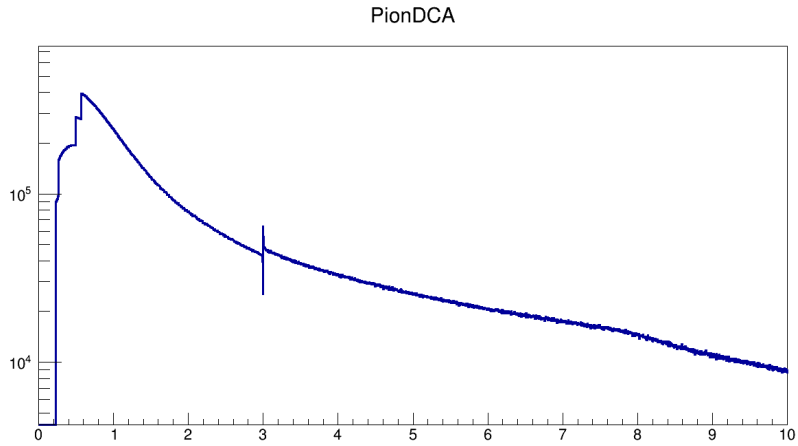

Figure 4.51: Counts vs. pion DCA to the primary vertex (cm) for 19GeV collisions.

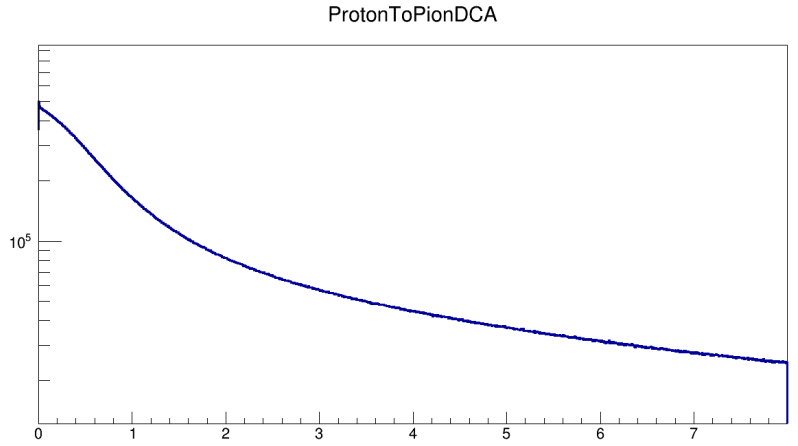

Figure 4.52: DCA of one daughter track to another (cm) for 19GeV collisions.

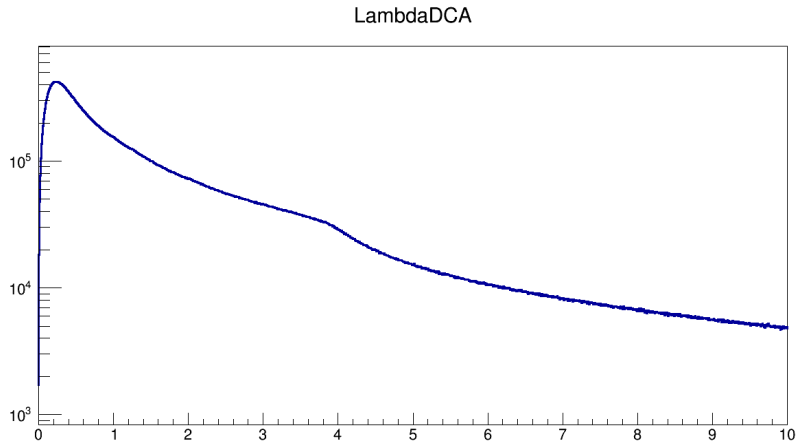

Figure 4.53: Counts vs. Lambda DCA to the primary vertex (cm) for 19GeV collisions.

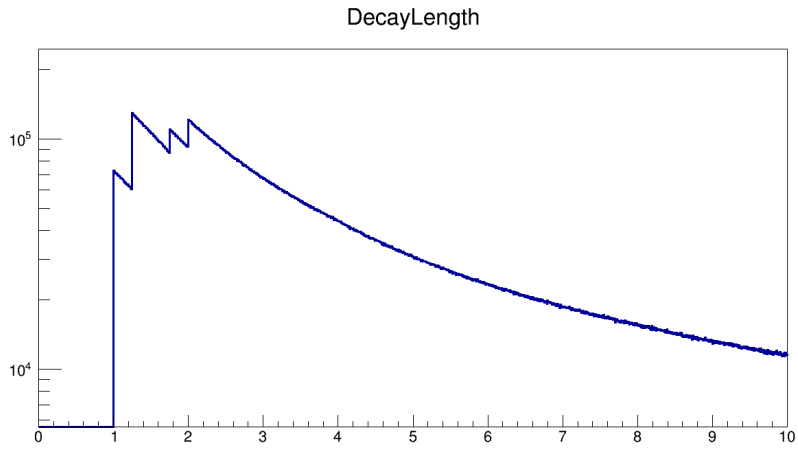

Figure 4.54: Counts vs. Lambda decay length (cm) for 19GeV collisions.

of the Lambdas. This is shown in fig. 4.55. As mentioned a cut is made around the peak to make sure that as many of the particles as can be drawn from this distribution are real Lambdas.

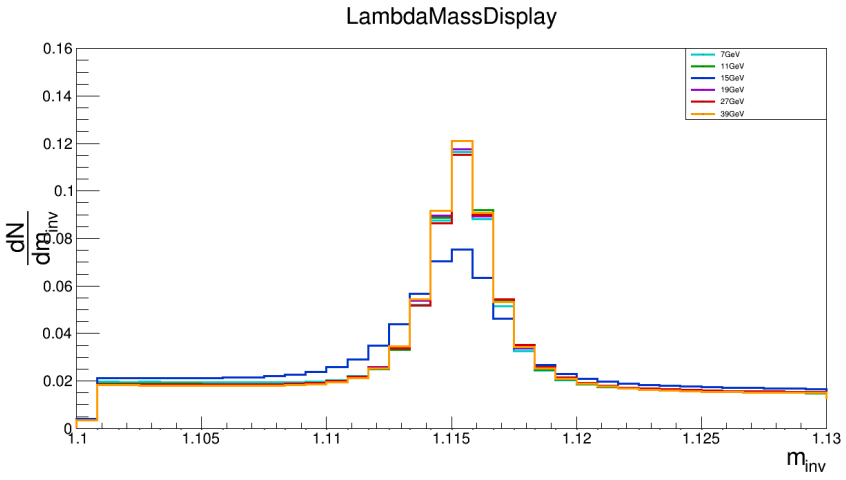

Figure 4.55: $\frac{\mathrm{dN}}{\mathrm{d}m_\Lambda}$ vs. m_Λ(GeV). Note the strange mass distribution at 15GeV, probably from the HFT

Lambda quantities

Now that we have reconstructed Λs and $\overline{\Lambda}$s it is worth looking at some of the quantities intrinsic to these particles. In this section there are plots for the p_T the rapidity and the ϕ distributions. For Λs these are fig. 4.56, fig. 4.57, and fig. 4.58. For $\overline{\Lambda}$s these are fig. 4.59, fig. 4.60, and fig. 4.61 respectively. One might note that the ϕ distributions are not in fact flat. Physically, of course, they must be. The TPC is made of 12 sectors with some finite gap between the sectors. This leads to the gaps in the acceptance seen in these figures. The effect is somewhat washed out by the fact that the ϕ of the Lambda is not exactly the ϕ of its daughters, which are really effected. Furthermore it is typical for tracks to be detected across multiple TPC pad rows. In such a case not being detected in the boundary is not too detrimental. This ladder effect is, naturally, less for low momentum tracks. Furthermore some sectors do not perform as well as others. This can be seen in the relative number of counts at a given ϕ.

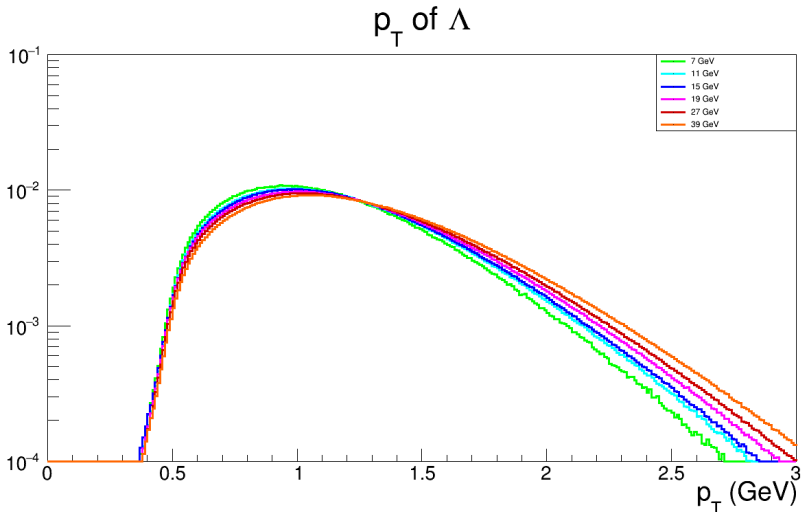

Figure 4.56: Λ p_T. The y axis is counts in bin scaled by the total counts so that all $\sqrt{s_{\mathrm{NN}}}$ can be shown together.

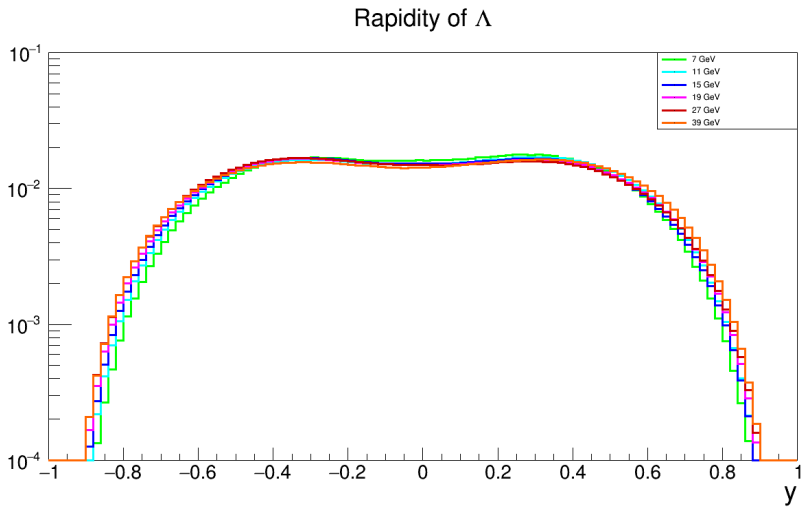

Figure 4.57: Λ y (rapidity). The y axis is counts in bin scaled by the total counts so that all $\sqrt{s_{\mathrm{NN}}}$ can be shown together.

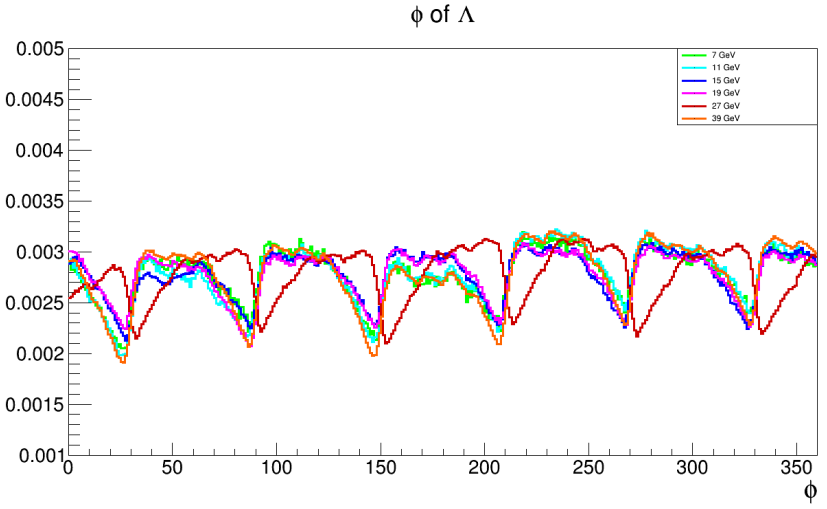

Figure 4.58: Λ ϕ. The y axis is counts in bin scaled by the total counts so that all $\sqrt{s_{\mathrm{NN}}}$ can be shown together. Note the opposite direction of the 27GeV data. This is due to the fact that the magnetic field orientation in 27GeV was "Full Field", while for the rest of the BES it was "Reversed Full Field" (which is same magnitude, opposite polarity).

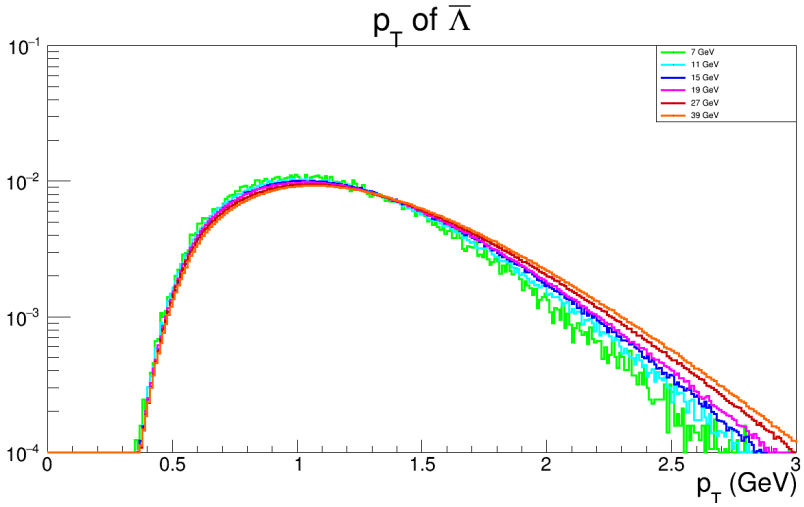

Figure 4.59: $\overline{\Lambda}$ p_T. The y axis is counts in bin scaled by the total counts so that all $\sqrt{s_{\mathrm{NN}}}$ can be shown together.

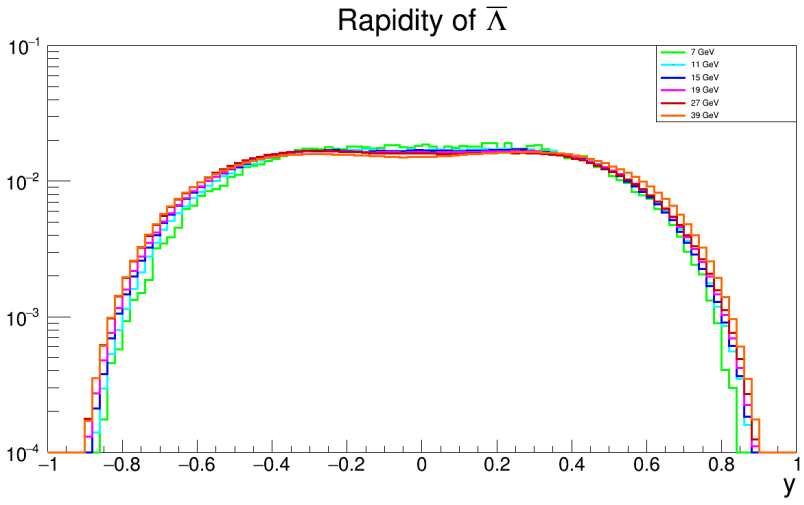

Figure 4.60: $\overline{\Lambda}$ y (rapidity). The y axis is counts in bin scaled by the total counts so that all $\sqrt{s_{\mathrm{NN}}}$ can be shown together.

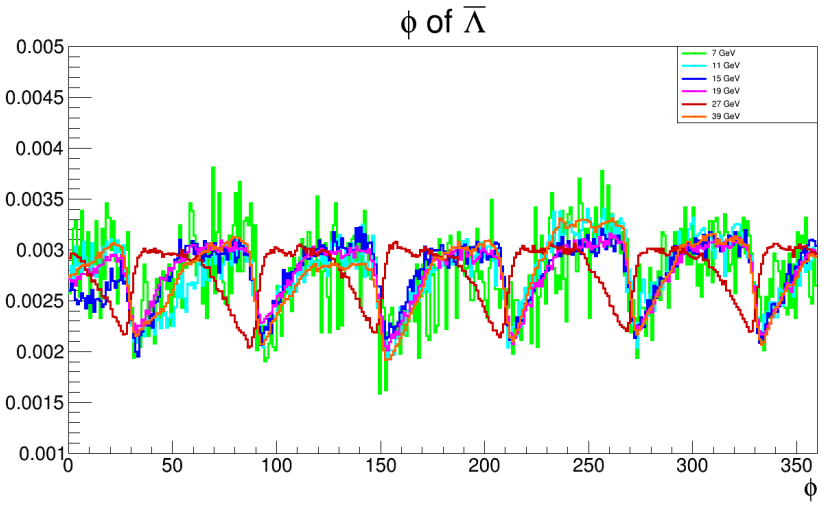

Figure 4.61: $\overline{\Lambda}$ ϕ. The y axis is counts in bin scaled by the total counts so that all $\sqrt{s_{\mathrm{NN}}}$ can be shown together. Note the opposite direction of the 27GeV data. This is due to the fact that the magnetic field orientation in 27GeV was "Full Field", while for the rest of the BES it was "Reversed Full Field" (which is same magnitude, opposite polarity).

Chapter 5

SYSTEMATIC ERRORS

Summary of systematic errors to be discussed in detail later in this section

- Mass purity/residual mass background correction (sec. 5.2): This is the primary source of errors.
- Error in α_H (sec. 5.3): $\sim 2\%$ scaling error.
- Error in resolution correction (sec. 4.2.1 and sec. 5.3): $< 1\%$
- Error in $A0$ determination (tab. 3.1 and sec. 5.3): $< 0.03\%$
- There is an error in the helicity efficiency effect on the data (sec. 3.5.2 and sec. 5.3): $< 3.5\%$
- Error in resolution correction from momentum conservation effects (sec. 5.4): $\sim 2\%$
- For feed down corrected results (relevant to sec. 7) there is a factor 2 systematic error coming from uncertainty in the temperature T (sec. 5.5)

5.1 Topological cut dependencies

A typical source of systematic errors is the dependence of the signal on the cutset. In this section we look for systematic dependecies of the polarization on our specific choices of topological cuts. The nominal cuts used in the analysis can be found in sec. 4.4.2. The first thing we tried doing was making each cut individually tighter or looser so we had $\pm$ 25% of the number of Lambdas used in the analysis. The idea was that we could estimate the systematic error by comparing the tight-cut and the loose-cut results. The difference turned out to be possible contribution to systematic error (see sec. 5.1.4). In order to get a finer

handle on this difference we tried to look at the covariance of the polarization with the topological cuts. The result from this study is that "systematic errors are smaller than statistical". The statistical fluctuations simply dominate any deviation from zero covariance that we can see.

5.1.1 Covariance method idea

The covariance of two variables (say P for polarization and X for some cut quantity e.g. pion DCA) is defined to be

$$Cov(P,X) = \langle PX \rangle - \langle P \rangle \langle X \rangle. \tag{5.1}$$

This, of course, tells us how the cut quantities and the polarization measure co-vary. We look at each covariation with each variable separately. The advantage here is that we can use much more Lambda candidates that wouldn't pass the nominal cuts in order to understand a trend rather than a simple difference. What we really want to get systematic errors is a description of how the polarization depends on the variable. A slope parameter can be made that treats the variation as approximately linear:

$$\begin{aligned} Slope(P(X)) &= \frac{Covariance(P,X)}{Variance(X)} \\ &= \frac{\langle PX \rangle - \langle P \rangle \langle X \rangle}{\langle X^2 \rangle - \langle X \rangle^2}. \end{aligned} \tag{5.2}$$

Once we have a slope that describes the variation of the polarization with X we can get the systematic error by multiplying by a *reasonable* range in the cut quantity (ΔX):

$$Error = \Delta X * Slope. \tag{5.3}$$

A reasonable range for ΔX is, for each cut, the difference between where you might make a loose version and a tight version of the cut. As it happens the ΔX is just a scaling and, since we don't get a significant slope value, it is not necessary to use when we find no clear non-statistical deviation from zero for the slope.

There is a subtlety here I've glossed over which is that the apparent magnitude of the polarization depends on the purity of Lambda sample which, in turn, depends on the value of the quantity I'm cutting on. To account for this I can scale the slope by the purity of the mass distribution. Doing this requires a

characterization of the slope of the purity distribution. For example: suppose I want to know the covariance of the polarization with the pion DCA. If I look in bins of pion DCA for Lambda candidates the ones with the largest DCA have the purest Lambda distribution. Since we normally scale the measured polarization by $(S+B)/S$ (assuming zero polarization in the mass background) the polarization will be of a greater magnitude than that measured at low pion DCA. So, even if there is no dependence of the polarization on the specific cut, if no purity correction is made to account for the purer sample, one will measure a larger *apparent* polarization for the tighter cutset. Thus a positive covariance between the polarization and the cut will be seen. Given that we have a positive net polarization we might expect a trivial positive covariance for pion DCA to appear just from variation of the purity with pion DCA.

What we measure without correcting for the purity is the so called "measured" slope, we can recast eq. 5.2 as

$$Slope(P(X))^M = \frac{d}{dX}P^M \tag{5.4}$$

where M denotes the "measured" quantity and T denotes a "true" quantity. We can relate this to the true polarization which we get from purity correcting the measured values, provided we assume that we can describe the variation of $S/(S+B)$ with X by a linear function with slope m_X

$$\begin{aligned} Slope(P(X))^M &= \frac{d}{dX}\left(\frac{S}{S+B}P^T\right) \\ &= \frac{S}{S+B}\frac{d}{dX}P^T + \left(\frac{d}{dX}\frac{S}{S+B}\right)P^T \\ &= \frac{S}{S+B}Slope^T + m_X P^T \\ &\approx \left\langle\frac{S}{S+B}\right\rangle Slope^T + m_X\left\langle P^T\right\rangle \end{aligned} \tag{5.5}$$

5.1.2 Mass purity

An example of purity changing with a cut quantity:

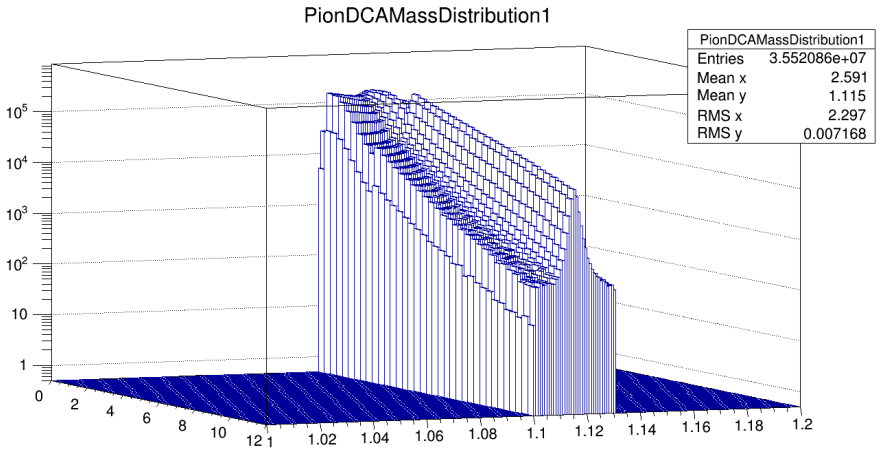

Figure 5.1: Invariant mass (GeV – right axis) as a function of pion DCA (cm – left axis) for cut index 1 (proton has TOF info, pion does not). Vertical axis is counts.

A linear fit of the purity for various quantities can be seen below

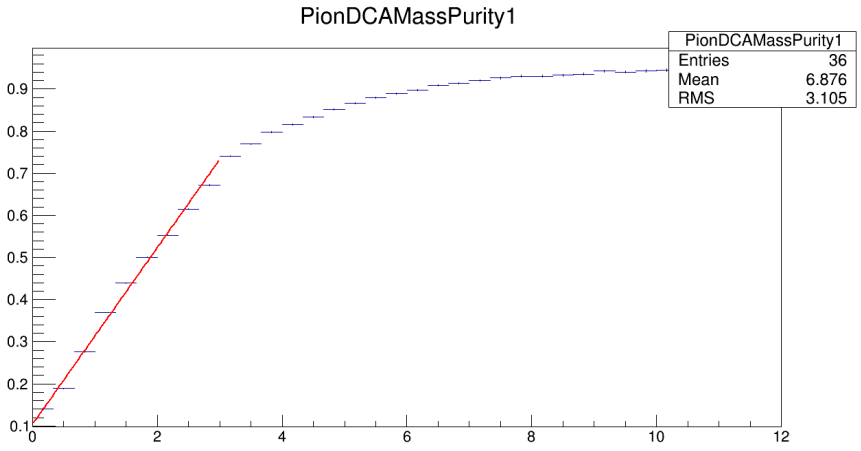

Figure 5.2: Lambda invariant mass purity as a function of pion DCA fit with a linear function ($p_0 + p_1 * x$) for cut index 1

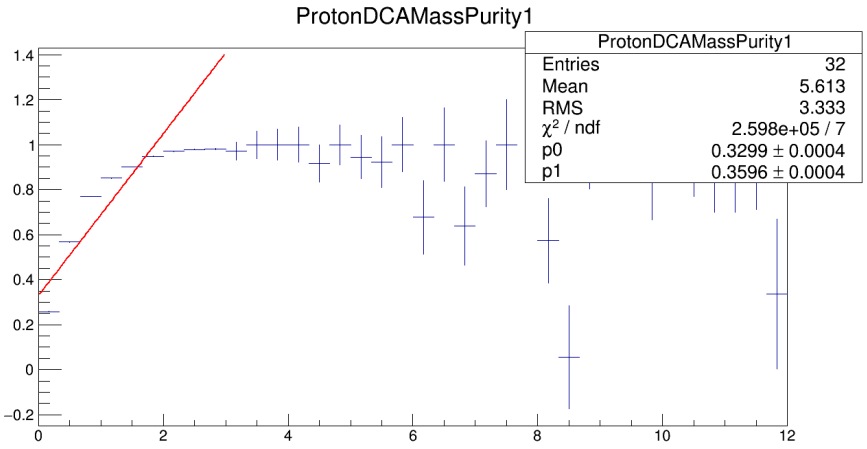

Figure 5.3: Lambda invariant mass purity as a function of proton DCA fitted with a linear function ($p_0 + p_1 * x$) for cut index 1

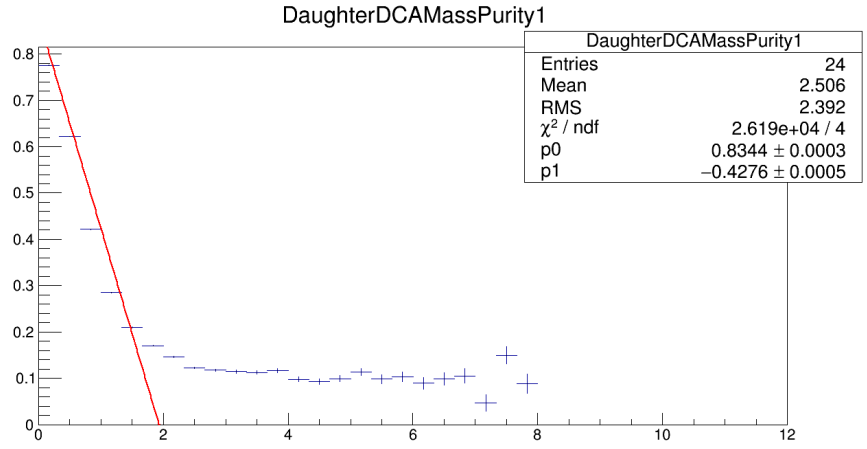

Figure 5.4: Lambda invariant mass purity as a function of daughter DCA fit with a linear function ($p_0 + p_1 * x$) for cut index 1

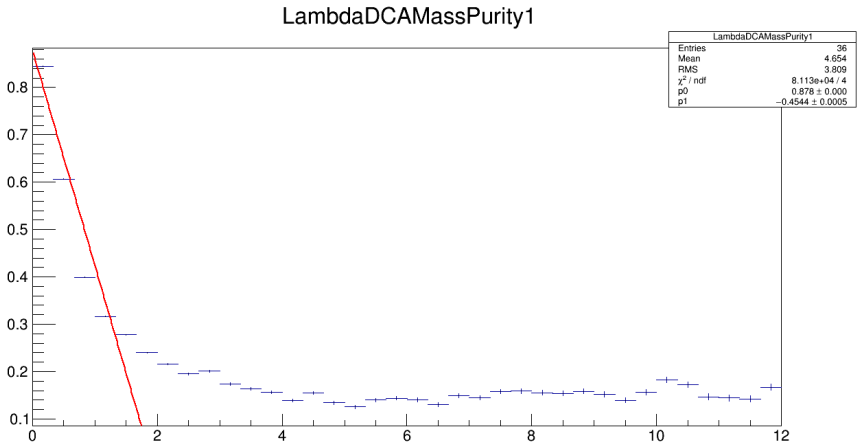

Figure 5.5: Lambda invariant mass purity as a function of Lambda DCA fitted with a linear function ($p_0 + p_1 * x$) for cut index 1

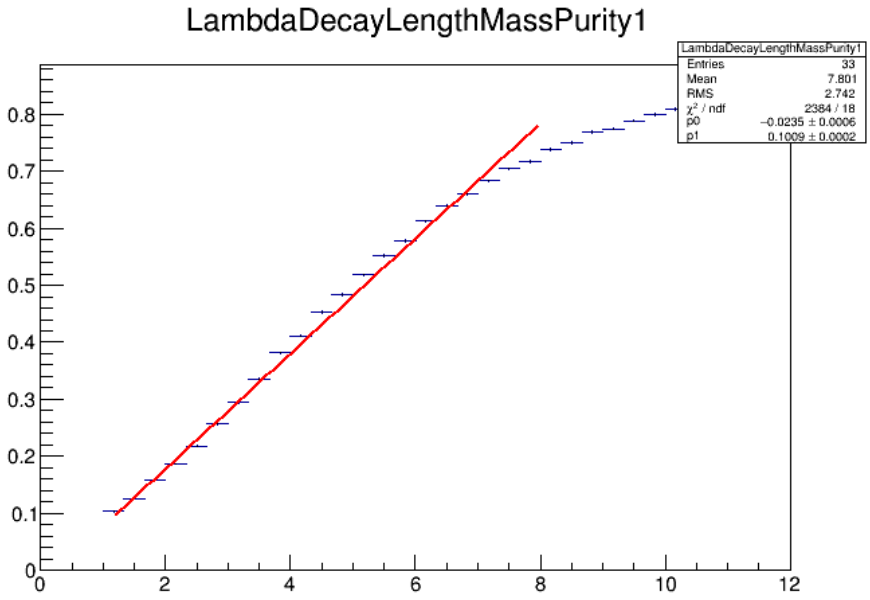

Figure 5.6: Lambda invariant mass purity as a function of Lambda decay length fitted with a linear function ($p_0 + p_1 * x$) for cut index 1

Clearly a linear approximation is not ideal for several of these functions, though it is worth noting that where it really breaks down is generally beyond the aforementioned reasonable cut range. The only thing to be done is to change the range over which the fit is done and try to overestimate m_X. The range was varied but the nominal fit range for these functions is (where Min. refers to the lower value of the cut and max refers to the upper value)

Cut description	cut index 0	cut index 1	cut index 2	cut index 3
PionDCA min	0.0	0.0	0.5	0.5
PionDCA max	3.0	3.0	3.0	3.0
ProtonDCA min	0.0	0.0	0.0	0.0
ProtonDCA max	3.0	3.0	3.0	3.0
DaughterDCA min	0.0	0.0	0.0	0.0
DaughterDCA max	2.0	2.0	2.0	2.0
LambdaDCA min	0.0	0.0	0.0	0.0
LambdaDCA max	2.0	2.0	2.0	2.0
LambdaDecayLength min	1.167	1.167	3.0	3.0
LambdaDecayLength max	8.0	8.0	8.0	8.0

Table 5.1: Range of linear fit of mass purity as a function of respective cut quantity

5.1.3 Results

Since the error bars depend so much on which cut I'm considering and the cut index of the Lambda I may have to duplicate a few of the plots zoomed in. What we're looking for is a clear non-statistical deviation of the slope. Each point on the following plots represents the covariance of the polarization with various cut quantities (e.g. pion DCA). There is a separate point for each type of Lambda (cut index 0, 1, 2, or 3).

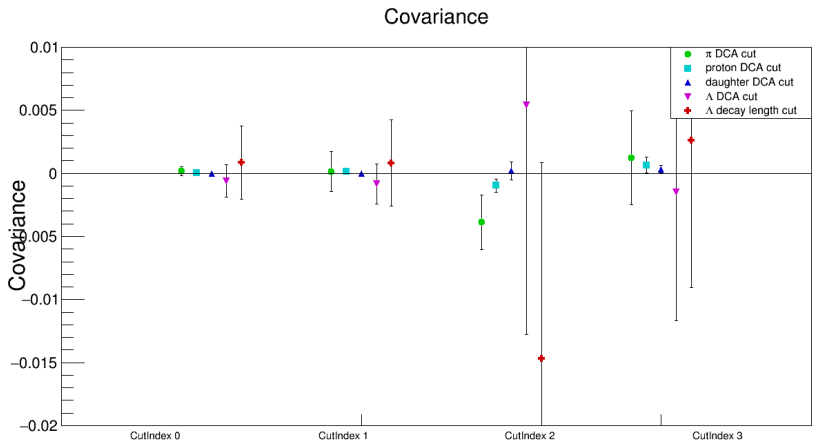

Figure 5.7: Λ polarization covariance with cut quantities for each Λ cut index.

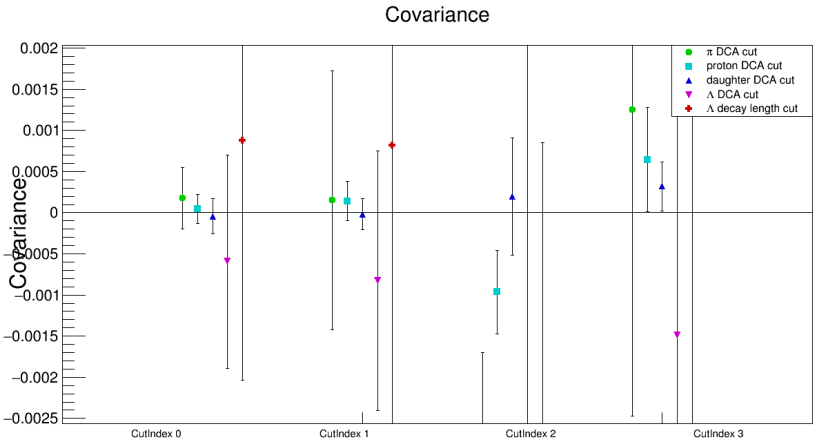

Figure 5.8: Λ polarization covariance with cut quantities for each Λ cut index; zoomed in.

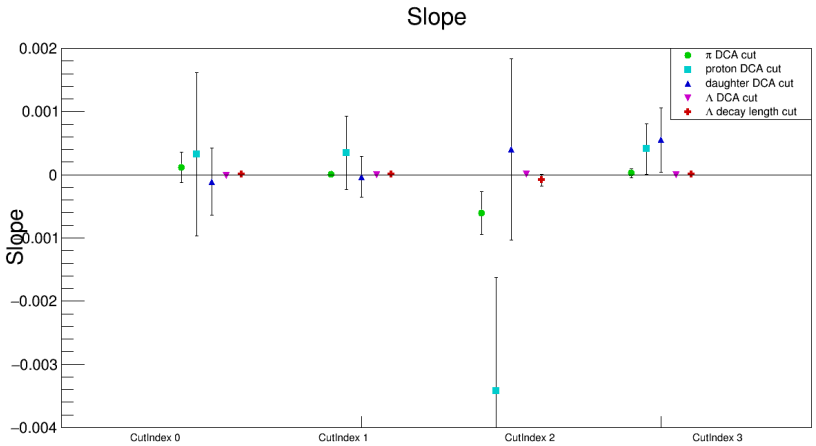

Figure 5.9: Λ polarization "slope" from covariance with cut quantities for each Λ cut index. This is not corrected for mass purity.

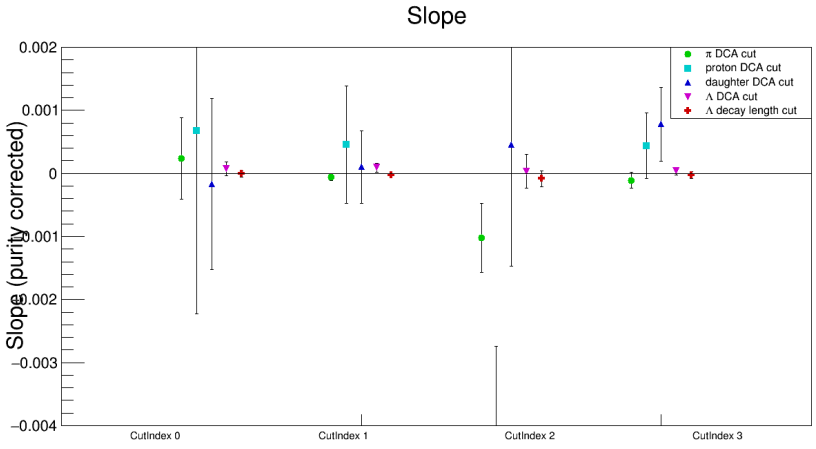

Figure 5.10: Λ polarization "slope" from covariance with cut quantities for each Λ cut index. This is corrected for mass purity.

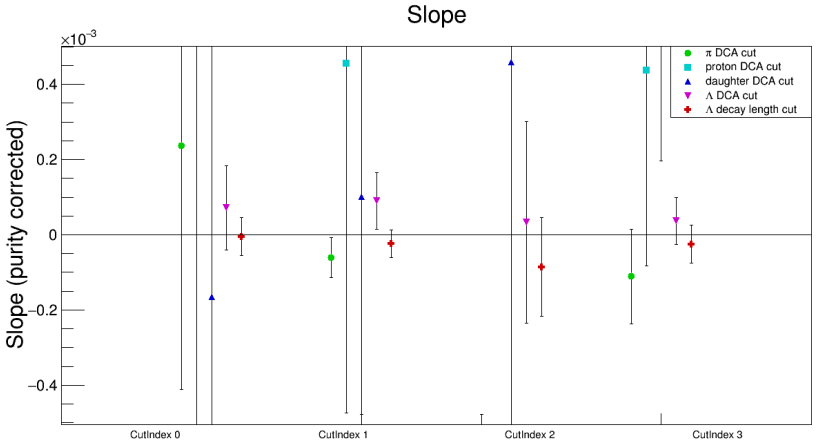

Figure 5.11: Λ polarization "slope" from covariance with cut quantities for each Λ cut index; zoomed in. This is corrected for mass purity.

The only hints of non-statistical deviation comes from cut index 2, but cut index 2 is only 3% of the data. Cut index 2 represents Lambda's whose daughter proton has no TOF information while the pion daughter does. This is a very poor quantity Lambda candidate and since it is such a small percentage of the total number of Lambdas we can throw these Lambdas out with impunity. There is no bias introduced here, these are simply poor quality Lambdas. Therefore (throwing out cut index 2 Lambdas) there is no non-statistical deviations from covariation of the polarization and any of the cut quantities. To double check this conclusion I've increased/decreased the maximum of the fit range for the purity slope m_X. In the following plots the the maximum of the fit is multiplied by a rangefactor.

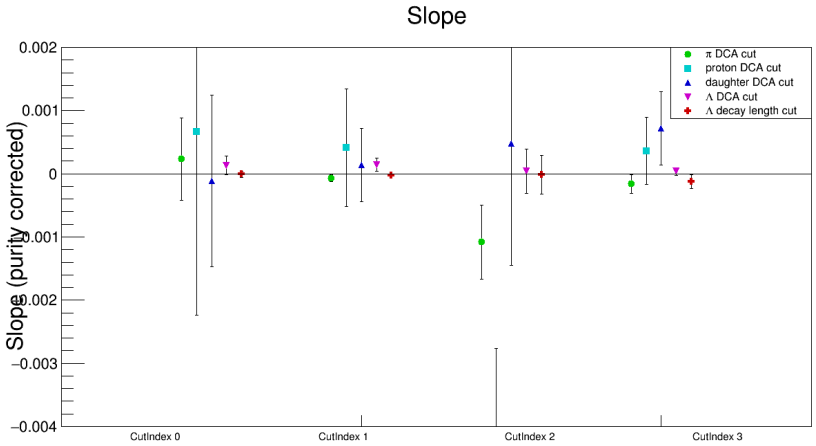

Figure 5.12: Λ polarization "slope" from covariance with cut quantities for each Λ cut index. This is corrected for mass purity. The rangefactor is 0.5.

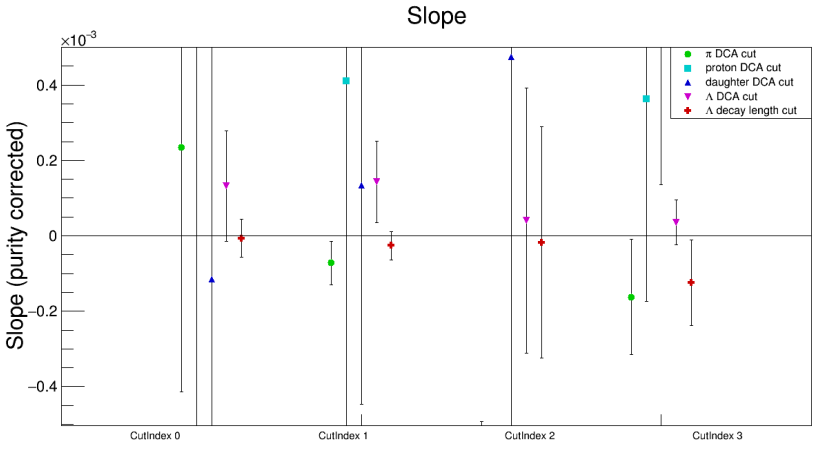

Figure 5.13: Λ polarization "slope" from covariance with cut quantities for each Λ cut index; zoomed in. This is corrected for mass purity. The rangefactor is 0.5.

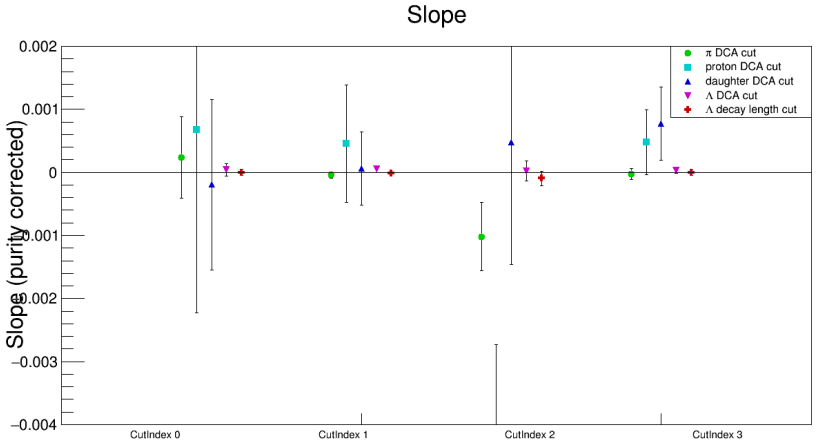

Figure 5.14: Λ polarization "slope" from covariance with cut quantities for each Λ cut index. This is corrected for mass purity. The rangefactor is 2.

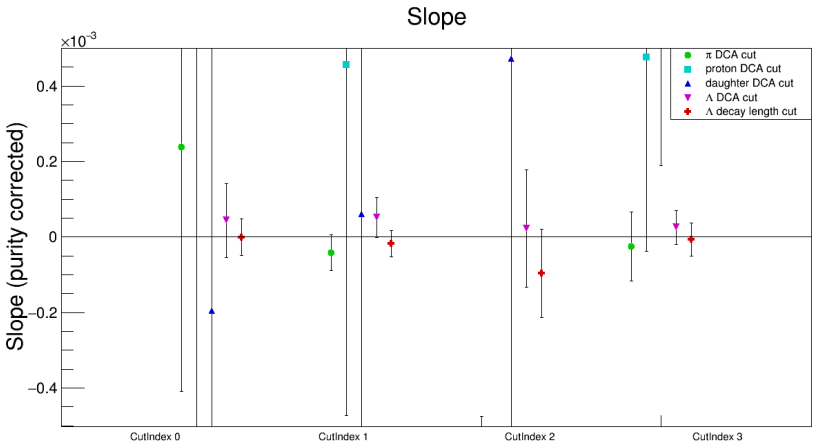

Figure 5.15: Λ polarization "slope" from covariance with cut quantities for each Λ cut index; zoomed in. This is corrected for mass purity. The rangefactor is 2.

5.1.4 Simple cut variation

This section is for historical purposes. The results shown here do not provide final systematic errors.

I'll focus on errors from the topology cuts for the Lambda as they are the ones specific to my analysis. To get a handle on the errors I varied each cut for 19GeV by either making the cut tighter so that I had 75% of the Lambdas as would be found using nominal cuts or I made the cut looser so that 125% of the Lambdas were found. The result for each cut for both Λ and $\bar{\Lambda}$ are shown in fig. 5.16 and fig. 5.17.

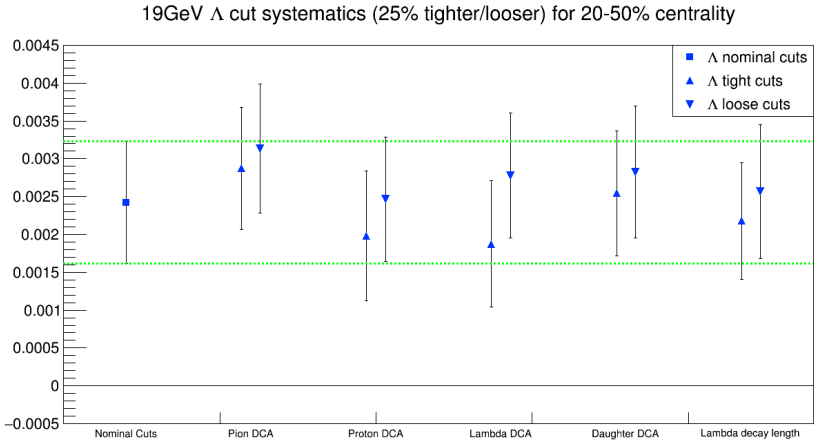

Figure 5.16: $\langle \sin\left(\Psi_1 - \phi^*_{\Lambda}\right)\rangle$ as a function of cut variation. One cut at a time is loosed or tightened so that 125% or 75% of the Lambdas are found.

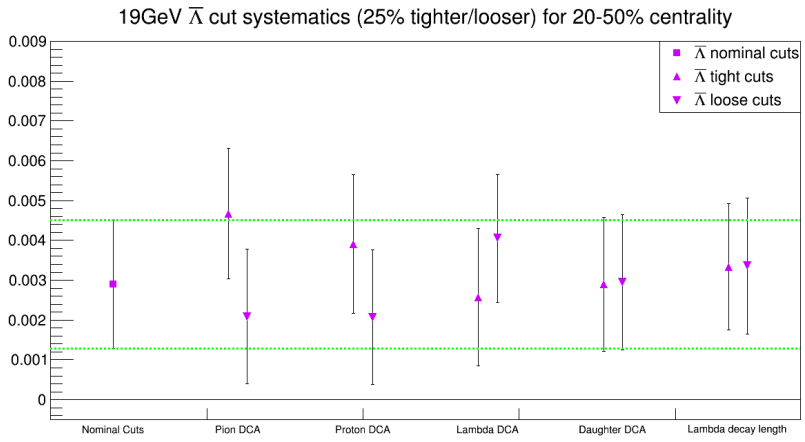

Figure 5.17: $\langle \sin\left(\Psi_1 - \phi^*_{\overline{\Lambda}}\right)\rangle$ as a function of cut variation. One cut at a time is loosed or tightened so that 125% or 75% of the Lambdas are found.

Note that in the previous two figures each data point is scaled by the (Signal+Background)/Signal of the mass distribution so that the results are not affected by the purity changes that would occur by loosening/tightening a cut. The systematic error is determined to be the largest variation between the tight cuts and loose cuts (e.g. for Λ the difference between Lambda DCA tight and Lambda DCA loose).

5.2 Residual effect

There is a systematic error from the residual signal we see in the wings of the mass distribution which should be in the mass background of the results (see sec. 3.4). In sec. 3.4 we posit that this small residual effect comes from Lambdas which have proton daughters that get matched up with pion who does not come from a Lambda. Many of the protons in an event come from Lambdas and it is a much smaller percent of the pions. A Lambda candidate made from these particles might well have a small residual polarization since the proton carries the larger percentage of the Lambda momentum, and thus a fair bit of the spin information. The following are corrected for resolution.

$\sqrt{s_{NN}}$ (GeV)	$P^{\Lambda_{\text{uncorrected}}}$ (%)	$P^{\overline{\Lambda}_{\text{uncorrected}}}$ (%)
7.7	1.6%	6.6%
11.5	1.0%	2.3%
14.5	0.6%	0.9%
19.6	0.7%	1.2%
27	0.7%	1.1%
39	0.3%	0.8%

Table 5.2: Uncorrected results for Au+Au 20-50%.

$\sqrt{s_{\mathrm{NN}}}$ (GeV)	$P^{\Lambda_{\mathrm{noresidual}}}$ (%)	$P^{\overline{\Lambda}_{\mathrm{noresidual}}}$ (%)	Level of correction Λ	Level of correction $\overline{\Lambda}$
7.7	2.4%	8.1%	155.4%	121.8%
11.5	1.5%	2.8%	151.7%	123.8%
14.5	1.2%	1.5%	192.3%	168.7%
19.6	1.0%	1.5%	151.5%	129.1%
27	1.1%	1.5%	153.0%	134.2%
39	0.5%	1.1%	149.2%	135.4%

Table 5.3: Results for Au+Au 20-50% corrected for mass purity without taking into account residual mass background polarization.

$\sqrt{s_{\mathrm{NN}}}$ (GeV)	$P^{\Lambda_{\mathrm{withresidual}}}$ (%)	$P^{\overline{\Lambda}_{\mathrm{withresidual}}}$ (%)	Level of correction Λ	Level of correction $\overline{\Lambda}$
7.7	2.3%	7.0%	148.5%	106.0%
11.5	1.2%	2.7%	125.0%	116.7%
14.5	0.9%	2.2%	142.2%	245.9%
19.6	0.9%	1.7%	129.0%	138.4%
27	1.0%	1.3%	136.3%	119.9%
39	0.3%	1.2%	95.2%	136.6%

Table 5.4: Results for Au+Au 20-50% corrected for mass purity while taking into account residual mass background polarization.

$\sqrt{s_{\mathrm{NN}}}$ (GeV)	$P^{\Lambda_{\mathrm{withresidual}}}/P^{\Lambda_{\mathrm{noresidual}}}$	$P^{\overline{\Lambda}_{\mathrm{withresidual}}}/P^{\overline{\Lambda}_{\mathrm{noresidual}}}$	$P^{\Lambda_{\mathrm{noresidual}}} - P^{\Lambda_{\mathrm{withresidual}}}$	$P^{\overline{\Lambda}_{\mathrm{noresidual}}} - P^{\overline{\Lambda}_{\mathrm{withresidual}}}$
7.7	95.6%	87.0%	−0.11%	−1.05%
11.5	82.4%	94.3%	−0.26%	−0.16%
14.5	73.9%	145.8%	−0.33%	0.69%
19.6	85.1%	107.2%	−0.15%	0.11%
27	89.1%	89.3%	−0.12%	−0.16%
39	63.8%	100.9%	−0.18%	0.01%

Table 5.5: Comparison between residual and non-residual corrections to data.

There are large statistical error bars associated with scale of the residual background correction. If fact this difference between considering and not considering the residual effect is well within statistical errors but we would like to associate a systematic error to our lack of understanding about the correct way of dealing with this residual effect. We can roughly average over the difference of the ratio of the two scaling methods to get final systematic errors. 15GeV is a special energy that will have an exception, but the average ratio not including 15GeV $\left\langle P^{\Lambda}{}_{\text{withresidual}}/P^{\Lambda}{}_{\text{noresidual}} \right\rangle \sim 0.85$ and $\left\langle P^{\overline{\Lambda}}{}_{\text{withresidual}}/P^{\overline{\Lambda}}{}_{\text{noresidual}} \right\rangle \sim 0.95$.

$\sqrt{s_{\text{NN}}}$ (GeV)	$P^{\Lambda}{}_{\text{noresidual}}$ (%)	$P^{\overline{\Lambda}}{}_{\text{noresidual}}$ (%)	$0.85P^{\Lambda}{}_{\text{noresidual}}$	$0.95P^{\overline{\Lambda}}{}_{\text{noresidual}}$ (%)	diff Λ	diff $\overline{\Lambda}$
7.7	2.4%	8.1%	2.019%	7.686%	0.4136%	0.4045%
11.5	1.5%	2.8%	1.228%	2.679%	0.2516%	0.1410%
14.5	1.2%	1.5%	1.036%	1.442%	0.2122%	0.0759%
19.6	1.0%	1.5%	0.8466%	1.471%	0.1734%	0.0774%
27	1.1%	1.5%	0.9172%	1.434%	0.1879%	0.0755%
39	0.5%	1.1%	0.4374%	1.083%	0.08959%	0.0570%

Table 5.6: Results for Au+Au 20-50% corrected for mass purity without taking into account residual mass background polarization. "Diff" is the difference between the first column and the previous relevant column.

Roughly averaging over the results in table 5.6 we get the following range of systematic errors (upper and lower)

$\sqrt{s_{NN}}$ (GeV)	Λ	Λ up sys	Λ down sys	$\overline{\Lambda}$	$\overline{\Lambda}$ up sys	$\overline{\Lambda}$ down sys
7.7	2.43%	0.00%	0.20%	8.09%	0.00%	1.00%
11.5	1.48%	0.00%	0.20%	2.82%	0.00%	0.15%
14.5	1.25%	0.00%	0.30%	1.52%	0.40%	0.15%
19.6	1.02%	0.00%	0.20%	1.55%	0.00%	0.15%
27	1.11%	0.00%	0.20%	1.51%	0.00%	0.15%
39	0.50%	0.00%	0.20%	1.14%	0.00%	0.15%

Table 5.7: Results for Au+Au 20-50% polarization results corrected for resolution correction and purity correction as well as systematic error.

5.3 Scaling errors

As discussed in the beginning of sec. 3 the data is subject to a few scalings: that of $\alpha_H = 0.647 \pm 0.013$ – the decay parameter, that of the resolution correction – as discussed in sec. 4.2.1, and the acceptance correction $A0$ – as seen in table 3.1. All of these have associated errors, which are very very small compared to the statistical error of the measure. The α_H is the largest at 2%. These are included as a statement in the paper about the uncertainty in the scaling.

Additionally given the interplay between helicity efficiency and non-zero polarization (discussed in sec. 3.5.2) we know (from simple simulation) that we should scale the data by about $7\% \pm 3.5\%$. This error is a consequence of fig. 3.26.

5.4 Conservation of momentum effects on event plane resolution

There are possible conservation of momentum effects on the event plane determination. This was studied as part of the BES v_1 paper [45] using MevSim with and without momentum conservation (with the version used it could be turned off and on) using sub-event planes made by using diffent subsections of the BBC. This was estimated to be a 2% systematic on the event plane resolution for the BES. We're using this same dataset so the results are expected to be the same.

5.5 Feeddown

There is uncertainty with our estimation of the yields for particles that feeddown into Lambdas. The feeddown is discussed in detail in section 7. Initially yield discrepancies between UrQMD and THERMUS made our systematic errors. Now we are using a very explicitly thermal approach. We want to get a sense of how sensitive to the results are to the specifics of the THERMUS yields.

For this study we will vary the f_Rs (fractions of Lambdas coming from a given source) for each source species (primary Lambda (Λ'), Σ^0, Ξ^0, Ξ^-, Σ^{*-}, Σ^{*0}, Σ^{*+}, other) in accordance with the procedure in sec. 7. Naturally the same is done in parallel for the sources of $\overline{\Lambda}$ The variation is going to be from sampling a Gaussian distribution centered around 0, so

$$f_R = f_R^{\text{THERMUS}} \left(1 + \text{TRandom3.Gaus}(0,\sigma)\right) \tag{5.6}$$

for some σ where .Gaus$(0,\sigma)$ is a function of a TRandom3 whereby a Gaussian of width σ centered around 0 is sampled. Naturally once this has done for all f_R on must renormalize them so that they are fractions again. There is always a finite chance that that f_R will be negative. To correct for this $if(f_R == 0) f_R = 0$. Such a sampling is done many (10^7) times to get a statistically significant value and repeated for different choices of σ. It has been found that the width of the $\hbar\omega/k_BT$ or $\mu_N B/k_BT$ distributions when fit by a Gaussian of width ρ are proportional to σ, so that $\rho_{N\cdot\omega} \approx N \cdot \rho_\omega$. This scaling seemed consistent even to fairly large σ (e.g $\sigma = 0.5$) where zeroing out f_Rs could lead to more asymmetric vortical or magnetic distributions. The width of these distributions for different values of σ can be seen

The last step is to actually fit what is shown in fig. 5.18 and fig. 5.19. The width of the fit (discussed above as ρ) is to be the systematic error from feed down for the final results. What is evident from the aforementioned figures is that the variation falls well within the statistical limits of the measurement, so this shouldn't be a dominant error. We have a fair level of trust in THERMUS so we use the ρ found for the $\sigma = 0.2$ curve which we think should include any reasonably different particle production model. This fit can be seen below, the results of ρ numerically for $\hbar\omega/k_BT$ or $\mu_N B/k_BT$ as percentages in order of increasing $\sqrt{s_{\text{NN}}}$ are:

float RhoVorticity[8] = {1.30, 0.19, 0.28, 0.18, 0.14, 0.12, 0.19, 0.18};

float RhoMagnetic[8] = {1.70, 0.29, 0.42, 0.28, 0.23, 0.18, 0.32, 0.29};

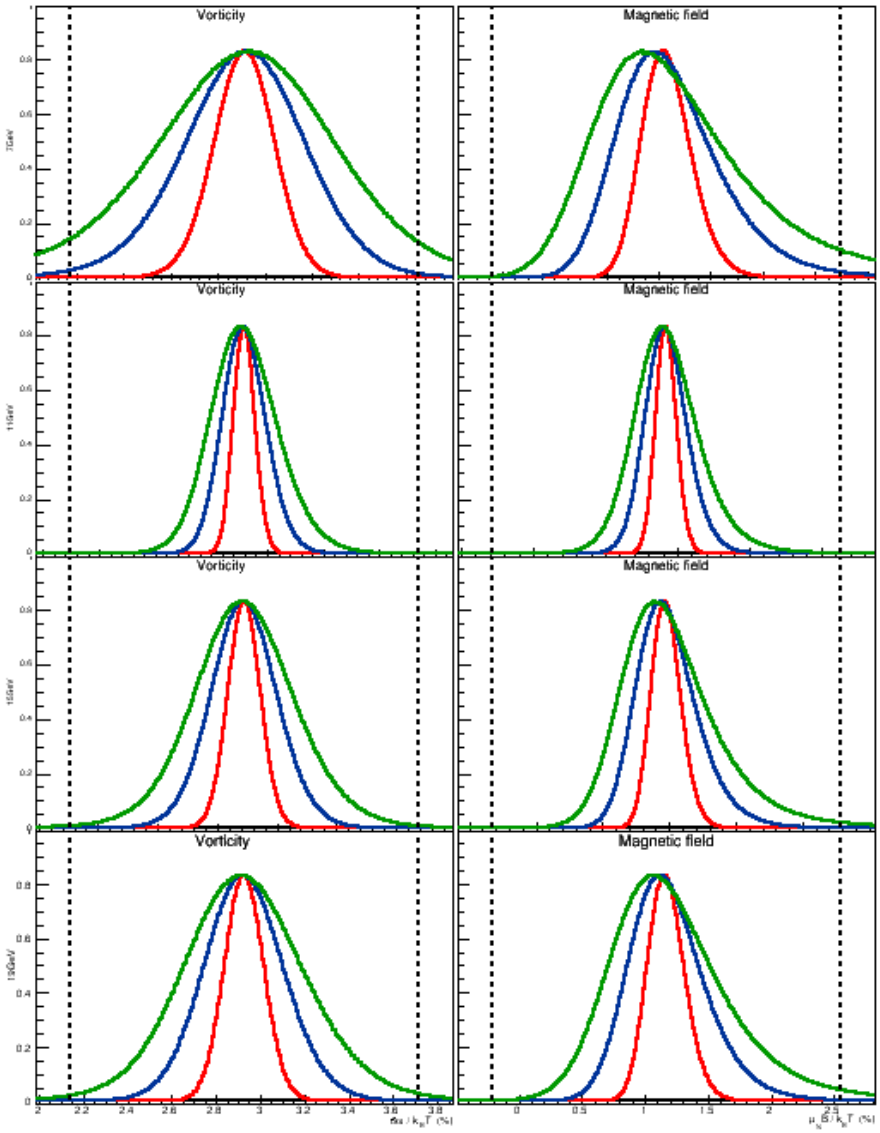

Figure 5.18: Feed down variation away from THERMUS for low $\sqrt{s_{\mathrm{NN}}}$ with some width σ. Different widths can be seen in the colors for $\sigma = 0.1$, $\sigma = 0.2$, and $\sigma = 0.3$. The left column depicts $\hbar\omega/k_BT$ as $\sqrt{s_{\mathrm{NN}}}$ goes down and the right depicts $\hbar\omega/k_BT$ or $\mu_N B/k_BT$ (both are as percentages). The rows are, in descending order, for $\sqrt{s_{\mathrm{NN}}}$ = 7.7GeV, $\sqrt{s_{\mathrm{NN}}}$ = 11.5GeV, $\sqrt{s_{\mathrm{NN}}}$ = 14.5GeV, and $\sqrt{s_{\mathrm{NN}}}$ = 19.6GeV. The dashed lines represent the statistical errors of the measure for nominal f_Rs. The y axis shows counts with the top bin normalized to 1/1.2, while the x axis is vorticity or magnetic field centered about the nominal measure.

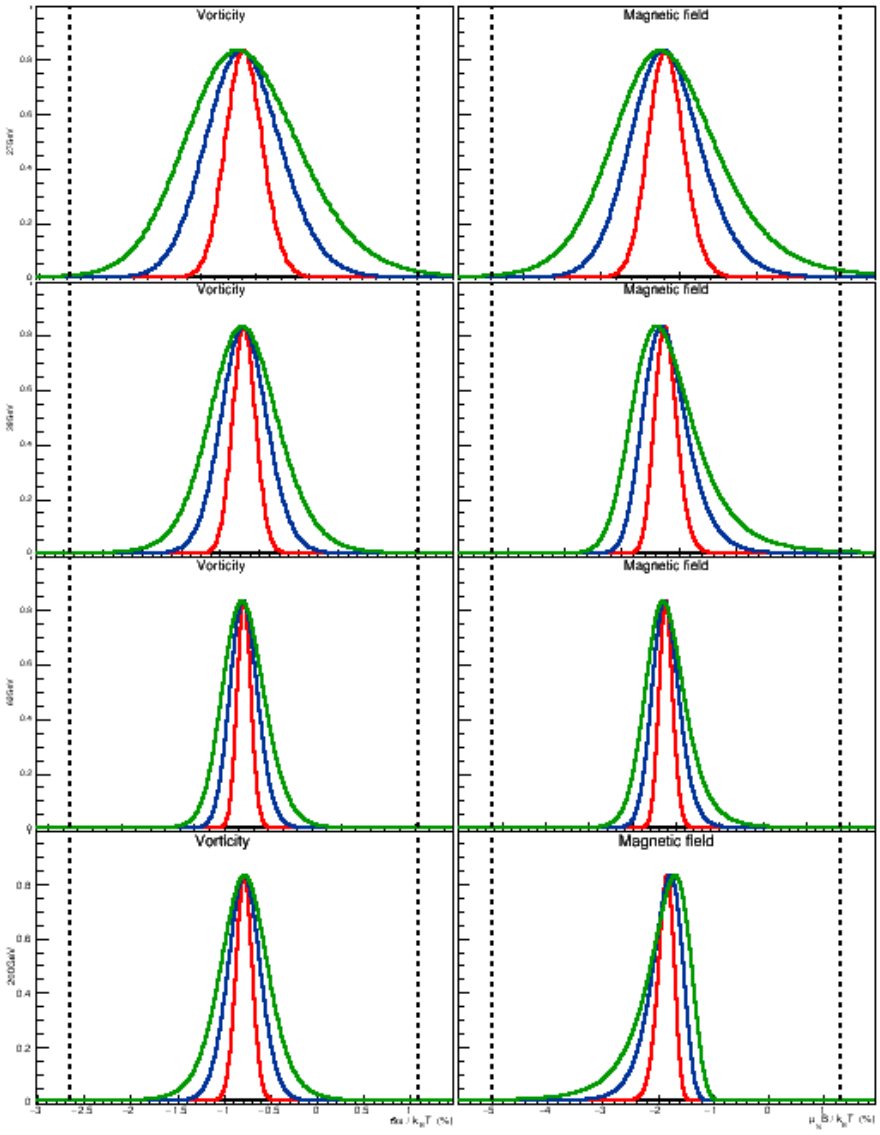

Figure 5.19: Feed down variation away from THERMUS for high $\sqrt{s_{\mathrm{NN}}}$ with some width σ. Different widths can be seen in the colors for $\sigma = 0.1$, $\sigma = 0.2$, and $\sigma = 0.3$. The left column depicts $\hbar\omega/k_BT$ as $\sqrt{s_{\mathrm{NN}}}$ goes down and the right depicts $\hbar\omega/k_BT$ or $\mu_N B/k_BT$ (both are as percentages). The rows are, in descending order, for $\sqrt{s_{\mathrm{NN}}} = 27GeV$, $\sqrt{s_{\mathrm{NN}}} = 39GeV$, $\sqrt{s_{\mathrm{NN}}} = 62GeV$, and $\sqrt{s_{\mathrm{NN}}} = 200GeV$. The dashed lines represent the statistical errors of the measure for nominal f_Rs. The y axis shows counts with the top bin normalized to 1/1.2, while the x axis is vorticity or magnetic field centered about the nominal measure.

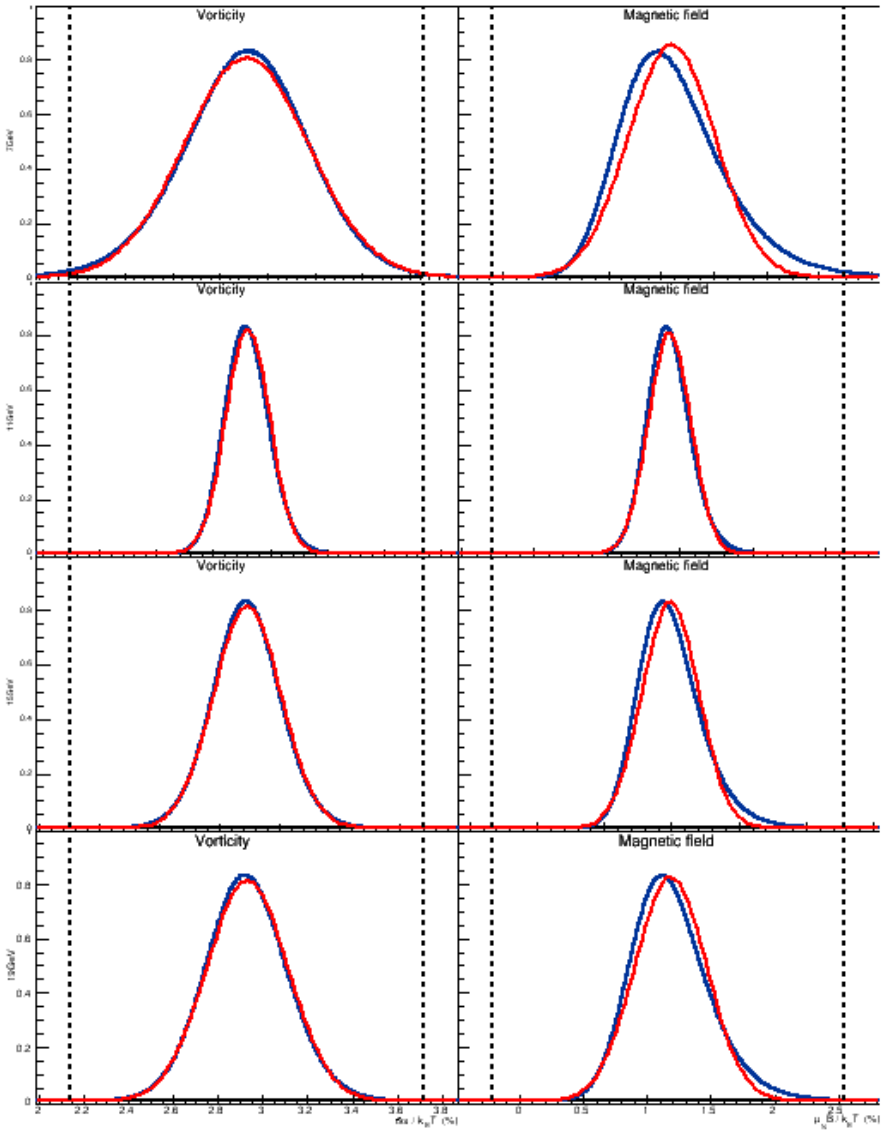

Figure 5.20: Gaussian fits (shown in red) of the feed down variation away from THERMUS for low $\sqrt{s_{\mathrm{NN}}}$ with $\sigma = 0.2$. The left column depicts $\hbar\omega/k_BT$ as $\sqrt{s_{\mathrm{NN}}}$ goes down and the right depicts $\hbar\omega/k_BT$ or $\mu_N B/k_BT$ (both are as percentages). The rows are, in descending order, for $\sqrt{s_{\mathrm{NN}}} = 7.7GeV$, $\sqrt{s_{\mathrm{NN}}} = 11.5GeV$, $\sqrt{s_{\mathrm{NN}}} = 14.5GeV$, and $\sqrt{s_{\mathrm{NN}}} = 19.6GeV$. The dashed lines represent the statistical errors of the measure for nominal f_Rs. The y axis shows counts with the top bin normalized to 1/1.2, while the x axis is vorticity or magnetic field centered about the nominal measure.

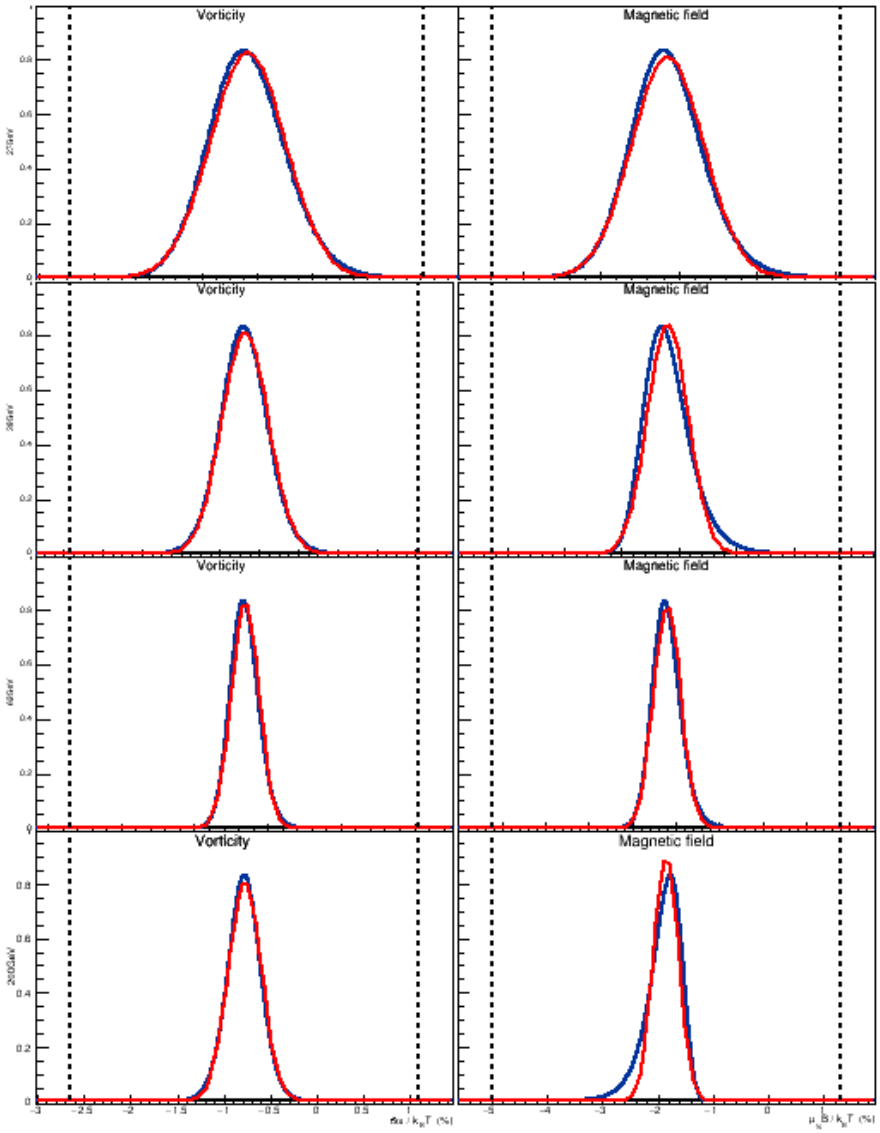

Figure 5.21: Gaussian fits (shown in red) of the feed down variation away from THERMUS for high $\sqrt{s_{\mathrm{NN}}}$ with $\sigma = 0.2$. The left column depicts $\hbar\omega/k_BT$ as $\sqrt{s_{\mathrm{NN}}}$ goes down and the right depicts $\hbar\omega/k_BT$ or $\mu_N B/k_BT$ (both are as percentages). The rows are, in descending order, for $\sqrt{s_{\mathrm{NN}}} = 27GeV$, $\sqrt{s_{\mathrm{NN}}} = 39GeV$, $\sqrt{s_{\mathrm{NN}}} = 62GeV$, and $\sqrt{s_{\mathrm{NN}}} = 200GeV$. The dashed lines represent the statistical errors of the measure for nominal f_Rs. The y axis shows counts with the top bin normalized to 1/1.2, while the x axis is vorticity or magnetic field centered about the nominal measure.

Chapter 6

SIGNAL FALSIFICATION

The purpose of this section is to provide examples of work that was done to attempt to falsify the signal.

6.1 Mass background contribution

As discussed in sec. 3.4 it is expected that the the signal from combinatoric Lambdas is zero, but it might be possible for some of the signal to leak into the combinatoric Lambdas if the associated proton was from a real polarized Lambda. We tried a few methods of verifying the expected null signal in the mass background. The first method is to simply look at the off-mass-peak polarization signal using the nominal cutset. In order to avoid daughters of real Lambdas to a point we left a gap between the on-peak Lambdas and the considered off-peak ones. The mass distribution of considered Lambdas is shown in fig. 6.1 (it is identical to fig. 3.10).

Using these Lambdas from the yellow region of fig. 6.1 yields the polarization signals seen in fig. 6.2.

The polarization signal in fig. 6.2 is consistent with zero, but, since the signal itself is so small we've tried to check this a few different ways. For these cross checks I'll tighten and loosen the nominal topological cuts described in sec. 4.4.2. For reference, if $R = S/B$ is the ratio of the signal to the background for the BES Λs $R \sim 1.8$. If the cuts are tightened tremendously we can check to see if the on-mass-peak signal changes. If the polarization measure stays the same it is safe to say that the background does not contribute significantly to the on-peak signal. Of course with much tighter cuts it is not feasible to use the off-mass-peak Lambdas as any sort of cross check. One such cutset with $R \sim 30$ (see fig. 6.4) is compared to the data in fig. 6.5 and fig. 6.6.

The datapoints for the two sets of cuts in fig. 6.5 and fig. 6.6 are very close. Of course the errors are correlated so it is somewhat difficult to gauge how close they are. Identical polarization measures would

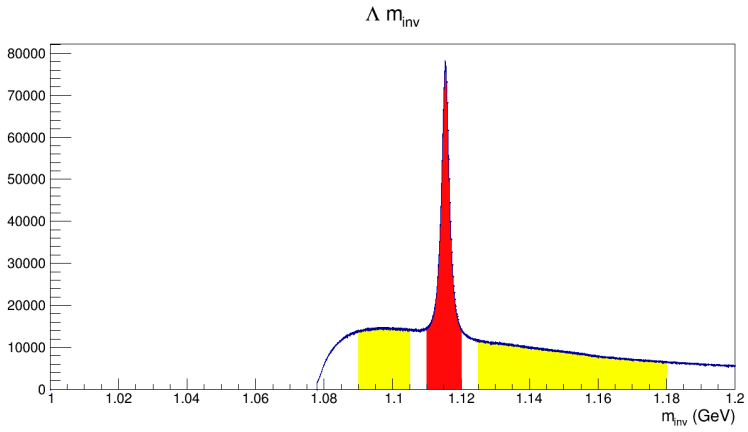

Figure 6.1: Λ counts as a function of invariant mass. The signal region ($1.108\text{GeV} < m_{\text{inv}} < 1.125\text{GeV}$) is highlighted in red. The off-mass regions for the cross-check are shown as yellow bands. The region at very low invariant mass are avoided because of the rapidly changing phasespace.

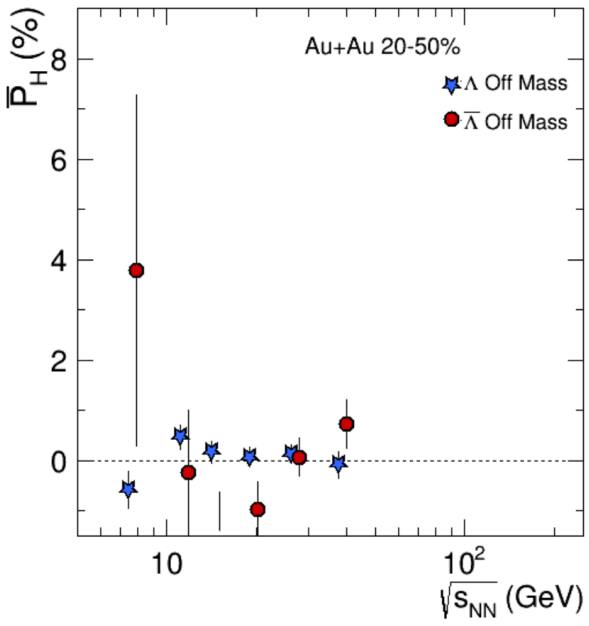

Figure 6.2: Polarization signal in the off-mass region using nominal analysis cuts.

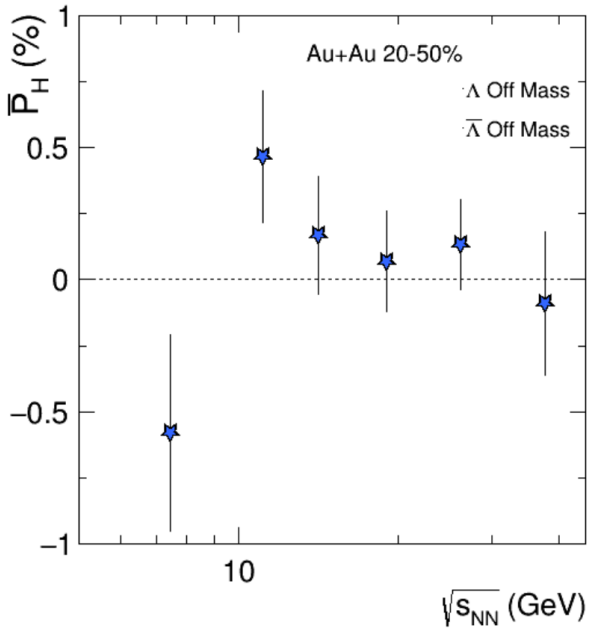

Figure 6.3: Polarization signal in the off-mass region using nominal analysis cuts. This is just a zoomed in version of fig. 6.2 which only shows the Λ polarization.

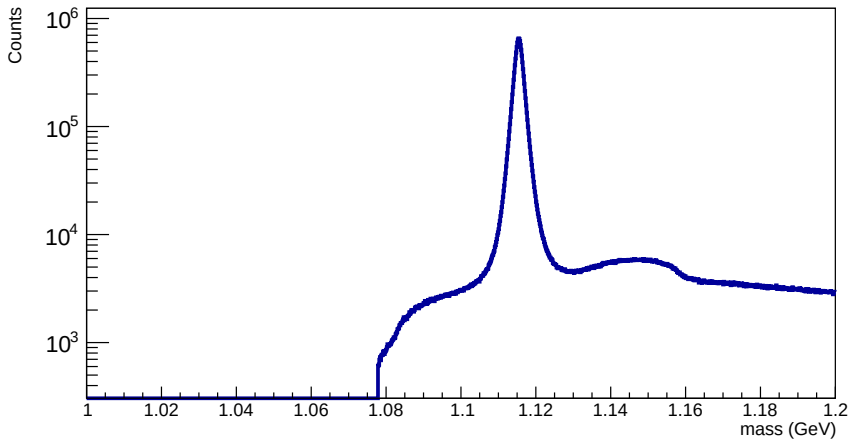

Figure 6.4: Λ mass distribution for the $R \sim 30$ cutset.

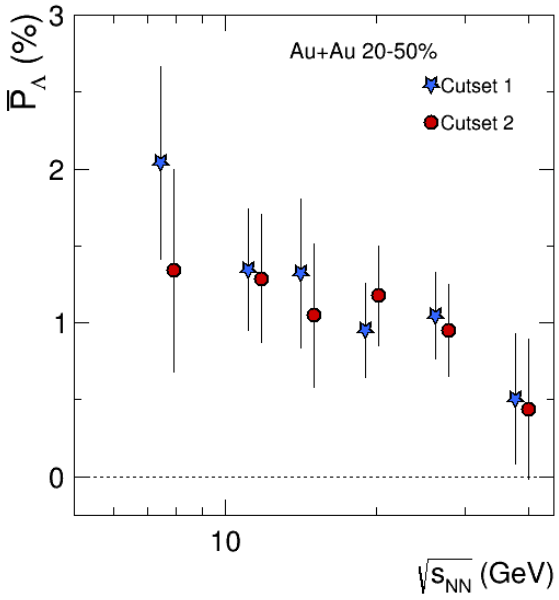

Figure 6.5: Λ Polarization for two different cut sets. "Cutset 1" is the collection of nominal cuts with $R \sim 1.8$. "Cutset 2" is the collection of nominal cuts with $R \sim 30$.

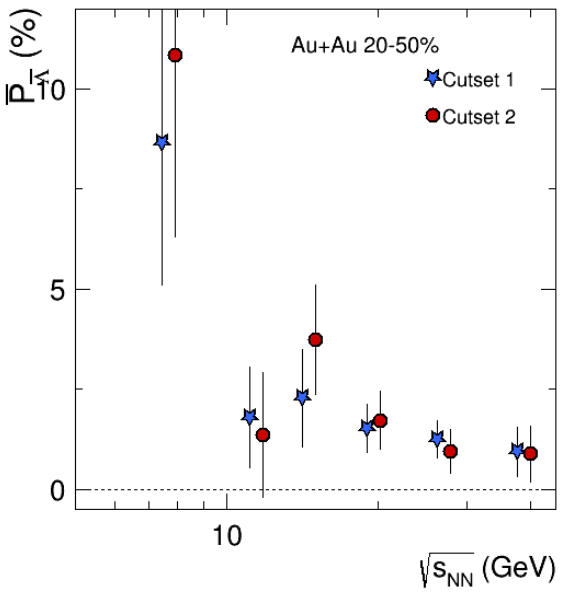

Figure 6.6: $\overline{\Lambda}$ Polarization for two different cut sets. "Cutset 1" is the collection of nominal cuts with $R \sim 1.8$ (for Λs). "Cutset 2" is the collection of nominal cuts with $R \sim 30$ (for Λs).

imply that the on-mass-peak signal is not modified by any apparent signal from combinatoric Lambdas.

In an effort to get around the statistical challenges of the measurement we also tried completely removing the topological cuts. Naturally this doesn't address the possibility of the off-mass-peak signal being modified by the cuts themselves, that is more related to the systematic error considerations of sec. 5.1. In order to remove any of the correlation from daughters of real Lambdas a harsh condition was instituted whereby if a Lambda candidate shared a daughter with any other Lambda candidate which was in the nominal mass range consideration ($1.108\text{GeV} < m_{\text{inv}} < 1.125\text{GeV}$) both candidates where thrown out. This process has been been given the name "thunderdome" in our group. Before the thunderdome vetting was applied the no-cut cutset had $R \sim 0.03$. The off-peak distribution is shown in fig. 6.7.

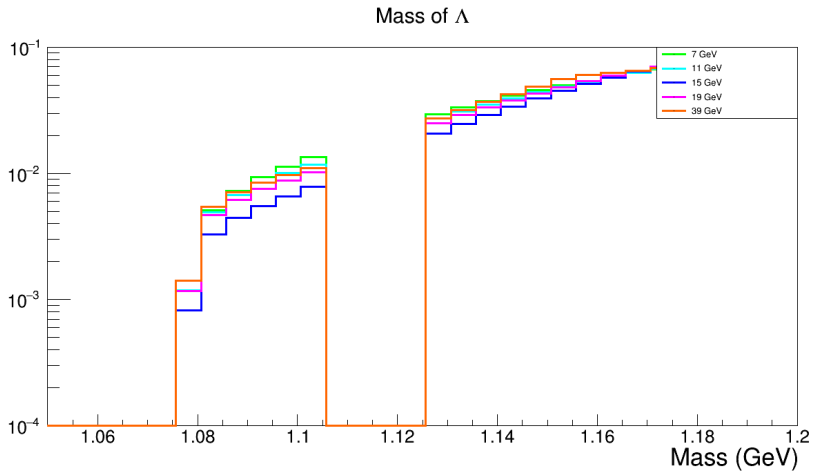

Figure 6.7: Λ mass distribution for the off-mass region when no topological cuts are applied.

Clearly the thunderdome off-mass-peak results are null. Overall every cross-check we've performed via cut variation and off-mass-peak combinatoric Lambdas follow the expectation that there should be no polarization signal for purely combinatoric Lambdas and that any residual signal which could come from proton daughters does not significantly impact the polarization measure.

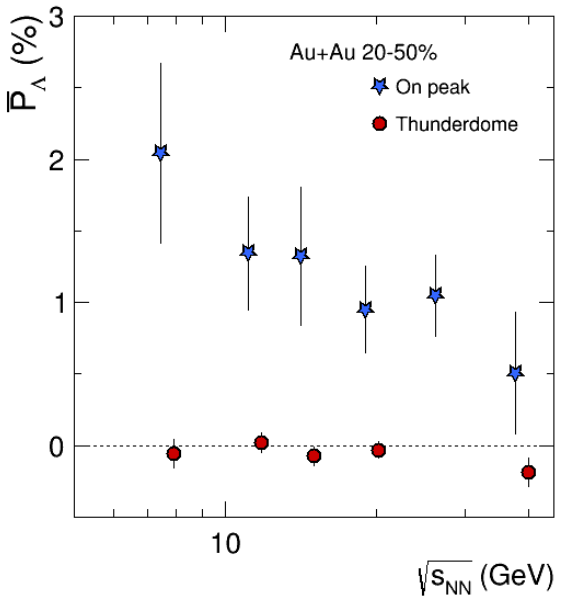

Figure 6.8: Λ Polarization results for the off-mass-peak thunderdome compared to nominal on-mass-peak polarization results.

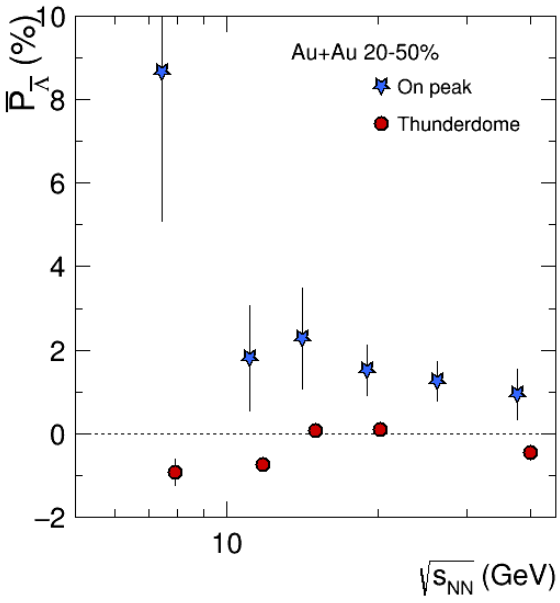

Figure 6.9: $\overline{\Lambda}$ Polarization results for the off-mass-peak thunderdome compared to nominal on-mass-peak polarization results.

6.2 Simulation comparison

Typically a natural place to look to verify or falsify an experimental signal are the many models that exist. No available simulation (at least as far as I am aware) has vorticity or spin coupling so simulation can, at best, be used for falsifying the results and attempting to see if one sees the signal appear as a consequence of acceptance or kinematics. Since the analysis is so simple it is unlikely that such a falsification could occur. The tools available I have used in this analysis are HIJING, embedded Lambdas in real events, and UrQMD.

Since HIJING simulations in the STAR framework have included a cut such that primary particles have $-4.5 < \eta < 2.5$ it isn't really possible to use the BBC and thus it is not possible to make any attempt at falsifying the results, aside from assuming that Ψ_1 is zero or random for every event. Because of the η cut many of the particles reaching the BBCs are secondary and thus there can be a large auto correlation effect with daughters of Lambdas and the "measured" Ψ_1. Assuming that $\Psi_1 = 0$ (the default) for every event gives a result that falls right on zero, namely -0.002 ± 0.15

Embedding data is very statistically challenged. Since the Lambdas in embedding aren't polarized and

are not made to have any correlation with Ψ_1 they can't give a number more sensitive than other simulation results.

UrQMD (in which the reaction plane is known) for 19.6GeV has given $P_H = 1.95^{-4} \pm 2.95^{-4}$ which means $N_\sigma = 0.66$. For UrQMD data I am given a list of Lambdas and I have to decay them myself. I give them an isotropic decay geometry so it is hardly a surprise that the results fall on zero. I do not have UrQMD tracks run through the GEANT model of STAR so I can only analyze the data as similarly to real data up to a point.

6.3 Rotated pions

Another way to try to falsify the signal is the run the same code but rotate all of the pions in the event by π in the $x-y$ plane. This should provide realistic Lambda candidates without providing any residual effects from real Lambdas leaking in. There should be a null signal in this measure. The following results are for resolution corrected polarization ($\sin(\Psi_1 - \phi^*_\Lambda)$) with no scaling by $8/(\pi\alpha)$.

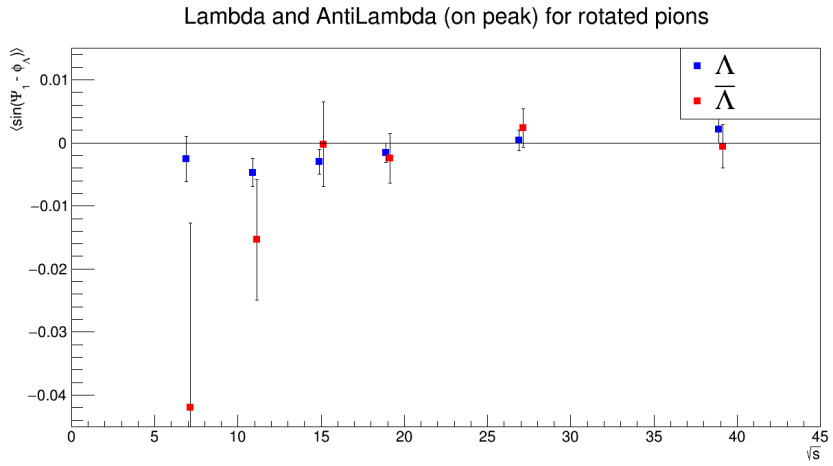

Figure 6.10: $\sin(\Psi_1 - \phi^*_\Lambda)$ as a function of $\sqrt{s_{\rm NN}}$ for Λ and $\overline{\Lambda}$ where the momenta of the pions in the events have been rotated 180 degrees in azimuth.

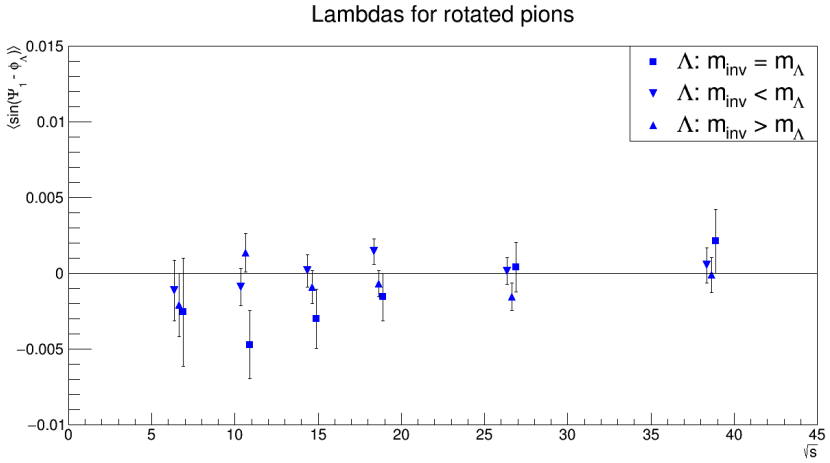

Figure 6.11: $\sin(\Psi_1 - \phi^*_\Lambda)$ as a function of $\sqrt{s_{\mathrm{NN}}}$ for Λ candidates that have large or small invariant mass - also referred to as off mass (both cases of $m_{\mathrm{inv}} > m_\Lambda$ and $m_{\mathrm{inv}} < m_\Lambda$) - where the momenta of the pions in the events have been rotated 180 degrees in azimuth.

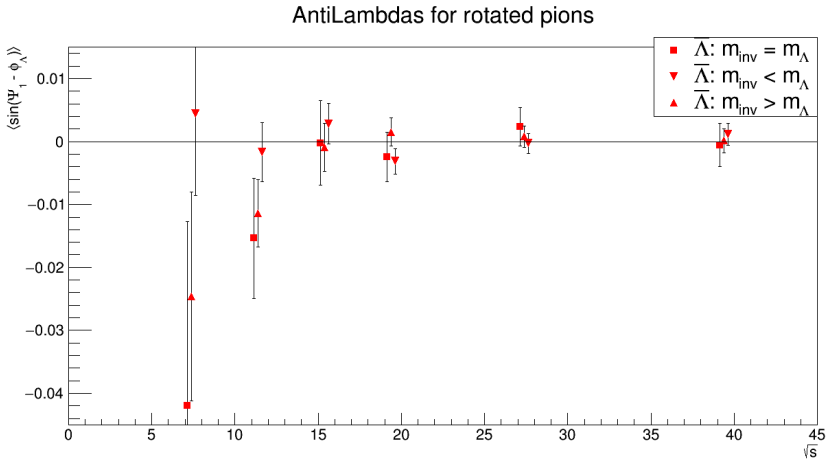

Figure 6.12: $\sin(\Psi_1 - \phi^*_\Lambda)$ as a function of $\sqrt{s_{\mathrm{NN}}}$ for $\overline{\Lambda}$ candidates that have large or small invariant mass - also referred to as off mass (both cases of $m_{\mathrm{inv}} > m_\Lambda$ and $m_{\mathrm{inv}} < m_\Lambda$) - where the momenta of the pions in the events have been rotated 180 degrees in azimuth.

6.4 Random event plane

The final trivial cross-check is to see if the results are consistent with zero if the event plane in a real event is taken randomly from a flat $0-2\pi$ distribution. This can only really serve as a code check. The results are in fig. 6.13.

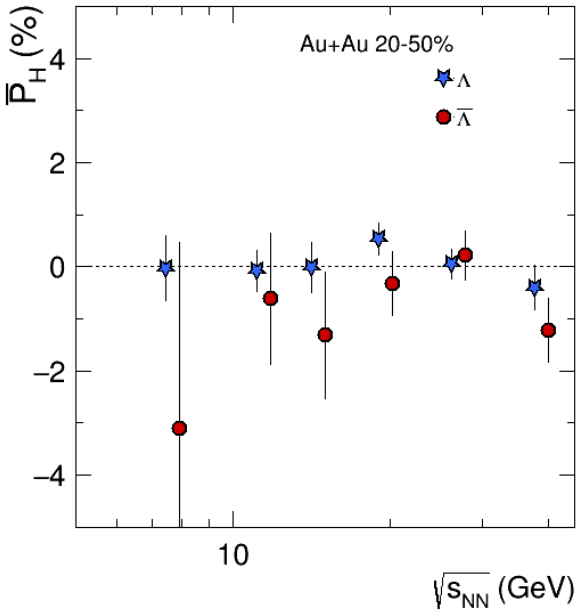

Figure 6.13: Polarization for a Ψ_1 randomly chosen from a flat distribution between $0-2\pi$.

Chapter 7

POLARIZATION AS VORTIMETER AND MAGNETOMETER

As described in sec. 2 hyperon polarization is a consequence of net vorticity, which itself is a consequence of a net angular momentum deposited into the system in the early stages of the collision. Thus the positive Λ and $\overline{\Lambda}$ polarization in fig. 7.6 indicates a positive vorticity in the system.

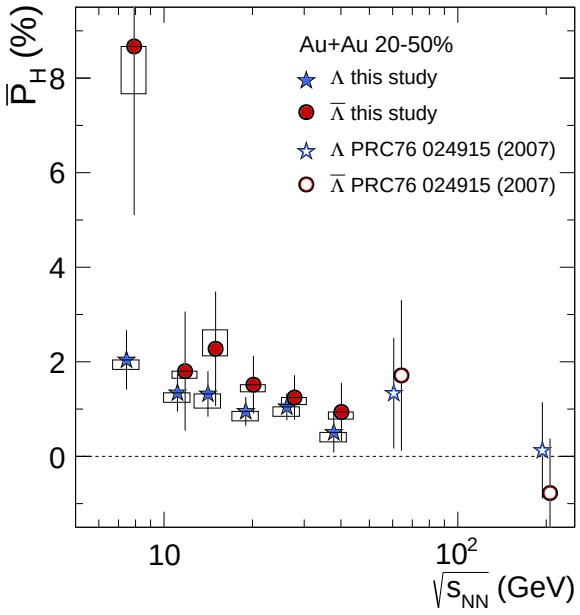

Figure 7.1: $\left\langle \frac{8}{\pi\alpha} \sin\left(\Psi_1 - \phi^*_{\Lambda,\bar{\Lambda}}\right)\right\rangle$ vs. $\sqrt{s_{NN}}$ for 20-50% centrality [1]. P_H characterizes the global correlation between Λ ($\overline{\Lambda}$) net spin and system angular momentum. Also seen in fig. 2.2.

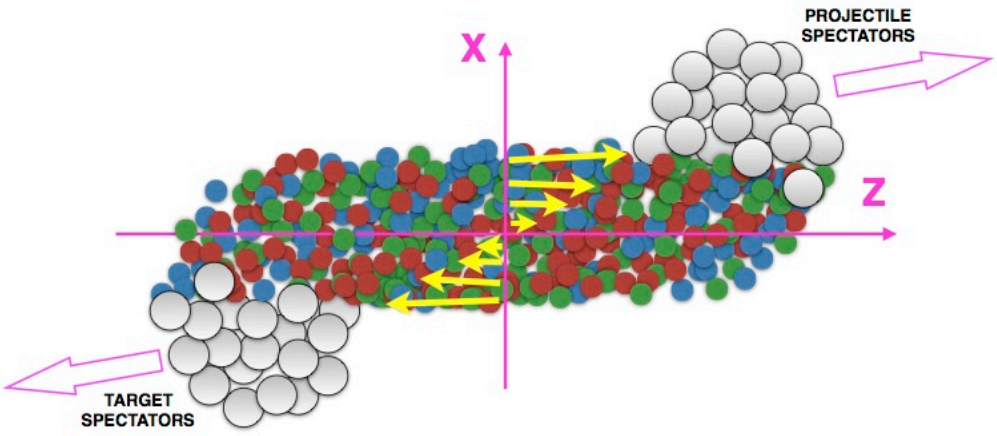

Figure 7.2: Cartoon of a heavy-ion collision.

Interestingly one may noticed that the $\overline{\Lambda}$ polarization is consistently, though not statistically, larger than the Λ polarization for all energies. It has been noted that positive baryochemical potential could make it more difficult for the medium to polarize particles than anti-particles due to Pauli blocking [46, 34]. Another possible source for asymmetry in the Λ and $\overline{\Lambda}$ polarization is magnetic coupling. The projectile and target spectators (as depicted in fig. 7.2) quickly moving charged objects which create a large rapidly changing magnetic field at midrapidity. The magnetic field points in the same direction (on average) as the angular momentum of the system. It's not known whether or not such a magnetic field would be sufficiently long lived to effect a polarization on final state hadrons via hadron magnetic moments. In principal, the constituent quarks of the QGP may themselves be polarized in such a way. Since anti-particles have opposite magnetic moments to particles, spin coupling to magnetic field would cause a splitting. The Λ magnetic moment is negative and thus one would expect the polarization due to a magnetic field on primary Λs to be negative and the polarization due to the magnetic field on primary $\overline{\Lambda}$s to be positive and of equal magnitude (assuming equal freeze-out times).

In this section the goal is to describe a simplistic way to get to the vorticity and magnetic field given measurements of particle and anti-particle global polarization. It is possible to make such a connection under the assumption of local thermodynamic equilibrium. Such an assumption is by no means exotic and is made in all of the hydrodynamic calculations discussed in sec. 2. Furthermore the same procedure has been used in calculations which do not explicitly require such an equilibrium [40, 41]. This discussion will

closely track, with less detail, a paper we've published on the subject [2].

Consider an equilibrated non-relativistic particle in a fluid cell rotating with angular velocity $\boldsymbol{\omega}$ inside a thermal bath of temperature T acted upon by a constant magnetic field $\boldsymbol{B}$. To find the spin of such a particle we can start with the density operator $\widehat{\rho}$, which can be described in terms of a partition function Z, some conserved charge $\widehat{Q}$ with corresponding chemical potential ν (an example of such a charge would be baryon number with its corresponding baryochemical potential)

$$\begin{aligned}\widehat{\rho} &= \frac{1}{Z}\exp\left[-\widehat{H}/T + \nu\widehat{Q}/T + \boldsymbol{\omega}\cdot\widehat{\boldsymbol{J}}/T + \widehat{\boldsymbol{\mu}}\cdot\boldsymbol{B}/T\right] \\ &= \frac{1}{Z}\exp\left[-\widehat{H}/T + \nu\widehat{Q}/T + \boldsymbol{\omega}\cdot\left(\widehat{\boldsymbol{L}}+\widehat{\boldsymbol{S}}\right)/T + \widehat{\boldsymbol{\mu}}\cdot\boldsymbol{B}/T\right].\end{aligned} \tag{7.1}$$

In the above equation the S denotes the particle spin and μ denoted its intrinsic magnetic moment. If the angular velocity is parallel to the magnetic field (as is expected) $\widehat{\rho}$ can be diagonalized in the basis of eigenvectors of particle spin pointing along this direction. The probability, w, of getting a particle with some spin projection m is

$$w[T,B,\omega](m) = \frac{\exp\left[\frac{\mu B/S+\omega}{T}m\right]}{\sum_{m=-S}^{S}\exp\left[\frac{\mu B/S+\omega}{T}m\right]}. \tag{7.2}$$

In the case of the data we can conclude that the polarization is small (of order a few percent). In which case we can expand the exponential and the spin is can be estimated by

$$\boldsymbol{S} \simeq \frac{S(S+1)}{3}\frac{\boldsymbol{\omega}+\mu\boldsymbol{B}/S}{T}. \tag{7.3}$$

Of course, in heavy-ion collisions one ought to take into account quantum mechanics so a Boltzmann statistical approach isn't generally correct. A generalization proceeds with a Wigner function and the spin tensor to describe the local polarization of emitted particles. I'll leave the details to [2]. Again using the small polarization the spin can be expressed analogous to eq. 7.3, this time using the thermal vorticity ϖ (defined in eq. 2.1) and magnetic field (both as axial vectors in the particle co-moving frame)

$$S^{\nu}(x,p) \simeq \frac{S(S+1)}{3}\left(\varpi_{c}^{\nu} + \frac{\mu}{S}B_{c}^{\nu}\right). \tag{7.4}$$

Looking at eq. 7.4 it's clear that the polarization of a particle/anti-particle pair would differ only in

the second term due to the sign of μ. In principal this means that by measuring the polarization of any particle/anti-particle (say $\Lambda/\overline{\Lambda}$) one can, with fairly modest assumptions, measure the fluid vorticity (which is quite a fundamental property of the fluid) and the magnetic field (which is of fundamental interest to the field). I'll expand a bit more more on the context of these observables in sec. 7.6.

Unfortunately, there is a complication when it comes to the actual measurements. The calculation is made for particles emitted directly from the fireball (primary particles). In an experimental context there is no way of guaranteeing that a given particle is primary. In actual fact only about a quarter of all measured Lambdas are primary. The rest come from a zoo of heavier particles primarily Σ^0, Σ^*, and Ξ. Most are spin 1/2 (with the notable exception of the Σ^*s) so they're expected to have the same coupling with the vorticity, however the magnetic moments of all of these particles can be quite different. Aside from this, in any decay scenario the daughter Lambda does not carry away the spin of its parent. The fraction (and sign) of the spin that the daughter Lambda carries away can be worked out, but they must be done for every resonance. Correcting the results for the effects due to the parents of a particle of interest is commonly referred to as a feed-down correction. Much of the rest of this section will describe how this correction can be made for the $\Lambda/\overline{\Lambda}$ system and show results with particle yields taken from the THERMUS model.

7.1 Feed-down procedure for Lambdas

As mentioned previously the most important decays to consider are the following: the strong decays of the form $\Sigma^* \to \Lambda + \pi$, the electromagnetic decays of the form $\Sigma^0 \to \Lambda + \gamma$, and the weak decays of the form $\Xi \to \Lambda + \pi$. This formalism will not consider any higher mass states. The reason for this restriction is essentially that these particles (along with primary Lambdas) make up the great majority of the sources for Lambdas seen in a collision. This is discussed in more detail in sec. 7.2.2.

In principal the transfer of spin of a parent to a daughter depends on the daughter momentum in the rest frame of the parent. In two body decays conservation laws may constrain that momentum which allows for simple Clebsch-Gordan calculations. In either case one can calculate the average spin transfer taking the momentum dependence into account, which will be denoted C. Tab 7.1 is a table of the transfer factors.

Many resonances (including the Σ^* resonances) can decay either directly into a Λ or a Σ^0 which, in turn, decays into a Λ itself. Because of this we consider the Σ^0 as a special case. For some decay of a particle R

Decay	C
parity-conserving: $\frac{1}{2}^+ \to \frac{1}{2}^+\ 0^-$	$-1/3$
parity-conserving: $\frac{1}{2}^- \to \frac{1}{2}^+\ 0^-$	1
parity-conserving: $\frac{3}{2}^+ \to \frac{1}{2}^+\ 0^-$	$1/3$
parity-conserving: $\frac{3}{2}^- \to \frac{1}{2}^+\ 0^-$	$-1/5$
$\Xi^0 \to \Lambda + \pi^0$	+0.900
$\Xi^- \to \Lambda + \pi^-$	+0.927
$\Sigma^0 \to \Lambda + \gamma$	-1/3

Table 7.1: Polarization transfer factors C for important decays $X \to \Lambda(\Sigma)$

of the form $R \to \Lambda$ ($R \to \Sigma^0 \to \Lambda$) let $f_{\Lambda R}$ ($f_{\Sigma^0 R}$) be the branching ratio of the Λ channel and $C_{\Lambda R}$ ($C_{\Sigma^0 R}$) be the spin transfer factors as described before. In this case the measured Λ spin can be written in terms of the parent spin as

$$\mathbf{S}_\Lambda^{*,\text{meas}} = \sum_R \left[f_{\Lambda R} C_{\Lambda R} - \tfrac{1}{3} f_{\Sigma^0 R} C_{\Sigma^0 R} \right] \mathbf{S}_R^*. \tag{7.5}$$

Note that the $-1/3$ in the second term is coming from the $C_{\Lambda\Sigma^0}$ from tab. 7.1. Ultimately we're interested in the polarization. For the spin 1/2 particles there are only two possible spin projections on a given axis so the meaning of polarization is more obvious, but for the spin 3/2 states (e.g. the Σ^*s) this needs to be made explicit. The mean spin vector can be expressed in terms of the mean density operator and the spin operator $\widehat{\boldsymbol{S}}$

$$\langle \widehat{\boldsymbol{S}} \rangle = \text{tr}\left(\widehat{\rho}\, \widehat{\boldsymbol{S}} \right). \tag{7.6}$$

The polarization is thus the average spin of a particle scaled by its total spin to normalize it to 1

$$\mathbf{P} = \widehat{\boldsymbol{S}}/S. \tag{7.7}$$

Using this definition it is possible to rewrite eq. 7.5 in terms of the polarization

$$P_\Lambda^{\text{meas}} = 2 \sum_R \left[f_{\Lambda R} C_{\Lambda R} - \tfrac{1}{3} f_{\Sigma^0 R} C_{\Sigma^0 R} \right] S_R P_R. \tag{7.8}$$

Thus from eq. 7.8 and eq. 7.4 we can make a 2×2 matrix to relate measured Λ and $\overline{\Lambda}$ polarization to the

magnetic field and thermal vorticity.

$$\begin{pmatrix} \varpi_c \\ \\ B_c/T \end{pmatrix} = \begin{bmatrix} \frac{2}{3}\sum_R \left(f_{\Lambda R} C_{\Lambda R} - \frac{1}{3} f_{\Sigma^0 R} C_{\Sigma^0 R}\right) S_R(S_R+1) & \frac{2}{3}\sum_R \left(f_{\Lambda R} C_{\Lambda R} - \frac{1}{3} f_{\Sigma^0 R} C_{\Sigma^0 R}\right) (S_R+1)\mu_R \\ \\ \frac{2}{3}\sum_{\overline{R}} \left(f_{\overline{\Lambda R}} C_{\overline{\Lambda R}} - \frac{1}{3} f_{\overline{\Sigma^0 R}} C_{\overline{\Sigma^0 R}}\right) S_{\overline{R}}(S_{\overline{R}}+1) & \frac{2}{3}\sum_{\overline{R}} \left(f_{\overline{\Lambda R}} C_{\overline{\Lambda R}} - \frac{1}{3} f_{\overline{\Sigma^0 R}} C_{\overline{\Sigma^0 R}}\right) (S_{\overline{R}}+1)\mu_{\overline{R}} \end{bmatrix}^{-1} \begin{pmatrix} P_\Lambda^{\text{meas}} \\ \\ P_{\overline{\Lambda}}^{\text{meas}} \end{pmatrix}. \tag{7.9}$$

Here, $f_{\Lambda R}$ ($f_{\overline{\Lambda R}}$) is the fraction of measured Λs ($\overline{\Lambda}$s) that arise from the direct decay of a baryon $R \to \Lambda + X$ ($\overline{R} \to \overline{\Lambda} + X$). Similarly, $f_{\Sigma^0 R}$ ($f_{\overline{\Sigma^0}\overline{R}}$) is the fraction of measured Λs ($\overline{\Lambda}$s) that arise from the direct decay $R \to \Sigma^0 + X \to \Lambda + \gamma + X$ ($\overline{R} \to \overline{\Sigma^0} + X \to \overline{\Lambda} + \gamma + X$). (Note carefully the last sentence: $f_{\Sigma^0 R}$ does not give the fraction of *Sigmas* coming from parent R, but the fraction of *Lambdas* coming from (grand)parent R.) The branching ratio for $\Sigma^0 \to \Lambda + \gamma$ is essentially 100%.

The constants C are the spin transfer coefficients, listed in table 7.1, and S_R and μ_R are the spin and magnetic moment of particle R. For the antibaryons, $S_{\overline{R}} = S_R$, $C_{\overline{XY}} = C_{XY}$, and $\mu_{\overline{R}} = -\mu_R$. The sums in equation 7.9 are understood to include the contributions of *primary* Λs and Σ^0s, too.

The magnetic moments of the particles and the branching ratios for the decays are given in tab. 7.2. The branching ratios will be important when we estimate the yields in later sections as it modifies the effective yield of Lambda parent.

index i	particle	J^P	μ (μ_N)	BR$\to \Lambda + X$	BR$\to \Sigma^0 + X$
0	Λ'	$\frac{1}{2}^+$	-0.613 [47]	(100%)	-
1	Σ^0	$\frac{1}{2}^+$	+0.79 (quark model [47])	100%	-
2	Ξ^-	$\frac{1}{2}^+$	-0.651 [47]	100%	0
3	Ξ^0	$\frac{1}{2}^+$	-1.25 [47]	100%	0
4	Σ^{*-}	$\frac{3}{2}^+$	-2.41 [48]	87%	7%
5	Σ^{*0}	$\frac{3}{2}^+$	+0.30 [48]	87%	1%
6	Σ^{*+}	$\frac{3}{2}^+$	+3.02 [48]	87%	7%

Table 7.2: Particles that may feed down to our Λ sample. Λ' refers to primary Λs. The index, i, is used in the computer code implementation of this calculation; it is included just for reference. Magnetic moments, μ, are given in units of the nuclear magneton, $\mu_N \equiv \frac{e\hbar}{2m_{\text{proton}}}$. Branching ratios to Λ and Σ^0 baryons are needed to calculate f factors in equation 7.9.

7.2 Particle yields for feed-down correction

The only ingredients we're missing in eq. 7.9 is the relative yield fractions. For these we need some model to estimate the yields. THERMUS [49] is a C++ package that estimates particle yields given a set of parameters. The package is capable of drawing from a few different distributions. In this calculation the Grand-Canonical Ensemble (GCE) was used which conserves baryon number, strangeness, and electric charge. The inputs of the model are the temperature (T), system volume (V), chemical potentials (μ_i) for conserved charges, and a phenomenological parameter (γ_S) which accounts for incomplete equilibration in the strangeness sector. THERMUS provides particle yields, but it doesn't describe the dynamics of a full collision. It may seem strange initially that $\mu_S \neq 0$, but net strangeness is allowed to be nonzero in given rapidity windows, and is found to be nonzero in real detector acceptance. The same is true for baryon number and charge, though a real physical process (baryon stopping) also provide a significant deviation from zero in integrated phasespace. The GCE partition function is given by

$$Z_i(T,V,\mu_i) = \mathrm{tr}\left[e^{-\left(\hat{H}-\mu_i\hat{N}_i\right)/T}\right]. \tag{7.10}$$

The γ_S parameter comes into play as a multiplicative factor γ_S^S on the Boltzmann factor for any hadron of strangeness S

THERMUS was run by Bill Llope using parameters from from Sabita Das' thesis [50] (It can be found most easily on the STAR drupal page https://drupal.star.bnl.gov/STAR/system/files/Thesis_SabitaDas_26thOct.pdf). Quantities of interest are enumerated in "Table 4.4: Freeze-out parameters obtained from yields in GCE and($\mu_Q = 0$)." Like Sabita, the parameter $\mu_Q = 0$ and the system volume is a hard sphere with radius based of nuclear parameters and overlap size. Naturally numbers were chosen to match the 20-50% of the analysis. Sabita uses THERMUS for the STAR results so it is not a surprise that they match.

Lambda's coming from some higher mass state have a different decay topology from primary Lambdas. This could effect how efficiently our detector finds such Lambdas. This is discussed in the next section. Ultimately The effects were found to be so small that the efficiencies are ignored. There is no serious variation of the results from slight relative yield changes.

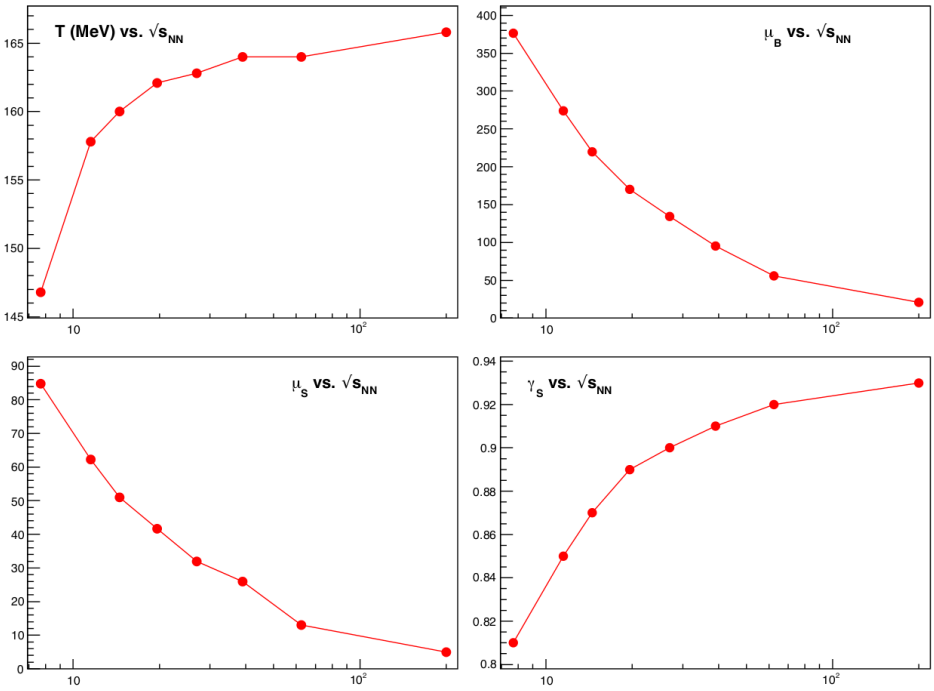

Figure 7.3: Input numbers for THERMUS simulation

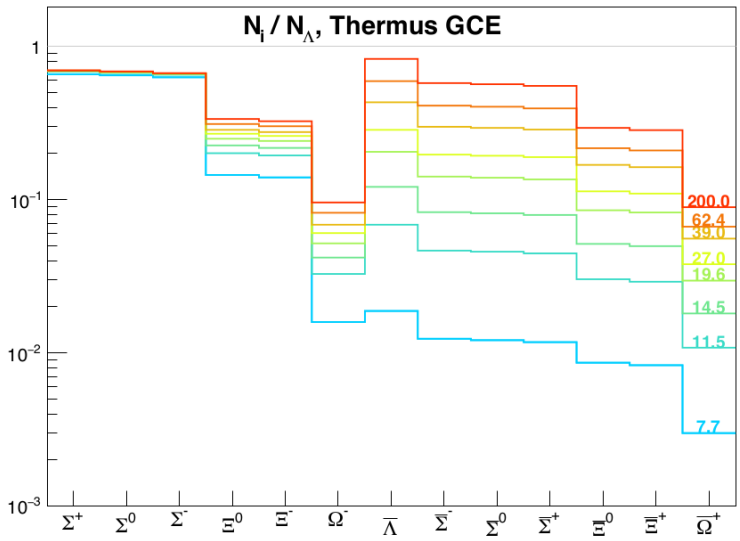

Figure 7.4: Output particle ratios for THERMUS simulation, unfortunately these do not include Σ^* baryons.

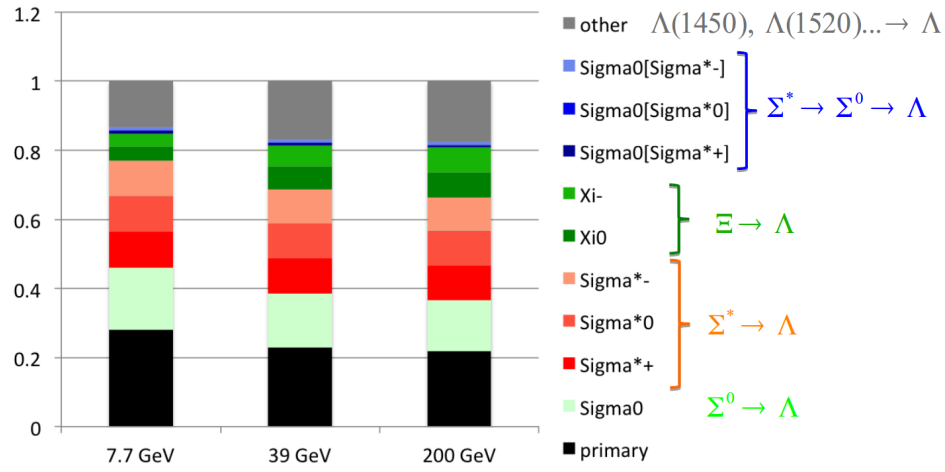

Figure 7.5: Contributions to Λ multiplicity for different $\sqrt{s_{\rm NN}}$. All higher resonances and mass states (including the Ω) are grouped together in the "other" category. Clearly there is not a strong $\sqrt{s_{\rm NN}}$ dependence on the percentages.

7.2.1 HIJING efficiency

Since the Σ^0 decay is electromagnetic the Λ daughter has basically the same decay kinematics as a primary Λ. On the other hand, weak decays like the Ξ^-, Ξ^0, and the Ω^0 have lifetimes similar to the Λ. Because of this the *apparent* decay length of the Λ which is a daughter of one of these multi-strange particles is longer than average decay length of actual primary Λ. Similarly such a secondary Λ would have a larger reconstructed DCA and (generally) larger DCA of each secondary Λ daughter to the primary vertex. In order to account for this effect we used HIJING data and compared the efficiency of the multi-strange hadrons to the efficiency of the Lambdas. This relative efficiency was used because the yields we got from UrQMD and THERMUS are with respect to Lambdas. Quoting the yields this way somewhat mitigates the tendency for models like UrQMD to underestimate strangeness.

In order to get the efficiency for reconstructing a Ξ^- relative to reconstructing a primary Λ we first get a Ξ^- efficiency. This is accomplished by dividing the number of MC Ξ^- tracks in the HIJING by the number of HIJING Ξ^-s that are associated via the association maker and pass our normal reconstruction cuts. This quantity is then divided by the same thing (# pure MC tracks/# reconstructed Λ) for primary Λs. The corollary is done for anti-particles (that is efficiency is quoted with respect to the $\overline{\Lambda}$). All such efficiencies were calculated with STAR production HIJING events at 19GeV. It is assumed that it should not

vary significantly for different values of $\sqrt{s_{\mathrm{NN}}}$. These final efficiencies can then be multiplied by the yields of Ξ^- per Λ that we have for the UrQMD and THERMUS.

Particle	relative efficiency
Ξ^-	1.12728
Ξ^0	1.01695
Ω^0	0.97769
$\overline{\Xi}^+$	1.09458
$\overline{\Xi}^0$	1.00359
$\overline{\Omega^0}$	1.00907

Table 7.3: Relative efficiency [(# Multi-strange particle passing cuts)/(# Multi-strange particle simulated)]/[(# primary Lambda passing cuts)/(# primary Lambda simulated)]

These numbers are all close enough to 1 for us to feel comfortable ignoring such an effect.

7.2.2 Which particles are included?

As can be seen in fig. 7.5 only about 15% of the Lambdas come from the "other" category, which represents a tremendous number of particles. These include things like $\Lambda(1405)$ and $\Lambda(1530)$ and the Ω. In fact, the higher mass Lambdas that I mention each contribute about 1% of the yield. Others contribute less.

This 15% we will consider as unpolarized. If there were no magnetic field, but only vorticity-induced polarization, we [2] have checked that the alternating signs of the spin transfer coefficients C effectively make all their contributions cancel each other out; so, our assumption of (effective) zero polarization is justified. To definitively say what would happen if there *is* a magnetic field, we would have to know the magnetic moments of these contributors, and they are not measured. It is very reasonable to assume, however, that, as in the vortical case, they would effectively cancel each other out. In any event, these "other" parents are assumed to be a zero-polarization component to the measured Λs. Hence, they suppress the signal by "diluting" it by $\sim 15\%$.

The relevant values of $f_{\Lambda R}$, $f_{\overline{\Lambda R}}$, $f_{\Sigma^0 R}$, and $f_{\overline{\Sigma}^0 \overline{R}}$, using the THERMUS yields, are given in table 7.4.

7.3 Feed-down matrix elements

Now that we have the full yield ratios as discussed in sec. 7.1 they can be listed in tab. 7.4.

f	7.7 GeV	11.5 GeV	14.5 GeV	19.6 GeV	27 GeV	39 GeV	62.4 GeV	200 GeV
$f_{\Lambda'}$	2.800e-01	2.492e-01	2.418e-01	2.350e-01	2.313e-01	2.273e-01	2.239e-01	2.183e-01
$f_{\Lambda\Sigma^0}$	1.806e-01	1.666e-01	1.627e-01	1.591e-01	1.569e-01	1.547e-01	1.524e-01	1.493e-01
$f_{\Lambda\Sigma^{*+}}$	1.044e-01	1.052e-01	1.045e-01	1.037e-01	1.027e-01	1.022e-01	1.007e-01	9.984e-02
$f_{\Lambda\Sigma^{*0}}$	1.039e-01	1.047e-01	1.040e-01	1.032e-01	1.023e-01	1.017e-01	1.002e-01	9.938e-02
$f_{\Lambda\Sigma^{*-}}$	1.018e-01	1.028e-01	1.020e-01	1.013e-01	1.004e-01	9.987e-02	9.840e-02	9.763e-02
$f_{\Lambda\Xi^0}$	4.056e-02	4.992e-02	5.438e-02	5.842e-02	6.208e-02	6.464e-02	6.970e-02	7.308e-02
$f_{\Lambda\Xi^-}$	3.906e-02	4.822e-02	5.256e-02	5.649e-02	6.004e-02	6.254e-02	6.743e-02	7.073e-02
$f_{\Sigma^0\Sigma^{*+}}$	8.402e-03	8.466e-03	8.405e-03	8.343e-03	8.267e-03	8.220e-03	8.099e-03	8.033e-03
$f_{\Sigma^0\Sigma^{*0}}$	1.194e-03	1.204e-03	1.195e-03	1.186e-03	1.175e-03	1.169e-03	1.152e-03	1.142e-03
$f_{\Sigma^0\Sigma^{*-}}$	8.188e-03	8.268e-03	8.211e-03	8.154e-03	8.080e-03	8.036e-03	7.917e-03	7.855e-03
$f_{\Lambda,\text{other}}$	1.319e-01	1.555e-01	1.602e-01	1.650e-01	1.667e-01	1.696e-01	1.701e-01	1.746e-01
$\overline{f}_{\overline{\Lambda}'}$	2.327e-01	2.192e-01	2.162e-01	2.143e-01	2.153e-01	2.144e-01	2.175e-01	2.159e-01
$\overline{f}_{\overline{\Lambda}\overline{\Sigma}^0}$	1.502e-01	1.465e-01	1.455e-01	1.451e-01	1.461e-01	1.459e-01	1.480e-01	1.477e-01
$\overline{f}_{\overline{\Lambda}\overline{\Sigma}^{*-}}$	8.681e-02	9.254e-02	9.341e-02	9.454e-02	9.567e-02	9.638e-02	9.774e-02	9.871e-02
$\overline{f}_{\overline{\Lambda}\overline{\Sigma}^{*0}}$	8.636e-02	9.210e-02	9.297e-02	9.409e-02	9.522e-02	9.593e-02	9.729e-02	9.826e-02
$\overline{f}_{\overline{\Lambda}\overline{\Sigma}^{*+}}$	8.461e-02	9.037e-02	9.126e-02	9.239e-02	9.350e-02	9.421e-02	9.555e-02	9.652e-02
$\overline{f}_{\overline{\Lambda}\overline{\Xi}^0}$	1.071e-01	9.659e-02	9.200e-02	8.909e-02	8.565e-02	8.373e-02	7.931e-02	7.675e-02
$\overline{f}_{\overline{\Lambda}\overline{\Xi}^+}$	1.031e-01	9.329e-02	8.892e-02	8.614e-02	8.283e-02	8.100e-02	7.672e-02	7.428e-02
$\overline{f}_{\overline{\Sigma}^0\overline{\Sigma}^{*-}}$	6.985e-03	7.446e-03	7.516e-03	7.606e-03	7.697e-03	7.754e-03	7.864e-03	7.942e-03
$\overline{f}_{\overline{\Sigma}^0\overline{\Sigma}^{*0}}$	9.926e-04	1.059e-03	1.069e-03	1.082e-03	1.094e-03	1.103e-03	1.118e-03	1.129e-03
$\overline{f}_{\overline{\Sigma}^0\overline{\Sigma}^{*+}}$	6.807e-03	7.271e-03	7.343e-03	7.433e-03	7.523e-03	7.580e-03	7.688e-03	7.766e-03
$\overline{f}_{\overline{\Lambda},\text{other}}$	1.344e-01	1.536e-01	1.637e-01	1.683e-01	1.694e-01	1.719e-01	1.713e-01	1.751e-01

Table 7.4: f's from THERMUS.

The numbers in tab. 7.4 may be plugged into eq. 7.9, to get the matrix elements listed in table 7.5. To be very clear, these are the matrix elements of the *inverted* matrix. In other words, to get the physical quantities of interest, use equation 7.11, below, with the values of a, b, c, d from table 7.5.

$$\begin{pmatrix} \varpi_c \\ B_c/T \end{pmatrix} = \begin{bmatrix} a & b \\ c & d \end{bmatrix} \begin{pmatrix} P_\Lambda^{\text{meas}} \\ P_{\overline{\Lambda}}^{\text{meas}} \end{pmatrix}. \tag{7.11}$$

f	7.7 GeV	11.5 GeV	14.5 GeV	19.6 GeV	27 GeV	39 GeV	62.4 GeV	200 GeV
a	1.4601	1.4260	1.4038	1.3856	1.3635	1.3512	1.3195	1.3029
b	1.0462	1.0930	1.1274	1.1513	1.1752	1.1913	1.2230	1.2456
c	-1.7853	-1.9134	-1.9357	-1.9539	-1.9616	-1.9722	-1.9709	-1.9877
d	1.7928	1.9162	1.9503	1.9676	1.9726	1.9817	1.9757	1.9898

Table 7.5: The matrix elements of the INVERTED matrix. Multiply this by the polarization "vector" as per equation 7.11.

7.4 Application to STAR data

The STAR measurements on hyperon polarization are listed in table 7.6. Applying equation 7.11 with the matrix elements listed in table 7.5 yields the physical parameters, listed in table 7.7.

In table 7.8 are listed the physical parameters *if feed-down is neglected*. This is obviously for comparison only. In this case, $f_{\Lambda'} = \overline{f}_{\overline{\Lambda}'} = 1$ and all other fs are zero, so that for every energy, the matrix is

$$\begin{bmatrix} a & b \\ c & d \end{bmatrix}_{\text{no feed-down}} = \begin{bmatrix} 0.5 & -0.613 \\ 0.5 & 0.613 \end{bmatrix}^{-1} = \begin{bmatrix} 1 & 1 \\ -0.8157 & +0.8157 \end{bmatrix} \tag{7.12}$$

Comparing tables 7.7 and 7.8 shows that accounting for feed-down increases ϖ by $\sim 20\%$, and increases B by a factor of 2.

About units As is common, we have been using units such that $\hbar = c = k_B = 1$. Furthermore, we've used $\mu_N = 1$. In this case, $\varpi_c = \omega_c/T$ and B/T are both dimensionless. That's why they are quantified in percentages in the second and third columns of tables 7.7 and 7.8.

In human units, vorticity is measured in s^{-1} (usually not written as Hz) and B in Tesla. In order to get to these units, we will need to assume a temperature. Here, we will assume $k_B T = 160$ MeV.

The conversions are

$$\omega\ [\text{in s}^{-1}] = (k_B T) \cdot \left(\frac{\omega}{T}\ [\text{dimensionless}] \right) / \hbar \tag{7.13}$$

$$B\ [\text{in Tesla}] = (k_B T) \cdot \left(\frac{B}{T}\ [\text{dimensionless}] \right) / \mu_N \tag{7.14}$$

Explicitly, $\hbar = 6.58 \times 10^{-22}$ MeV $\cdot$ s and $\mu_N = 3.15 \times 10^{-14}$ MeV/Tesla.

(To make the connection to equation 7.9, the $\frac{2}{3}$ in front of everything is basically $1/(S_\Lambda + 1)$. The units

of this cancel with the (S_R+1) factor found inside of every sum. That leaves S_R in the left columns; this is the spin of particle R. In our matrix, we have been using, e.g. $S_{\Sigma^*} = \frac{3}{2}$, when in reality it is $S_{\Sigma^*} = \frac{3}{2}\hbar$. Likewise, in our matrix, we have been using, e.g. $\mu_{\Sigma^{*+}} = +3.02$, when in reality it is $\mu_{\Sigma^{*+}} = +3.02\mu_N$.)

$\sqrt{s_{NN}}$ (GeV)	$\overline{P}_\Lambda$ (%)	$\overline{P}_{\overline{\Lambda}}$ (%)
7.7	2.27 +/- 0.63	7.56 +/- 3.61
11.5	1.38 +/- 0.40	2.63 +/- 1.27
14.5	1.17 +/- 0.49	1.42 +/- 1.31
19.6	0.96 +/- 0.31	1.45 +/- 0.61
27.0	1.03 +/- 0.28	1.41 +/- 0.47
39.0	0.49 +/- 0.42	1.06 +/- 0.61
62.4	1.25 +/- 1.09	1.60 +/- 1.49
200.0	0.12 +/- 0.95	-0.73 +/- 1.08

Table 7.6: STAR measurements on polarization for 20-50% centrality Au+Au collisions.

$\sqrt{s_{NN}}$ (GeV)	ϖ_c (%)	B/T (%)	ω (s^{-1})	B (Tesla)
7.7	11.23 +/- 3.89	9.49 +/- 6.58	2.7e+22 +/- 9.5e+21	4.8e+14 +/- 3.3e+14
11.5	4.85 +/- 1.50	2.40 +/- 2.55	1.2e+22 +/- 3.7e+21	1.2e+14 +/- 1.3e+14
14.5	3.24 +/- 1.63	0.51 +/- 2.73	7.9e+21 +/- 4.0e+21	2.6e+13 +/- 1.4e+14
19.6	2.99 +/- 0.82	0.98 +/- 1.34	7.3e+21 +/- 2.0e+21	5.0e+13 +/- 6.8e+13
27.0	3.06 +/- 0.68	0.76 +/- 1.09	7.5e+21 +/- 1.6e+21	3.8e+13 +/- 5.5e+13
39.0	1.93 +/- 0.93	1.13 +/- 1.48	4.7e+21 +/- 2.3e+21	5.8e+13 +/- 7.5e+13
62.4	3.60 +/- 2.32	0.70 +/- 3.64	8.8e+21 +/- 5.6e+21	3.6e+13 +/- 1.8e+14
200.0	-0.75 +/- 1.83	-1.68 +/- 2.86	-1.8e+21 +/- 4.4e+21	-8.5e+13 +/- 1.5e+14

Table 7.7: The vorticities and magnetic fields extracted from STAR polarization data, using equation 7.11 and the matrix elements from table 7.5.

The figures for this data in various units are also included.

The vorticity is relatively insensitive to the particle yield. The scale of the magnetic field is quite sensitive to the yield of Σ^* baryons due to their very large magnetic moments. This mostly affects the scale of the measurement and does not change the sign or otherwise have much effect on the relative number of standard deviations from 0.

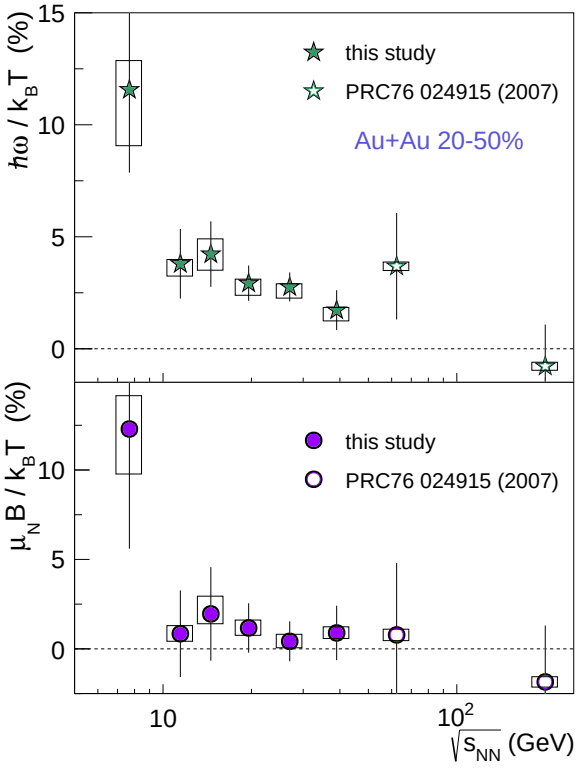

Figure 7.6: Measured vorticity and B field in % corrected for feed-down. μ_N is the nuclear magneton. There is a clear vortical signal, but only a hint of a magnetic field as anticipated.

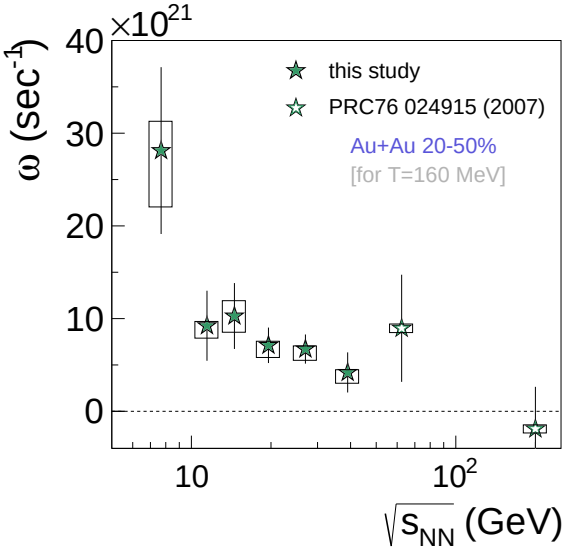

Figure 7.7: Measured vorticity in units of s^{-1}. The temperature is taken to be 160MeV. The temperature is merely a scaling of the data so it is trivial to change it. It does not effect the significance of the datapoints.

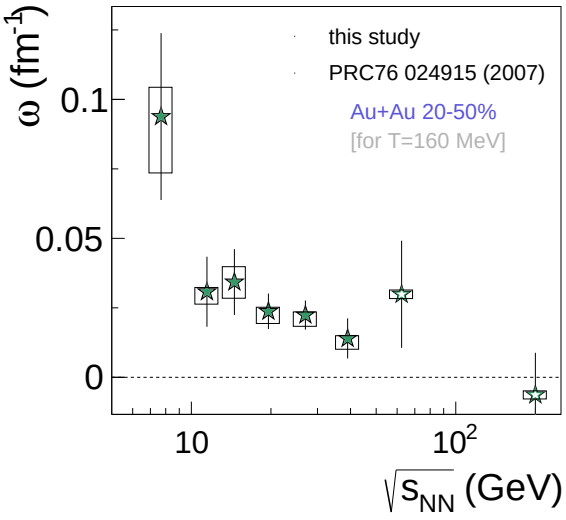

Figure 7.8: Measured vorticity in units of fm^{-1}. The temperature is taken to be 160MeV. The temperature is merely a scaling of the data so it is trivial to change it. It does not effect the significance of the datapoints.

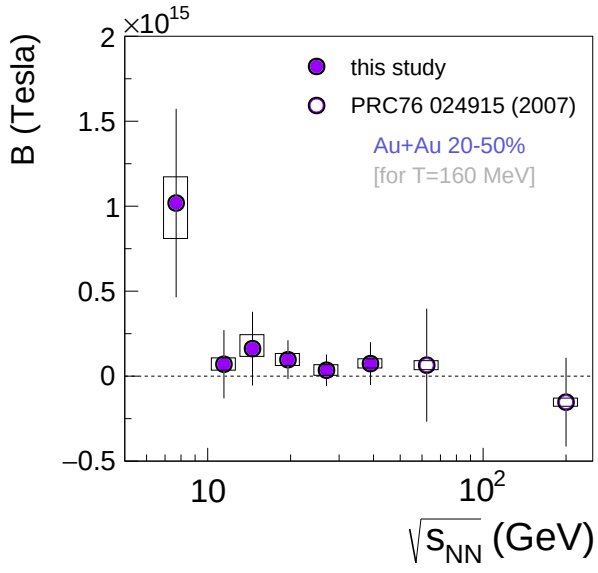

Figure 7.9: Measured magnetic field in units of Tesla. The temperature is taken to be 160MeV. The temperature is merely a scaling of the data so it is trivial to change it. It does not effect the significance of the datapoints.

$\sqrt{s_{NN}}$ (GeV)	ϖ_c (%)	B/T (%)	ω (s^{-1})	B (Tesla)
7.7	9.83 +/- 3.67	4.31 +/- 2.99	2.4e+22 +/- 8.9e+21	2.2e+14 +/- 1.5e+14
11.5	4.02 +/- 1.33	1.02 +/- 1.09	9.8e+21 +/- 3.2e+21	5.2e+13 +/- 5.5e+13
14.5	2.58 +/- 1.40	0.21 +/- 1.14	6.3e+21 +/- 3.4e+21	1.0e+13 +/- 5.8e+13
19.6	2.40 +/- 0.68	0.40 +/- 0.56	5.8e+21 +/- 1.7e+21	2.0e+13 +/- 2.8e+13
27.0	2.44 +/- 0.55	0.31 +/- 0.45	5.9e+21 +/- 1.3e+21	1.6e+13 +/- 2.3e+13
39.0	1.55 +/- 0.75	0.46 +/- 0.61	3.8e+21 +/- 1.8e+21	2.4e+13 +/- 3.1e+13
62.4	2.85 +/- 1.84	0.29 +/- 1.50	6.9e+21 +/- 4.5e+21	1.5e+13 +/- 7.6e+13
200.0	-0.61 +/- 1.44	-0.69 +/- 1.17	-1.5e+21 +/- 3.5e+21	-3.5e+13 +/- 6.0e+13

Table 7.8: The vorticities and magnetic fields extracted from STAR polarization data, using equation 7.11 but a matrix that ignores feed-down, i.e. $f_{\Lambda'} = \overline{f}_{\overline{\Lambda}'} = 1$ and all other fs are zero. The matrix used is given in equation 7.12. See text for details.

7.5 Vorticity and magnetic field: theory comparison

Several theory comparisons where made to the polarization data in sec. 2. Since the polarization signal seems to come entirely from the vorticity of system, it should be no surprise that the vorticity matches model results quite well. Many theory models tend to have polarization on the scale of a few hundredths of a fm^{-1}. Two such results from models are shown in fig. 7.10 and fig. 7.11.

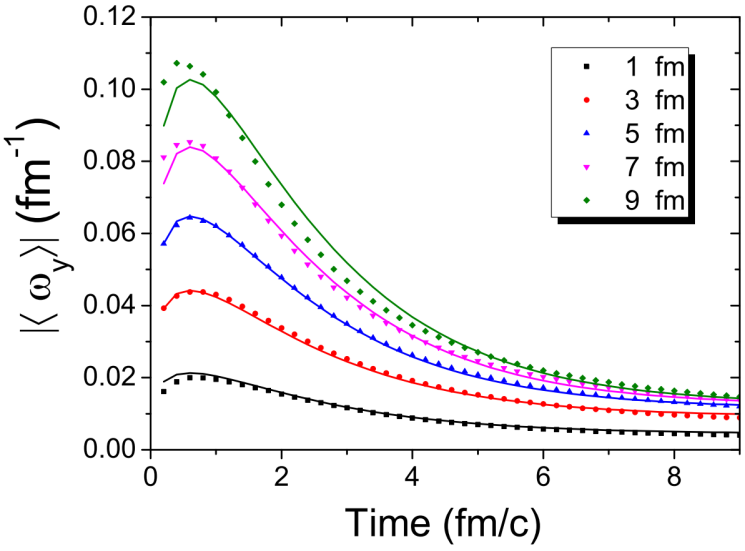

Figure 7.10: Vorticity in an AMPT calculation for different impact parameters as a function of time [39]. The scale of a few hundredths of a fm^{-1} matches the data quite well.

TABLE I. Time dependence of average vorticity projected to the reaction plane for heavy-ion reactions at the NICA energy of $\sqrt{s_{NN}} = 4.65 + 4.65$ GeV.

t (fm/c)	Vorticity (classical) (c/fm)	Thermal vorticity (relativistic) (1)
0.17	0.1345	0.0847
1.02	0.1238	0.0975
1.86	0.1079	0.0846
2.71	0.0924	0.0886
3.56	0.0773	0.0739

Figure 7.11: Vorticity in a PICR hydrodynamic calculation at NICA energies [25]. We get a similar scale of vorticity in our analysis.

None of the models references in sec. 2 involve any sort of magnetic field calculation. There are magnetohydrodynamic efforts underway in the field, but these do not included calculations of hyperon polarization. The magnetic field itself is pretty poorly constrained at present. Any understanding that does exist is entirely theoretical as there is no direct measurement possible. A subtlety which has been glossed over is that it isn't at all obvious what magnetic field could primarily effect a polarization. The Lambdas themselves are emitted quite late in the collision and the magnetic field is expected to be short lived. Perhaps a measurement of the magnetic field through polarization would be some late-time averaged magnetic field, or perhaps the polarization occurs on the constituent quark level while they're still part of the QGP. Since the QGP itself is charged it is expected to have a finite conductivity and thus display a Lenz's law interaction which would work to slow the decay of the magnetic field over time. This might have a significant effect on the magnetic field as a feasible measure in to polarization observables. A calculation including a conductivity from a lattice QCD calculation is shown in fig. 7.12.

In fig. 7.12 the field is given in terms of the pion mass, which is a typical (though initially confusing) way of quoting field strength. A field of 10^{14}Tesla (which is more or less the scale seen in the data in fig. 7.9) would be $\sim 1 m_\pi^2$. Since the calculation in fig. 7.12 is done at 200GeV one would expect the magnetic field to peak at a lower value in the BES, however the medium is be more charged, due to baryon stopping, in the BES which could increase the conductivity. At any rate the data is far too uncertain to reach any clear conclusions. At this point we will have to be satisfied with noting that the *sign* of the datapoints in fig. 7.9 is as expected and the scale is a little on the high side, but on a nearly correct scale.

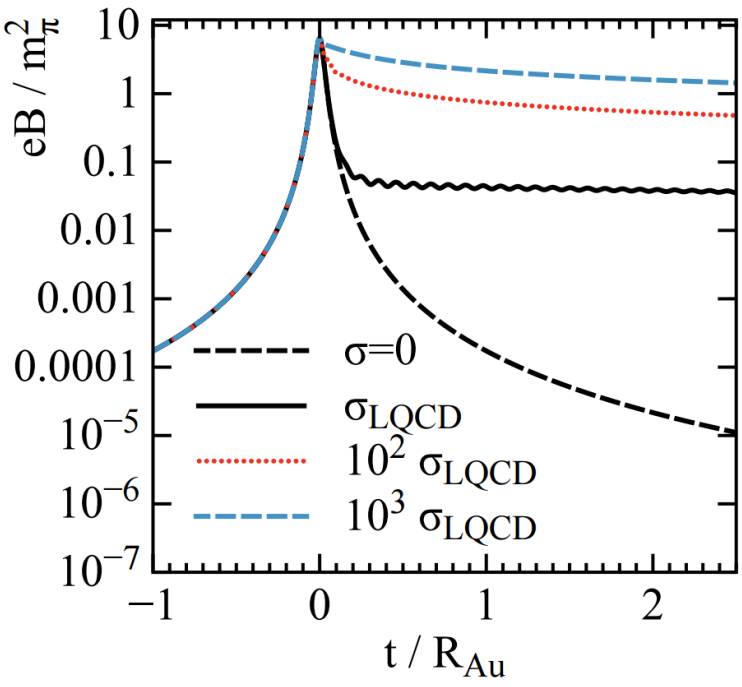

Figure 7.12: A calcualtion of magnetic field over time and how it is modified by the conductivity of the QGP at top RHIC energy [51]. The conductivity is taken from a lattice QCD calculation and slows the decay of the field. Also dislayed are arbitrary multiples of the conductivity.

7.6 Chiral effects

Aside from being of fundamental interest the values of the vorticity and magnetic field are of great relevance to chiral measurements. It isn't my intention to go into detail on the quite complicated subjects of the Chiral Magnetic Effect (CME) or the Chiral Vortical Effect (CVE), since these are beyond the work of this thesis. I simply want to provide a glimpse into the context in which this measurement has been made. Interested readers looking for a review article may wish to read [52].

The Lagrangian of the strong nuclear force does not explicitly break CP (that is, charge and parity) symmetry, but no violations are known to exist. This lack of known violations is quite famous and is regularly referred to as the "strong CP problem". Since the strong force doesn't conserve chirality it is possible for any QGP to have large fluctuations in chirality. The size of these fluctuations, which is related to the Chern-Simons number, has almost no theoretical or experimental constraint at present. Such a fluctuation into net-chirality is known as the chiral anomaly. Furthermore, as mentioned earlier in this section, heavy-

ion collisions are both highly vorticus and are acted on by a strong magnetic field.

In the presence of a magnetic field quark spins align or anti-align (depending on their charge) with the field due to their intrinsic magnetic moment. If a chirality imbalance is also in place the magnetic field will induce an electric charge current, $\vec{J}_e$, along the direction it points. Reminiscent of a conductivity this constant of the linear relation between the magnetic field and the induced current is the "chiral magnetic conductivity", σ_5. The relation is

$$\begin{aligned} \vec{J}_e &= \sigma_5 \vec{B} \\ &= \frac{Q\mu_5}{2\pi^2}\vec{B} \end{aligned} \tag{7.15}$$

where σ_5 has been expanded in the second term in terms of the charge, Q, and the axial chemical potential, μ_5. μ_5 is proportional to the difference of the number of right-handed and left-handed quarks. The effect is called the CME. A schematic is shown in fig. 7.13.

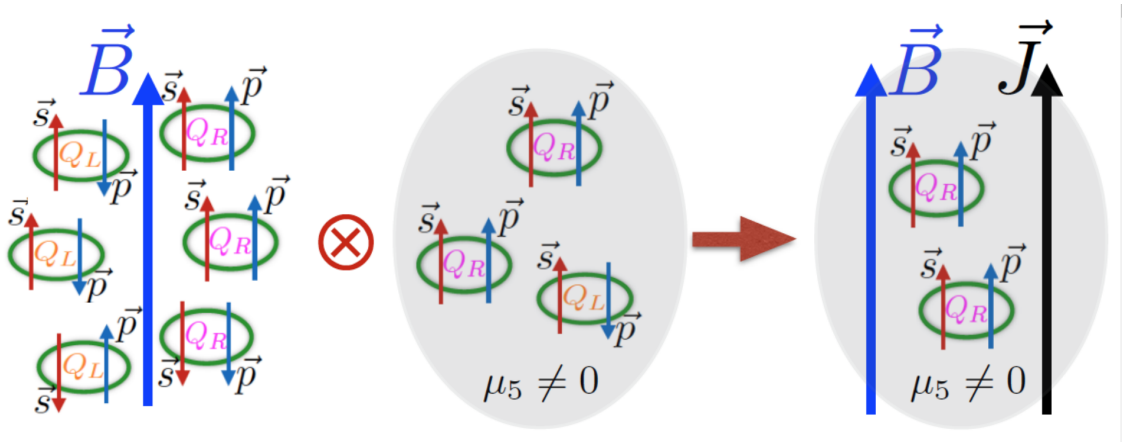

Figure 7.13: This illustration of the CME [52] is for a single type of massless, positively-charged quark in an event with $\mu_5 > 0$. The left panel demonstrates a magnetic field with $\mu_5 = 0$, the middle panel depicts $\mu_5 > 0$ and $\vec{B} = 0$, and the right panel depicts $\mu_5 > 0$ and $\vec{B} \neq 0$. Including a negative anti-particle would create negative particles moving downwards, which would contribute equally to the electric current.

The CVE is completely analogous, except it is typically measured via net baryon number coupling to

vorticity.

$$\vec{J}_v = \frac{\mu_5 \mu_B}{\pi^2} \vec{\omega} \tag{7.16}$$

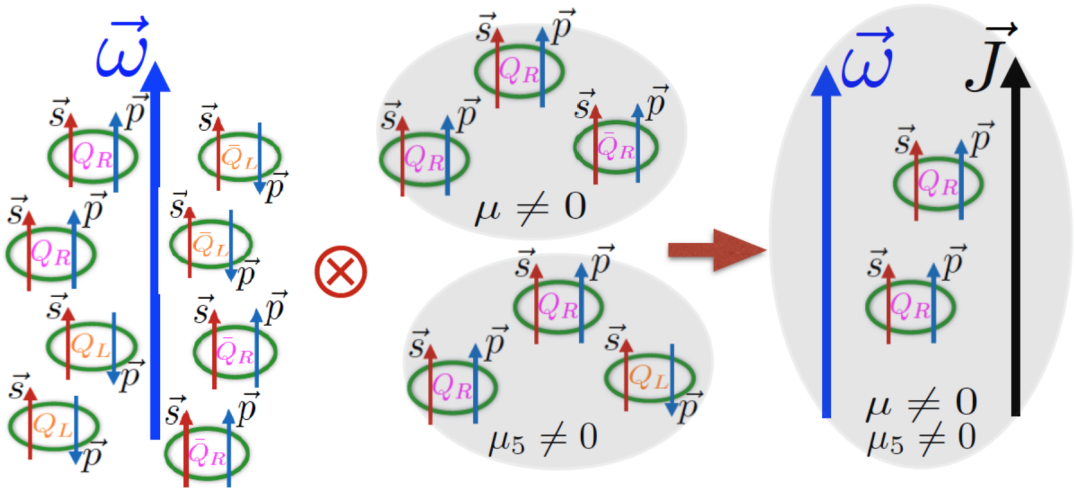

Figure 7.14: This illustration of the CVE [52] is for a set of massless quark/anti-quark pair in an event with both $\mu_5 \neq 0$ and $\mu_B \neq 0$ with $\vec{\omega} \neq 0$. The left panel demonstrates a vorticity with $\mu_5 = 0$, the middle panel depicts $\mu_5 \neq 0$, $\mu_B \neq 0$, and $\vec{\omega} = 0$, and the right panel depicts $\mu_5 > 0$, $\mu_B \neq 0$, and $\vec{\omega} = 0$.

Both the CME and CVE are difficult measurements to make, primarily because the signal is small and the background is large and difficult to constrain. The description of both phenomena also necessarily includes a μ_5 term which is very poorly constrained theoretically. To put both types of measurement on firm ground it's important to have a sense of the size of effect. Lambda polarization offers, in principal, a unique way of getting at both the vorticity and the magnetic field which are also central to these measurements.

Chapter 8
CONCLUSION

This thesis concerns a Lambda global polarization measurement made by STAR in the BES [1]. This measurement represents the first non-trivial measurement of this kind. The polarization is proportional to the gradients of the velocity fields heavy-ion collisions. An entirely new measurement provides an additional lever arm with which to test and refine models. The polarization has been shown to be directly relatable to the vorticity in the fluid and the magnetic field caused by the spectators, both of which are fundamental features of a collision. The results indicate a positive vorticity and hint at the effects of a magnetic field. These observables are both necessary for various chiral measurements and an understanding of them would be tremendously important to add context to chiral phenomena.

The results have *not* been corrected for Lambda detection efficiency which will be important to do for future results. Currently analyzers across STAR, ALICE, and HADES are working on this and similar measurements in different systems and for different types of hyperons. RHIC plans on a second beam energy scan which will take considerably more data at the same values of $\sqrt{s_{\rm NN}}$. At the same time STAR will implement a number of upgrades to the detector. The reduction of errors in BES-II will be considerable and allow for further systematic studies of the polarization as it depends on Centrality, rapidity, p_T, and ϕ_Λ, all of which are currently not possible due to large statistical errors. Furthermore it may be possible to detect a magnetic field with the reduced error bars, which would be of tremendous interest. STAR also installed a gold foil inside the beam pipe (but not covering the path of the ions) at z =211cm. Collisions of the beam on the fixed target make low energy collisions, beyond the range feasible at a collider. These energies may also be analyzed. It would certainly be interesting to see if the apparent increasing trend of the polarization with decreasing $\sqrt{s_{\rm NN}}$ continues into very low energies.

Appendix A
RELATED STUDIES

A.1 Previous STAR result

Part of this document is quoting the 2007 global polarization results from STAR [44]. The first thing to make clear is that there is a sign error in the 2007 analysis due to a mistake about the angular momentum direction, so quoted results are going to be off by a sign, though this was fixed in a recent erratum. To compare we need results integrated over p_T in 20-50% centrality. We got these numbers from the 2010 rows of https://drupal.star.bnl.gov/STAR/files/starpublications/79/data.html. To properly weight the centrality bins we assume that the number of Λs ($\overline{\Lambda}$s) in one bin centrality relative to another is the same as the ratio is for charged particles (RefMult). We get the refmult from "Centrality_def_refmult.txt" from StRefMultCorr averaging the two 5% centrality bins in the table.

Centrality	62.4GeV	200GeV
20-30%	167	226.5
30-40%	111.5	151.5
40-50%	71	96

Table A.1: StRefMultCorr averaged tables for 62.4GeV and 200GeV

Centrality	P_H	error	RefMult$\cdot P_H$	$(\text{RefMult}\cdot\text{error})^2$
20-30%	-0.0001	0.0174	-0.0167	8.44367364
30-40%	0.044	0.02	4.906	4.9729
40-50%	-0.0032	0.0253	-0.2272	3.22669369

Table A.2: 62.4GeV Λ results from 2007 paper

A.2 BBC gain correction

This is complicated by tile pairs 7&9 and 13&15. In the discussion most channels will be indexed with an i while the shared channels are indexed a j and $ADC_j \equiv 1/2(\text{measured ADC of tile } j)$. For a given "ring" of tiles all tiles have to have the same average corrected ADC. This is surprisingly tricky, so it's good to be careful with the difference between tile (of which there are 18) and ADC channels or PMT (of which there

Centrality	P_H	error	RefMult$\cdot P_H$	$(\text{RefMult}\cdot\text{error})^2$
20-30%	0.0096	0.024	1.6032	16.064064
30-40%	0.0282	0.027	3.1443	9.06311025
40-50%	0.0174	0.034	1.2354	5.827396

Table A.3: 62.4GeV $\overline{\Lambda}$ results from 2007 paper

Centrality	P_H	error	RefMult $\cdot P_H$	(RefMult $\cdot$ error)^2
20-30%	0.000177	0.015	0.0400905	11.54300625
30-40%	-0.016	0.0178	-2.424	7.27219089
40-50%	0.031	0.0221	2.976	4.50118656

Table A.4: 200GeV Λ results from 2007 paper

Centrality	P_H	error	RefMult $\cdot P_H$	(RefMult $\cdot$ error)^2
20-30%	-0.00795	0.017	-1.800675	14.82635025
30-40%	-0.011	0.02	-1.6665	9.1809
40-50%	-0.0022	0.025	-0.2112	5.76

Table A.5: 200GeV $\overline{\Lambda}$ results from 2007 paper

are 16). Thus $Q_{1,x}$ is (of course $Q_{1,y}$ is the same with a sin instead of a cos)

$$\begin{aligned}
Q_{1,x} &= \frac{1}{N_{\text{(tile)}}} \sum_{k\text{(tile)}}^{N_{\text{(tile)}}} \frac{\text{ADC}_{k\text{(tile)}}}{\langle \text{ADC}_{k\text{(tile)}} \rangle} \cos\phi_{k\text{(tile)}} \\
&= \frac{1}{N_{i\text{(tile)}} + N_{j\text{(tile)}}} \left[\sum_{i\text{(tile)}} \frac{\text{ADC(tile)}_{i\text{(tile)}}}{\langle \text{ADC(tile)}_{i\text{(tile)}} \rangle} \cos\phi_{i\text{(tile)}} + \sum_{j\text{(tile)}} \frac{\text{ADC(tile)}_{j\text{(tile)}}}{\langle \text{ADC(tile)}_{j\text{(tile)}} \rangle} \cos\phi_{j\text{(tile)}} \right] \\
&= \frac{1}{N_{i\text{(tile)}} + N_{j\text{(tile)}}} \left[\sum_{i\text{(PMT)}} \frac{\text{ADC(PMT)}_{i\text{(PMT)}}}{\langle \text{ADC(PMT)}_{i\text{(PMT)}} \rangle} \cos\phi_{i\text{(PMT)}} + 2 \sum_{j\text{(PMT)}} \frac{\frac{1}{2}\text{ADC(PMT)}_{j\text{(PMT)}}}{\langle \frac{1}{2}\text{ADC(PMT)}_{j\text{(PMT)}} \rangle} \cos\phi_{j\text{(PMT)}} \right] \\
&= \frac{1}{N_{i\text{(PMT)}} + 2N_{j\text{(PMT)}}} \left[\sum_{i\text{(PMT)}} \frac{\text{ADC(PMT)}_{i\text{(PMT)}}}{\langle \text{ADC(PMT)}_{i\text{(PMT)}} \rangle} \cos\phi_{i\text{(tile)}} + 2 \sum_{j\text{(PMT)}} \frac{\text{ADC(PMT)}_{j\text{(PMT)}}}{\langle \text{ADC(PMT)}_{j\text{(PMT)}} \rangle} \cos\bar{\phi}_{j\text{(tile)}} \right]
\end{aligned} \tag{A.1}$$

Type	P_H	error
62.4GeV Λ	0.0133393419	0.0116727212
62.4GeV $\overline{\Lambda}$	0.0171184549	0.015918979
200GeV Λ	0.0012491361	0.0101871395
200GeV $\overline{\Lambda}$	-0.0077602848	0.0115104159

Table A.6: 2007 final 20-50% centrality results tabulated from tables A.2-A.5

A.3 Lambda decay parameter

The decay parameter, α, was first proposed by T.D. Lee and C.N. Yang in 1957 [53] and measured for the Λ in 1963 by J. Cronin and O. Overseth [54]. There is some confusion early on about what a positive decay parameter means, see this more modern paper which has a clear explanation [55]. $\alpha_\Lambda \neq \alpha_{\overline{\Lambda}}$ would imply a breaking of CP symmetry. There is considerable interest in knowing these parameters well. It has been assumed in this analysis that no such difference exists which I think is a reasonable null hypothesis.

A.4 Production plane polarization

In a collision of two point-like particles a created Lambda can pick up a polarization perpendicular to the plane spanned by the Lambda's momentum and the incoming particles momentum. Such a plane is called the production plane and is the way α_Λ and $\alpha_{\overline{\Lambda}}$ are measured in [55]. The same effect has been seen in p+p collisions [56] for Λs, but, curiously, not for $\overline{\Lambda}$s. This effect is odd in η and ϕ. The production plane in unknowable in a heavy-ion collision and many of the Λs are expected to be created thermally, rather than in hard scatterings. Furthermore since the effect is odd it is expected to cancel out in our symmetric detector. There is a small caveat here, which is that if the production plane is statistically aligned with the impact parameter *and* the event has finite v_1 it would be possible for this to have some effect on global polarization, since the v_1 itself is odd in η and ϕ. We expect this to be negligible, particularly as our detector does not extend greatly in η.

A.5 Event plane decorrelation

As mentioned in sec. 3.2 the resolution we calculation did not take into account decorrelation with rapidity. At forward rapidities event planes begin to decorrelate from mid-rapidity event planes. We have no estimate for this for the first order event plane and have thus made no provision for it. It is not obvious what effect this has on the resolution since the subevents are very separated and even in rapidity. One would expect the decorrelation between the midrapidity particles and the forward event plane to be half that of one subevent to another.

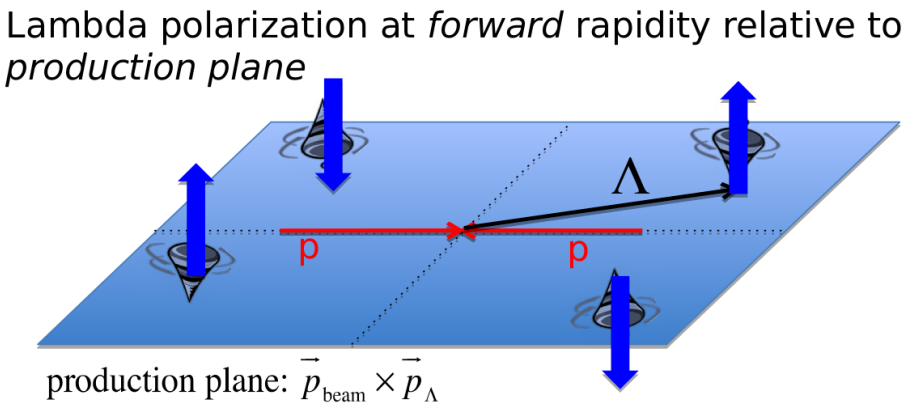

Figure A.1: Polarization perpendicular from the production plane in p+p collisions is shown as a schematic. Λs are depicted as blue tops. The large blue arrows demonstrate the qualitative polarization direction depending on which quadrant of the $\eta - \phi$ space the Λ is emitted in.

BIBLIOGRAPHY

[1] L. Adamczyk *et al.*, "Global Λ hyperon polarization in nuclear collisions: evidence for the most vortical fluid," *Nature*, vol. 548, pp. 62–65, 2017.

[2] F. Becattini, I. Karpenko, M. Lisa, I. Upsal, and S. Voloshin, "Global hyperon polarization at local thermodynamic equilibrium with vorticity, magnetic field and feed-down," *Phys. Rev.*, vol. C95, no. 5, p. 054902, 2017.

[3] R. Hagedorn, "Statistical thermodynamics of strong interactions at high-energies," *Nuovo Cim. Suppl.*, vol. 3, pp. 147–186, 1965.

[4] J. Rafelski and T. Ericson, "The tale of the Hagedorn temperature," *CERN Cour.*, vol. 43N7, pp. 30–33, 2003. [Reprint: ,41(2016)].

[5] P. Sorensen, "Highlights from Heavy Ion Collisions at RHIC and the Acoustics of the Little Bangs," 2012.

[6] W. Broniowski, W. Florkowski, and L. Ya. Glozman, "Update of the Hagedorn mass spectrum," *Phys. Rev.*, vol. D70, p. 117503, 2004.

[7] M. Cheng *et al.*, "The QCD equation of state with almost physical quark masses," *Phys. Rev.*, vol. D77, p. 014511, 2008.

[8] Y. Akiba *et al.*, "The Hot QCD White Paper: Exploring the Phases of QCD at RHIC and the LHC," 2015.

[9] T. M. Schwarz, S. P. Klevansky, and G. Papp, "The Phase diagram and bulk thermodynamical quantities in the NJL model at finite temperature and density," *Phys. Rev.*, vol. C60, p. 055205, 1999.

[10] M. G. Alford, A. Schmitt, K. Rajagopal, and T. Schfer, "Color superconductivity in dense quark matter," *Rev. Mod. Phys.*, vol. 80, pp. 1455–1515, 2008.

[11] C. Shen and U. Heinz, "The road to precision: Extraction of the specific shear viscosity of the quark-gluon plasma," *Nucl. Phys. News*, vol. 25, no. 2, pp. 6–11, 2015.

[12] L. Adamczyk *et al.*, "Bulk Properties of the Medium Produced in Relativistic Heavy-Ion Collisions from the Beam Energy Scan Program," *Phys. Rev.*, vol. C96, no. 4, p. 044904, 2017.

[13] C. Gale, S. Jeon, B. Schenke, P. Tribedy, and R. Venugopalan, "Event-by-event anisotropic flow in heavy-ion collisions from combined Yang-Mills and viscous fluid dynamics," *Phys. Rev. Lett.*, vol. 110, no. 1, p. 012302, 2013.

[14] U. W. Heinz, "Towards the Little Bang Standard Model," *J. Phys. Conf. Ser.*, vol. 455, p. 012044, 2013.

[15] S. Pratt, E. Sangaline, P. Sorensen, and H. Wang, "Constraining the Eq. of State of Super-Hadronic Matter from Heavy-Ion Collisions," *Phys. Rev. Lett.*, vol. 114, p. 202301, 2015.

[16] J.-H. Gao, S.-W. Chen, W.-t. Deng, Z.-T. Liang, Q. Wang, and X.-N. Wang, "Global quark polarization in non-central A+A collisions," *Phys. Rev.*, vol. C77, p. 044902, 2008.

[17] Z.-T. Liang and X.-N. Wang, "Globally polarized quark-gluon plasma in non-central A+A collisions," *Phys. Rev. Lett.*, vol. 94, p. 102301, 2005. [Erratum: Phys. Rev. Lett.96,039901(2006)].

[18] S. A. Voloshin, "Polarized secondary particles in unpolarized high energy hadron-hadron collisions?," 2004.

[19] Z.-T. Liang and X.-N. Wang, "Spin alignment of vector mesons in non-central A+A collisions," *Phys. Lett.*, vol. B629, pp. 20–26, 2005.

[20] S. J. Barnett, "Magnetization by rotation," *Science*, vol. 42, no. 1074, pp. 163–164, 1915.

[21] S. J. Barnett, "Magnetization by rotation," *Phys. Rev.*, vol. 6, pp. 239–270, Oct 1915.

[22] Z.-t. Liang, "Global polarization of QGP in non-central heavy ion collisions at high energies," *J. Phys.*, vol. G34, pp. S323–330, 2007.

[23] F. Becattini, F. Piccinini, and J. Rizzo, "Angular momentum conservation in heavy ion collisions at very high energy," *Phys. Rev.*, vol. C77, p. 024906, 2008.

[24] F. Becattini, L. Csernai, and D. J. Wang, "Λ polarization in peripheral heavy ion collisions," *Phys. Rev.*, vol. C88, no. 3, p. 034905, 2013. [Erratum: Phys. Rev.C93,no.6,069901(2016)].

[25] L. P. Csernai, D. J. Wang, M. Bleicher, and H. Stcker, "Vorticity in peripheral collisions at the Facility for Antiproton and Ion Research and at the JINR Nuclotron-based Ion Collider fAcility," *Phys. Rev.*, vol. C90, no. 2, p. 021904, 2014.

[26] L. P. Csernai, F. Becattini, and D. J. Wang, "Turbulence, Vorticity and Lambda Polarization," *J. Phys. Conf. Ser.*, vol. 509, p. 012054, 2014.

[27] F. Becattini, G. Inghirami, V. Rolando, A. Beraudo, L. Del Zanna, A. De Pace, M. Nardi, G. Pagliara, and V. Chandra, "A study of vorticity formation in high energy nuclear collisions," *Eur. Phys. J.*, vol. C75, no. 9, p. 406, 2015.

[28] L.-G. Pang, H. Petersen, Q. Wang, and X.-N. Wang, "Vortical Fluid and Λ Spin Correlations in High-Energy Heavy-Ion Collisions," *Phys. Rev. Lett.*, vol. 117, no. 19, p. 192301, 2016.

[29] Y. L. Xie, M. Bleicher, H. Stcker, D. J. Wang, and L. P. Csernai, "Λ polarization in peripheral collisions at moderate relativistic energies," *Phys. Rev.*, vol. C94, no. 5, p. 054907, 2016.

[30] I. Karpenko and F. Becattini, "Study of Λ polarization in relativistic nuclear collisions at $\sqrt{s_{\rm NN}} = 7.7$ 200 GeV," *Eur. Phys. J.*, vol. C77, no. 4, p. 213, 2017.

[31] Y. Xie, D. Wang, and L. P. Csernai, "Global polarization in high energy collisions," *Phys. Rev.*, vol. C95, no. 3, p. 031901, 2017.

[32] Yu. B. Ivanov and A. A. Soldatov, "Vorticity in heavy-ion collisions at the JINR Nuclotron-based Ion Collider fAcility," *Phys. Rev.*, vol. C95, no. 5, p. 054915, 2017.

[33] I. Karpenko and F. Becattini, "Vorticity in the QGP liquid and polarization at the RHIC Beam Energy Scan," *Nucl. Phys.*, vol. A967, pp. 764–767, 2017.

[34] H. Li, H. Petersen, L.-G. Pang, Q. Wang, X.-L. Xia, and X.-N. Wang, "Local and global Λ polarization in a vortical fluid," *Nucl. Phys.*, vol. A967, pp. 772–775, 2017.

[35] F. Becattini and I. Karpenko, "Collective Longitudinal Polarization in Relativistic Heavy-Ion Collisions at Very High Energy," *Phys. Rev. Lett.*, vol. 120, no. 1, p. 012302, 2018.

[36] B. Betz, M. Gyulassy, and G. Torrieri, "Polarization probes of vorticity in heavy ion collisions," *Phys. Rev.*, vol. C76, p. 044901, 2007.

[37] F. Becattini and F. Piccinini, "The Ideal relativistic spinning gas: Polarization and spectra," *Annals Phys.*, vol. 323, pp. 2452–2473, 2008.

[38] F. Becattini, V. Chandra, L. Del Zanna, and E. Grossi, "Relativistic distribution function for particles with spin at local thermodynamical equilibrium," *Annals Phys.*, vol. 338, pp. 32–49, 2013.

[39] Y. Jiang, Z.-W. Lin, and J. Liao, "Rotating quark-gluon plasma in relativistic heavy ion collisions," *Phys. Rev.*, vol. C94, no. 4, p. 044910, 2016. [Erratum: Phys. Rev.C95,no.4,049904(2017)].

[40] H. Li, L.-G. Pang, Q. Wang, and X.-L. Xia, "Global Λ polarization in heavy-ion collisions from a transport model," *Phys. Rev.*, vol. C96, no. 5, p. 054908, 2017.

[41] Y. Sun and C. M. Ko, "Λ hyperon polarization in relativistic heavy ion collisions from a chiral kinetic approach," *Phys. Rev.*, vol. C96, no. 2, p. 024906, 2017.

[42] S. Shi, K. Li, and J. Liao, "Searching for the Subatomic Swirls in the CuCu and CuAu Collisions," 2017.

[43] C. Patrignani *et al.*, "Review of Particle Physics," *Chin. Phys.*, vol. C40, no. 10, p. 100001, 2016.

[44] B. I. Abelev *et al.*, "Global polarization measurement in Au+Au collisions," *Phys. Rev.*, vol. C76, p. 024915, 2007. [Erratum: Phys. Rev.C95,no.3,039906(2017)].

[45] L. Adamczyk *et al.*, "Beam-Energy Dependence of the Directed Flow of Protons, Antiprotons, and Pions in Au+Au Collisions," *Phys. Rev. Lett.*, vol. 112, no. 16, p. 162301, 2014.

[46] R.-h. Fang, L.-g. Pang, Q. Wang, and X.-n. Wang, "Polarization of massive fermions in a vortical fluid," *Phys. Rev.*, vol. C94, no. 2, p. 024904, 2016.

[47] K. Nakamura *et al.*, "Review of particle physics," *J. Phys.*, vol. G37, p. 075021, 2010.

[48] H. Dahiya and M. Gupta, "Octet and decuplet baryon magnetic moments in the chiral quark model," *Phys. Rev.*, vol. D67, p. 114015, 2003.

[49] S. Wheaton and J. Cleymans, "THERMUS: A Thermal model package for ROOT," *Comput. Phys. Commun.*, vol. 180, pp. 84–106, 2009.

[50] S. Das, *Identified Particle Production and Freeze-our Dynamics in Star at RHIC Beam Energy Scan Program*. PhD thesis, Institute of Physics. Bhubaneswar, Institute of Physics, Bhubaneswar - 751005, India, 10 2015. Available on the STAR drupal page https://drupal.star.bnl.gov/STAR/theses/phd/sabita-das.

[51] L. McLerran and V. Skokov, "Comments About the Electromagnetic Field in Heavy-Ion Collisions," *Nucl. Phys.*, vol. A929, pp. 184–190, 2014.

[52] D. E. Kharzeev, J. Liao, S. A. Voloshin, and G. Wang, "Chiral magnetic and vortical effects in high-energy nuclear collisionsA status report," *Prog. Part. Nucl. Phys.*, vol. 88, pp. 1–28, 2016.

[53] T. D. Lee and C.-N. Yang, "General Partial Wave Analysis of the Decay of a Hyperon of Spin 1/2," *Phys. Rev.*, vol. 108, pp. 1645–1647, 1957.

[54] J. W. Cronin and O. E. Overseth, "Measurement of the decay parameters of the Lambda0 particle," *Phys. Rev.*, vol. 129, pp. 1795–1807, 1963.

[55] M. Ablikim *et al.*, "Measurement of the asymmetry parameter for the decay $\bar{\Lambda} \to \bar{p}\pi^+$," *Phys. Rev.*, vol. D81, p. 012003, 2010.

[56] G. Bunce *et al.*, "Lambda0 Hyperon Polarization in Inclusive Production by 300-GeV Protons on Beryllium.," *Phys. Rev. Lett.*, vol. 36, pp. 1113–1116, 1976.